

**RESPONSE OF A SWIRL-STABILIZED FLAME TO TRANSVERSE
ACOUSTIC EXCITATION**

A Thesis
Presented to
The Academic Faculty

by

Jacqueline O'Connor

In Partial Fulfillment
of the Requirements for the Degree
Doctor of Philosophy in the
School of Aerospace Engineering

Georgia Institute of Technology
May 2012

COPYRIGHT 2011 BY JACQUELINE O'CONNOR

RESPONSE OF A SWIRL-STABILIZED FLAME TO TRANSVERSE ACOUSTIC EXCITATION

Approved by:

Dr. Tim Lieuwen, Advisor
School of Aerospace Engineering
Georgia Institute of Technology

Dr. Jerry Seitzman
School of Aerospace Engineering
Georgia Institute of Technology

Dr. Suresh Menon
School of Aerospace Engineering
Georgia Institute of Technology

Dr. Lakshmi Sankar
School of Aerospace Engineering
Georgia Institute of Technology

Dr. Ari Glezer
School of Mechanical Engineering
Georgia Institute of Technology

Date Approved: December 15, 2011

To my family and Alex

ACKNOWLEDGEMENTS

This thesis would not have been possible without the selfless and unfailing contribution of so many important people in my life. First, I want to thank my entire family, but especially to my parents, John and Sheryl; you've inspired and challenged me and prepared me for a successful and happy life, and for that I can never thank you enough. Finishing this thesis, I am more proud than I have ever been and it is a credit to your love and encouragement. I love you both so much. Thanks also to my brother Tom for making me laugh and think the deep thoughts. And to Alex, for being there every step of the way and being the bright spot in each and every day. I couldn't have done this without your constant love and support!

I also want to thank two of the most incredible mentors I've had in my technical career – my advisor, Tim Lieuwen, and my mentor, Keith McManus. To Tim, I couldn't have asked for a better advisor and it's truly been an honor to work with you. Thank you for treating our group as family; you've inspired us to be better thinkers and better people. To Keith, thank you for getting me into combustion instabilities in the first place and being a constant source of support all these years. I value your friendship and owe so much of this to you.

A special thanks to my best friends in the world, Eleanor Crane and Brittany Montgomery, for being the most honest and supportive friends I've ever had. You both inspire me beyond words and I look forward to a lifetime of crazy with the two of you. You saw something in me while we were all at the beginning of this journey and I'm a better person for having you in my life.

A world of thanks to the students of the Combustion Lab throughout the (many) years I've been here. First, to my sages, Preetham, Santosh S., and Santosh H., for making me believe in myself in the face of what seemed like the insurmountable task of a Ph.D. – I can't tell you how much I appreciate it. To my compatriots, Dong-hyuk Shin, Jack Crawford, and Shreekrishna – I would have never guessed that any of us would be here today without each other's support and fights over acoustics; I'm proud to have you as my co-graduates. To the Family, Chris Foley, Prabhakar Venkateswaran, and Andrew Marshall – I can't say that you kept me sane, but you kept me laughing, and for that I am

forever grateful. To my Team, Michael Aguilar and Michael Malanoski – good luck, I couldn't have asked for a better team. And to the rest of my Combustion Lab family, Sai, Bobby, Ben W., Ben E., Brad, Nick, Jordan, Vishal, Alberto, Michael Kolb, Brandon, Jim, Matt, Aimee, Julia, and all the others – thanks for being a network of support and ideas for so many years. I will miss it here and I couldn't have imagined doing this with a better group.

A very special thanks to the kids, Lee, Travis, Daniel, Colin, Jared, Charles, Charlotte, and especially Shweta Natarajan, for all your help and for teaching me to be a better mentor. You all brought a joy to this experience that I will miss.

Also, the extensive PIV and PLIF data in this thesis would not have been possible without Callum Gray and the team at LaVision.

Finally, I gratefully acknowledge the support of the National Science Foundation, the Department of Energy University Turbine Systems Research Program, GE Energy, and GE Aviation for their financial support to make this work possible.

TABLE OF CONTENTS

ACKNOWLEDGEMENTS	iv
LIST OF TABLES	ix
LIST OF FIGURES	x
LIST OF SYMBOLS AND ABBREVIATIONS	xxii
SUMMARY	xxiv
CHAPTER 1 - Introduction	1
Flame transfer function development	8
CHAPTER 2 – Experimental Method	32
Time-average flow field.....	36
Acoustic forcing.....	43
Diagnostics.....	47
Particle Image Velocimetry	47
Flame Luminosity	50
Smoke Visualization	50
Global Chemiluminescence Measurements	51
Pressure Measurements.....	52
CHAPTER 3 – Flame Transfer Function Results.....	54
Transverse to longitudinal velocity transfer function	54
Flame transfer function results.....	65

CHAPTER 4 – Recirculation Zone Dynamics	73
Analysis Methods.....	74
No forcing results, non-reacting flow	77
Effect of acoustic forcing on time-average flow, non-reacting flow	89
Dynamical response of flow to acoustic forcing, non-reacting flow	94
Reacting flow results.....	107
CHAPTER 5 – Shear Layer Dynamics.....	119
Behavior of the unforced flow	120
Effect of acoustic forcing on shear layer dynamics	125
Response of the flame to shear layer motion	165
CHAPTER 6 – Conclusions and Recommendations	170
Summary of contributions.....	170
Formulation of velocity-coupled flame response description.....	170
Description of response of swirling flow to transverse forcing based on flow stability.....	174
Recommendations for future work	176
APPENDIX A – Technical Drawings of Combustor	179
Details of combustor	179
Details of acoustic driving system	182
Speaker tubes	182
Sound system	182

Details of flow system	183
Flow path	183
APPENDIX B – Technical Drawings of Swirler.....	185
APPENDIX C – Details of Smoke System	187
APPENDIX D – Overview of Experimental Data.....	191
REFERENCES	261
VITA	271

LIST OF TABLES

Table 1. Azimuthal mode number conventions for jets and wakes after Ref. [75].	76
Table 2. Average phase difference between vorticity disturbances in the left and right jet centers at several conditions at a bulk velocity of $U_o=10$ m/s and a forcing frequency of $f_o=400$ Hz.....	140
Table 3. Value of swirling flow parameters from Loiseleux et al. formulation for stability calculation.	149
Table 4. Two-wave model conditions for non-reacting and reacting cases at 400 Hz out- of-phase acoustic forcing and 10 m/s bulk flow velocity.	161
Table 5. Overview of PIV data sets.	191
Table 6. Overview of luminescence flame data.....	252
Table 7. Overview of PLIF data.	254
Table 8. Overview of global chemiluminescence and two-microphone method pressure data.....	255

LIST OF FIGURES

Figure 1. Basic combustion instability feedback loop.	1
Figure 2. Combustion instability feedback loop with coupling mechanism.....	2
Figure 3. Mode geometry for a can (left) and annular (right [4]) combustor geometry showing the 1) longitudinal, 2) radial, and 3) azimuthal (or circumferential) mode..	3
Figure 4. Physical mechanisms causing heat release oscillations due to velocity fluctuations.....	5
Figure 5. Velocity disturbance mechanisms present in a longitudinally forced flame....	10
Figure 6. Velocity disturbance mechanisms in a transversely forced flame.....	12
Figure 7. Time-average structure of an annular swirling jet with vortex breakdown. The spanwise shear layers, vortex breakdown bubble, and flame are shown here.	16
Figure 8. Possible flow (a and b) and flame (c and d) configurations for two different vortex breakdown bubble structures where a,c) the bubble is lifted, and b,d) the bubble is merged with the centerbody wake.	18
Figure 9. Results from OH PLIF images for a harmonically excited, swirl-stabilized flame at $f = 270$ Hz and $u'/u_o = 0.21$ [50].	20
Figure 10. Flame CH* chemiluminescence fluctuation response as a function of longitudinal forcing amplitude at two frequencies for a swirl-stabilized flame [50].	21
Figure 11. Flame modeling configuration, where the solid line is the instantaneous flame location, the dotted line is the time-average flame location, ζ is the flame location, and β is the time-average flame aspect ratio.....	24

Figure 12. Experimental facility.	32
Figure 13. Comsol Multiphysics acoustic simulation of combustion geometry, amplitude of pressure fluctuations is shown for an out-of-phase forcing case.....	33
Figure 14. Specifications for the swirler nozzle cavity.....	35
Figure 15. Renderings of a) 30° swirler and b) centerbody.	36
Figure 16. Time-average a) normalized velocity and b) normalized vorticity for non-reacting flow at $u_0=10$ m/s, $S=0.85$	38
Figure 17. Time-average a) normalized velocity and b) normalized vorticity for reacting flow at $u_0=10$ m/s, $S=0.85$, $\phi=0.9$	39
Figure 18. Time-average a) normalized velocity and b) normalized vorticity for non-reacting flow at $u_0=10$ m/s, $S=0.5$	40
Figure 19. Time-average a) normalized velocity and b) normalized vorticity for reacting flow at $u_0=10$ m/s, $S=0.5$, $\phi=0.9$	41
Figure 20. Time-average velocity in the $r-\theta$ plane at a,b) $x/D = 0$, c,d) $x/D = 1$, and e,f) $x/D = 2$ for the unforced, non-reacting annular swirling jet, at $u_0=10$ m/s, $S=0.85$	42
Figure 21. Nozzle configuration, flame shape, and acoustic velocity and pressure perturbations for in-phase and out-of-phase acoustic forcing, from the side view (acoustic waves not shown to scale).	44
Figure 22. Amplitude of the reference transverse velocity fluctuations at the forcing frequency as a function of speaker input voltage, at $u_0=10$ m/s, $S=0.85$	46
Figure 23. Smoke injection points for both inner and outer shear layer visualization in an annular nozzle.	51

Figure 24. Experimental setup for flame transfer function measurements, with PMT for CH* chemiluminescence and pressure measurements.	52
Figure 25. Spectra of a) axial velocity fluctuations at $x/D=0.05$ and b) transverse velocity fluctuations along the centerline for an unforced reacting flow at a bulk velocity of $u_o=10$ m/s and equivalence ratio of 0.95.....	55
Figure 26. Axial velocity fluctuation amplitude for reacting flow with a) in-phase and b) out-of-phase forcing at a bulk velocity of $u_o=10$ m/s, $u'_{T,a}=1$ m/s, and a forcing frequency of $f_o=400-1800$ Hz.	56
Figure 27. Transverse to longitudinal velocity transfer function a) gain ($ F_{TL} $), and b) phase ($\angle F_{TL}$), for reacting flow with in-phase acoustic forcing, a bulk flow velocity of $u_o=10$ m/s, and equivalence ratio 0.9.....	57
Figure 28. Transverse to longitudinal velocity transfer function a) gain ($ F_{TL} $), and b) phase ($\angle F_{TL}$), for reacting flow with out-of-phase acoustic forcing, a bulk flow velocity of $u_o=10$ m/s, and equivalence ratio 0.9.....	57
Figure 29. Transverse to longitudinal velocity transfer function a) gain ($ F_{TL} $), and b) phase ($\angle F_{TL}$), for non-reacting flow with out-of-phase acoustic forcing, and a bulk flow velocity of $u_o=10$ m/s.....	58
Figure 30. Transverse to longitudinal velocity transfer function a) gain ($ F_{TL} $), and b) phase ($\angle F_{TL}$), for all cases.	59
Figure 31. Transverse to longitudinal velocity transfer function a) gain ($ F_{TL} $) on a log scale, and b) coherence squared, for all cases.....	59

Figure 32. Axial velocity spectra at $x/D=0.05$ for a) 400 Hz in-phase and b) 1800 Hz in-phase acoustic forcing a bulk flow velocity of $u_o=10$ m/s and equivalence ratio 0.9.	61
Figure 33. Magnitude of the normalized axial velocity fluctuations at the forcing frequency throughout the flow field for a) 400 Hz in-phase and b) 1800 Hz in-phase acoustic forcing a bulk flow velocity of $u_o=10$ m/s and equivalence ratio 0.9.	63
Figure 34. Flame transfer function a) gain, b) phase, c) coherence, and d) uncertainty in gain and phase for in-phase transverse forcing, out-of-phase transverse forcing, and longitudinal forcing at a bulk velocity of $u_o=10$ m/s, equivalence ratio of 0.9.	67
Figure 35. Flame transfer function gain comparison between F_{TL} weighted transfer function and standard flame transfer function based on a longitudinal acoustic reference velocity, at a bulk velocity of $u_o=10$ m/s, equivalence ratio of 0.9.	69
Figure 36. Variable flame anchoring position as a result of longitudinal mass flow fluctuations during transverse instability of an annular combustor, reproduced from Staffebach et al. [25].	71
Figure 37. Comparison of a) time-average and b) instantaneous vorticity for the unforced flow, $S=0.85$. Arrows in each plot indicated normalized velocity; zero velocity contours are plotted in light grey.	78
Figure 38. Spectra of normalized a,c,e) axial component and b,d,f) transverse component of velocity along the time-average centerline (a,b), left-hand vortex breakdown boundary (c,d – zoomed in), and right-hand vortex breakdown boundary (e,f – zoomed in) for non-reacting flow with no acoustic forcing, at $u_o=10$ m/s, $S=0.85$. Fluctuation amplitude is normalized by the bulk velocity, $u_o=10$.	80

Figure 39. Precessing vortex core shown through the filtered velocity field in the $r-\theta$ plane at $x/D=1$ and a) $t=0.5$ ms, b) 4.1 ms, c) 10.1 ms, d) 13.1 ms, e) 17.1 ms, f) 20.1 ms, for a non-reacting, non-forced flow at $u_o=10$ m/s, $S=0.85$. Gray regions indicate approximate location of inner and outer shear layer at $x/D=1$	83
Figure 40. Notional picture of self-excited motion showing both the jet deformation ($m = -2$ mode) and coherent structure motion ($m = -1$ mode) for an unforced flow.	83
Figure 41. Spectra of mode numbers at $r/D = 0.6$ $r-\theta$ plane at $x/D = 1$, for a non-reacting, unforced flow at $u_o=10$ m/s, $S=0.85$	86
Figure 42. Modal energy distribution of energy integrated from 0-200 Hz plotted as a function of a) mode number at three radii and b) radius at five mode numbers, for a non-reacting, unforced flow at $u_o=10$ m/s, $S=0.85$. Gray regions in b) indicate the approximate location of the inner and outer shear layer.....	87
Figure 43. Dependence of jet spreading angle upon transverse acoustic forcing amplitude for non-reacting flow at $u_o=10$ m/s, $S=0.85$	91
Figure 44. Flow fields for the transversely forced bifurcation case, 800 Hz out-of-phase, at four excitation amplitudes where a) 3.3 m/s and b) 4.3 m/s transverse velocity cases show the velocity field before the flow bifurcation, and c) 4.6 m/s and d) 5.2 m/s show the velocity field after. All flow conditions are non-reacting at $u_o=10$ m/s, $S=0.85$. Colorbar shows axial velocity normalized by bulk flow velocity.....	92
Figure 45. Precessing vortex core shown through the filtered velocity field in the $r-\theta$ plane at $x/D = 1$, for a non-reacting flow, 400 Hz out-of-phase forcing at $v'/\bar{u} = 0.1$, $u_o=10$ m/s, $S=0.85$	97

Figure 46. Precessing vortex core shown through the filtered velocity field in the $r - \theta$ plane at $x/D = 1$, for a non-reacting flow, 400 Hz out-of-phase forcing at $v'/\bar{u} = 0.7$, $u_o = 10$ m/s, $S = 0.85$	99
Figure 47. Mode strength for three forcing amplitudes at $r/D = 0.6$ for a) 400 Hz, b) 800 Hz, c) 1200 Hz out-of-phase forcing at $u_o = 10$ m/s, $S = 0.85$	102
Figure 48. Mode strength for three forcing amplitudes at $r/D = 0.6$ a) 400 Hz, b) 800 Hz, c) 1200 Hz in-phase forcing at $u_o = 10$ m/s, $S = 0.85$. Note: mode $m = -2$ and $m = -3$ have very similar amplitudes at $v/u_o = 0.06$ in a) and the symbols overlap.	104
Figure 49. Modal energy distribution (per Hertz) for radially integrated a) low frequency motion below 200 Hz and b) motion at the forcing frequency, 400 Hz, for 400 Hz out-of-phase forcing at $u_o = 10$ m/s, $S = 0.85$	106
Figure 50. Spectra of normalized a) axial component and b) transverse component of velocity along the time-average centerline for reacting flow with no acoustic forcing, at $u_o = 10$ m/s, $S = 0.5$, and equivalence ratio of 0.9. Also shown is a comparison of the normalized non-reacting and reacting c) axial and d) transverse velocity fluctuations along the centerline of the flow field at $x/D = 1$	109
Figure 51. Dependence of time-average flame angle upon transverse acoustic forcing for a) out-of-phase and b) in-phase forcing for reacting flow at $u_o = 10$ m/s, $S = 0.5$, and equivalence ratio of 0.9.....	110
Figure 52. Line-of-sight overlays of 500 images of the flame at several forcing amplitudes a) 0.1 m/s, b) 0.5 m/s, c) 0.6 m/s and d) 0.7 m/s transverse velocity.	

Acoustic forcing is in-phase at 1800 Hz, flow velocity of 10 m/s, swirl number of 0.5, and equivalence ratio of 0.9.	111
Figure 53. Flame luminescence images for 400 Hz a) out-of-phase and b) in-phase forcing conditions for a flow velocity of 10 m/s, swirl number of 0.5, and equivalence ratio of 0.9.	112
Figure 54. Absolute value of vorticity field showing the flame wrinkling due to inner shear layer rollup for 900 Hz out-of-phase at a flow velocity of 10 m/s, swirl number of 0.5, and equivalence ratio of 0.9.	113
Figure 55. Vorticity in a swirling flow showing inner and outer shear layer vortex rollup for an a) $r - x$ cut and b) a three-dimensional vorticity isosurface at $\Omega = 75,000 s^{-1}$ [130].	114
Figure 56. Acoustic parameter space for non-reacting and reacting test cases. Plus marks the location of reproducible bifurcation behavior, and circle marks the location of intermittent bifurcation behavior	117
Figure 57. Instances of shear layer rollup in an unforced annular swirling jet in both the a) axial and b) azimuthal shear layers, with mean flow velocity of 10 m/s, swirl number of 0.85.	122
Figure 58. Six time instances of unforced, non-reacting jet flow show natural shear layer rollup, for $u_o=10$ and $S=0.85$. Normalized vorticity is shown in color; images are 0.1 ms apart.	124
Figure 59. Collective interaction in shear layers from Ho and Nossier [157] (left) and from the current study (center and right) in the inner shear layer of the annular jet	

with acoustic forcing, out-of-phase forcing at 400 Hz at an amplitude of $v'/U_o=0.35$ and a bulk velocity of 10 m/s and swirl number of 0.85.....	126
Figure 60. Collective interaction event in the inner shear layer with a bulk velocity of 10 m/s, swirl number of 0.85, and out-of-phase acoustic forcing at 400 Hz at an amplitude of $v'/U_o=0.35$	127
Figure 61. Collective interaction even showing the structure formation and separation at the same conditions as Figure 60. Each image is 0.3 ms apart.	128
Figure 62. Collective interaction as seen in a velocity field from PIV for a non-reacting case at a bulk velocity of 10 m/s, swirl number of 0.85, and out-of-phase acoustic forcing at 400 Hz at an acoustic amplitude of $v'/U_o=0.35$. Structure from collective interaction is shown in the black circle.	129
Figure 63. Notional picture of the flow field for a transversely forced swirling jet with a) out-of-phase and b) in-phase acoustic forcing. Coherent structures in the inner shear layer (ISL) and outer shear layer (OSL) travel downstream, bending the jet column as they pass.	133
Figure 64. Comparison of instantaneous (top) and filtered (bottom) velocity at the forcing frequency for in-phase forcing at 400 Hz, non-reacting flow at $u_o=10$ m/s, $S=0.85$. White lines trace the vortex.	134
Figure 65. Comparison of instantaneous (top) and filtered (bottom) velocity at the forcing frequency for out-of-phase forcing at 400 Hz, non-reacting flow at $u_o=10$ m/s, $S=0.85$. White lines trace the vortex.	135

Figure 66. Normalized instantaneous (left) and filtered (right) velocity and vorticity field for a) out-of-phase and b) in-phase acoustic forcing for reacting flow at a bulk velocity of $U_o=10$ m/s and a forcing frequency of $f_o=400$ Hz.	137
Figure 67. Snapshot of a helical shear layer instability in a swirling annular jet, used to visualize coherent structures from LES simulation [158] under longitudinal, self-excited oscillations.	138
Figure 68. Phase of vorticity along shear layers for a) non-reacting and b) reacting flow at a bulk velocity of $U_o=10$ m/s and a forcing frequency of $f_o=400$ Hz out-of-phase.	139
Figure 69. Distribution of mode amplitude at the forcing frequency integrated over radii $r/D=0-1$ plotted as a function of mode number at $x/D=0$ for a non-reacting, flow forced with a) 400 Hz, b) 800 Hz and c) 1200 Hz forcing at $u_o=10$ m/s, $S=0.85$...	142
Figure 70. Distribution of mode amplitude at the forcing frequency plotted as a function radius for several mode numbers for a non-reacting, flow forced at 400 Hz a) in-phase and b) out-of-phase forcing at $u_o=10$ m/s, $S=0.85$. Gray areas approximate the location of the inner and outer shear layers at $x/D=0$, where these data were taken.	144
Figure 71. Distribution of mode amplitude at the forcing frequency integrated over radii $r/D=0-1$ plotted as a function of mode number at $x/D=1$ for a non-reacting, flow forced with 400 Hz forcing at $u_o=10$ m/s, $S=0.85$	146
Figure 72. Swirling flow stability map as a function of swirl number (S) and backflow ratio (a) showing helical mode absolute (shaded region) and convective (white	

region) stability boundaries, from Loiseleux et al. [153]. Green lines indicate values of S and a for current flow field.....	147
Figure 73. Time-average axial velocity profiles at three downstream stations for unforced flow at $u_o=10$ m/s and $S=0.85$	148
Figure 74. Amplitude of modes a) $m = -1$, b) $m = 0$, and c) $m = 1$ at the forcing frequency and integrated over $r/D=0-1$ for non-reacting flow in the $r-\theta$ plane for 400 Hz forcing at $u_o=10$ and $S=0.85$	151
Figure 75. Spectra of several mode numbers integrated over radius and frequency in the $r-\theta$ plane at $x/D=1$, for a non-reacting, flow forced at 400 Hz a) in-phase and b) out-of-phase at $u_o=10$ m/s, $S=0.85$	153
Figure 76. Distribution of mode amplitude at the low frequencies integrated over radii $r/D=0-1$ plotted as a function of mode number at $x/D=1$ for a non-reacting, flow forced with 400 Hz forcing at $u_o=10$ m/s, $S=0.85$	154
Figure 77. Normalized amplitude of axial velocity fluctuations for a) non-reacting and b) reacting flow at the forcing frequency at a bulk velocity of $u_o=10$ m/s and a forcing frequency of $f_o=400$ Hz out-of-phase.	156
Figure 78. Normalized amplitude of transverse velocity fluctuations for a) non-reacting and b) reacting flow at the forcing frequency at a bulk velocity of $u_o=10$ m/s and a forcing frequency of $f_o=400$ Hz out-of-phase.....	157
Figure 79. Normalized amplitude of vorticity fluctuations for a) non-reacting and b) reacting flow at the forcing frequency at a bulk velocity of $u_o=10$ m/s and a forcing frequency of $f_o=400$ Hz out-of-phase.	158

Figure 80. Time-average vorticity in shear layers for the a) non-reacting and b) reacting cases at a bulk velocity of $u_o=10$ m/s and a forcing frequency of $f_o=400$ Hz out-of-phase. Dotted lines indicate exponential curve fits to calculate decay rates with downstream distance.	160
Figure 81. Comparison of transverse velocity fluctuation amplitude in left and right jet of the a) non-reacting and b) reacting data and the two-wave interaction model. The bulk velocity was $u_o=10$ m/s and the forcing frequency was $f_o=400$ Hz out-of-phase.	162
Figure 82. Comparison of transverse velocity fluctuation amplitude in left and right jet of the a) non-reacting and b) reacting data and the two-wave interaction model. The bulk velocity was $u_o=10$ m/s and the forcing frequency was $f_o=400$ Hz in-phase.	163
Figure 83. Comparison of transverse velocity fluctuation amplitude in left and right jet of the non-reacting data and the two-wave interaction model. The bulk velocity was $u_o=40$ m/s, non-reacting flow and the forcing frequency was $f_o=400$ Hz in-phase. Here, a) shows the amplitude of transverse fluctuations over the entire flow field, while b) shows the cuts at the jet centers as above.	164
Figure 84. Time series of OH PLIF images showing centerbody stabilized swirl flame forced at 400 Hz out-of-phase, $u_o=10$ m/s, $S=0.5$, $\phi=0.9$. Yellow circles indicate locations of flame wrinkling due to vortex rollup in a helical pattern.	166
Figure 85. Examples of flame response, via luminescence imaging, for a) in-phase (symmetric) and b) out-of-phase (asymmetric) forcing conditions for a flow velocity of 10 m/s, swirl number of 0.5, and equivalence ratio of 0.9. Images are 0.6 ms apart in each filmstrip.	168

Figure 86. Velocity disturbance mechanisms in a transversely forced flame.....	171
Figure 87. Isoview of combustor	180
Figure 88. Details of the swirler box at the dump plane.....	181
Figure 89. Details of the dump plane around the swirler box. Includes two unused air ports (left- and right-most holes) as well as port for hydrogen torch igniter. Swirler box mates with this part in the notched section detailed in the upper right of the figure.	181
Figure 90. Details of the exit plane, including location of laser window and laser window bracket.....	182
Figure 91. Drawing of 45° swirler.	185
Figure 92. Drawing of 30° swirler.	186
Figure 93. Olive oil smoke production device with air-in port, flow exit port, and indications for the location of torch heating and optimal oil level.	187
Figure 94. Specifications on the inner shear layer smoke delivery system.	188
Figure 95. Specifications for the outer shear layer smoke delivery with a) technical drawings, b) plenum configuration, and c) outer shear layer smoke delivery holes.	189

LIST OF SYMBOLS AND ABBREVIATIONS

A	Amplitude
A_m	Counter-clockwise spatial mode amplitude
B_m	Clockwise spatial mode amplitude
D	Nozzle diameter
F	Flame transfer function
F_L	Longitudinal flame transfer function
$F_{L\omega}$	Longitudinal to vortical velocity transfer function
F_T	Transverse flame transfer function
F_{TL}	Transverse to longitudinal velocity transfer function
$F_{T\omega}$	Transverse to vortical velocity transfer function
G	Flame surface
R	Centerbody radius
Re	Reynolds number
RG	Rayleigh gain
S	Swirl number
S_L	Laminar flame speed
T	Period
d_{inner}	Inner annulus diameter
d_{outer}	Outer annulus diameter
f	Frequency
h	Nozzle dimension
m	Mode number
\hat{n}	Flame normal vector
p'	Acoustic pressure fluctuation
q'	Heat release fluctuation
\bar{q}	Time-average heat release
r	Radial coordinate
t	Time
u	Axial velocity
u'	Axial velocity fluctuation
\vec{u}	Velocity vector
\bar{u}	Time-average velocity
$u_{c,v}$	Vortex convection speed
\hat{u}	Frequency domain velocity
u_L	Longitudinal reference velocity
$u'_{L,a}$	Longitudinal acoustic velocity fluctuation
u_o	Bulk velocity

u_T	Transverse reference velocity
$u'_{T,a}$	Transverse acoustic velocity fluctuation
v	Transverse velocity
v'	Transverse velocity fluctuation
x	Axial coordinate
z	Into plane coordinate
Ω	Vorticity
α	Vorticity decay rate
β	Flame aspect ratio
ζ	Flame location
θ	Azimuthal coordinate
φ	Equivalence ratio
ϕ	Phase
ω	Angular frequency

SUMMARY

This work addresses the issue of transverse combustion instabilities in annular gas turbine combustor geometries. While modern low-emissions combustion strategies have made great strides in reducing the production of toxic emissions in aircraft engines and power generation gas turbines, combustion instability remains one of the foremost technical challenges in the development of next generation combustor technology. To that end, this work investigates the response of a swirling flow and swirl-stabilized flame to a transverse acoustic field using a variety of high-speed laser techniques, especially high-speed particle image velocimetry (PIV) for detailed velocity measurements of this highly unsteady flow phenomenon.

Several important issues are addressed. First, the velocity-coupled pathway by which the unsteady velocity field excites the flame is described in great detail. Here, a transfer function approach has been taken to illustrate the various pathways through which the flame is excited by both acoustic and vortical velocity fluctuations. It has been shown that while the direct excitation of the flame by the transverse acoustic field is a negligible effect in most combustor architectures, the coupling between the transverse acoustic mode in the combustor and the longitudinal mode in the nozzle is an important pathway that can result in significant flame response. In this work, the frequency response of this pathway as well as the resulting flame response is measured using PIV and chemiluminescence measurements, respectively.

Next, coupling between the acoustic field and the hydrodynamically unstable swirling flow provides a pathway that can lead to significant flame wrinkling by large

coherent structures in the flow. Swirling flows display two types of hydrodynamic instability: an absolutely unstable jet and convectively unstable shear layers. The absolute instability of the jet results in vortex breakdown, a large recirculation zone along the centerline of the flow. Experiments in this study showed that high amplitudes of acoustic forcing could alter both the time-average and dynamical characteristics of this structure, although very little effect was measured at low amplitude forcing. The convectively unstable shear layers, however, displayed significant response to the acoustics, even at low levels of acoustic forcing, and are responsible for the majority of the flame wrinkling and resultant heat release fluctuation of the flame. The modal structure of the transverse acoustic field played a large role in the characteristics of the response of these structures.

The two major contributions of this work are the development of a detailed velocity-coupled pathway for transversely forced flames, as well as a methodology based on the principles of hydrodynamic stability theory by which to assess the response of complex combusting flows to acoustic fields. Additionally, a large archival data set has been produced with measurements of velocity and flame behavior for future modeling and analysis.

CHAPTER 1

INTRODUCTION

Combustion instabilities have long plagued the development and operation of high performance combustion technologies. These instabilities, the result of a coupling between flame heat release fluctuations and resonant acoustics inside the combustion chamber, have proven to be destructive to engine hardware, burdensome on engine operation, and detrimental to engine performance and emissions. The coupling between fluctuating heat release sources and sound fields was predicted by Lord Rayleigh [1], where he described the process by which heat release sources, when fluctuating in phase with acoustic fluctuations in the chamber, can add energy to the sound field and create a feedback loop between the heat release source and the acoustic field. The basic structure of this feedback loop is shown in Figure 1.

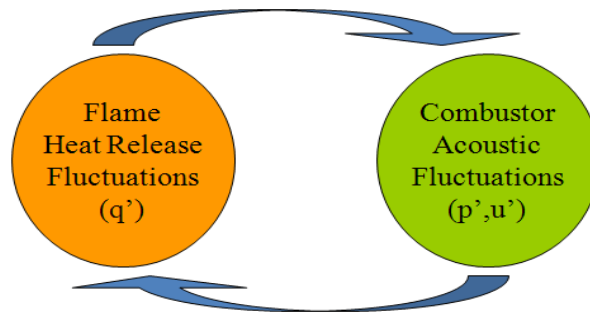


Figure 1. Basic combustion instability feedback loop.

In the case described in Figure 1, the interaction between the sound field and heat release source is direct. In the situation where the heat release source is a flame, the coupling between heat release fluctuations and the acoustic field often contains a coupling mechanisms, or intermediary step between the acoustic fluctuations and the flame heat release fluctuations. These processes can produce heat release fluctuations in

a variety of ways, including fluctuations in fuel flow, flame area, flame speed, and heat of reaction of the mixture [2, 3]. This modified feedback loop is shown in Figure 2.

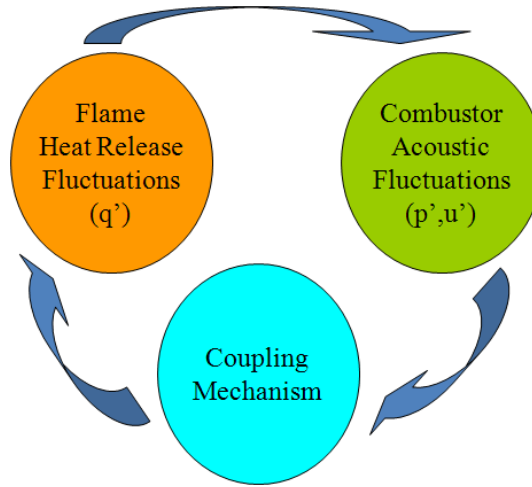


Figure 2. Combustion instability feedback loop with coupling mechanism.

This feedback mechanism, a coupling between flame heat release fluctuations, combustor acoustics, and one or more coupling mechanisms, is the basis for combustion instability events in a variety of high performance combustion technologies. Often these instability events are differentiated based on the acoustic mode excited in the combustion chamber. The three components of the acoustic modes possible in a combustion chamber are the longitudinal, circumferential (or azimuthal), and the radial modes, each of which is shown in Figure 3 for both a can combustor and annular combustion geometry.

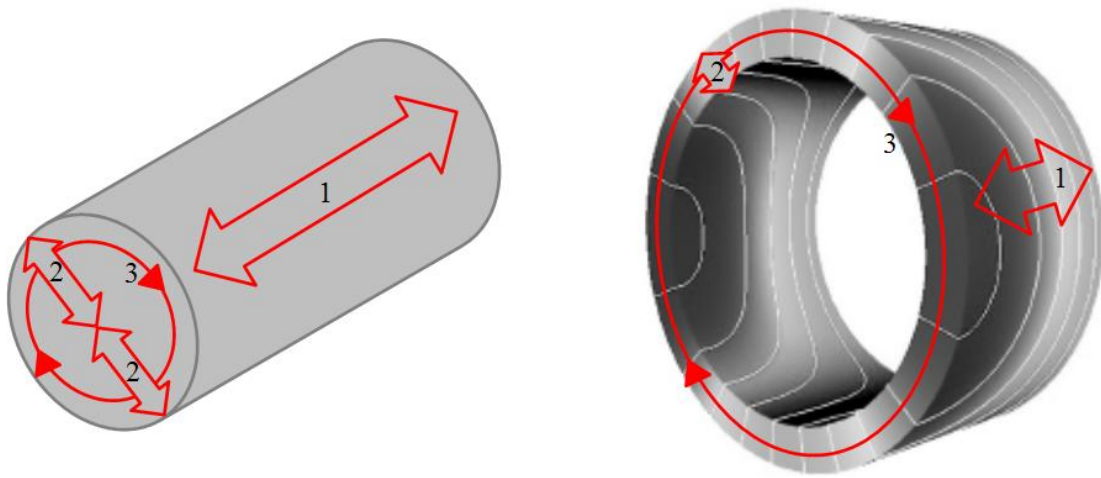


Figure 3. Mode geometry for a can (left) and annular (right [4]) combustor geometry showing the 1) longitudinal, 2) radial, and 3) azimuthal (or circumferential) mode.

The longitudinal mode instabilities have been studied in a variety of combustion technologies, but in gas turbine engines in particular [5-11]. More specifically, instabilities have caused major challenges in the development of lean, premixed combustors used in low NO_x gas turbines [12]. In this mode of instability, fluctuations in the acoustic field oscillate in the direction of flow.

The radial and azimuthal modes are collectively referred to as “transverse” modes, as the acoustic field oscillates in a direction transverse to the direction of flow. Transverse instabilities have been discussed frequently in the afterburner [13-16], solid rocket [17, 18], and liquid rocket literature [19-24]. Significantly less work has been done on the analysis and characterization of transverse instabilities for gas turbine applications, typically characterized by a swirling, premixed flame [11, 25-29]. There are two key application areas where transverse acoustic oscillations are of significant

practical interest. The first occurs in annular combustion systems, such as the instabilities in the Solar Mars 100, Alstom GT24, GE LM6000, Siemens V84.3A, and other engines [26, 30-32]. Because of the larger length scales involved, these instabilities often occur at the “lower” frequencies (e.g., 100’s of Hertz) that are typical of the longitudinal oscillations observed in can combustion systems. While these modes cannot typically be simulated without the full annulus, several of these studies report the results of longitudinal instability tests obtained on single nozzle rigs scaled to have similar longitudinal acoustic frequencies as the observed transverse instabilities [30, 33, 34]. The second application where transverse instabilities are of interest is the higher frequency transverse oscillations encountered in can combustion systems. These instabilities occur at relatively high frequencies, e.g., in the 1-5 kHz range, and scale with the combustor can diameter. While relatively little treatment of these high frequency oscillations can be found in the technical literature, there is significant discussion of them in the gas turbine operator/user community; e.g., see Combined Cycle Journal [35] or Sobieski and Sewell’s chapter in *Combustion Instabilities in Gas Turbine Engines* [31].

One of the significant issues associated with transverse instabilities in annular gas turbines is the fact that each nozzle is subjected to a different acoustic field than its neighbors. In the case of a longitudinal instability, the oscillations in the acoustic field, moving in the same direction as the flow, are the same at each azimuthal location and affect each nozzle equally. During a standing wave transverse instability, the acoustic field strength may vary for each nozzle as the fluctuation amplitude varies in the circumferential direction. In this case, it is possible for several nozzles to be positioned at pressure anti-nodes, and several at pressure nodes, two very different acoustic forcing

conditions for both the flame and the nozzle flow field. For a traveling wave instability, where the transverse mode shape may spin or wander in the azimuthal direction, the difference between the acoustic field experienced by each nozzle is a function of the forcing frequency and the speed of rotation of the wave. In both these cases, the acoustic field that results from a transverse mode is fundamentally different from that in the longitudinal direction, and, as will be discussed in the ensuing chapters, can have a significant effect on the resulting flow and flame response.

In this work, the key problem of interest is the manner in which the flame responds to oscillations in flow velocity. This is referred to as the “velocity coupled” response mechanism [36-40], to be distinguished from the also important “fuel/air ratio coupling” [9, 41] mechanism, or the probably negligible “pressure coupling” mechanism [3]. Flow oscillations lead to flame wrinkling that, in turn, causes oscillations in flame surface area and rate of heat release. This pathway of flame heat release fluctuation is shown in Figure 4, which has been reproduced from Shreekrishna and Lieuwen [42].

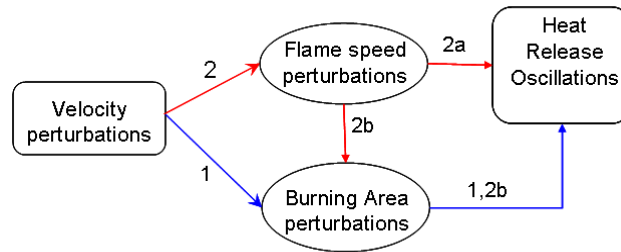


Figure 4. Physical mechanisms causing heat release oscillations due to velocity fluctuations.

While acoustic flow oscillations can directly excite the flame, they also excite organized flow instabilities associated with shear layers, wakes, or the vortex breakdown

bubble [10, 43, 44]. These velocity coupling mechanisms are the focus of Chapters 4 and 5 of this thesis. Taken together, there are a number of potential sources of flow disturbances that can lead to heat release oscillations. Two of these sources are directly acoustic in origin - transverse acoustic motions associated with the natural frequencies/mode shapes of the combustion system, and longitudinal oscillations in the nozzle due to the oscillating pressure difference across the nozzle. Simulations by Staffelbach (2009) suggest that it is these longitudinal mass flow oscillations that most significantly control the flame response to the imposed transverse disturbance.

Studies suggest that vortical flow oscillations also have a significant role in the flame's heat release response [45-47]. In other words, acoustic oscillations excite flow instabilities that, in turn, excite the flame. As such, the receptivity of these flow instabilities to both transverse and longitudinal acoustic oscillations must be considered. For example, consider the convectively unstable shear layers, which form tightly concentrated regions of vorticity through the action of vortex rollup and collective interaction [48]. The transverse acoustic oscillation will disturb them in both normal and parallel directions. Normally incident transverse acoustic oscillations will push the shear layers from side to side in a flapping manner, while parallel incidence will graze over them. In contrast, longitudinal oscillations will lead to an axially oscillating core flow velocity that will excite an oscillation in shear layer strength [49, 50]. Other literature on the response of wakes and swirling flows to longitudinal and transverse excitation can be found in several references [10, 51, 52].

These disturbance modes are difficult to separate in complicated geometries and all play some role in exciting the flame. Although the initial disturbance is transverse,

the disturbance velocity field that is created in the region of the flame is highly three-dimensional [25, 26]. This is significant in that the flame will experience a varying type of disturbance along its length. For example, a point in the middle of the flame may experience a strong transverse acoustic excitation source locally, as well as the disturbance from a vortex that was excited at the nozzle exit and has convected downstream. Complex interactions like these are difficult to separate, and it is one of the goals of this work to understand these characteristics of the disturbance field.

Having discussed some basic features of the transverse forcing problem, the focus of this thesis, the response of a swirl-stabilized flame to transverse acoustic excitation, is discussed in more depth. To start, the nature of the flame response to these acoustic modes is discussed before delving further into the response of the swirling flow itself to a range of acoustic forcing conditions.

Returning to the combustion instability feedback loop, shown in Figure 3, the flame response metric that controls the gain of this feedback loop is the global flame response, or the heat release fluctuation of the entire flame over an acoustic cycle. Quantification of global flame response is often in the form of a flame transfer function. In the case of velocity coupled flame response, the definition of the flame transfer function is given as the normalized flame heat release fluctuation divided by a normalized reference velocity fluctuation [53], as is shown in Equation (1).

$$F = \frac{q'(f_o, A)/\bar{q}}{u'_{ref}(f_o, A)/\bar{u}} \quad (1)$$

Flame transfer functions have been measured and calculated for longitudinally excited flames in several studies [54-59]. Here, the reference velocity has usually been

defined as the axial velocity fluctuation at the nozzle exit, measured using a two microphone technique or hot-wire anemometry. An important motivation for determining these transfer functions is that they isolate the flame response and can be used as a submodel in a larger system dynamics model. However, because the actual velocity field along the flame front, $u' x$, may vary substantially in amplitude and phase from u'_{ref} , F should not be interpreted as describing the flame response alone – it also depends upon certain features of the combustor system. This dependence is particularly important for transversely forced flames, which are the focus of the present study. The remainder of this section describes the motivation behind measuring flame transfer functions and how a detailed understanding of the velocity coupling physics informs a better understanding of the definition and meaning of the flame transfer function for both longitudinally and transversely forced flames.

Flame transfer function development

The behavior of self-excited combustion instabilities is dictated by the Rayleigh gain [60], which is given in Equation (2),

$$RG = \frac{1}{T} \int_0^T p'(t)q'(t)dt \quad (2)$$

where $p'(t)$ is the pressure fluctuation in time, $q'(t)$ is the flame heat release fluctuation in time, and T is the period of the fluctuation cycle.

The Rayleigh criterion states that the gain of the thermoacoustic instability is determined by the phase between the pressure and heat release fluctuations. If the absolute value of this phase is less than $\pi/2$, the Rayleigh gain (RG) will be greater than

zero, indicating that the instability will amplify. Conversely, if this phase is greater than $\pi/2$, the instability is damped. While the pressure fluctuation term, $p'(t)$, can be solved for by analyzing the acoustic modes of the combustion chamber, the heat release fluctuation term, $q'(t)$, is dependent on complicated flow and flame dynamics.

A transfer function approach has been historically used to describe these flame-flow dynamics. The form of the transfer function depends on the dominant coupling mechanism. In a velocity-coupled instability, the heat release fluctuation takes the form,

$$q' = Fu'_{ref} \quad (3)$$

where q' is the globally integrated heat release fluctuation, u'_{ref} is the reference velocity fluctuation, and F is the flame transfer function describing the relationship between flame heat release fluctuations and reference velocity perturbations. Thus, F is a global quantity that describes overall flame heat release fluctuations that are excited by a chosen reference quantity.

As discussed above, the reference velocity for a longitudinally forced flame has been well established as the acoustic velocity fluctuation at the base of the flame. This reference velocity is not only experimentally tractable, but captures the driving physics behind the flame response. The initial longitudinal acoustic velocity fluctuation causes disturbances on the flame surface through the action of a “base wave” or “root wave” [61, 62], but also excites vortical velocity motions that wrinkle the flame [63-66]. These velocity disturbance field pathways are shown in Figure 5.

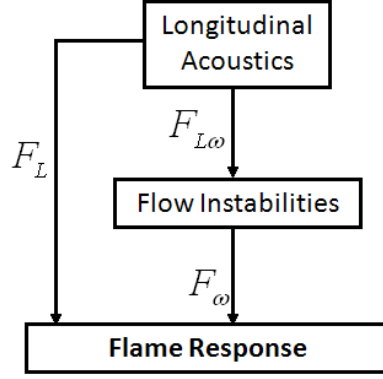


Figure 5. Velocity disturbance mechanisms present in a longitudinally forced flame.

F can be expressed in terms of the pathways shown in Figure 5. The flame is excited directly by acoustic velocity disturbances, as well as acoustically excited vortical disturbances. The flame responds quite differently to velocity disturbances arising from acoustic and vortical disturbances because of their substantially different phase speeds and length scales. As such, the same value of u'_{ref} may lead to very different characteristics of the vortical velocity field downstream [67]. To illustrate, the heat release expression for the longitudinally forced case is broken into two constituent disturbance parts:

$$q' = F_L + F_{L,\omega} F_\omega u'_{L,a} \quad (4)$$

where F is now the sum of two components, the flame transfer function due to acoustic velocity fluctuations, F_L , and the product of the velocity transfer function describing the coupling between acoustic and vortical motions, $F_{L,\omega}$, and the flame transfer function describing the flame response to vortical motion, F_ω . It should be noted, though, that an assumption of linearity has been made in this framework by the multiplication of $F_{L,\omega}$ and F_ω . If either of these sub-transfer functions are highly nonlinear in nature, this

framework would not be applicable. Historically, though, flame transfer function measurements have been made in the linear regime and so this nonlinearity should appear rarely.

The reference velocity here is the incident longitudinal acoustic velocity, $u'_{L,a}$. Significantly, it shows that by using a single reference velocity, $u'_{L,a}$, the flame transfer function is not only a function of the actual flame response, F_L and F_ω , but also the shear layer response, $F_{L,\omega}$. Thus, the exact same flame could exhibit different transfer function characteristics if the shear layer response is different.

These pathways have long been established in the case of longitudinal forcing and efforts towards measuring and predicting both the F_L [62] and $F_{L,\omega}F_\omega$ [63, 66] terms have been made. Transverse modes of combustion instability open new velocity disturbance pathways that incorporate both transverse and longitudinal acoustic motion, as well as the acoustic to vortical coupling mechanisms. The incident transverse acoustic perturbation may directly disturb the flame, as seen in the work by Ghosh *et al.* [68] for rocket injectors. The transverse acoustic pressure field also leads to longitudinal acoustic fluctuations in the flame nozzle region, as shown by Staffelbach *et al.* [25] in simulation and in experimental results from O'Connor *et al.* [69]. The longitudinal acoustic disturbance, a result of the fluctuating pressure from the transverse mode, leads to excitation of a longitudinal acoustic field in and around the nozzle area. Additionally, vortical velocity disturbances are excited through both longitudinal and transverse acoustic excitation. A study by Rogers and Marble [15] shows an example of this coupling in a high blockage-ratio combustor, where a self-excited transverse instability

lead to asymmetric vortex shedding from the edges of the triangular bluff-body. These disturbance mechanisms and their pathways are shown in Figure 6.

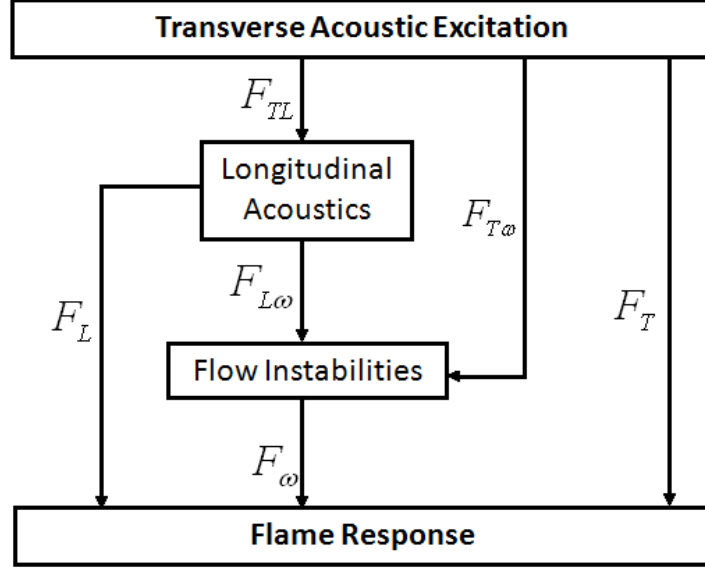


Figure 6. Velocity disturbance mechanisms in a transversely forced flame.

Similar to the decomposition of the longitudinally forced disturbance field in Equation (4), the processes in Figure 6 can be expressed as:

$$q' = [F_T + F_{TL}F_L + F_{T\omega} + F_{TL}F_{L\omega} \quad F_{\omega}] u'_{T,a} \quad (5)$$

where F_T is the flame transfer function describing the coupling between flame response and transverse acoustic fluctuations, F_{TL} is the velocity transfer function describing the coupling between the transverse and longitudinal acoustic motion at the nozzle exit, F_L is the flame transfer function describing the coupling between flame response and longitudinal acoustic fluctuations, $F_{T\omega}$ and $F_{L\omega}$ are the velocity transfer functions describing the acoustic to vortical velocity coupling, F_{ω} is the flame transfer function describing the coupling between flame heat release fluctuations and vortical motion, and

$u'_{T,a}$ is the transverse acoustic velocity, or the reference velocity for this form of the transfer function.

Each of these sub-transfer function describe can describe a variety of processes, particularly in the case of the excitation of vortical structures by acoustic fluctuations (several different vortical structures could be excited at once, each with different coupling characteristics). Additionally, these transfer functions can be a function of frequency as well as forcing amplitude, as will be seen in the work described in Chapters 3-5.

Although quantifying each of these “sub” transfer functions (F_T , F_L , F_{TL} , etc.) is an essential step towards a more complete understanding of flame response to transverse acoustic excitation, two important considerations stand out. First, what is the relative contribution of each of these sub-functions to the overall flame transfer function, F ? Second, what is the proper reference velocity for the resulting flame transfer function in light of the relative importance of each of these sub-functions? In the longitudinally forced example, the longitudinal acoustic velocity fluctuation, $u'_{L,a}$, is the proper reference velocity because it is not only a source of direct flame disturbance (via F_L), but also the source of the vortical velocity fluctuations (via $F_{L\omega}$) that cause significant flame heat release fluctuation.

For the transversely forced flame, it would seem intuitive that the transverse acoustic velocity is the proper reference velocity since it is the “source” disturbance, but several issues arise. First, where is the location of this reference velocity? Second, is the direct flame heat release fluctuation from the transverse acoustic excitation branch (F_T)

significant enough to warrant the transverse velocity as a proper reference? Third and more significantly, how important is the transverse to longitudinal coupling branch and could the gain of the transfer function F_{TL} be large enough to cause longitudinal motions to dominate the flame response? The answer to the third question may supersede the first two questions. Determining the role of F_{TL} and the relative strength of the transverse and longitudinal acoustic motion is the first step towards developing a flame transfer function with physical significance. The transverse to longitudinal velocity transfer function is given as,

$$F_{TL} = \frac{u'_{L,a}(f_o, A)}{u'_{T,a}(f_o, A)} \quad (6)$$

This transfer function describes the resulting axial velocity fluctuation divided by the incident transverse velocity fluctuation. If the gain of this transfer function is significantly greater than one, the flame response may be largely a result of the longitudinally driven pathways – in this case, the more appropriate reference velocity for the transversely excited flame is the longitudinal acoustic velocity. Conversely, if the amplitude of the transfer function is significantly less than unity, the dominant acoustic velocity fluctuation would be in the transverse direction and would drive both the vorticity generation, through $F_{T,\omega}$, and the flame response.

As the frequency of transverse acoustic excitation is modulated, the amplitude of longitudinal velocity fluctuations changes due to acoustic response of the nozzle section. Studies by Schuller *et al.* [70] and Noiray *et al.* [71] have both used external transverse acoustic disturbances to characterize the resonant frequencies of unconfined burners. This same concept can be applied to the case of transverse instabilities. The axial

velocity fluctuations will be greatest at the resonant frequencies of the inlet nozzle cavity (not of the combustor), and this coupling will be highly dependent upon system geometry. The transverse to longitudinal velocity transfer function will therefore be highly frequency dependent and its magnitude will give an indication of the dominant acoustic disturbance imposed on the flame at the nozzle.

The importance of this coupling implies that the flame transfer function, in the case of transverse forcing, will be neither decoupled from the hydrodynamic fluctuations nor the system acoustics, as the longitudinal transfer function was. It is important to note, then, that the quantitative results shown in these experiments cannot necessarily be extrapolated to other systems because of the geometric dependence built into the definition of this transfer function. One goal, then, is to propose a formulation by which flame transfer functions for transversely forced flames can be measured and understood.

The second goal of this work is to further characterize the response of the swirling flow to transverse acoustic excitation. This work supports the efforts of the first part by provide phenomenological understanding of the pathways shown in Figure 6, in particular, the coupling between acoustic fluctuations and vortical fluctuations. To understand this issue, an approach is taken that first considers the hydrodynamic stability issues in the swirling flow before considering the response of that flow to acoustic excitation. The ideas behind this approach are developed below.

Figure 7 illustrates the basic geometry considered in this study, showing an annular, swirling jet that is excited by a transverse acoustic field. This notional picture shows the annular swirling jet with two spanwise shear layers, emanating from each edge of the annular nozzle, and the large central recirculation zone downstream of a

centerbody. Here, the flame is stabilized on the centerbody and resides in the inner shear layer.

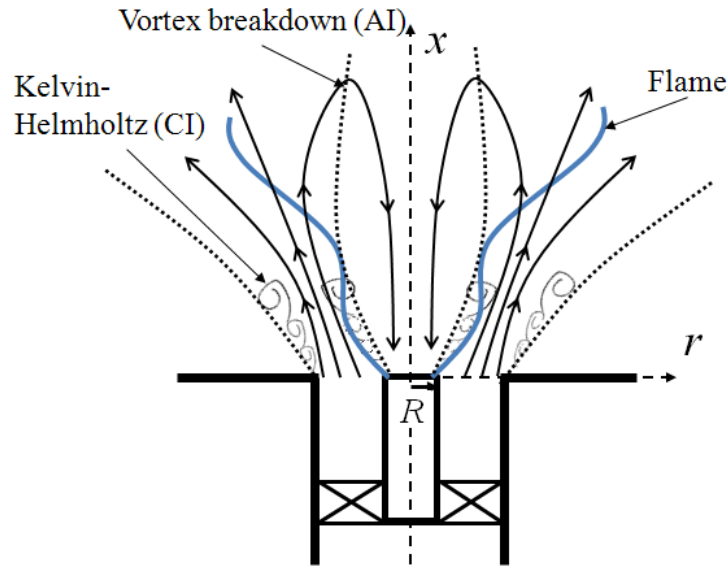


Figure 7. Time-average structure of an annular swirling jet with vortex breakdown.

The spanwise shear layers, vortex breakdown bubble, and flame are shown here.

This flow is an example of a typical high swirl number jet with vortex breakdown as is often encountered in a gas turbine main combustor geometry. Vortex breakdown stems from an absolute instability of the swirling jet and arises from the conversion of radial and axial vorticity to azimuthal vorticity [72, 73]. Though several states of vortex breakdown are possible [74], the one of primary interest here is the bubble-type vortex breakdown state (VBB), which appears at higher swirl numbers. This bubble creates a time-average "blockage" in the flow, forcing the fluid to flow around the bubble and converting even circular jets into a sort of annular jet downstream of the breakdown bubble stagnation point. A large literature on the mechanisms of breakdown and swirling flow structure exists, e.g., see Liang and Maxworthy [75], Billant et al. [76], Sarpkaya [77, 78], Hall [79], Faler and Leibovich [74, 80], and others [81-90].

Combustion significantly alters swirling flow features [91-93]. Combustion induced heat release, and the associated gas expansion, increases the average axial flow velocity, but has little effect on the average azimuthal velocity, leading to a decrease in swirl number and an increase in axial velocity gradients and shear. As such, both the time-average (bubble length, width, backflow velocity) and dynamical features of the flow are effected by heat release, but in a manner that appears to be a strong function of the configuration and operating conditions of the device, so that general comments on heat release effects are difficult to make.

Next, the annular, swirling jet is considered in more detail. As is evident in Figure 7, this geometry introduces two spanwise shear layers originating from the inner and outer annulus edges, and two streamwise shear layers associated with the azimuthal flow. These shear layers are subject to the Kelvin-Helmholtz instability, which can be convectively or absolutely unstable, depending upon the reverse flow velocity and swirl number [94, 95]. In addition, the centerbody introduces a wake flow. For small centerbody diameters and/or weak swirl, the time-average wake closes upstream of the upstream stagnation point of the vortex breakdown region, and thus the two flow structures (centerbody wake and VBB) are distinct, as shown in Figure 8a. For larger centerbodies and strong swirl, the wake and vortex breakdown bubble merge into a single, interacting structure, as shown in Figure 8b [96]. This, in turn, influences the potential flame shapes that can be present in both geometries, as shown in Figure 8c and d. When the vortex bubble is detached as in Figure 8c, flame stabilization is possible in the stagnation region preceding the VBB or in one or both of the low velocity shear layers. In this way, four different flame topologies (all of which have been

experimentally observed [50, 97-99]) are possible. For example, the OH PLIF image in Figure 9 shows a flame stabilized by the stagnation region preceding the VBB and the outer shear layer. In contrast, when the centerbody wake and vortex breakdown bubble are merged, as in Figure 8d, no nearfield stagnation point is present in the flow, and the flame stabilizes in the shear layers.

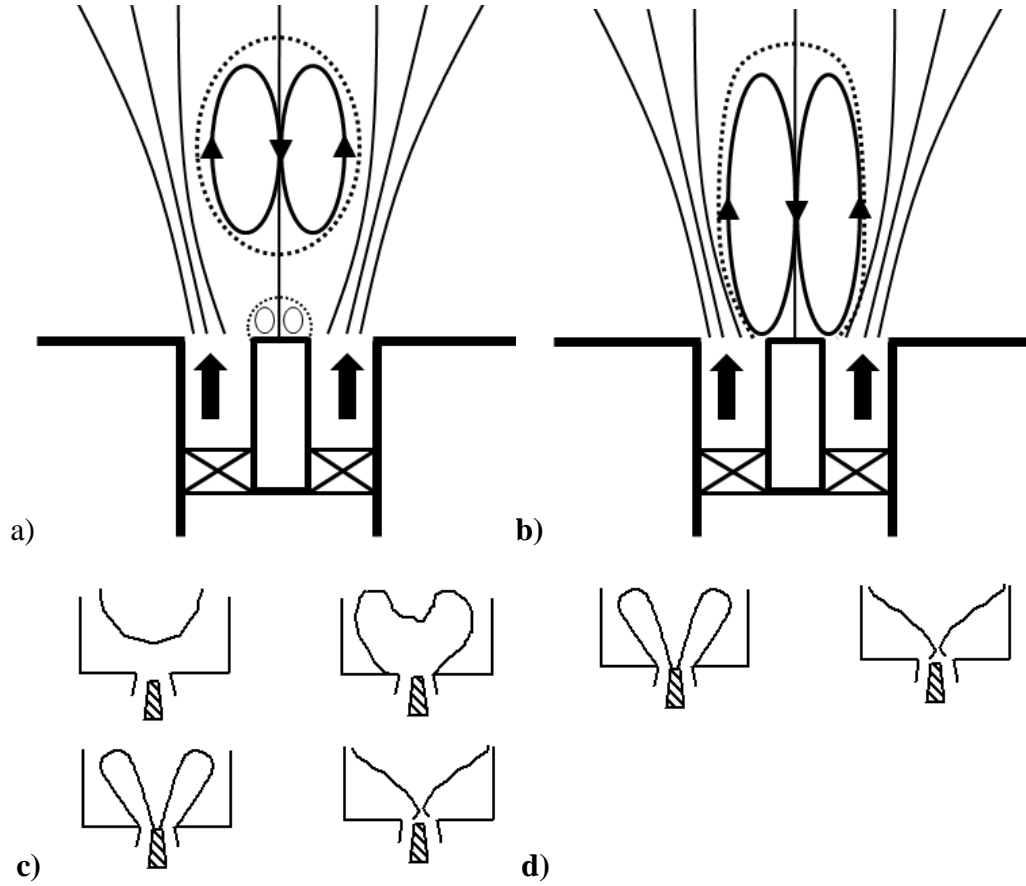


Figure 8. Possible flow (a and b) and flame (c and d) configurations for two different vortex breakdown bubble structures where a,c) the bubble is lifted, and b,d) the bubble is merged with the centerbody wake.

Next, the effects of harmonic acoustic forcing on the flow and, particularly, the effects of excitation amplitude are considered. In this discussion, it is important to

recognize the different types of instabilities present in the flow, particularly their absolute or convectively unstable nature. This specific flow field can be roughly broken into the convectively unstable shear layers and the absolutely unstable swirling jet, which results in a vortex breakdown bubble (VBB). While useful, this demarcation should not be taken too far, though, as interactions between flow structures does exist, particularly between the flow structures in the VBB and the inner shear layer.

The convectively unstable shear layers are treated first. A free shear layer is a convectively unstable flow, where the separating vortex sheet rolls up into concentrated regimes of vorticity that pair with downstream distance [95, 100]. As a disturbance amplifier, shear layers respond strongly to acoustic forcing [94, 101-104]. In this case, the vortex passage frequency locks onto the forcing frequency, generally through a vortex pairing or collective interaction phenomenon [105]. Acoustic forcing has been shown to have similar effects on the shear layers in a variety of flow geometries, including circular, annular, and swirling jets [49, 106-112].

Consider next forcing effects on the VBB, a result of absolute instability in the flow field. The effect of harmonic motions on the stagnation point in the flow is, as argued above, an important consideration for flows with small centerbodies and/or weak swirl. Khalil et al. [113] showed that high levels of forcing, over a limited range of forcing frequencies, could elicit a response in the vortex breakdown bubble. The response of the bubble, measured by movement of the upstream stagnation point, grew monotonically with forcing amplitude at a variety of different swirl numbers. In the presence of a flame, bulk pulsations of the flow buffet the entire VBB, such as can be seen in the OH PLIF images in Figure 9.

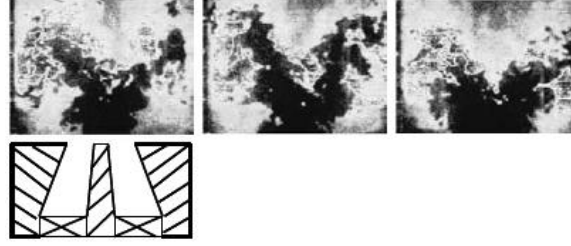


Figure 9. Results from OH PLIF images for a harmonically excited, swirl-stabilized flame at $f = 270$ Hz and $u'/u_o = 0.21$ [50].

The response of the bubble to acoustic forcing will be highly dependent on the shape and strength of the bubble. As described above, the merged bubble lacks the vertical degree of freedom that the lifted bubble retains. Additionally, characteristics like the bubble length, internal turbulence level, recirculation strength and other quantities dependent on swirl number may also influence its susceptibility acoustic forcing. Indeed, several investigations of harmonically forced swirl flames have attributed some characteristics of the unsteady heat release to the dynamics of the stagnation point and bubble motion [43, 50]. For example, Figure 10 illustrates the measured relationship between unsteady heat release of a longitudinally forced swirl flame upon excitation amplitude [50]. Curve (a) represents a typical manifestation of the nonlinear characteristics of the flame response [114-118]. Curve (b) shows a result with a highly non-monotonic flame response-excitation amplitude relationship, illustrative of a few similar type response curves measured in swirl flames. In this study, measurements at different forcing amplitudes provided strong evidence that this behavior could be directly attributed to the nonlinear dynamics of the VBB stagnation point that, in turn, directly influenced the time evolution of the central portion of the flame. In other words, it was suggested that the nonlinear flame response shown in curve (b) is not due to some

intrinsically nonlinear characteristic of the flame itself, but the flame adjusting to the highly nonlinear flow field.

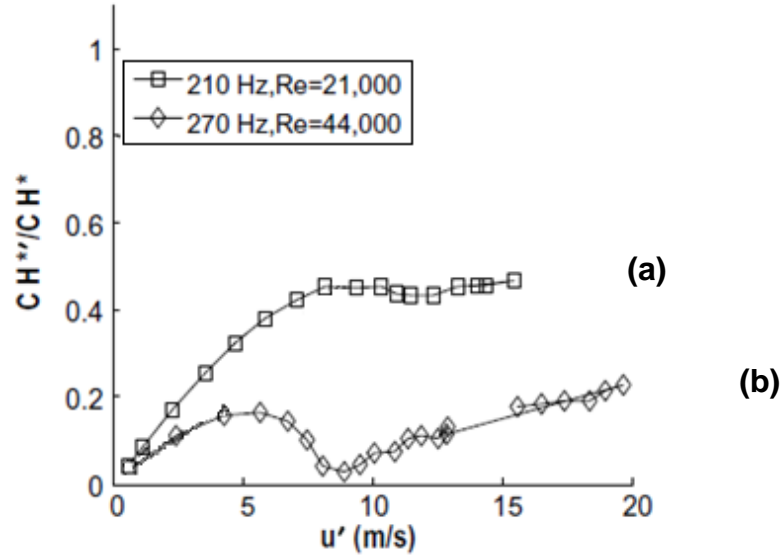


Figure 10. Flame CH^* chemiluminescence fluctuation response as a function of longitudinal forcing amplitude at two frequencies for a swirl-stabilized flame [50].

Another effect of forcing is on the dynamics of the internal structure of the VBB [43, 113, 119]. Here, the absolutely unstable nature of vortex breakdown appears to be key to understanding the response characteristics. Absolutely unstable systems execute self-excited, limit cycle motions, even in the absence of external forcing [120]. For this reason, low amplitude forcing has minimal impacts on the VBB. This behavior is to be contrasted with that exhibited by the convectively unstable shear layers and the entire VBB itself, whose space/time position is influenced by the outer flow oscillations. LES simulations of a forced swirl flow by Wang and Yang [49] showed periodic fluctuations in size of the vortex breakdown bubble under limit-cycle amplitude acoustic forcing. In

this case, the size of the bubble fluctuated in accordance with the longitudinal acoustic forcing.

Swirl flows can also display narrowband oscillations in the form of the precessing vortex core (PVC) [43]. Several factors influence the response of the PVC to acoustic forcing, including both flow and geometric parameters. In some cases where the bubble has intrinsic narrowband oscillations, external excitation at that natural frequency of oscillation can cause further amplification of this oscillation [121]. For example, LES studies by Iudiciani and Duwig [122] show that low frequency forcing ($St < 0.6$) resulted in a decrease in the strength of the PVC fluctuation amplitude, while higher frequency fluctuations resulted in increases in PVC fluctuation amplitude.

As the amplitude of acoustic excitation reaches very high amplitudes, significant changes in the shape and natural oscillations of the vortex breakdown bubble can occur. This is due to a phenomenon known as lock-in or entrainment, where the system oscillations are entrained by the external forcing and oscillate at the forcing frequency rather than the unforced frequency [121]. Additionally, high amplitude acoustic forcing can change the time-average shape of the flow, causing the vortex breakdown bubble to grow in both size and strength. Several authors [110, 122, 123] showed changes in the time-average shape of the vortex breakdown bubble under strong longitudinal acoustic forcing. In these cases, the strength of the recirculation increases along the centerline, particularly near the nozzle exit. Finally, high amplitude acoustic forcing has been shown to inhibit, and even reverse, vortex breakdown in flows with lower swirl numbers in the hysteretic region [113]. In these cases, acoustic forcing has the ability to push the flow across the stability boundary and inhibit a bifurcation in flow structure.

The presence of transverse forcing adds an additional degree of freedom to the forced problem because of the non-axisymmetric nature of the forcing [112, 124-126]. Unforced swirling flows are not generally instantaneously symmetric [74]; e.g., swirl biases the strength of co- and counter-signed helical instabilities. Moreover, non axisymmetric forcing can preferentially excite certain non-axisymmetric modes in a different manner than they would otherwise naturally manifest themselves. Some studies using asymmetric acoustic forcing have shown that strong forcing can lead to bifurcations in the structure of a non-swirling jet, leading to such phenomena as "bifurcating" and "blooming" jets [127].

With this as background, the influence of these flow features on the response of attached flames to flow disturbances is discussed, such as shown in Figure 11. In particular, we are interested in understanding the nonlinear character of the flame response. To start, we note first that the flame response is controlled by both the unsteady and time-averaged features of the flow. To show this, consider the following level-set formulation for the flame dynamics, which is valid for premixed flamelets:

$$\frac{\partial G}{\partial t} + \vec{u} \cdot \hat{n} - S_L |\nabla G| = 0 \quad (7)$$

Here, the flame position is given by the level $G = 0$. Mapping this equation into physical space, we use the transformation $G(r, x, t) = x - \zeta(r, t)$, where ζ is the distance from the dump plane to the flame surface, as shown in Figure 11.

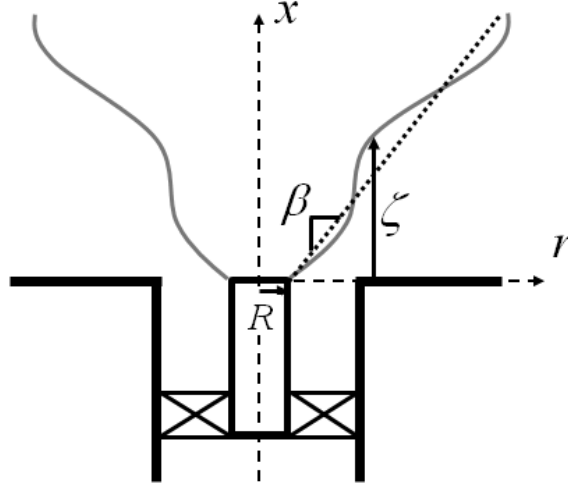


Figure 11. Flame modeling configuration, where the solid line is the instantaneous flame location, the dotted line is the time-average flame location, ζ is the flame location, and β is the time-average flame aspect ratio.

Given the geometry shown in Figure 11, Equation (8) describes the motion of the instantaneous flame front, assuming that ζ is a single valued function of r , where the subscript r denotes a spatial derivative [128].

$$\frac{\partial \zeta}{\partial t} = u - v\zeta_r - S_L \sqrt{\zeta_r^2 + 1} \quad (8)$$

Here, u and v are the axial and radial velocity components, and S_L is the laminar flame speed. While this equation could describe the motion of flames of several shapes, we set the flame shape by imposing the flame attachment condition at the edge of the centerbody, $r = R$, by enforcing the boundary condition $\zeta(r = R, t) = 0$. The expressions for the time-average flame location, $\bar{\zeta}$, and fluctuating flame location about the mean, ζ' , are shown in Equations (9) and (10).

$$\bar{u} - \beta \bar{v} \bar{\zeta}_r - S_L \sqrt{1 + \beta \bar{\zeta}_r^2} \quad (9)$$

$$\frac{\partial \zeta'}{\partial t} = u' - \beta \bar{v} \zeta_r' - \beta v' \bar{\zeta}_r - \frac{\beta^2 S_L \bar{\zeta}_r \zeta_r'}{\sqrt{1 + \beta^2 \bar{\zeta}_r^2}} \quad (10)$$

The cause/effect relationship between the flow and the flame shape and dynamics is evident from Equations (9) and (10). The space-time character of the disturbance field, particularly at the forcing frequency, plays a significant role in exciting disturbances on the flame. In this regard, the earlier distinction between the absolutely unstable (AI) vortex breakdown bubble and convectively unstable (CI) shear layers is fundamental to understanding the key unsteady flow structures that disturb the flame. The convectively unstable shear layers are amplifiers that respond to the external forcing. Moreover, since attached flames ride directly along the shear layer, as shown in Figure 7, the instability characteristics of the shear layers dominate the flame forcing through the fluctuations in u' and v' in Equation (10). The dynamics of the shear layers will be discussed at length at the end of this chapter.

In contrast, the absolutely unstable breakdown bubble exhibits intrinsic dynamics that are relatively independent of low amplitudes of excitation [49, 129]. Therefore, the basic dynamics of this flow remains unchanged in the presence of low amplitude acoustic forcing. It is postulated that the key way in which the VBB influences the flame response to excitation is by controlling the time-average flow field, \bar{u} and \bar{v} , and by influencing the downstream evolution of the shear layers (e.g., they appear to lose coherence much quicker in the presence of vortex breakdown [130]). It is also clear that VBB dynamics have a significant influence on the nonlinear dynamics of the flame. For attached flames, we postulate that this influence primarily occurs through changes in the time-average features in the VBB [113], i.e., \bar{u} and \bar{v} are functions of disturbance amplitude, and

lesser so because of temporally unsteady flow features in the VBB. Indeed, the motivation for this study resulted from visually obvious, abrupt changes that were observed in the time-average flame shape at high amplitude forcing, as detailed further in Chapter 4.

The first half of this part of the study particularly focuses on the VBB dynamics in response to transverse forcing of varying amplitude and frequency, with particular emphasis on nonlinear dependencies of instantaneous and time-average flow and flame features. The second portion focuses on the dynamics and response of the convectively unstable structures in the flow field, or the shear layers. The response of these structures is particularly important during combustion instability events, as they are convectively unstable and will respond in-kind to the acoustic forcing imposed on the flow.

Swirling jets, like non-swirling jets, are also convectively unstable and display shear layer rollup in both the spanwise and streamwise shear layers. Shear layer instability has been studied extensively and characteristics of the instability, such as most amplified frequency and disturbance growth rate, are now predictable by theory [95, 100, 131, 132]. As the shear layer rolls up, it forms vortices that are initially on the length scale of the momentum thickness of the mixing layer. As the growth rate of the sub-harmonic frequencies peak, vortex pairing events occur and lead to an almost step growth in the thickness of the shear layer [104]. In general, the stability of the shear layer does not change with heat release [133].

Shear layers are very susceptible to acoustic perturbations, which is a fact that has important implications during combustion instability events. As a convectively unstable flow, the shear layer acts like an amplifier for flow perturbations as the disturbances

convect downstream and grow in space [94, 101-103, 105]. In the presence of external excitation at only one frequency, the response of the shear layer at sub-harmonics, which happens naturally in an unforced shear layer, can be suppressed in favor of vortex shedding at the prescribed forcing frequency. Again, the nature of the shear layer response does not change in the presence of heat release, as has been seen in several combustion studies, which will be discussed at greater length below [9, 10, 49, 69, 134].

Convective instability in non-swirling jets has been studied by a variety of authors [106, 135-137], and theoretical, experimental, and computational work has shown that the coherent structures present in the jet shear layers significantly change the instantaneous topology of the jet. In these cases, the shear layer, created at the nozzle exit, rolls up and goes through a series of vortex pairing events until the end of the potential core. At this point, the two shear layers merge and the resulting coherent structure is quite large, on the order of the jet diameter. The structures then quickly dissipate in the highly turbulent region just downstream of the end of the potential core. This process is clearly shown in the flow visualizations by Crow and Champagne [106].

Similar processes occur in annular jets, but now two shear layers, one from the outer jet nozzle and one from the centerbody, are formed. Several experimental studies by Chan and Ko [108, 138] detail measurements of the pressure spectra of annular jets. From these measurements, the authors describe the structure of both the inner and outer shear layers, as well as interaction with the wake region behind the centerbody. In the case of annular jets, three regions of coherent structures exist: the inner shear layer, the outer shear layer, and the centerbody wake. Vortex rings of the same circulation are shed from both the inner and outer edges of the nozzle, and these two structures can interact as

they travel downstream. While issues of self-induced movement of these vortex rings (the inner inducing itself in the upstream direction, the outer in the downstream direction) is certainly a feature of these structures, it is not considered in this treatment as the mean flow velocity of the leads to downstream convection of both structures with very similar convection speeds, as is discussed in Chapter 5.

In annular swirling jets at high swirl numbers, the vortex breakdown bubble is an additional structure in this flow; this is the flow geometry considered in this study. Figure 7 shows the structure of the flow under consideration. In this flow, the swirl number is high enough that the vortex breakdown bubble has merged with the wake structure behind the centerbody, a process that was described by Sheen et al. [96]. Additionally, the action of swirl results in streamwise shear layers that emanate from both the inner and outer edges of the annular jet. The vorticity in these shear layers is created in the boundary layer formed by the swirling action inside the annular jet on the wall of both the centerbody and the swirler block. As the geometry of this nozzle features a high aspect ratio annular jet (small annular gap width), the interaction between these developing boundary layers and resultant shear layers could potentially lead to a reduction in the actual swirl number of the flow with downstream distance.

Several studies have focused on shear layer instabilities in swirling jets, particularly for combustion applications. Shear layer instability is a point of interest for swirl stabilized flames as the flame is normally stabilized in one or more shear layers in the flow, as will be discussed in more detail below. In a swirling flow, the shear layers instability often has a helical form. This has been shown by many authors [44, 75, 139, 140] in both simulation and experiment. Theoretical investigations of swirling flow

instability [82, 83] have indicated a preference in the direction of a helical disturbance that is created by the additional degree of freedom that swirl introduces in the solution space. This is true even when the jet is convectively unstable, indicating that the shear layer instability will manifest itself as a helix.

This can change, though, in the presence of acoustic forcing. It is well known that response of convectively unstable flows is dependent on the symmetry of the incident forcing. A good example of this phenomenon is forcing of circular jets. Longitudinal forcing, an axisymmetric forcing condition, results in an axisymmetric response as seen in Crow and Champagne [106]. Non-axisymmetric forcing, including transverse forcing, can lead to highly non-axisymmetric response in the jet, as seen in studies of bifurcating and blooming jets [127]. This principle also applies to swirling flows. Several studies, particularly in combustion applications, have measured axisymmetric shear layer response in a highly swirling flow in the presence of longitudinal forcing [9, 10, 66]. In these cases, swirling jets are confined by a quartz cylinder, creating a cylindrical combustor chamber with a dump plane. Large-scale shear layer vortices roll up in the outer shear layers and corner recirculation zones and convect downstream, leading to significant flame wrinkling. Non-axisymmetric forcing has lead to helical response in the shear layer and flame wrinkling in a number of transversely forced flames [28, 69, 111, 141].

For transversely forced flames, there exist several pathways of velocity disturbances. These pathways have been summarized in Figure 6. Each of the pathways shown represents a velocity fluctuation source that could lead to velocity coupled flame response. As described above, the velocity transfer function F_{TL} quantifies the coupling

between the transverse and longitudinal acoustic velocities at the nozzle. The acoustic fluctuations from both the transverse and longitudinal direction excite vortical velocity fluctuations, and this process is quantified by the velocity transfer functions $F_{T\omega}$ and $F_{L\omega}$. These two sources of fluctuating vortical velocity combine to result in flame response to vortical sources, described by the flame transfer function F_ω . In this type of description of the velocity disturbance field, the natural “transverse vs. longitudinal” decomposition of the velocity field has been chosen, where the flame response is attributed to one direction of motion verses another. Another natural decomposition would be to decompose the velocity field into the acoustic and vortical components, which is one of the results presented in Chapter 5. The methodology for this decomposition will be described there.

The combination of these two velocity disturbance mechanisms, vortical velocity fluctuations stemming from the shear layer instability and the acoustic fluctuations in both the transverse and longitudinal direction, can lead to interesting overall velocity field fluctuation amplitudes. These two disturbances have vastly different propagation speeds; vortical disturbances travel at a convection velocity close to the mean flow speed [142], while acoustic disturbance travel at the sound speed. The superposition of these two waves, as one would find in a transversely forced swirling flow, can lead to a cancellation phenomenon [111]. Here, the fluctuation amplitude varies periodically throughout the field, and if the amplitudes of both waves are similar, regions of near-zero fluctuation amplitude can appear at the nodal points of the interference pattern. This severe modulation in velocity fluctuation amplitude dictates the velocity disturbance field

to which the flame is subjected. These issues, as well as others pertaining to the response of the convectively unstable structures in the flow, are all discussed in Chapter 5.

The remainder of this thesis is organized as follows. Chapter 2 provides an overview of the experimental facility, diagnostic techniques and corresponding uncertainty analyses, as well as an overview of the time-average flow field for each of the flow conditions considered in this study. Next, Chapter 3 addresses the issue of global flame response to transverse acoustic instabilities with measurements of both the transverse to longitudinal velocity transfer function, F_{TL} , as well as the flame transfer function. Discussion of these results is provided there. Chapters 4 and 5 focus on the details of the flow response, for both non-reacting and reacting flow fields, to a variety of transverse acoustic forcing frequencies, amplitudes, and symmetry conditions. In Chapter 4, the response of the base flow, or vortex breakdown region, is investigated and the effects of acoustic forcing on both the time-average as well as the dynamical response of this structure are considered. Chapter 5 contains discussion of the response of the shear layers and jet structure to acoustic forcing, with a particular focus on response of these structures at the forcing frequency. Finally, Chapter 6 will discuss implications of this work to the greater field of combustion instabilities and provide several recommendations for future work in the area of transversely forced swirling flows and flames.

CHAPTER 2

EXPERIMENTAL METHOD

Experiments were conducted in a flow facility designed for transverse acoustic forcing of both non-reacting and reacting jets, as is shown in Figure 12. The design of this experiment was motivated by the need to create a strong transverse acoustic mode in the combustor without significant contributions from modes in the other two directions. See Appendix A for full technical drawings of the experiment.



Figure 12. Experimental facility.

The conceptual design of the experiment was inspired by the shape of an annular combustor, as is shown on the right in Figure 3. While building a laboratory-scale annular combustor was not tractable for this research, the current configuration was decided upon by essentially “cutting” and “unwrapping” an annular combustor into a Cartesian framework. The result is this high aspect ratio combustor that is long in the

transverse mode direction and shorter in the other two directions, inhibiting the appearance of non-transverse modes over a large range of frequencies. This geometry also mimics the flow boundary conditions present in these annular combustors, where the dump ratio isn't uniform around the circumference of the nozzle. While in an annular configuration the walls surrounding each nozzle are curved, the radius of curvature is much larger than the characteristic length scale of the nozzle (the nozzle diameter). This means that a straight-walled chamber closely mimics the boundary conditions of an annular chamber and differences in the flow dynamics should be minimal.

The initial design used a finite element solver, Comsol Multiphysics, to design the inner dimensions, and hence acoustic mode shape, of the combustion chamber. This program allows the user to either build or import geometries and uses the Helmholtz equation to solve for acoustic fields with given boundary and forcing conditions on each face. Example acoustic fields from this type of simulation are given in Figure 13.

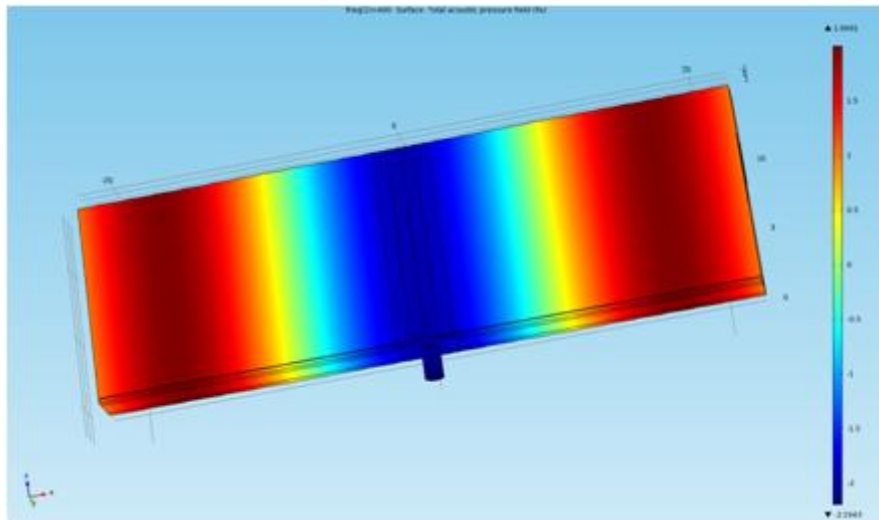


Figure 13. Comsol Multiphysics acoustic simulation of combustion geometry, amplitude of pressure fluctuations is shown for an out-of-phase forcing case.

This design ensured that transverse acoustic plane waves could be produced in the region of the nozzle. Purely transverse modes can be produced at frequencies up to approximately 1400 Hz before multi-dimension modes are formed. Although the mode shapes at these higher frequencies are two dimensional, with fluctuations in the axial direction appearing, the acoustic fluctuations in the interrogated region of the flow are not significantly impacted by this longitudinal combustor mode.

The main test section consists of a ceramic insulated stainless steel vessel with inner dimensions of 114.3 x 35.6 x 7.6 cm, where transverse forcing is applied in the longest direction (114.3 cm) and the flow direction is in the next longest direction (35.6 cm). The annular jet is located at the center of the test section; the outer diameter of the jet is $d_{outer} = 3.18$ cm and the inner diameter is $d_{inner} = 2.18$ cm. The exit plane of the test section has four circular exhaust ports, each with a diameter of 5.08 cm. This exhaust design was developed to minimize distortions of the incident planar acoustic field in the transverse direction. AutoCad Inventor was used for the detailed design of the experiment and fabrication was completed at the Aerospace Engineering Machine Shop and the Georgia Tech Research Institute (GTRI) Machine Shop.

The experiment is fed with a 20 psig air supply that is regulated with an orifice plate/differential pressure transducer setup. Air flows through a large settling chamber with a perforated plate to break up upstream flow structures before entering the nozzle cavity. The nozzle cavity, shown in Figure 14, has a length of $h = 9.5$ cm. It contains a swirler, located a distance $h_s = 3.8$ cm from the cavity entrance, with a centerbody of length $h_{CB} = 5.1$ cm extending downstream. Two swirlers were tested with geometric swirl numbers of 0.85 and 0.5 [143]; both flows exhibited bubble-type vortex breakdown

[80]. The nozzle cavity also contains two Kistler 211B5 piezoelectric pressure transducers, spaced $l_{mic} = 2.5$ cm apart. Experiments were run with an average nozzle velocity of $u_o = 10$ m/s, corresponding to a Reynolds number based on outer jet diameter of 21,000. During the reacting tests, natural gas and air were premixed to a stoichiometry of 0.9 three meters upstream of the settling chamber to ensure a spatio-temporally uniform mixture stoichiometry at the flame.

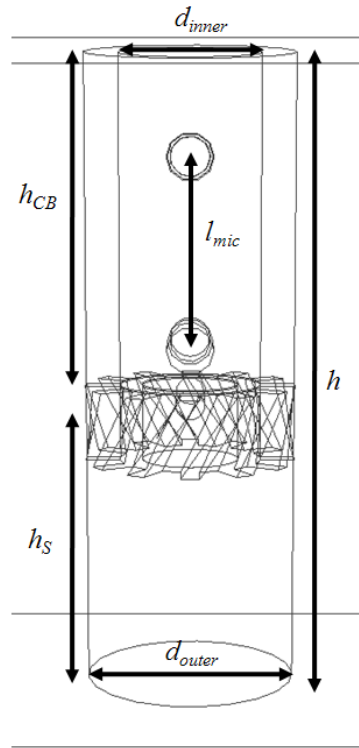


Figure 14. Specifications for the swirler nozzle cavity.

Further specification of the swirler is in Figure 15, which shows the 30° swirler. There are twelve non-aerodynamic blades with a straight sweep at angles 30 and 45 degrees. The inside is threaded to interface with the centerbody, also shown in the figure. The outer diameter of the swirler is 31.75 mm and the outer diameter of the centerbody is

22.1 mm. The inner diameter of the centerbody and swirler, at the interface location, is 14.6 mm wide. See Appendix B for full technical drawings.

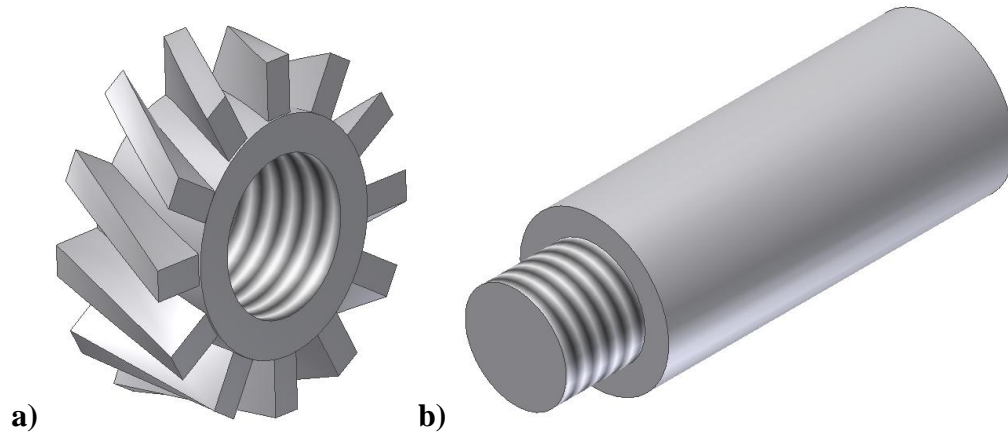


Figure 15. Renderings of a) 30° swirler and b) centerbody.

Time-average flow field

Here the time-average flow fields in the absence of forcing are shown for five testing conditions: non-reacting flow with a swirl number of 0.85 in the r - x plane, reacting flow with a swirl number of 0.85 in the r - x plane, non-reacting flow with a swirl number of 0.5 in the r - x plane, reacting flow with a swirl number of 0.5 in the r - x plane, and non-reacting flow with a swirl number of 0.85 in the r - θ plane.

In each of the r - x views, the structure of the swirling jet is evident. Along the centerline there is a central recirculation zone, a result of vortex breakdown, that has merged with the centerbody wake and extends to the face of the centerbody. A cut of the annular jet is seen as a high-speed jet on either side of the recirculation zone. There are two sets of shear layers, the inner shear layer between the jet and the vortex breakdown bubble, and the outer shear layer between the jet and the quiescent medium around the

jet. These results are shown in Figure 16 - Figure 19. For further details on these data sets, see Appendix D.

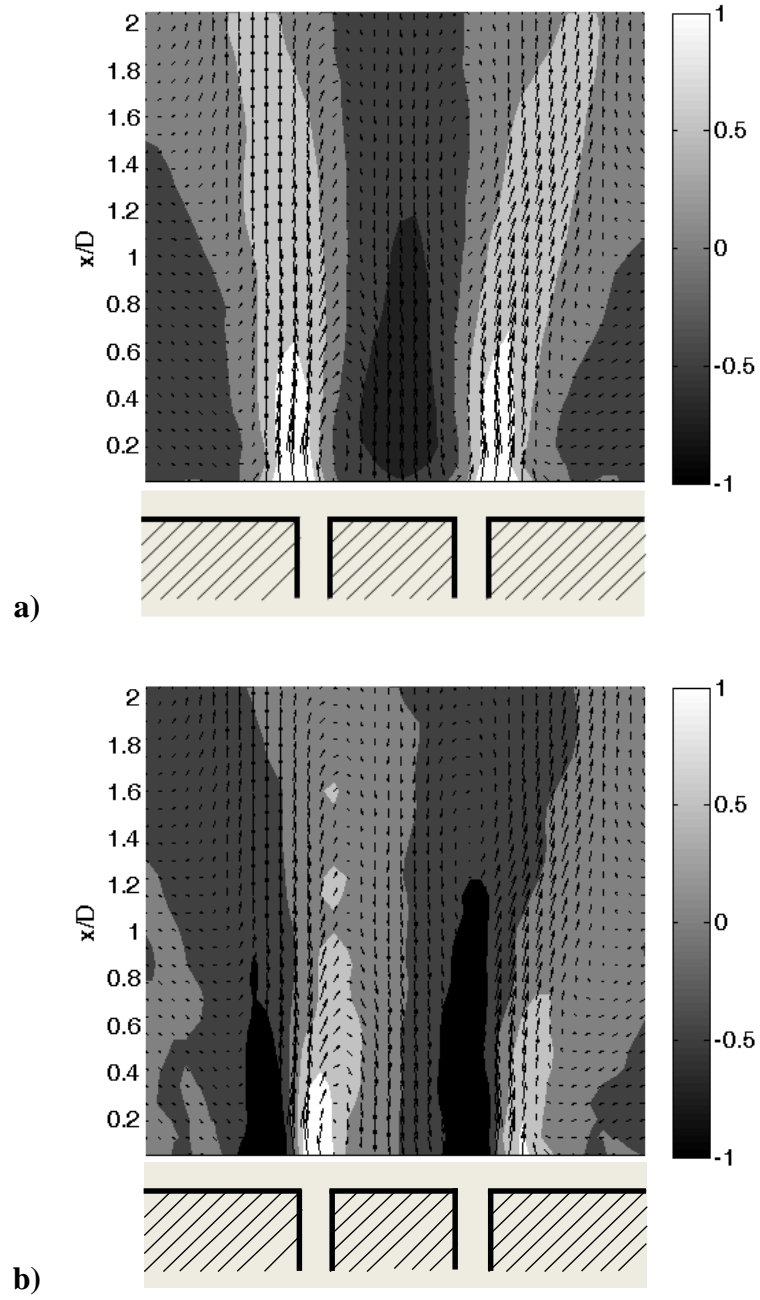


Figure 16. Time-average a) normalized velocity and b) normalized vorticity for non-reacting flow at $u_o=10$ m/s, $S=0.85$.

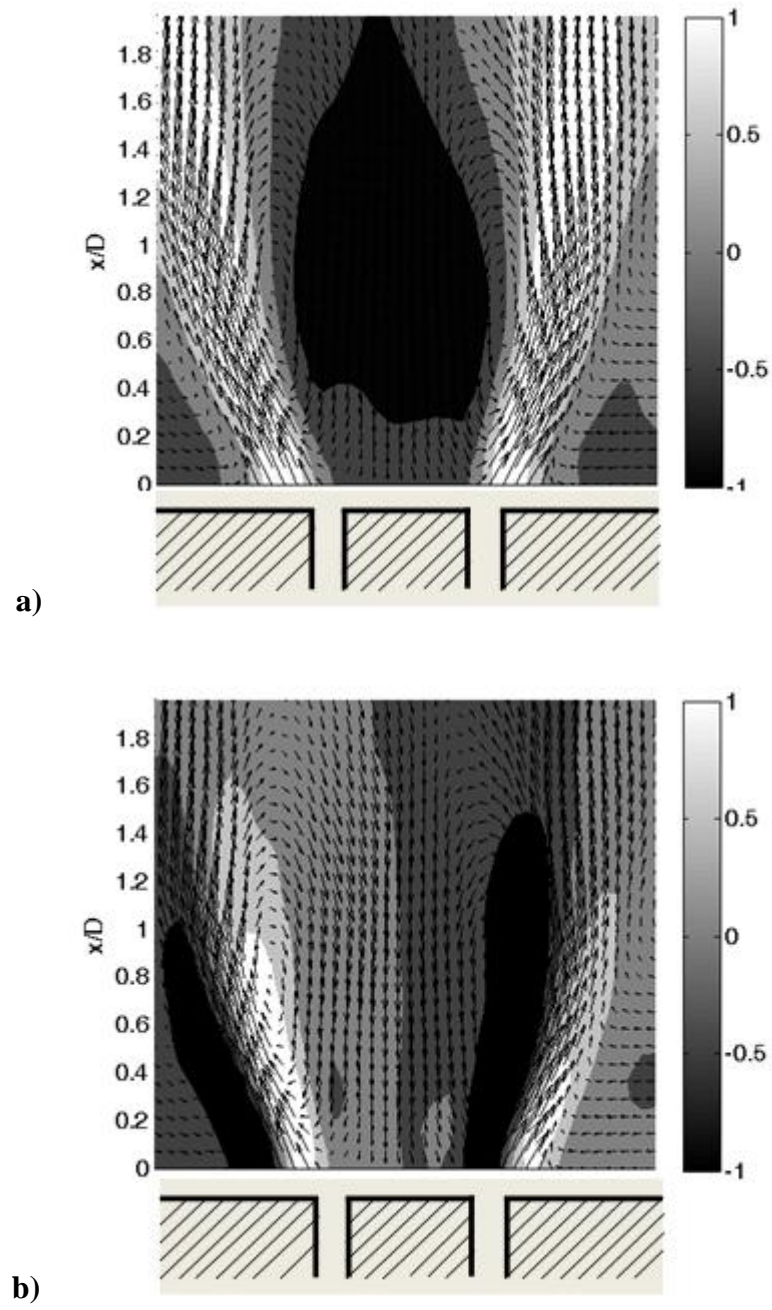


Figure 17. Time-average a) normalized velocity and b) normalized vorticity for reacting flow at $u_o=10$ m/s, $S=0.85$, $\varphi=0.9$.

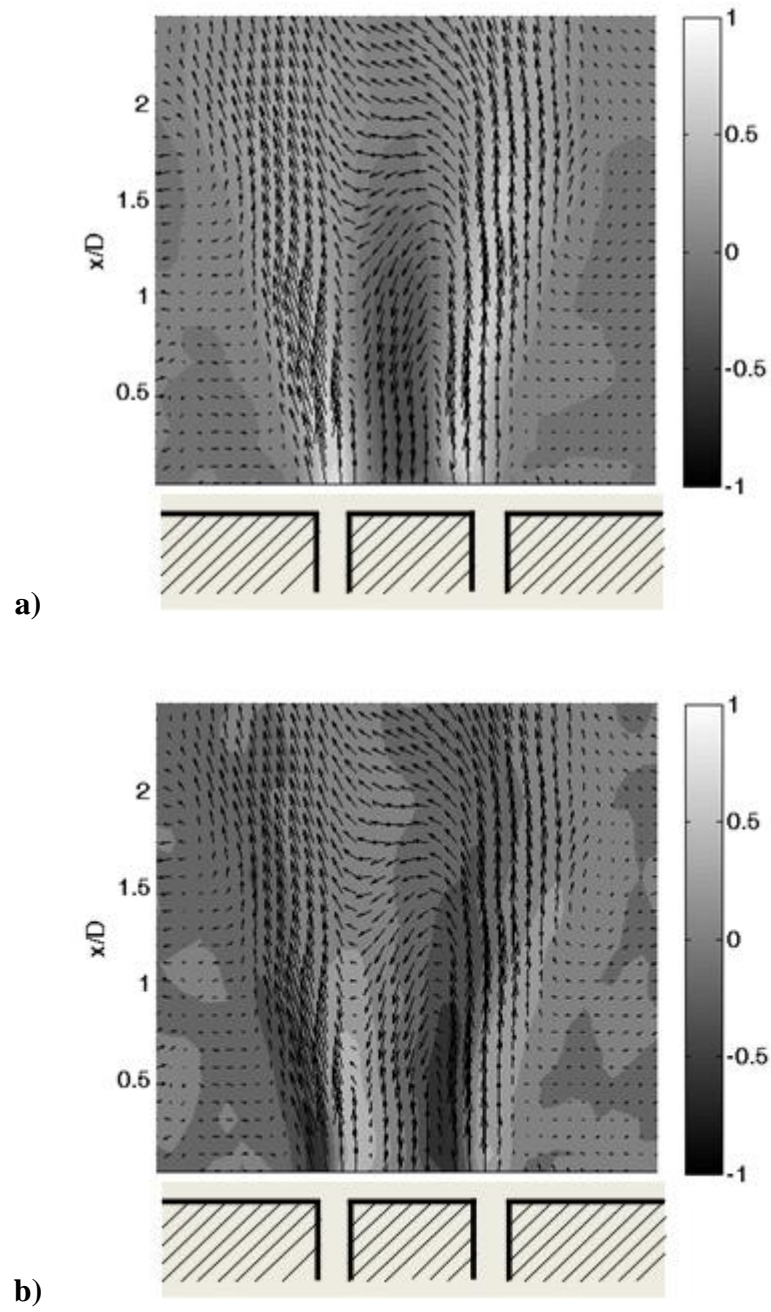


Figure 18. Time-average a) normalized velocity and b) normalized vorticity for non-reacting flow at $u_o=10$ m/s, $S=0.5$.

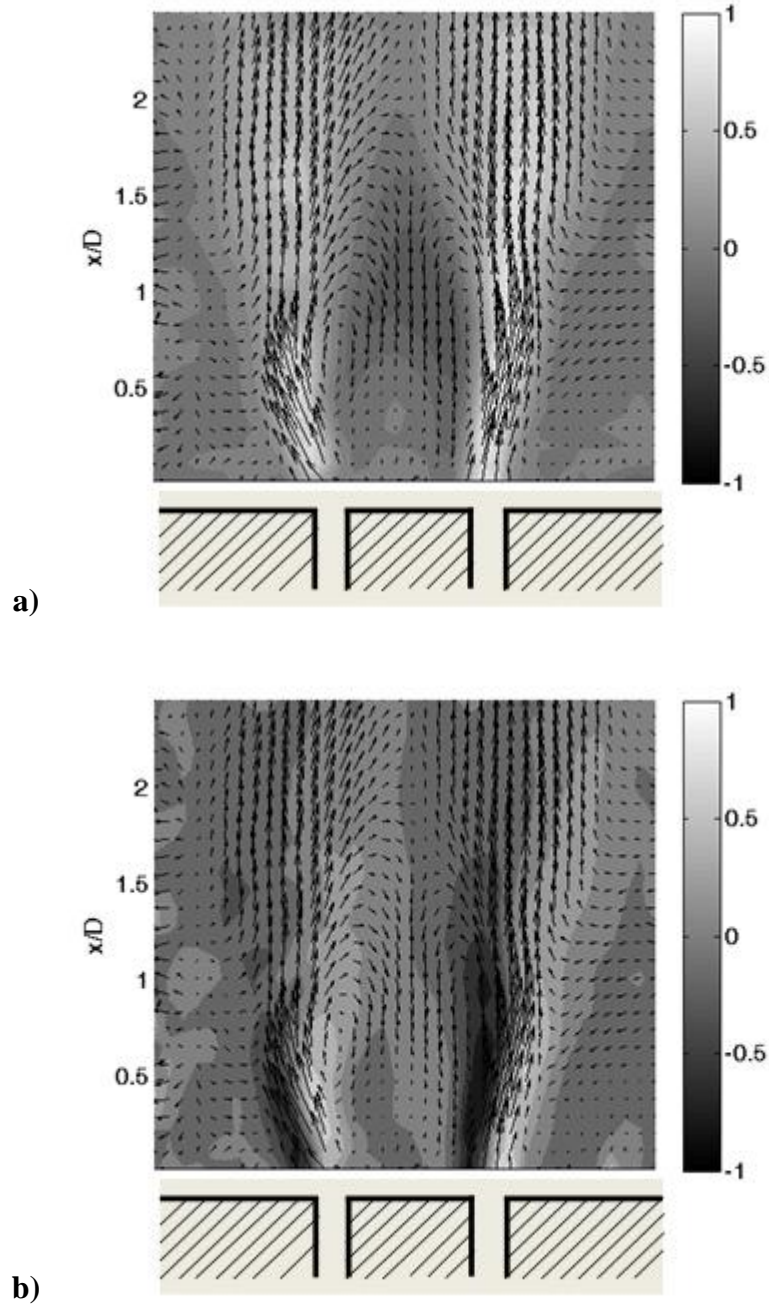


Figure 19. Time-average a) normalized velocity and b) normalized vorticity for reacting flow at $u_o=10$ m/s, $S=0.5$, $\phi=0.9$.

Figure 20 shows the time-average velocity field in the r - θ plane at three downstream distances. At $x/D=0$, the jet is clearly axisymmetric, but at further

distances downstream, the asymmetry of the combustion chamber causes the jet to spread on a bias, creating a more elliptical profile by $x/D = 1$.

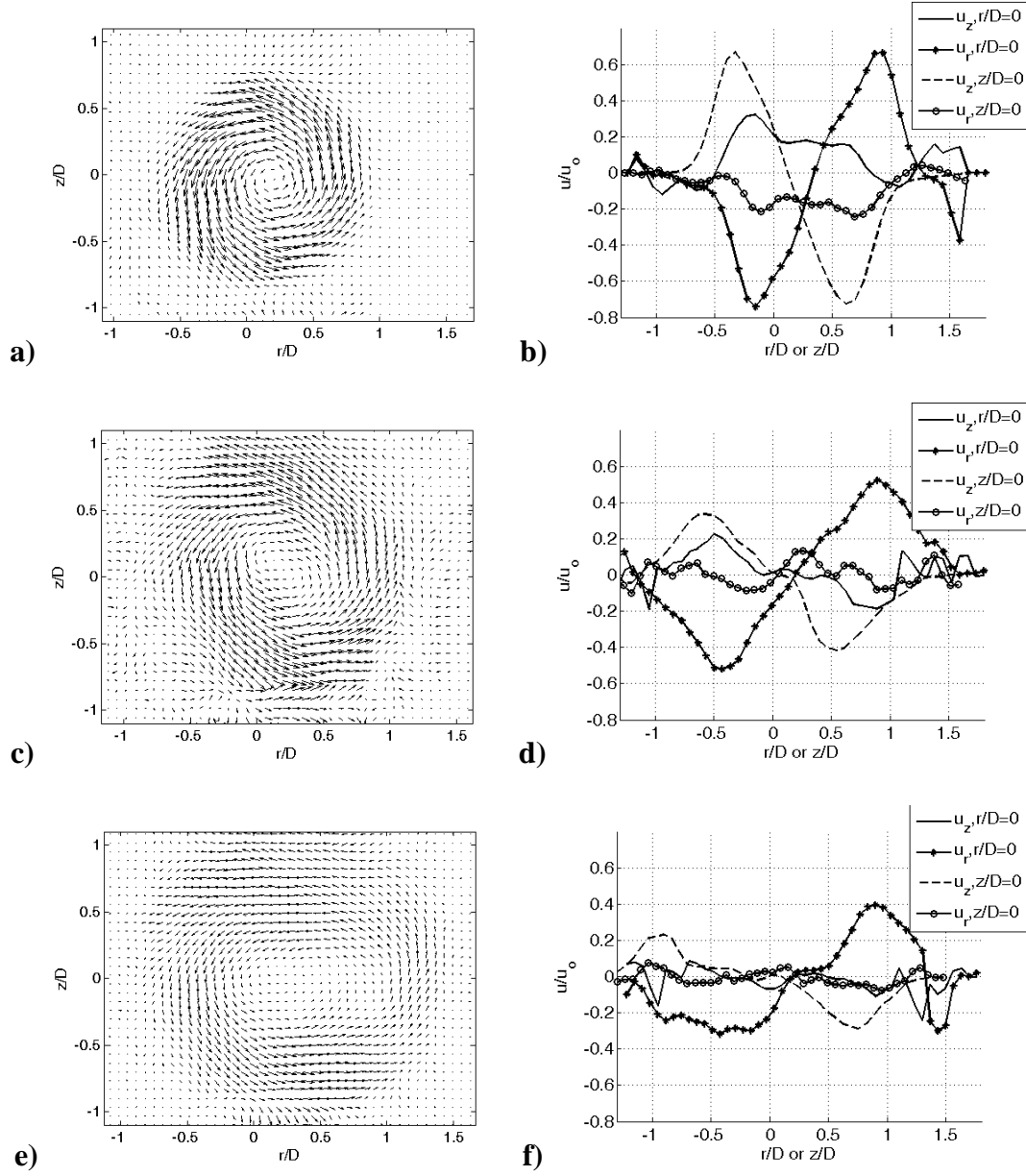


Figure 20. Time-average velocity in the $r-\theta$ plane at a,b) $x/D = 0$, c,d) $x/D = 1$, and e,f) $x/D = 2$ for the unforced, non-reacting annular swirling jet, at $u_o = 10$ m/s, $S = 0.85$.

Acoustic forcing

The transverse acoustic field is created using six speakers, three on either side of the test section. Each speaker is placed at the end of a 1 m tube to ensure they did not become overheated from the hot combustor test section. Extensive acoustic cold flow measurements and finite acoustic modeling of the system demonstrated that the acoustic field is nearly planar over the frequency range of 400 – 1200 Hz – indeed, modeling work done before the facility was fabricated was used to prescribe key facility dimensions to ensure that the evanescent, three-dimensional disturbance features excited near the driving tube's entrance into the system decayed before reaching the nozzle section.

A variety of different transverse acoustic fields, ranging from traveling to standing waves, can be set up by varying the relative amplitude and phasing of the speakers on the two sides of the combustor. In this study, the speakers were driven with the same excitation voltage either at 0 or 180 degrees with respect to each other to create a standing wave, referred to as "in-" and "out-of-phase", respectively. In-phase driving results in an acoustic pressure anti-node, a symmetric velocity field, and an acoustic velocity node along the centerline of the jet. Out-of-phase driving creates asymmetric velocity fluctuations about the centerline, an acoustic velocity anti-node and an acoustic pressure node along the center of the jet. These effects are shown in Figure 21.

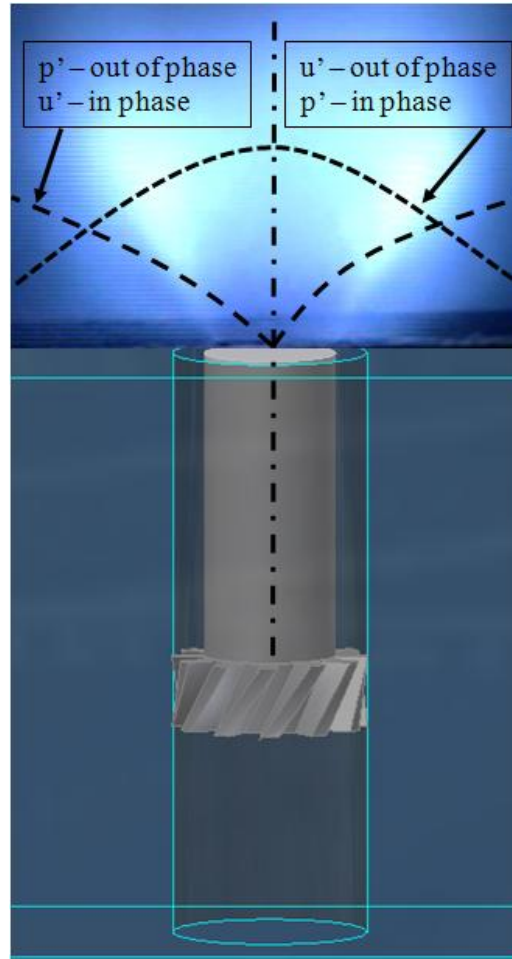


Figure 21. Nozzle configuration, flame shape, and acoustic velocity and pressure perturbations for in-phase and out-of-phase acoustic forcing, from the side view (acoustic waves not shown to scale).

While the acoustic wave shapes are not shown the scale in Figure 21, the issue of the relative length scales between the nozzle and the acoustic waves is an important feature of this combustor geometry. Over the range of frequencies tested, 400 Hz – 1800 Hz, the wavelength of the acoustic disturbances (in non-reacting conditions) is 0.85 m – 0.19 m, while the diameter of the nozzle is 0.03 m. While over this frequency range, the flow field could still be considered acoustically compact (where the characteristic length

scale of the flow is significantly less than that of the acoustic wavelength), the extent of this compactness certainly changes over the frequency range. As the wavelength shortens, the gradient of the acoustic field increases, which changes the overall topology of the velocity disturbance field.

Transverse acoustic forcing inevitably excites longitudinal fluctuations near the nozzle exit because of the oscillating pressure drop across the nozzle; this process has been described in the introduction. The fluctuating pressure at the nozzle exit excites axial acoustic oscillations in the swirler nozzle. These axial acoustic flow disturbances in and around the nozzle is a function of the nozzle geometry and upstream acoustic impedance. Both transverse and longitudinal reference velocities were calculated from the particle image velocimetry (PIV) data, the details of which are discussed later in this section. These reference velocities were calculated by spatially averaging velocity data over areas of interest. This process reduces random error caused by choosing data from a single point in the PIV calculation. The transverse reference velocity is a spatial average of the transverse velocity fluctuations along the centerline of the flow between one diameter and two diameters downstream. The axial reference velocity was calculated by integrating the axial velocity at each point along the radial direction at a downstream distance of $x/D=0.05$, the closest location of good data to the dump plane. This contour is referred to as S_l , and has a length of three nozzle diameters. The calculation of the spatially integrated velocity is shown in Equation (11).

$$\begin{aligned} u'_{L,a}(t) &= \frac{\pi}{S_l} \int_{S_l} u'(x=0, r, t) r dr \\ u'_{T,a}(t) &= \frac{1}{D} \int_D^{2D} v'(x, r=0, t) dx \end{aligned} \tag{11}$$

These spatially integrated velocities were chosen as being representative of the acoustic fluctuations in both directions. The spatially averaged transverse velocity fluctuation along the centerline seems representative of a characteristic acoustic velocity in that region because much of the random motion from the vortex breakdown region should be removed by the average. The axial velocity fluctuations, though, may contain significant vortical velocity components as the measurement was taken 0.64 cm downstream of the dump plane.

Figure 22 plots the measured spatially averaged transverse reference velocity fluctuation, u'_T , at the forcing frequency for the range of conditions presented in this work. It shows that the transverse disturbance amplitude rises almost linearly with excitation voltage.

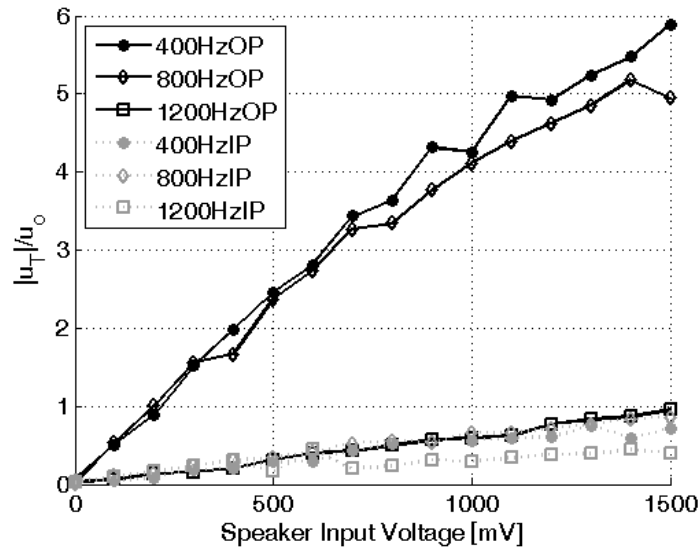


Figure 22. Amplitude of the reference transverse velocity fluctuations at the forcing frequency as a function of speaker input voltage, at $u_o=10$ m/s, $S=0.85$.

As expected, the out-of-phase cases shown in Figure 22 have higher transverse velocity amplitudes than their in-phase counterparts at the same frequency. Additionally, the 400 Hz and 800 Hz cases have strong transverse velocities, while the 1200 Hz case is weaker due to the reduced response of the drivers at these frequencies. The transverse acoustic fluctuations in the combustor also induce longitudinal velocity fluctuations in the nozzle cavity. These fluctuations tend to scale with the amplitude of transverse velocity fluctuations.

Diagnostics

Several diagnostic methods were used throughout this study, including high-speed PIV, flame luminosity, global chemiluminescence measurements, and pressure measurements. Each of these experimental techniques is described in detail here.

Particle Image Velocimetry

Velocity measurements in this study were made using high-speed particle image velocimetry (PIV). The laser is a Litron Lasers Ltd. LDY303He Nd:YLF laser with a wavelength of 527nm and a 5 mJ/pulse pulse energy at the 10 kHz repetition rate used for these experiments. The Photron HighSpeed Star 1.1 camera has a 640x448 pixel resolution with 20x20 micron pixels on the sensor at a frame rate of 10 kHz. A LaVision divergent sheet optic, with a $f = -20$ mm cylindrical lens, was used to create a 1 mm thick sheet. The first set of PIV data examined the flow in the axial direction of flow. In this case, the sheet entered the experiment from a window at the exit plane of the combustor and reached a width of approximately 12 cm at the dump plane. This alignment will be referred to as the $x-r$ alignment.

A second set of PIV data were taken to look at the swirling component of the flow. Here, a laser sheet with a thickness of approximately 1 mm and a width of 10 cm entered the front window at a height of 0.7 cm above the dump plane. An Edmunds Optics 45-degree first surface mirror was placed above the exit port window and the camera was aligned and focused on the image on this mirror. Special care was taken to ensure that there was no distortion in the particle image in the mirror; mirror/camera alignment was checked often. This alignment will be referred to as the $r-\theta$ alignment.

Aluminum oxide seed particles with a mean diameter of 2 μm were used. Image pairs were taken with a separation time, dt , of nominally 20 microseconds for the $x-r$ alignment and 25 microseconds for the $r-\theta$ alignment. This time varied slightly with swirl number, between 18 and 22 microseconds, as out-of-plane loss-of-pairs increases with larger swirl numbers. 500 image pairs were taken at each test condition.

Velocity field calculations were performed using DaVis 7.2 software from LaVision. The velocity calculation was done using a three-pass operation: the first pass at an interrogation window size of 64x64 pixels, the second two passes at an interrogation window size of 32x32, each with an overlap of 50%. Each successive calculation uses the previously calculated velocity field to better refine the velocity vector calculation; standard image shifting techniques are employed in the calculation. The correlation peak is found with two, three-point Gaussian fits and values of the correlation peak ranged from 0.4 to 1 throughout the velocity field. There were three vector rejection criteria used both in the multi-pass processing steps and the final post-processing step. First, velocity vectors with magnitudes greater than 25 m/s were rejected as unphysical for this specific flow. Second, median filtering was used to filter points where surrounding

velocity vectors had an RMS value greater than three times the local point. This filter is used to rid the field of spurious vectors that occur due to issues with imaging, particularly near boundaries. Third, groups of vectors greater than five vectors with an RMS significantly different than their neighbors were removed; this operation removes errors caused by local issues with the original image, including window spotting, and are aggravated by using overlapping interrogation windows. Finally, vector interpolation was used to fill the small spaces of rejected vectors.

Uncertainty Estimation

Uncertainty in the velocity calculation was estimate using a pseudo-synthetic image pair method that calculates the sensitivity of the velocity calculation to a variety of sources of error in the measurement and calculation [144]. Unlike purely synthetic images, pseudo-synthetic images use the first image from an experimental image pair as a baseline for the second image. In order to create the second image in the pair, the first image can be shifted, its intensity changed, its particles blocked, or a variety of other operations to mimic PIV errors. This new image pair is then processed using the current software and calculation settings, and the sensitivity of the calculation to these different error sources imposed on the second image can be calculated. This methodology showed that the major source of uncertainty stem from loss of particles due to highly swirling flow. Based on these calculations, the uncertainty in the calculated velocity is approximately 1 m/s.

Flame Luminosity

High-speed, line-of-sight video of flame luminosity was used to characterize the flame position. These images were taken using a Photron High Speed Star 1.1 camera at 5000 frames per second. The camera's CMOS sensor is sensitive between 400 and 1000 nm, with peak sensitivity in the 500 – 700 nm wavelength range. Each data set contains 500 images, resulting in a spectral resolution of 10 Hz.

Smoke Visualization

The small-scale vortices that rollup as a result of the Kelvin-Helmholtz instability in the cases without acoustic forcing cannot be resolved by the PIV. For that reason, smoke visualization was also used for visualization of these smaller structures. A diagram of the smoke injection scheme is shown in Figure 23. This system allows for smoke injection in a roughly axisymmetric manner for both/either the inner and outer shear layers. By varying the smoke injection points, separate or combined visualization of the inner shear layer, outer shear layer, and recirculation zone is possible. Such visualization approaches have been used in several studies in order to track coherent structures in shear layers as well as the vortex breakdown region in swirling flows [109, 127]. The system is viewed either directly with a camera to image the three dimensional smoke evolution, or with cuts by illumination with a laser. This technique has been helpful in visualizing the shear layer dynamics close to the nozzle exit. Farther downstream and inside the vortex breakdown region, though, the olive oil smoke is too diffuse to track. Further details of the smoke system can be found in Appendix C.

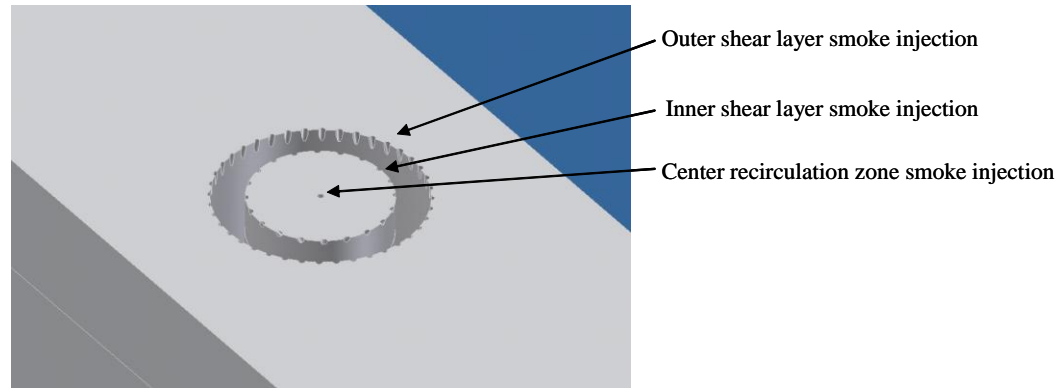


Figure 23. Smoke injection points for both inner and outer shear layer visualization in an annular nozzle.

Global Chemiluminescence Measurements

The chemiluminescence was measured with a Hamamatsu H5784-04 photomultiplier tube (PMT). CH^* chemiluminescence was filtered using a Newport Physics bandpass filter centered at 430 nm with a full-width half-maximum of 10 ± 2 nm. The data was recorded with a National Instruments NI9205 data acquisition system using Labview 9. The channel on the data acquisition board was in differential mode. Data were acquired at 30 kHz with sample lengths of 15,000 points. Data were ensemble averaged using ten ensembles. A schematic of the setup is shown in Figure 24.

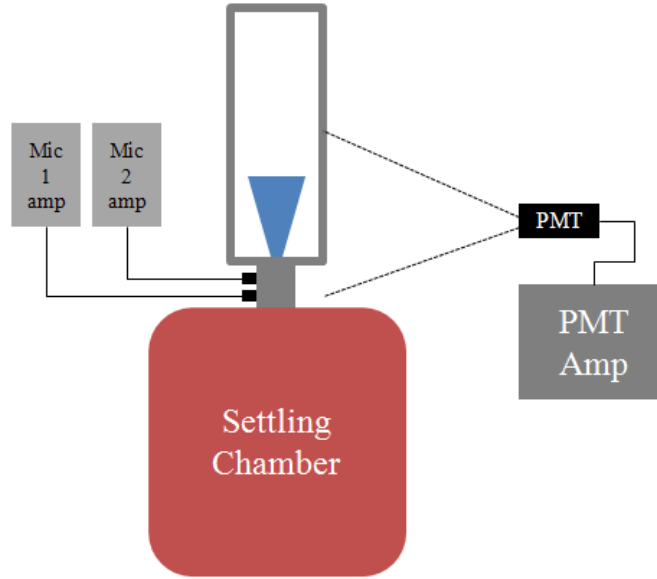


Figure 24. Experimental setup for flame transfer function measurements, with PMT for CH* chemiluminescence and pressure measurements.

Pressure Measurements

Pressure data were collected with two Kistler 211B5 piezoelectric pressure sensors located in the swirler nozzle, as shown in Figure 14. The pressure sensors are located $l_{mic}=0.0254$ meters center to center and 0.015 meters from the dump plane in the nozzle cavity. The data was recorded with a National Instruments NI9205 data acquisition system using Labview 9. Each channel on the data acquisition board was in differential mode. Pressure data were acquired at 30 kHz with sample lengths of 15,000 points. Data were ensemble averaged using ten ensembles.

Flame Transfer Function Uncertainty Estimation

The uncertainty in the flame transfer functions was calculated using standard Taylor series expansion uncertainty methodology [145]. The main source of error comes from the two microphone method, particularly at the lower frequency range. Given the

microphone spacing chosen for this experiment, the range of frequencies over which two microphone measurements are “good” is approximately 670 – 5350 Hz [146]. Over the range of frequencies tested, uncertainty in the measurements comes from two sources. First, there is random error from both the two microphone method and in the flame transfer function, and is defined using the coherence [147]. Second, and more importantly, bias error arises, particularly at the low frequencies, from the effective spacing of the two microphones being different from the physical spacing. According to estimates by Bodén and Åbom [146], this error can be up to 20% of the microphone spacing over the range of frequencies considered. This 20% quantity was used in our estimates.

CHAPTER 3

FLAME TRANSFER FUNCTION RESULTS

The motivating factor for the work encompassed in this thesis is to determine the mechanisms by which flame heat release fluctuations and acoustic fluctuations in a combustor couple. This chapter describes the measurement of flame response in a transversely forced, swirl-stabilized flame, as well as the measurements of the transverse to longitudinal velocity transfer function, F_{TL} . As described in Chapter 1, a transfer function cannot be defined for a transversely forced flame before the proper reference velocity is identified. The effort towards measuring and understanding F_{TL} is a necessary first step towards understanding flame response during these instabilities. The rest of the chapter is organized as follows. First, an overview of the measurements of the transverse to longitudinal velocity transfer function is presented. With this, relevant results pertaining to the velocity disturbance field and the transverse vs. longitudinal velocity field decomposition are also discussed. Next, flame transfer function results are presented with comparisons to theoretical predictions. Finally, these results and their implications are discussed.

Transverse to longitudinal velocity transfer function

Before discussing the transverse to longitudinal velocity transfer function, the fluctuating velocity field in the region of the nozzle is considered. Figure 25 shows the axial velocity spectrum along the dump plane at $x/D=0.05$ and the transverse velocity spectrum along the centerline for a reacting test with no acoustic forcing.

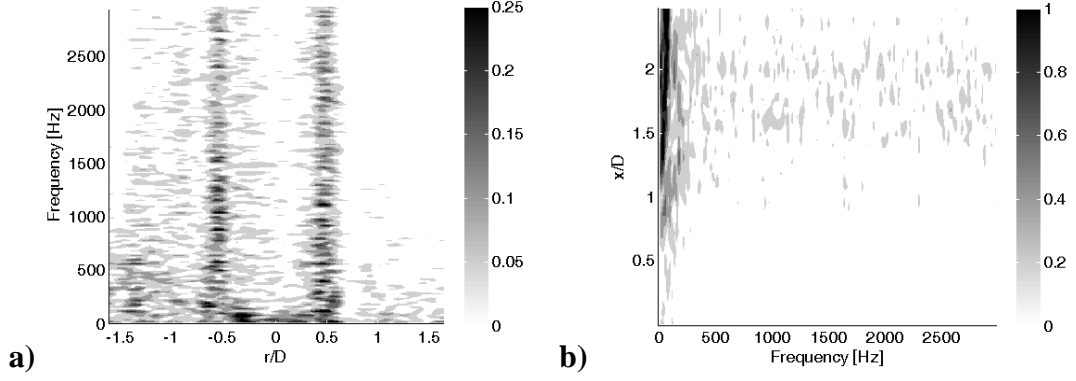


Figure 25. Spectra of a) axial velocity fluctuations at $x/D=0.05$ and b) transverse velocity fluctuations along the centerline for an unforced reacting flow at a bulk velocity of $u_o=10$ m/s and equivalence ratio of 0.95.

In the absence of forcing, the axial velocity fluctuations, shown in Figure 25a, are concentrated in the annular jet and shear layers, located at $r/D=0.5$ and $r/D=-0.5$, and are broadband. Similar low frequency content is seen in the transverse velocity fluctuations along the centerline, in the vortex breakdown region, as seen in Figure 25b. Very weak higher-frequency (>300 Hz) transverse motions exist along the centerline.

With transverse acoustic forcing present, the spectra of both the transverse and axial velocity change, as will be discussed shortly. As discussed previously, the relative strength of these fluctuations at the forcing frequency give us F_{TL} , the transverse to longitudinal velocity transfer function. The induced axial velocity fluctuations, as defined in Equation (11), are highly dependent on frequency, and this frequency dependence is presented in Figure 26, which shows results from both PIV and the two-microphone method. Comparison between the PIV and two-microphone data shows that these two methods yield similar velocity amplitude results across the frequency range of interest.

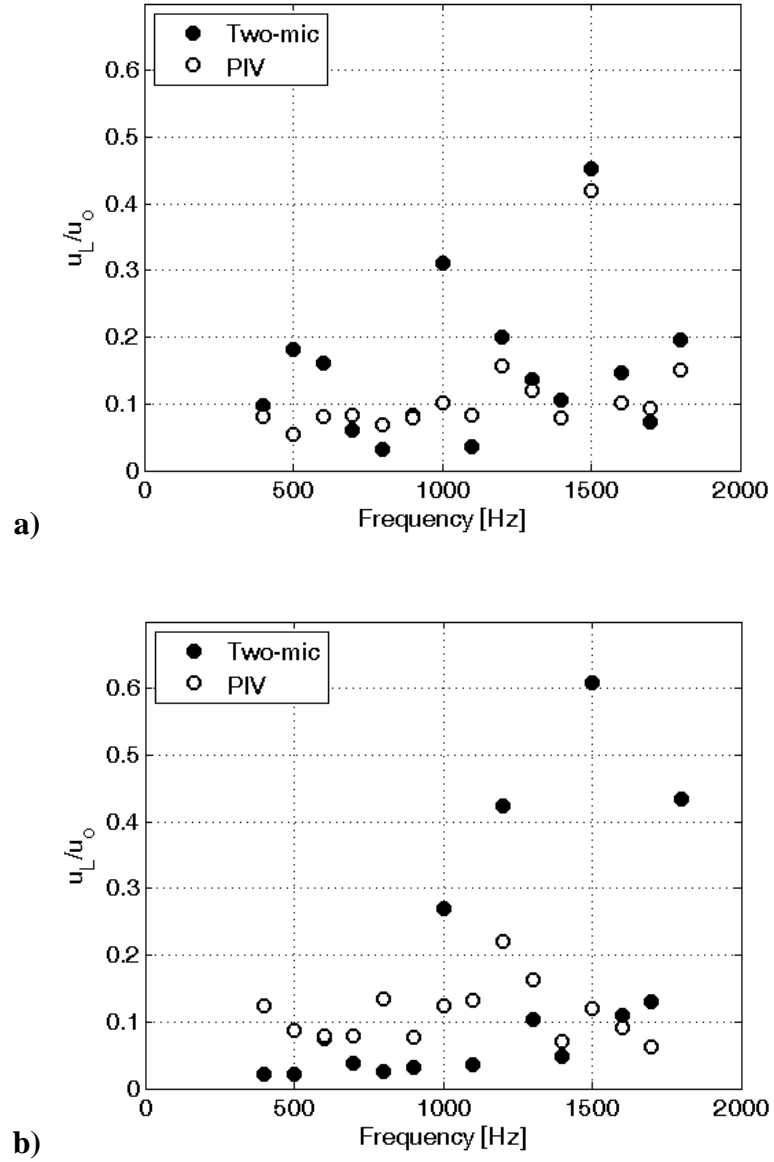


Figure 26. Axial velocity fluctuation amplitude for reacting flow with a) in-phase and b) out-of-phase forcing at a bulk velocity of $u_o=10$ m/s, $u'_{T,a}=1$ m/s, and a forcing frequency of $f_o=400$ -1800 Hz.

Figure 27 through Figure 31 show the measured transverse to longitudinal velocity transfer, F_{TL} , function for the non-reacting flow case at a bulk velocity of $U_o=10$ m/s and the reacting flow case at the same velocity and an equivalence ratio of 0.9. In the

transfer function gain (a) and phase (b) plots, the reacting in-phase data are offset by -20 Hz and the non-reacting out-of-phase data are offset by +20 Hz for clarity of the error bars in Figure 30 and Figure 31.

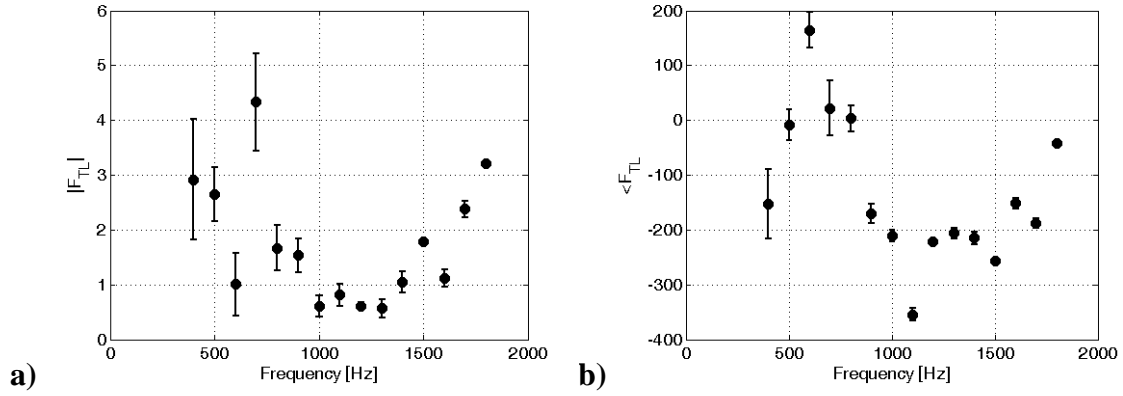


Figure 27. Transverse to longitudinal velocity transfer function a) gain ($|F_{TL}|$), and b) phase ($\angle F_{TL}$), for reacting flow with in-phase acoustic forcing, a bulk flow velocity of $u_o=10$ m/s, and equivalence ratio 0.9.

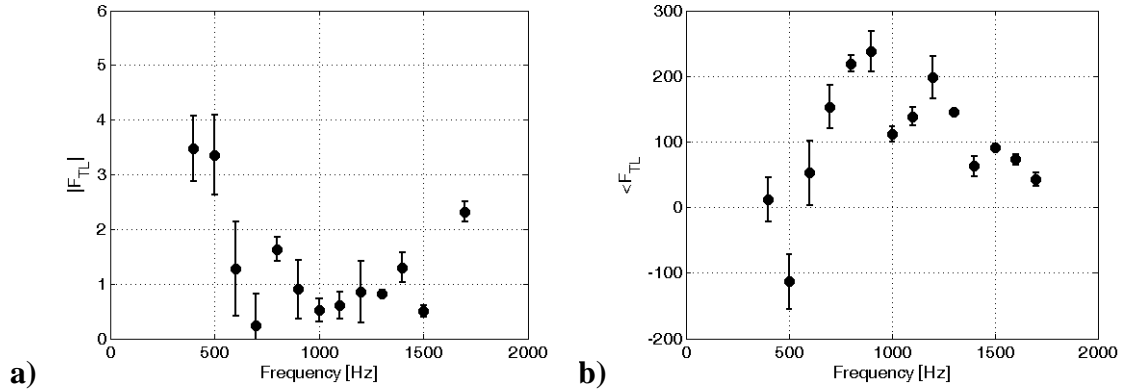


Figure 28. Transverse to longitudinal velocity transfer function a) gain ($|F_{TL}|$), and b) phase ($\angle F_{TL}$), for reacting flow with out-of-phase acoustic forcing, a bulk flow velocity of $u_o=10$ m/s, and equivalence ratio 0.9.

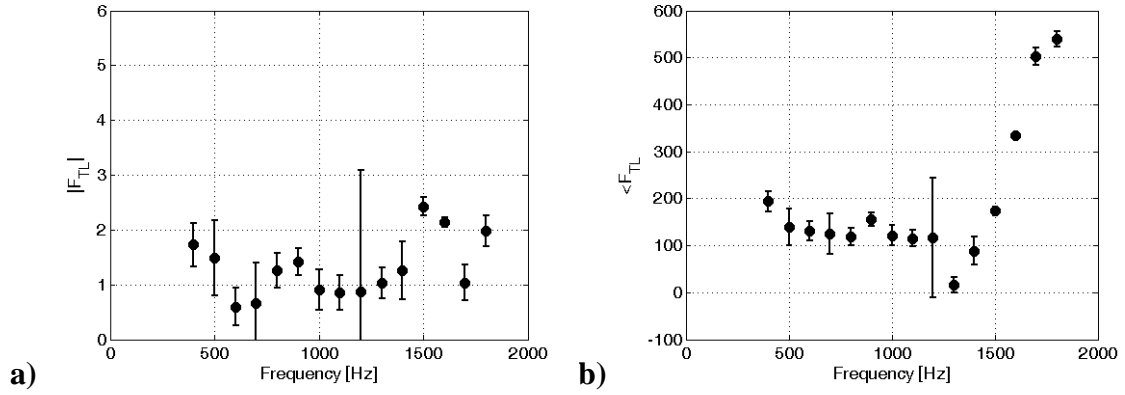
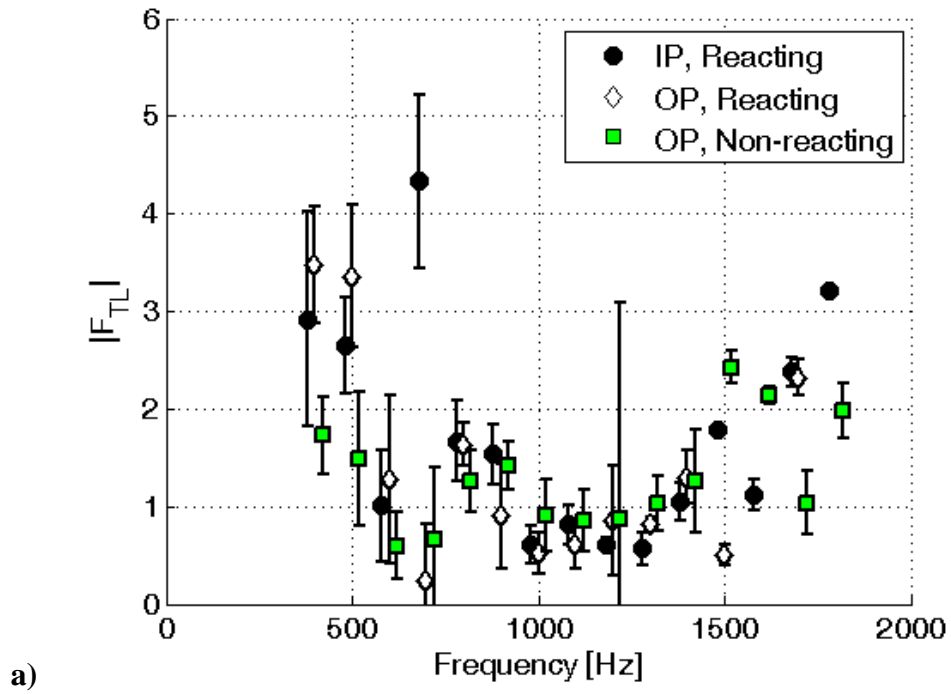


Figure 29. Transverse to longitudinal velocity transfer function a) gain ($|F_{TL}|$), and b) phase ($\angle F_{TL}$), for non-reacting flow with out-of-phase acoustic forcing, and a bulk flow velocity of $u_o = 10$ m/s.



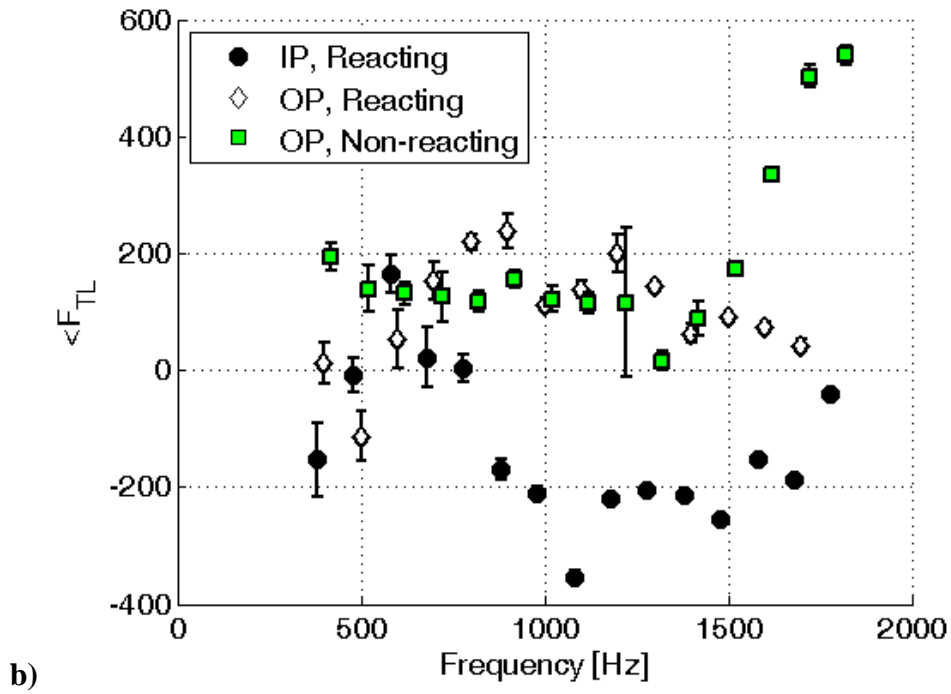


Figure 30. Transverse to longitudinal velocity transfer function a) gain ($|F_{TL}|$), and b) phase ($\angle F_{TL}$), for all cases.

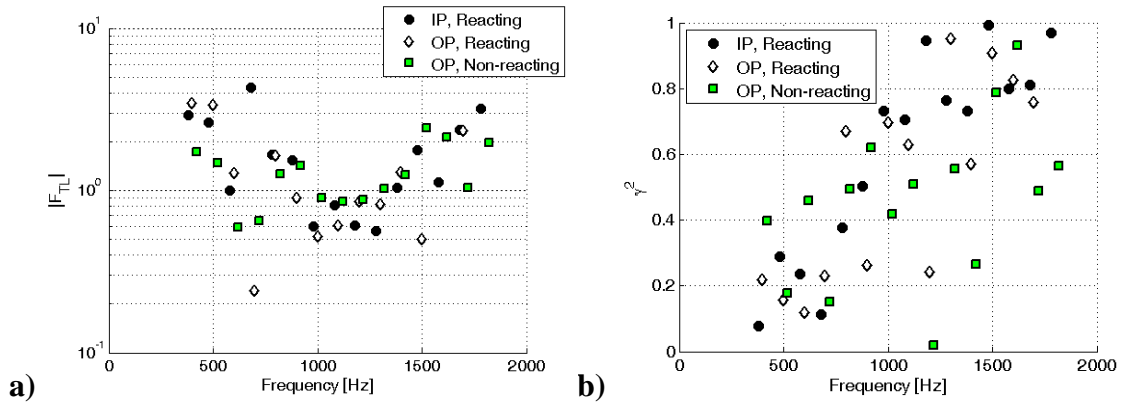


Figure 31. Transverse to longitudinal velocity transfer function a) gain ($|F_{TL}|$) on a log scale, and b) coherence squared, for all cases.

These transfer functions were obtained from data where the transverse velocity oscillation magnitude was nominally 10% of the mean axial velocity. Five ensemble

averages were used to calculate these transfer function gains and to estimate the uncertainties [147]. As an intrinsically acoustic quantity, F_{TL} can also be calculated using data from the two-microphone method as the reference axial velocity fluctuation. These results track closely with those shown in Figure 27.

The amplitude results from these transfer functions have two interesting features. First, the gain has high values at 400-500 Hz but drops to small values, below unity, between 900 Hz and 1400 Hz. Second, the amplitude peaks again at higher frequencies, particularly 1800 Hz. Although the transfer function amplitude at both the low and high frequencies is approximately equal, signifying non-negligible transverse to axial velocity coupling, the flow response in these two cases is fundamentally different. This can also be seen by looking at the spectrum as a function of radial location, as shown in Figure 32.

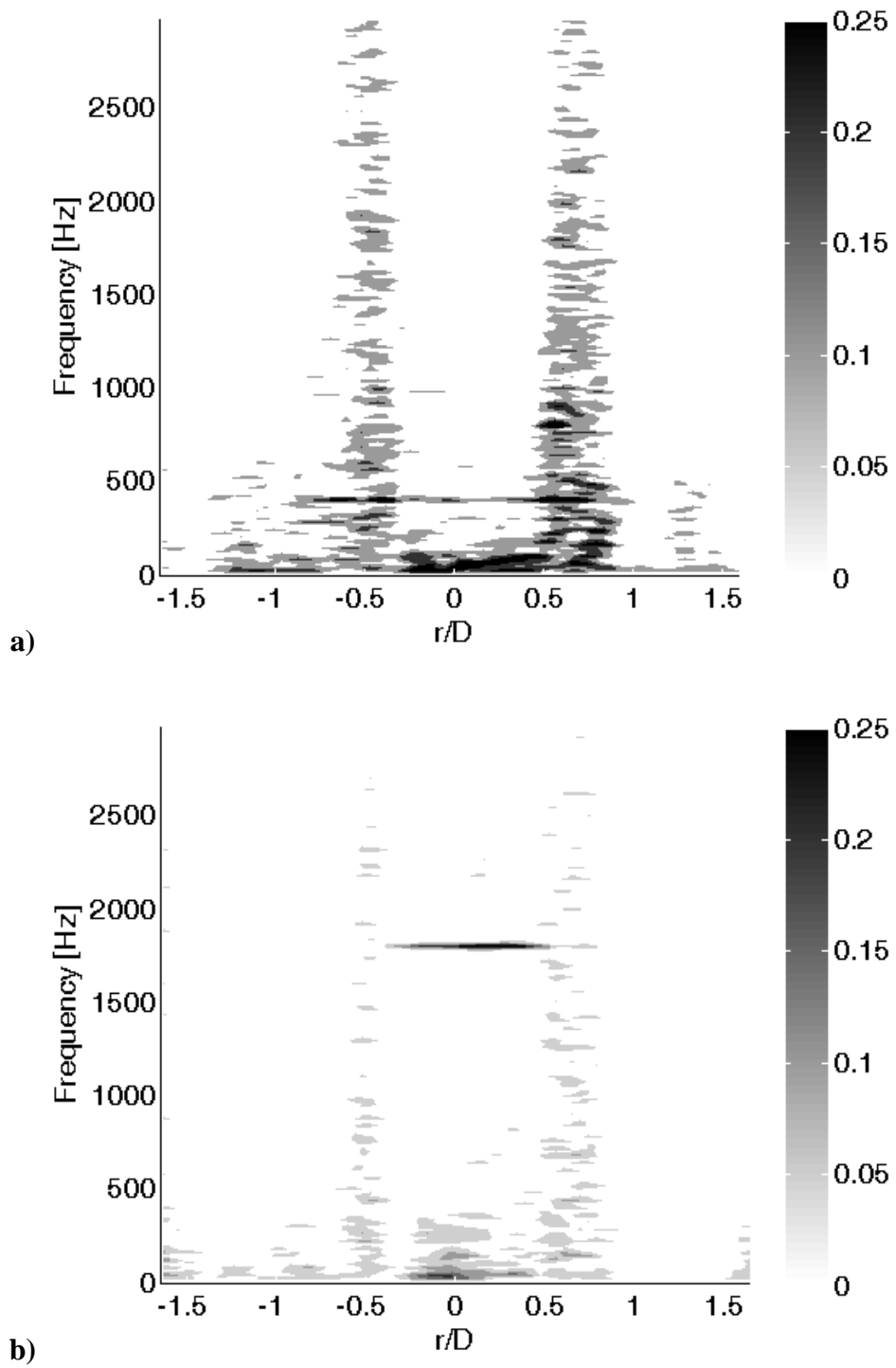
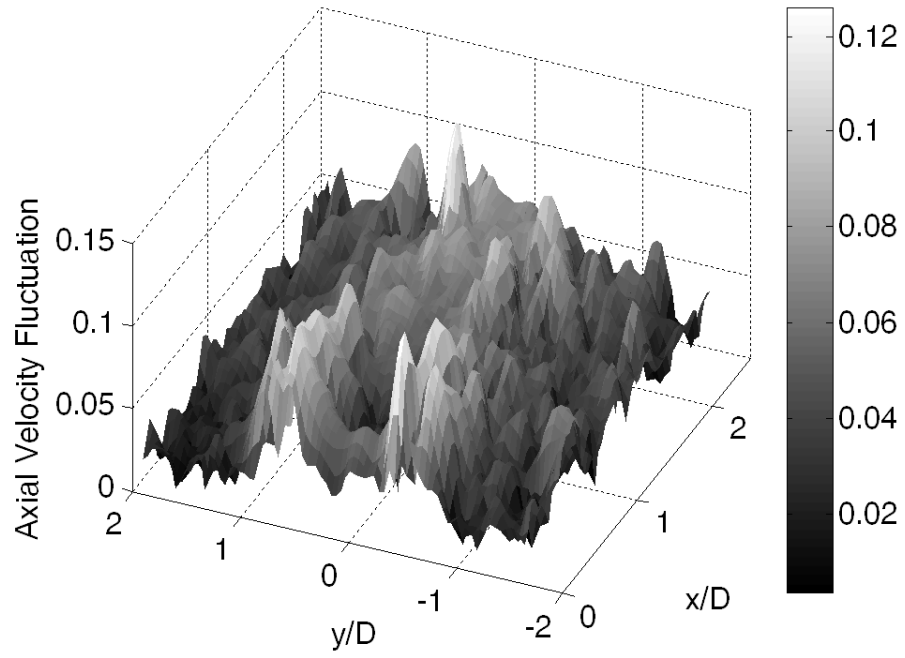
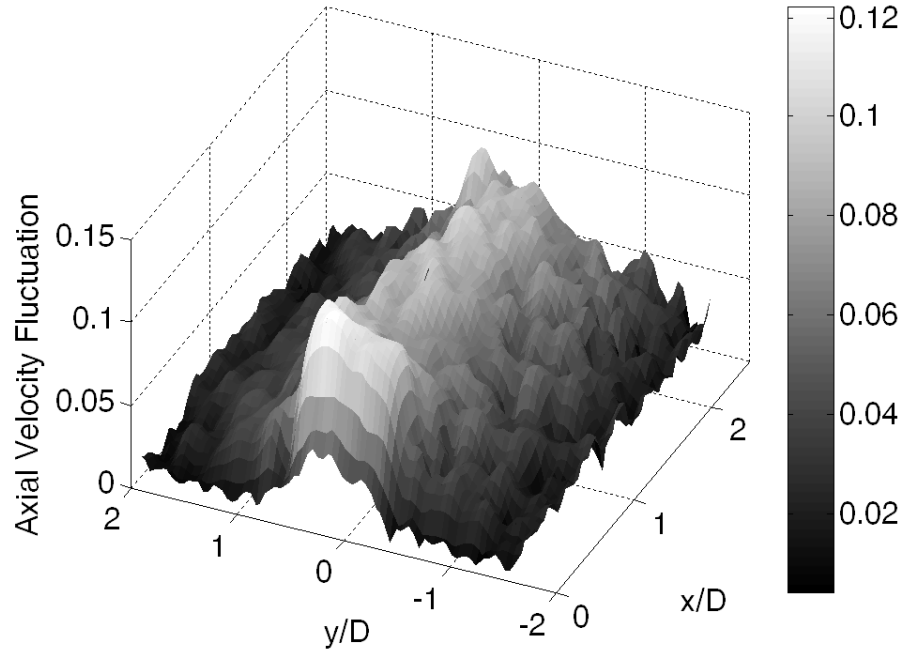


Figure 32. Axial velocity spectra at $x/D=0.05$ for a) 400 Hz in-phase and b) 1800 Hz in-phase acoustic forcing a bulk flow velocity of $u_o=10$ m/s and equivalence ratio 0.9.

Interesting changes to the velocity field can be seen in both Figure 32 and Figure 33. In the 400 Hz case, the axial velocity fluctuations are concentrated in the annular jet, while in the 1800 Hz case, the motion takes place across the entire diameter of the jet, including the vortex breakdown region. Further downstream, this region stretches even farther in the radial direction as the jet spreads. Additionally, the coherence of the axial and transverse velocity fluctuations is nearly unity at 1800 Hz, as well as several other higher frequencies, while the coherence is very low near 400 Hz. This trend continues downstream of the dump plane, as is shown in Figure 33. Here, the magnitude of the axial velocity fluctuations at the forcing frequency is shown for the entire flow field. Like the spectra in Figure 32, these plots show that the spatial distribution of axial velocity fluctuations is significantly different between the low frequencies and high frequencies, despite the similar magnitude in F_{TL} of the two.



a)



b)

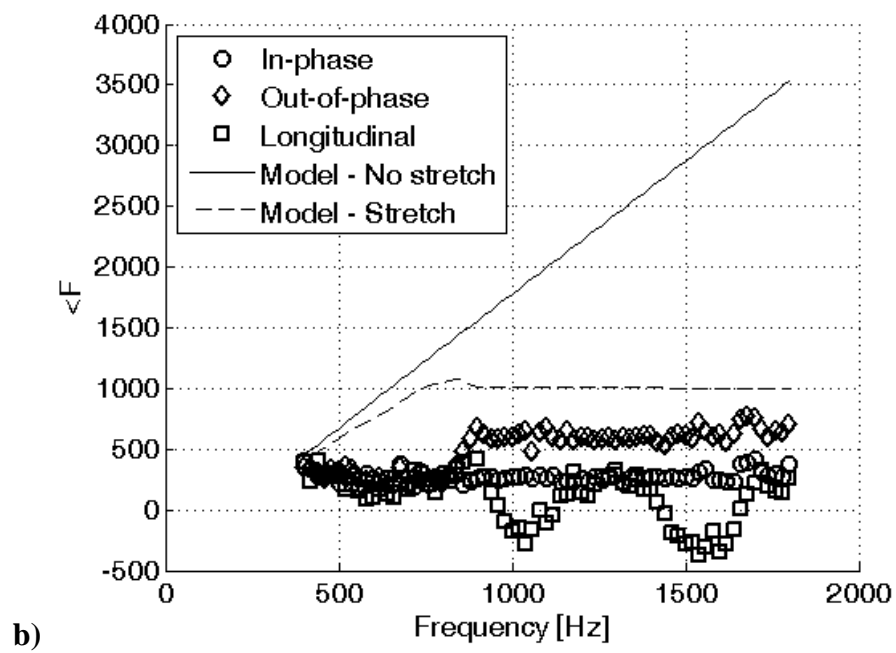
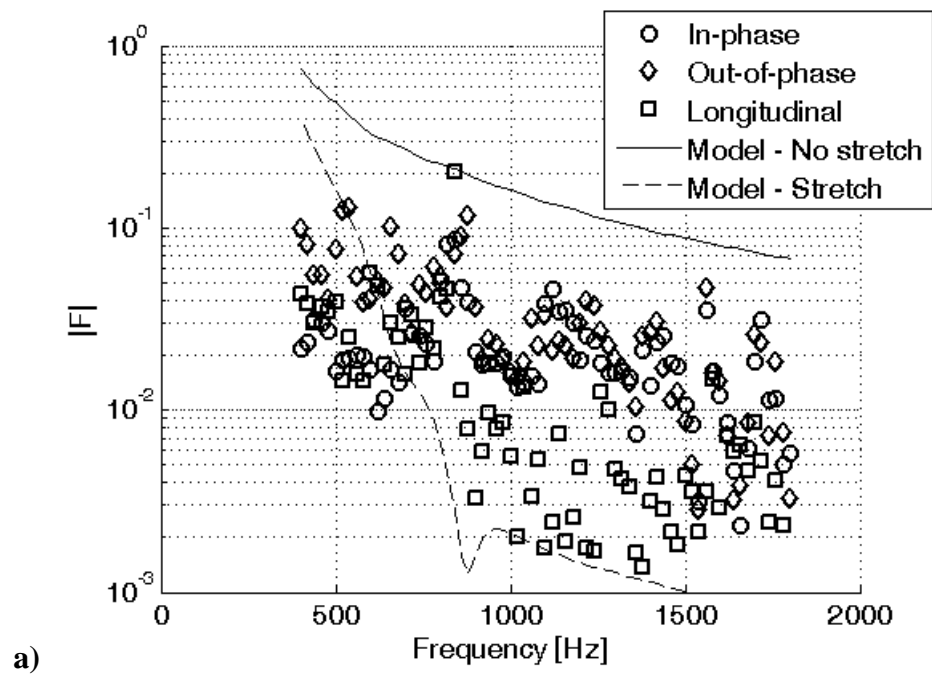
Figure 33. Magnitude of the normalized axial velocity fluctuations at the forcing frequency throughout the flow field for a) 400 Hz in-phase and b) 1800 Hz in-phase acoustic forcing a bulk flow velocity of $u_o=10$ m/s and equivalence ratio 0.9.

This difference in response may be a manifestation of the nozzle acoustics. A rough calculation of the natural frequency of the nozzle (a half-wave mode) is 1800 Hz, in the range of the high coherence, high amplitude response frequencies seen in Figure 30. This means that the external pressure fluctuation from the transverse field in the 1800 Hz forcing case is driving the fluctuations in the nozzle near the resonant frequency, resulting in a large-scale axial response in and around the nozzle. Through a series of short experimental tests at frequencies between 1700 Hz and 1900 Hz in 10 Hz increments, it was visually observed that the flow response was maximized in the 1790 – 1810 Hz region, indicating that the maximum axial flow oscillations occur in this frequency range.

The results from both measurement of F_{TL} and flow visualization clearly show that the response of the nozzle and the resultant longitudinal acoustic velocity fluctuations are key components to understanding disturbance field physics, and in turn, flame response. The pertinent flame disturbance pathways, described in Figure 6, change as a function of frequency. For example, in the range of 600 to 1000 Hz, the gain of F_{TL} is less than one, signaling that the transverse acoustics dominate the disturbance field. However, at frequencies such as 1500 Hz and 1800 Hz, the nozzle response is significant enough to induce significant changes in the flow field and flame, resulting in flame response that is driven by a longitudinal acoustic motion. The results from this portion of the study will inform the choice of flame transfer function form, discussed in the next section.

Flame transfer function results

The flame transfer function describes the response of a flame to an input velocity disturbance. As discussed previously, the choice of reference velocity for this transfer function is of paramount importance. The flame response has been measured for three different acoustic forcing conditions: in-phase transverse forcing, out-of-phase transverse forcing, and longitudinal forcing. The results of these tests, using the longitudinal acoustic velocity measured by the two-microphone method as the reference velocity, are shown in Figure 34.



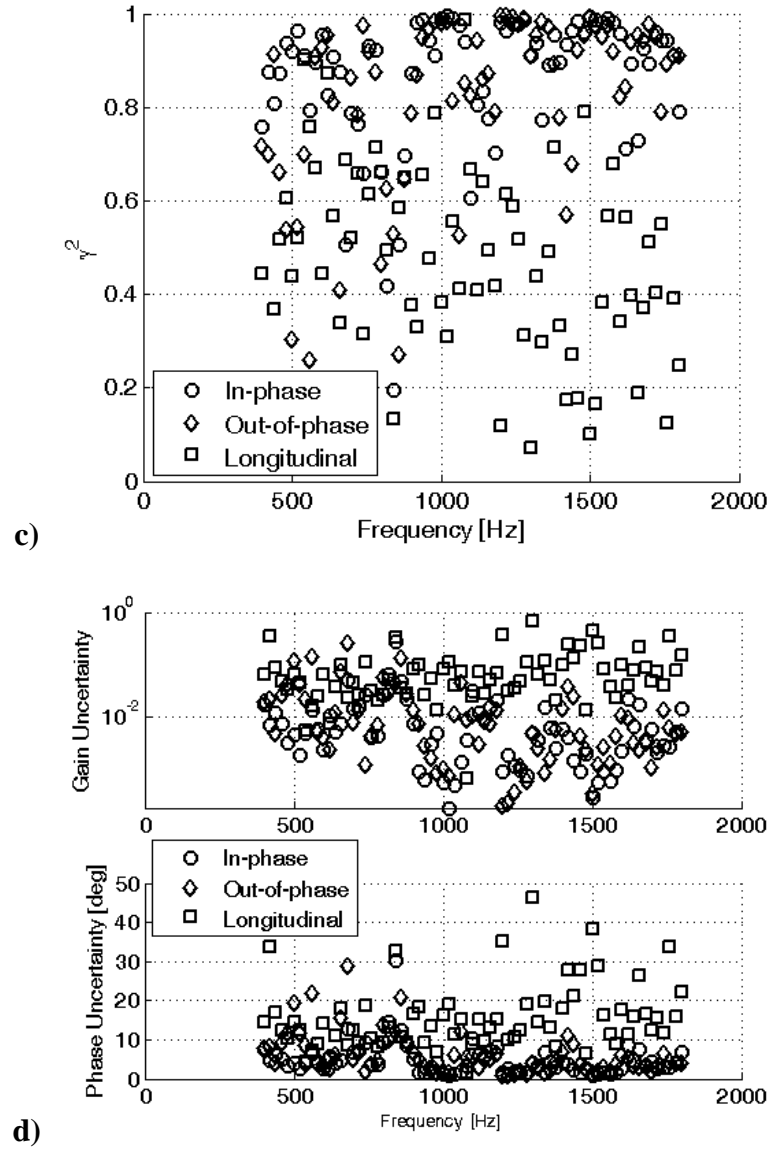


Figure 34. Flame transfer function a) gain, b) phase, c) coherence, and d) uncertainty in gain and phase for in-phase transverse forcing, out-of-phase transverse forcing, and longitudinal forcing at a bulk velocity of $u_o=10$ m/s, equivalence ratio of 0.9.

The measured flame transfer function results are plotted with the results from a longitudinally forced G-equation model, described in Equations (7) – (10) with and without flame stretch correction terms included; for more details on the model, see Refs.

[128, 148]. The measured transfer function results follow the trends in the gain from these models, although the phase measurements are significantly different than the predicted phase. The discrepancy in the phase stems from the very low amplitudes of the gain; at low levels of gain, phase measurements are typically unreliable.

The transfer functions for the transversely forced flames shown in Figure 34 use a more “traditional” reference velocity and do not account for the change in reference velocity frequency. To account for the system response issues described previously, Figure 35 shows the product of the flame transfer functions reported above and F_{TL} , the transverse to longitudinal velocity transfer function. Multiplying the flame transfer function by the velocity transfer function weights the flame transfer function results by the system response.

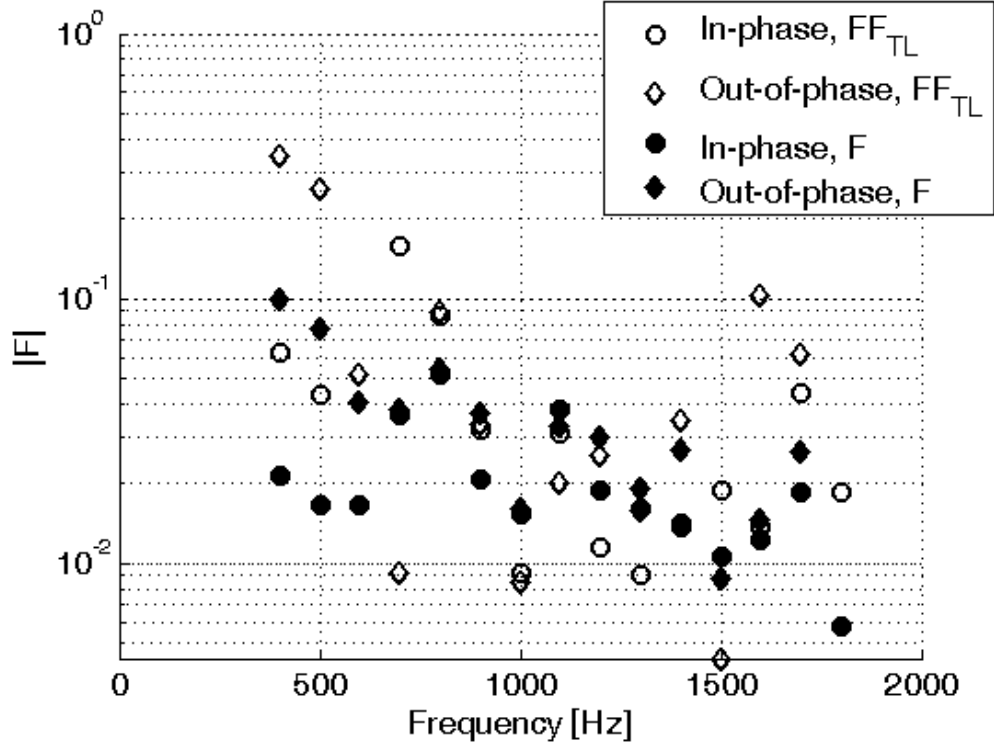


Figure 35. Flame transfer function gain comparison between F_{TL} weighted transfer function and standard flame transfer function based on a longitudinal acoustic reference velocity, at a bulk velocity of $u_o=10$ m/s, equivalence ratio of 0.9.

The gain results in Figure 35 therefore mimic the shape of the transverse to longitudinal velocity transfer function gain shown in Figure 27, particularly in the high frequency range where the nozzle response is high. This type of transfer function more accurately describes the response of the flame and the combustor system as it captures not only the amplitude of heat release but also the frequencies at which the system responds the greatest to the initial transverse perturbation.

Two issues need to be discussed with respect to these transfer function results. First, the magnitude of the flame transfer function gain is low compared to previously reported data, even with the reported uncertainty, which increases at the low frequencies

due to error in the two microphone method. This is most likely due to two effects. In the lower frequency range, the nozzle acoustics are not being excited and the response of the acoustically compact flame to purely transverse excitation is very low [149]. This is because the net flux of reactants through the flame over the course of the acoustic cycle, in the transverse direction, is negligible and so the flame heat release fluctuation sums to zero. This is not the case, though, for the higher frequencies where the acoustically compact assumption may no longer hold. That leads to the second point, though, that flame response is inherently low at high frequencies, as can be seen from the model results in Figure 34. This stems from the fact that the flame acts like a low pass filter as a result of the action of kinematic restoration along the flame front. Short wavelength wrinkles are quickly destroyed as the flame propagates into itself and contribute very little to the overall heat release fluctuation; this effect is even more drastic when stretch effects are accounted for.

These points being made, though, the flame response does jump in the weighted flame transfer function results at the frequencies at which the nozzle resonates. This intuitively makes sense; the flame is excited by a strongly longitudinal field that has been amplified by the action of the nozzle resonance. This point may further the understanding of under what conditions transverse instabilities are truly detrimental in gas turbine combustor geometries. The coupling between the azimuthal combustor mode and the longitudinal nozzle mode will be a function of combustor geometric and acoustic parameters, such as annular circumference, nozzle depth, and nozzle impedance, which is usually a function of pressure drop across the swirler. The frequencies at which these two modes, the azimuthal and longitudinal, align will be the most powerful drivers of

self-excited transverse combustion instabilities, resulting in high amplitude flame response to the nozzle acoustics that feeds energy into the azimuthal acoustic mode.

This type of coupling can be seen in the LES simulations of Staffelbach *et al.* [25], which aligns with the flame transfer function results presented here. Examples of the effect of the longitudinal fluctuations are shown in Figure 36, which shows flame position from Staffelbach *et al.* [25] at several adjacent nozzles. In this simulation, the flame anchoring location fluctuates in the downstream direction in phase with the mass flow fluctuations from the nozzle. The correlation between the pressure from the transverse acoustic field, shown on the bottom of Figure 36, and the flame anchoring position, shown on the top of the same figure, exemplifies the coupling between the transverse acoustic field in the combustor and the longitudinal mode in the nozzle, as measured in this study.

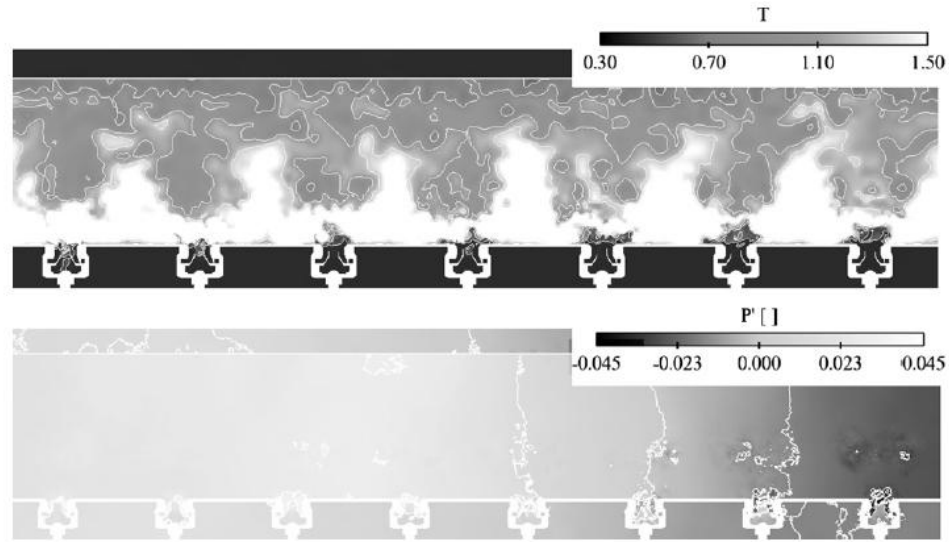


Figure 36. Variable flame anchoring position as a result of longitudinal mass flow fluctuations during transverse instability of an annular combustor, reproduced from Staffelbach *et al.* [25].

Understanding of this coupling and the resultant flame response can have great impact on the way that future gas turbine combustors are designed. While combustion instabilities have always been a serious consideration during the design process [150], these results can provide guidelines for relative sizing of annular combustor sections and nozzle geometries over the range of operating conditions (nozzle pressure drops or impedances) predicted for field operation. By “mistuning” the nozzle to the annular section, high amplitude transverse instabilities can be avoided as the transverse to longitudinal acoustic coupling mechanism will be weak at off-resonance frequencies. Simple acoustic modeling of proposed designs can be used to screen these designs for possible coupling and eliminate harmful transverse dynamics events during operation.

CHAPTER 4

RECIRCULATION ZONE DYNAMICS

In this chapter and the one following, a more detailed description of the velocity disturbance field is presented. In Chapter 3, the velocity field was decomposed in terms of the direction of velocity oscillation, transverse vs. longitudinal velocity fluctuations, in order to help formulate a flame transfer function approach to transverse instability characterization. In this section, the velocity is considered as having two constituents, an acoustic component and a vortical component, where the acoustic field perturbations excite fluctuations in the vortical velocity field. As discussed in the Introduction, the type of the response of the flow to acoustic forcing is highly dependent on the stability characteristics of the flow. As disturbance amplifiers, convectively unstable flows respond strongly to acoustic forcing and the frequency of response of the flow field will match that of the incident acoustic field. Absolutely unstable flows, being self-excited oscillators, are impervious to low levels of acoustic forcing, although nonlinear processes can lead to coupling between acoustics and the flow field at high excitation amplitudes. In this chapter, the details of the base flow, dominated by vortex breakdown – a result of the absolute instability of the swirling jet – is discussed and the response of this structure to acoustic forcing is investigated for both the time-average and dynamical behavior of the flow.

This section is organized as follows. First, an overview of the analysis methods used in studying the base flow is provided; this includes details of a spatial mode

decomposition upon which much of the later discussion is based. Second, the no forcing case is considered and the dynamics of the self-excited oscillations are detailed. Next, the response of the time-average flow field to acoustic forcing is discussed, followed by results pertaining to the response of the dynamical features of the vortex breakdown bubble to acoustic forcing. The last results presented in this chapter are those from reacting flow studies, and the influence of high amplitude acoustic forcing on the flame shape is detailed. Finally, a deeper discussion of some of these issues and their implications concludes the chapter.

Analysis Methods

Several techniques were used to quantify the behavior of the vortex breakdown region and the effect of transverse acoustic forcing. The use of high-speed PIV diagnostics allowed for spectral analysis of the data, which was used extensively in this study. First, spectra of several quantities were calculated using fast Fourier transforms. 500 images were taken at 10 kHz, resulting in a spectral resolution of 20 Hz and a maximum resolvable frequency of 5 kHz. In this way, the amplitude and phase of fluctuations at this range of frequencies can be seen across the field of view.

The frequency domain velocity was also used to decompose the flow field into spatial mode shapes in the $r-\theta$ cases. This type of decomposition can be used to quantify the mode shapes appearing in the θ -direction at different radii from the center of the flow. This technique has been used previously [151, 152] to calculate the mode shapes in jets and axisymmetric wakes. In this analysis, the radial and azimuthal velocities are extracted from the instantaneous velocity fields at 8 radial locations and 21

points around each radius. From there, the fast Fourier transform is performed at each point and a spectrum of velocity fluctuations at each point is produced. In this way, it is possible to decompose the fluctuations at each frequency into a set of spatial modes in the θ -direction at each radius with the expression in Equation (12):

$$\hat{u}(r, \theta, \omega) = \sum_{m=0}^N A_m(r, \omega) e^{im\theta} + B_m(r, \omega) e^{-im\theta} \quad (12)$$

Here, $\hat{u}(r, \theta, \omega)$ is a complex number, the Fourier transform of the velocity fluctuation. $A_m(r, \omega)$ and $B_m(r, \omega)$ are the amplitudes of the modes in the counter-swirl (clockwise) and co-swirl (counter-clockwise) waves, respectively. Finally, m is the mode number describing the spatial fluctuation in the azimuthal directions that can have integer values between $-(N-1)/2$ and $(N-1)/2$, where N is the number of points measured in the azimuthal direction.

It is important to note here that the literature has a variety of conventions for the sign of m and what this indicates in terms of the rotation of the instability with respect to the flow. In this study, the convention described by Liang and Maxworthy [75] and Loiseleux *et al.* [153] is used. Here, the sign/direction convection for the instability changes for jets and wakes, and can be described in Table 1. The “rotation” refers to the direction of the mode with respect to the direction of swirl, where the “winding” refers to the direction that the helical structure winds with respect to the swirl.

Table 1. Azimuthal mode number conventions for jets and wakes after Ref. [75].

Flow	Mode	Rotation	Winding
jet	$m>0$	co-rotating	counter-winding
jet	$m<0$	counter-rotating	co-winding
wake	$m>0$	counter-rotating	co-winding
wake	$m<0$	co-rotating	counter-winding

In this convention, the form of the perturbation is shown in Equation (13).

$$\Psi = \hat{\Psi} r \exp i kx + m\theta - \omega t \quad (13)$$

In this study, the flow profile most closely mimics that of a wake with counterflow as a result of the vortex breakdown bubble [153]. This can be seen by comparing flow profiles shown in Figure 16 - Figure 19 with the example profiles in Ref. [153]. Given that, the wake convention is adopted in this work. As will be seen later in the results section of this chapter, modes $m<0$ do indeed rotate in the direction of swirl.

Next, quantification of the shape of the flow was achieved by measuring the spreading angle of the annular jet (for the non-reacting cases) and the flame (for the reacting cases). The angle of both the jet and the flame provides a useful quantification of the vortex breakdown size; the wider the angle (from the vertical), the larger the vortex breakdown bubble. As discussed above, the vortex breakdown bubble size and shape controls many features of the "outer" flow field.

To measure the jet angle, the location of the jet was first calculated by finding the maximum time-average axial velocity at each downstream distance. Then, a nonlinear least-squares curve fit routine was used to fit a line to the jet path between $x/D = 0$ to $x/D = 0.5$. A similar process was used to calculate the flame angle. First, the luminosity flame images were thresholded and binarized in order to find the flame edge. Then, the

same nonlinear least-squares curve fit routine was applied to the flame edge from the binarized image between $x/D = 0$ to $x/D = 0.5$ and the flame angle calculated from the slope of that fit. The angle of the jet/flame was calculated for five ensembles separately; the average angle is reported and the standard deviation of these angles quantifies the uncertainty in this measurement.

No forcing results, non-reacting flow

This section presents a baseline characterization of the time-average flow without external forcing. Figure 16, in Chapter 2, shows the non-reacting axial velocity and azimuthal vorticity, normalized by the bulk velocity divided by the annular gap width. The axial velocity plot shows the jets on either side of the centerline with the reverse flow region in the center that is merged with the centerbody wake. The two shear layers on each side of the annular jets are evident in the vorticity plot.

The instantaneous flow field shows substantially more small scale structure, as shown in Figure 37. Natural fluctuations in the axial velocity due to turbulence can be seen in the jet, and the vortex breakdown bubble has a more contorted edge and more complicated internal structure on an instantaneous basis. The zero axial velocity contours have been plotted in these images to further emphasize this point.

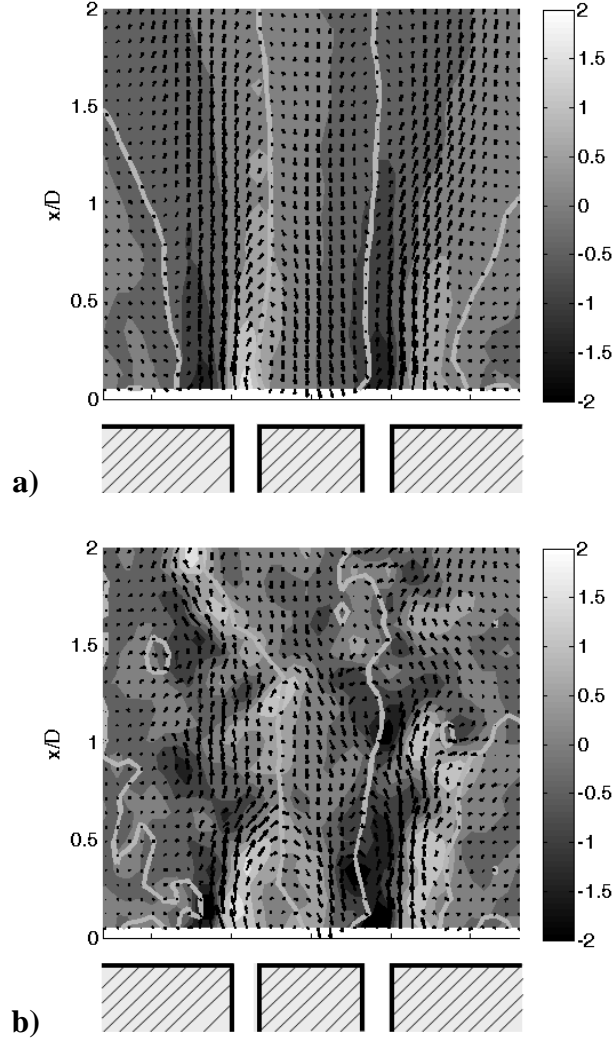
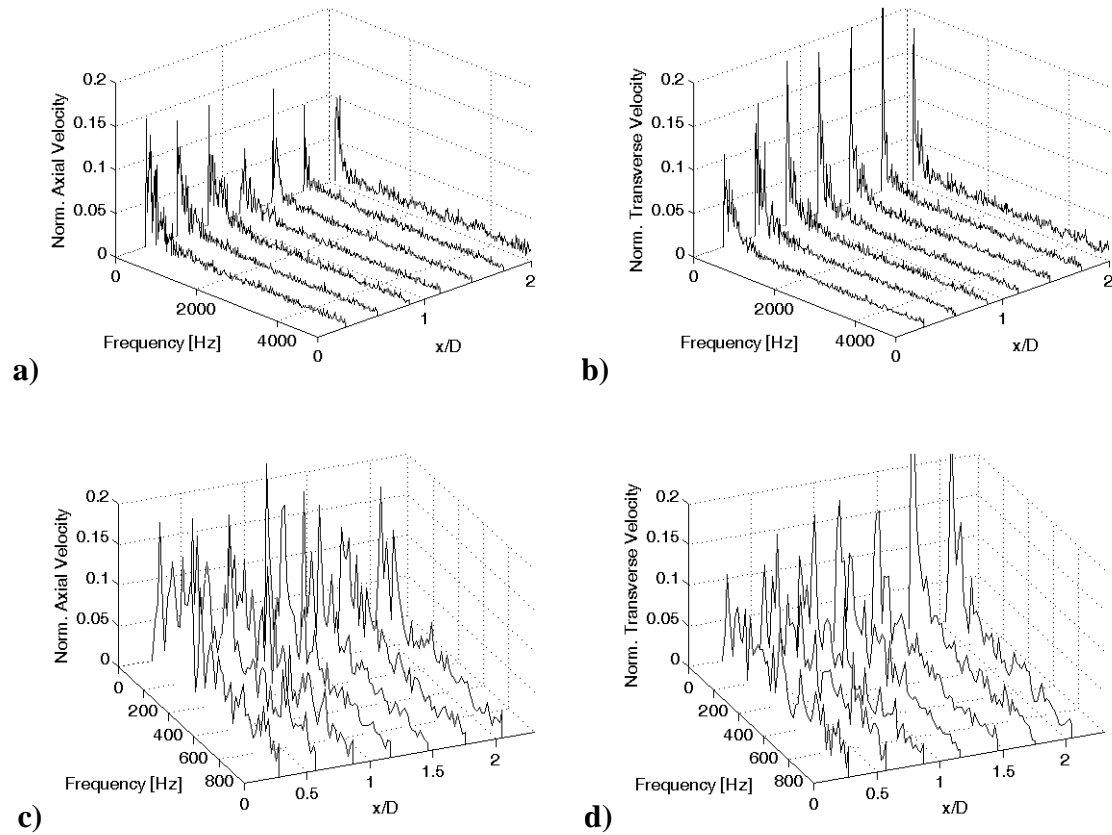


Figure 37. Comparison of a) time-average and b) instantaneous vorticity for the unforced flow, $S=0.85$. Arrows in each plot indicated normalized velocity; zero velocity contours are plotted in light grey.

The time-average azimuthal velocity field is shown in Figure 20, obtained at a measurement planes $x/D=0$, 1, and 2 above the bottom of the field of view, 0.7 cm from the dump plane. These time-average views show a swirling jet with a relatively uniform profile in the radial direction across the annular width at $x/D=0$, but the shape of the combustor affects the shape of the jet further downstream. At $x/D=1$, the jet is slightly

less axisymmetric, and by $x/D = 2$, the influence of the high aspect ratio combustor shape is evident. At this location, the flow is able to spread more in the r-direction, while it is confined in the z-direction.

Figure 38 shows axial and transverse velocity spectra at several axial locations at the flow centerline and at the left and right edges of the time-average vortex breakdown boundary. The velocity spectra show low frequency content in all these regions of the flow that oscillates at an amplitude of up to 20% of the mean flow velocity. The content of the remaining spectra is very similar to those shown in the non-reacting case in Figure 38.



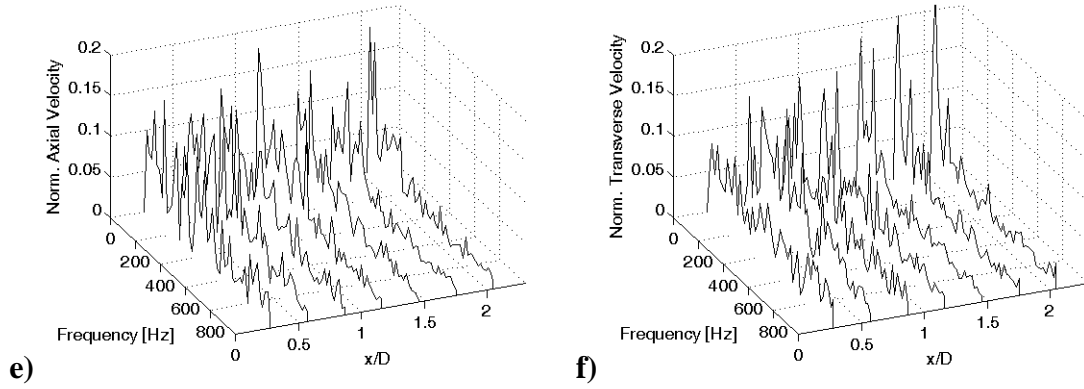
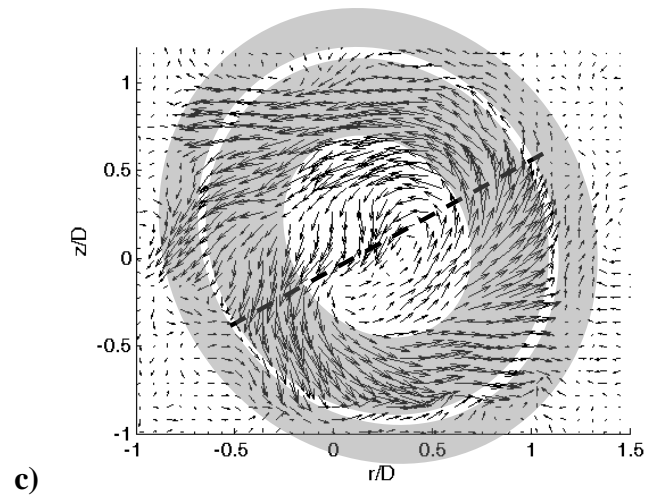
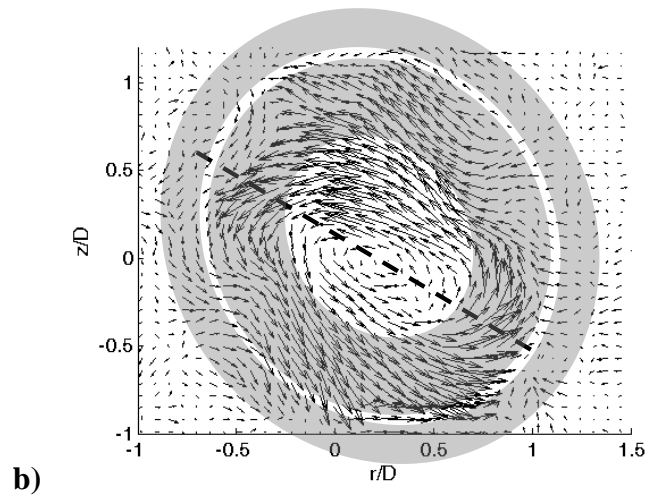
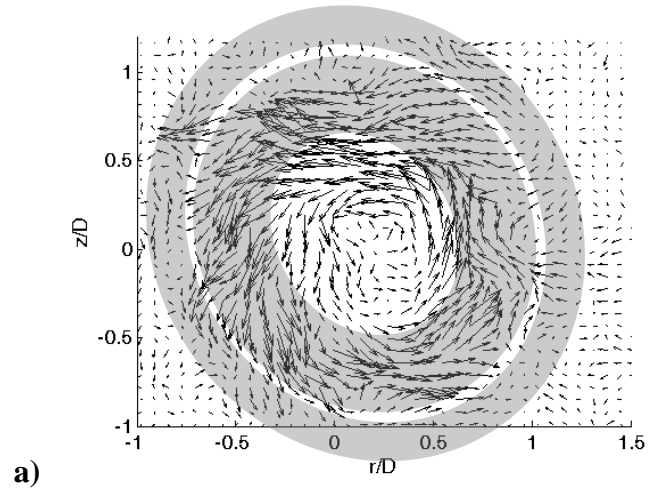


Figure 38. Spectra of normalized a,c,e) axial component and b,d,f) transverse component of velocity along the time-average centerline (a,b), left-hand vortex breakdown boundary (c,d – zoomed in), and right-hand vortex breakdown boundary (e,f – zoomed in) for non-reacting flow with no acoustic forcing, at $u_o=10$ m/s, $S=0.85$. Fluctuation amplitude is normalized by the bulk velocity, $u_o=10$.

Figure 38 show the presence of significant amounts of self-excited low frequency motion throughout the flow field with little higher frequency motion. Swirling flows are susceptible to a variety of self-excited motions, including shear layer rollup [110, 140], vortex breakdown bubble movement [92, 113], and other jet instabilities [82, 154]. In this case, the low frequency motion is the result of a precessing vortex core in the vortex breakdown region. To visualize this, filtered velocity data in the $r-\theta$ plane are shown in Figure 39 as a series of images at progressive instances in time. Here, the velocity data have been low-pass filtered at 200 Hz using a second order Butterworth filter to capture the lower frequency motion. Additionally, the gray regions represent the approximate areas of the inner and outer shear layers at this downstream location.



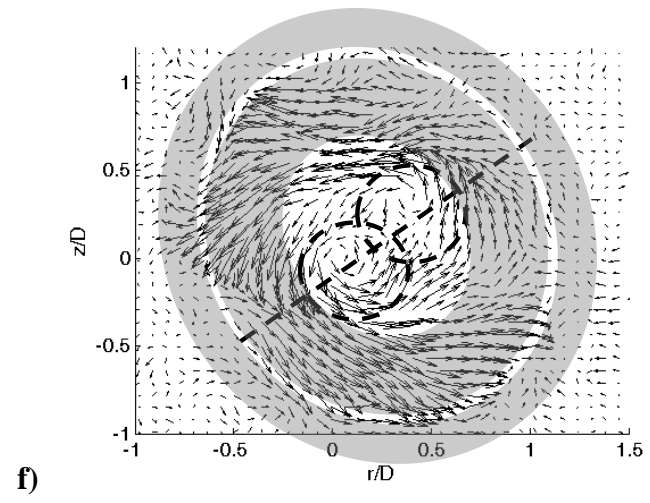
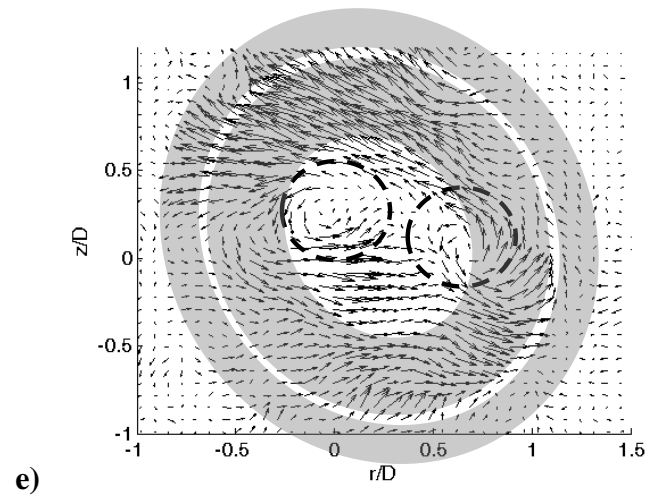
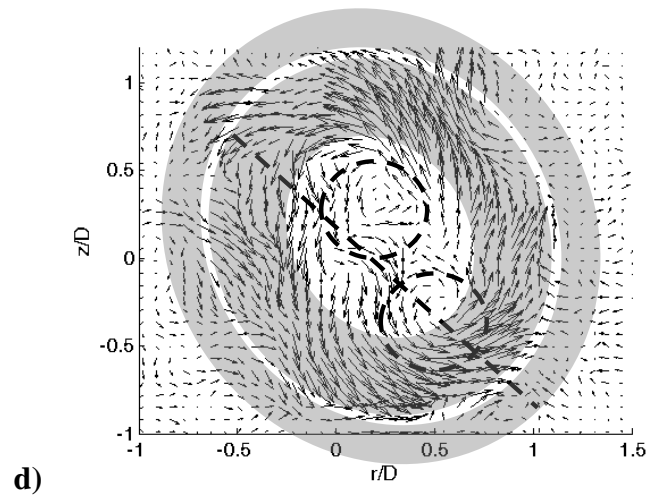


Figure 39. Precessing vortex core shown through the filtered velocity field in the $r-\theta$ plane at $x/D=1$ and a) $t=0.5$ ms, b) 4.1 ms, c) 10.1 ms, d) 13.1 ms, e) 17.1 ms, f) 20.1 ms, for a non-reacting, non-forced flow at $u_o=10$ m/s, $S=0.85$. Gray regions indicate approximate location of inner and outer shear layer at $x/D=1$.

Two concurrent motions are evident from this series of velocity fields in Figure 39. The first is a fluctuation in the overall shape of the jet, while the second is due to two smaller-scale coherent structures in the central recirculation zone. Notional sketches of these two motions are shown in Figure 40.

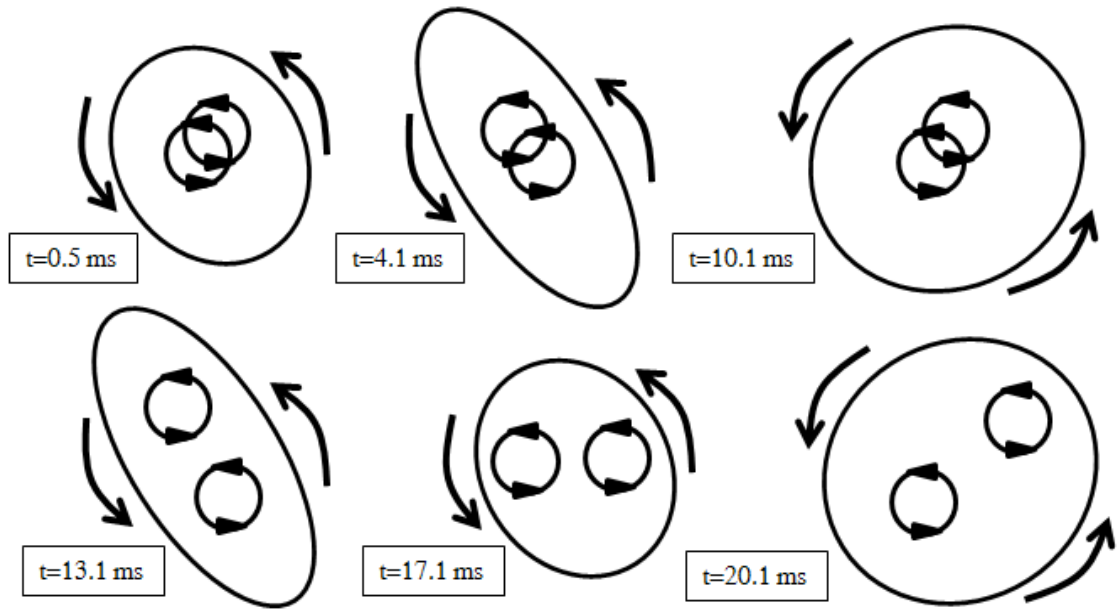


Figure 40. Notional picture of self-excited motion showing both the jet deformation ($m = -2$ mode) and coherent structure motion ($m = -1$ mode) for an unforced flow.

First, as is seen in the time-average image in Figure 20c, the jet at $x/D=1$ spreads preferentially towards the top-left and bottom-right quadrants of the image. In the time series of the low frequency motion, a semi-periodic stretching and contracting of the jet along the axis along which the jet is biased is observed. A notional picture of this

motion is shown in Figure 40. For example, this bias can be clearly seen in Figure 39b and Figure 39d, as is indicated with dotted lines. This is reflected in the sketch in Figure 40a in time-instances $t=0.5$ ms and $t=13.1$ ms. Motion of the jet in the opposite direction is evident at the subsequent time, in Figure 39c and Figure 39f and shown using dotted lines. This is reflected in the sketch in Figure 40 in time-instances $t=10.1$ ms and $t=20.1$, with a transitional time shown in time-instances $t=4.1$ ms and $t=17.1$ ms. This motion is indicative of a $m = -2$ mode in the jet, as discussed later; here the jet stretches in each direction twice as the motion rotates once around the center of the jet.

The second motion is smaller scale, and involves two coherent structures that precess about the center of the flow field. These can be seen in several of the images in Figure 39, circled with a dashed line. While these coherent structures clearly precess around the center of the flow field for parts of the “cycle,” they also overlap, as is shown in the instances in Figure 39a-c. This is reflected in the notional images shown in Figure 40, where at time-instances $t=13.1 - 20.1$ ms, the structures are separate, but at time-instances $t=0.5 - 10.1$ ms they seem to overlap.

The periods of rotation of these two motions are not the same, but instead the period of one rotation is twice that of the other. The longer period, referred to as T_1 , describes the motion of the two smaller scale coherent structures in the recirculation zone and is given by mode $m = -1$. This period is approximately $T_1 = 20$ ms, as is shown in Figure 40. The shorter period, referred to as T_2 , is the deformation of the jet column that rotates around the center axis over a period of approximately $T_2 = 10$ ms. This is a mode $m = -2$ motion.

The two small-scale structures follow the macro-movement of the jet described above, and may actually be the cause of this semi-periodic squeezing of the jet column, described as a $m = -2$ motion. Despite that, local to these two structures, the motion of the flow is better described by an $m = -1$ motion. In this case, the smaller structures pulse radially in two separate motions, over a time period T_1 , as the entire jet deforms over a time period of T_2 . During the time span that is half of period T_1 (one full rotation of the motion over period T_2), given by Figure 40a-c, the small-scale structures are tightly overlapped, appearing as a single structure that just deforms as the jet does. This can be seen in Figure 40b during time-instances $t=0.5 - 10.1$ ms and Figure 39a-c. During the second rotation of the jet column deformation over the second half of time period T_1 , the two structures are clearly separated, although the shape of the jet column does not differ significantly between this part of the cycle and the previous. This more separated motion can be seen in Figure 40 during time-instances $t=13.1 - 20.1$ ms and Figure 39d-f. Given that these smaller structures cycle through their oscillation during two rotations of the jet column deformation, they appear as oscillations in the mode $m = -1$, while the jet column deformation appears at oscillations of an $m = -2$ mode.

This motion is similar to that visualized by Huang et al. [45] in LES simulation. This study computed the flow in an annular swirling, reacting jet exiting into a cylindrical combustion chamber. In this paper, streamlines of motion in the $r-\theta$ plane are shown at two different times for downstream distances of $x/D = 1.2$, $x/D = 1.6$, and $x/D = 2.2$. During part of the cycle, two rotating fluid structures move around the center of the jet and are evident in all three axial planes. In other parts of the cycle, only a single structure can be seen.

To better quantify this motion, a spatial modal decomposition was used, as discussed with reference to Equation (12). Figure 41 shows a detail of the low frequency components of the modal decomposition of the radial velocity at one radial location, $r/D = 0.6$. Also, Figure 42 shows the distribution of energy amongst different modes (Figure 42a) and as a function of radius (Figure 42b).

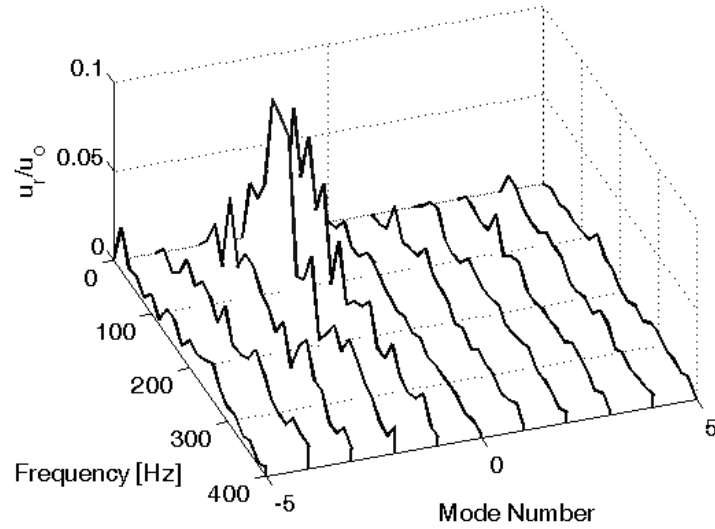


Figure 41. Spectra of mode numbers at $r/D = 0.6$ $r-\theta$ plane at $x/D = 1$, for a non-reacting, unforced flow at $u_o = 10$ m/s, $S = 0.85$.

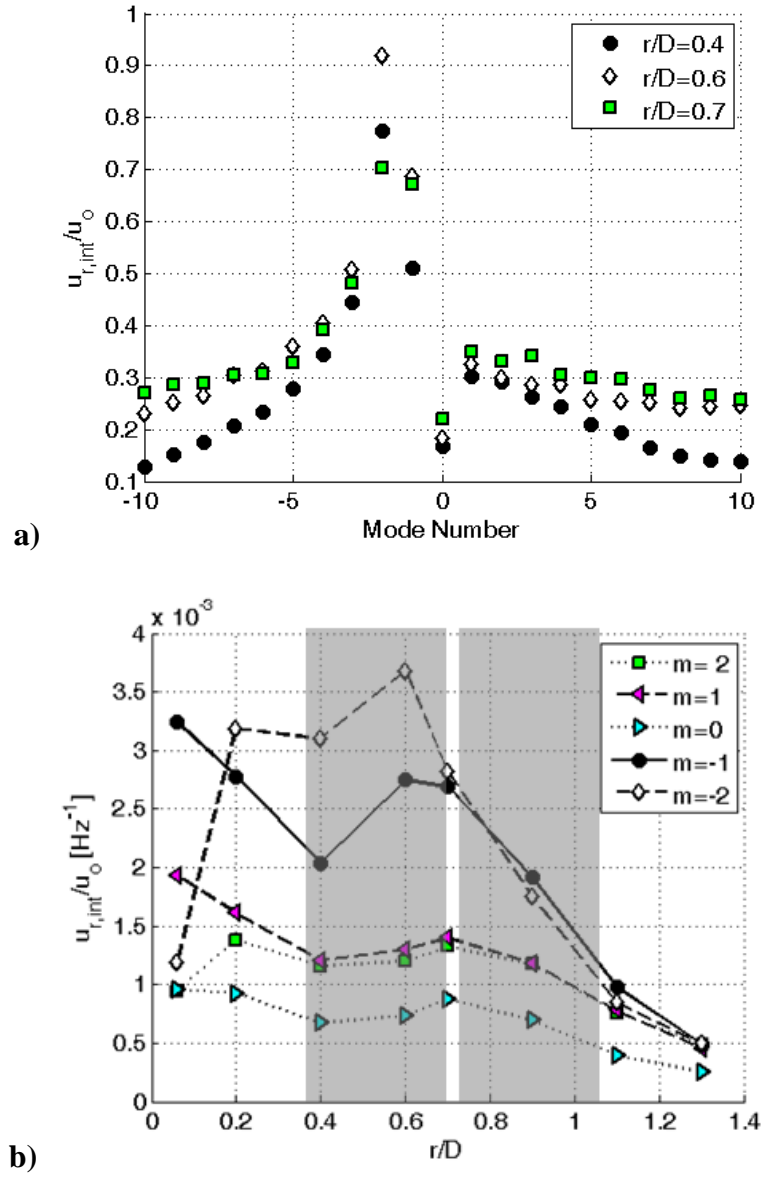


Figure 42. Modal energy distribution of energy integrated from 0-200 Hz plotted as a function of a) mode number at three radii and b) radius at five mode numbers, for a non-reacting, unforced flow at $u_o=10$ m/s, $S=0.85$. Gray regions in b) indicate the approximate location of the inner and outer shear layer.

The figures show that the main contributions to the motion of the unforced flow field come from the $m=-1$ and $m=-2$ modes at frequencies between 0 Hz and 200 Hz.

The $m = -2$ mode, given by the rotation of the jet column deformation, is stronger than the $m = -1$ mode at the radius shown here. This is consistent with physical observations; at the smaller radius of $r/D = 0.4$, the $m = -1$ mode is stronger as a result of the two coherent structures being located closer to the center of the jet. The $m = -2$ mode is stronger at larger radii, particularly $r/D = 0.6$, which is indicative of the fact that the jet deformation fluctuations are dominant at the outer regions of the jet. Very little energy is present in the symmetric, $m = 0$ fluctuations.

Several additional observations are apparent from these results. First, these results show that the energy in these modes changes as a function of radius. In the very center of the flow, only a few modes are present, including $m = -2$, $m = -1$, and $m = 1$. As the radius increases, the energy of every other mode varies with increasing r until $r/D = 0.7$, after which the strength of all the modes rapidly decreases. Most likely, this stems from increasing turbulence levels at the outer mixing regions of the jet. The inner region of the jet is dominated by the coherent motion from the $m = -1$ mode, while turbulent mixing between the jet and the quiescent medium around the jet dominates the motion at the outer region of the jet. Outside the jet, or at radii greater than $r/D = 0.7$, motion is mostly due to entrainment and fluctuates very little, leading to very low mode strengths.

Next, the distribution of energy amongst mode numbers at other downstream locations is similar to those at $x/D = 1$. At $x/D = 2$, energy is similarly distributed between modes $m = -1$ and $m = -2$, with a small amount of energy in $m = 1$. The appearance of additional modes at different downstream locations is not uncommon as

the developing profile of the jet may change the stability characteristics or dominant motions at different downstream locations. Examples of this can be found in Ref. [152]. At $x/D = 0$, very little energy is present in any of the modes; this is most likely due to the fact that the central recirculation zone is bounded by the centerbody a mere 0.7 cm from this measurement location. Due to the stagnation region associated with the no-slip condition at this boundary, velocities in the recirculation region at this location are small.

Theoretical analyses of swirling wake profiles, which are similar in flow structure to this flow (see Figure 16), also predict that lower order modes (i.e., $m = -1, -2, \dots$) spinning in the direction of swirl are absolutely unstable. The amplification rates of the resultant disturbances are highly dependent on swirl number and backflow ratio [153]. They similarly predict that the symmetric, $m = 0$, mode is stable and that the most amplified helical modes shift from negative mode numbers to positive mode numbers for flows with jet-like profiles.

Effect of acoustic forcing on time-average flow, non-reacting flow

Acoustic forcing can have either a minimal or a significant effect on the size and shape of the vortex breakdown bubble, depending upon acoustic forcing conditions. In general, this result reflects the absolutely unstable nature of the VBB. The range of motion of the VBB is constrained by the fact that it is merged with the centerbody wake, moving the lower stagnation point of the bubble to the centerbody face and effectively anchoring the structure in this location. Nevertheless, the shape of this structure exhibits sensitivity to disturbance amplitude and frequency, in some cases quite dramatically, as discussed in this section. Changes in the vortex breakdown bubble from acoustic forcing

reflect an overall change in the stability characteristics of the flow field, not just an influence that the acoustic forcing has on the bubble itself. High amplitude acoustic forcing can alter in-flow conditions in the nozzle, warp the symmetry of the swirling jet and bias it towards one side, and generally change the overall flow shape such that the vortex breakdown bubble is influenced. This is still a highly nonlinear process, as described above, though, because the overall jet is absolutely unstable, not just the vortex breakdown structure itself. The changes described below describe a macroscopic change in jet structure and behavior that results from high amplitude acoustics.

An important manifestation of the vortex breakdown size is in the time-average spreading angle of the annular jet. Figure 43 shows the increase in the jet angle based on data collected from velocity fields, due to the effect of amplitude of transverse acoustic forcing on the time-average jet angle (measured from the vertical) across the frequencies and forcing configurations considered.

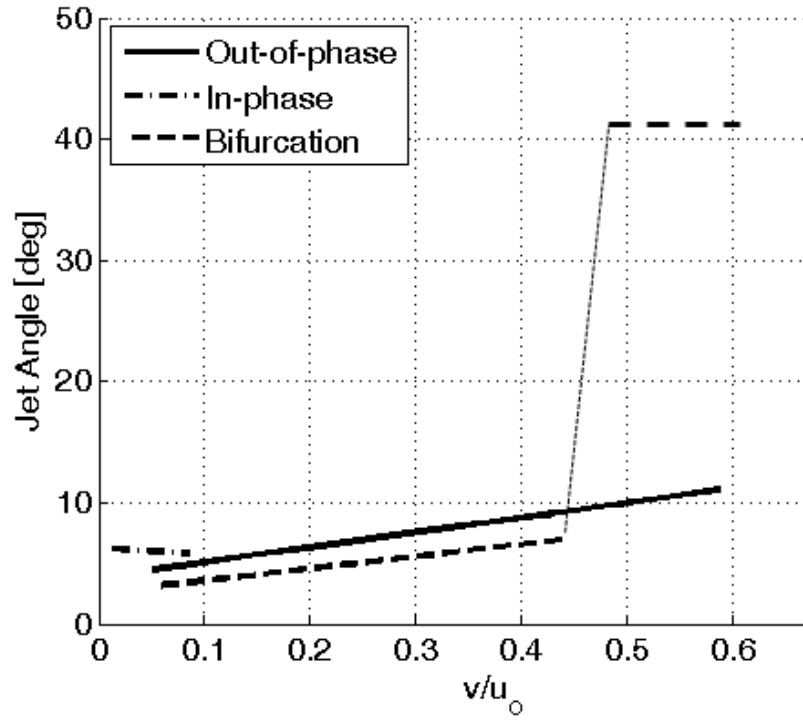


Figure 43. Dependence of jet spreading angle upon transverse acoustic forcing amplitude for non-reacting flow at $u_o=10$ m/s, $S=0.85$.

A key take-away from this graph is the slight influences of forcing in most cases, but also the significant effects that it can have in select cases. In the in-phase case, there is no discernible change in jet angle over the range of amplitudes and frequencies tested. Larger forcing amplitudes are achievable for the out-of-phase forcing cases, where some modest dependencies on forcing amplitude are observed. However, in one case, at 800 Hz out-of-phase forcing, a sharp change in flow angle occurs at $v/u_o = 0.46$. Figure 44 plots the velocity field at several forcing amplitudes showing an example of the bifurcation.

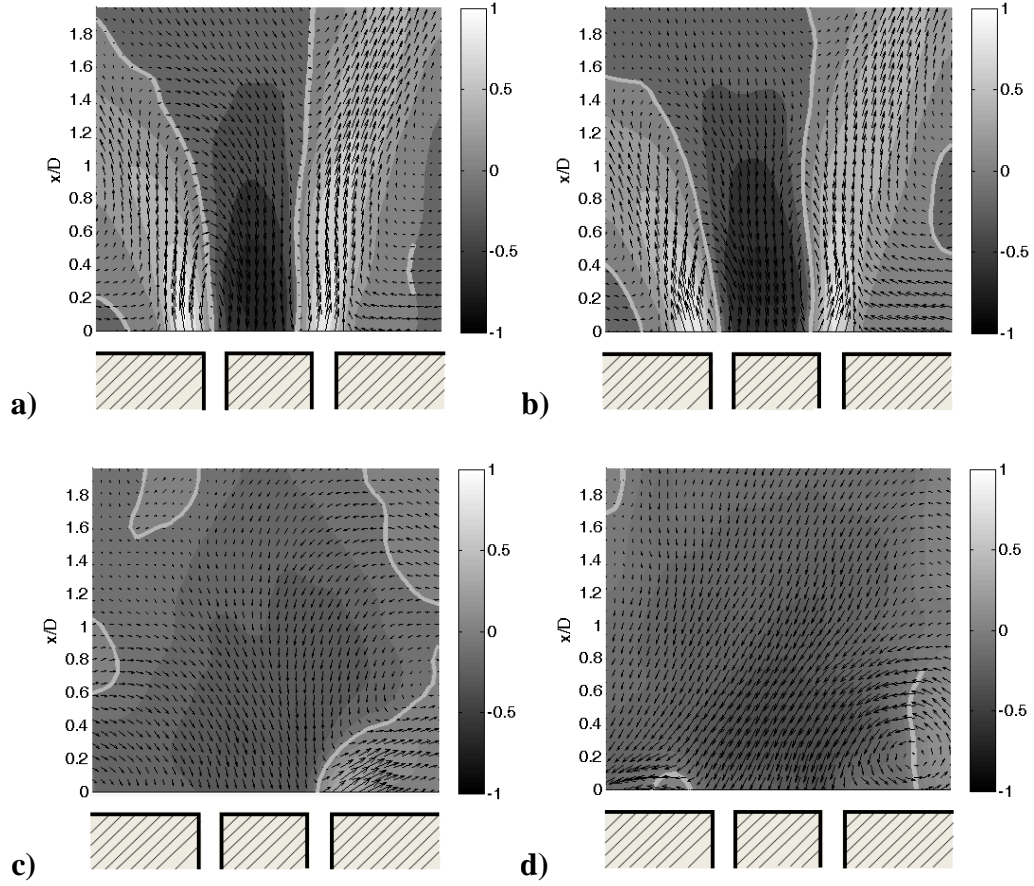


Figure 44. Flow fields for the transversely forced bifurcation case, 800 Hz out-of-phase, at four excitation amplitudes where a) 3.3 m/s and b) 4.3 m/s transverse velocity cases show the velocity field before the flow bifurcation, and c) 4.6 m/s and d) 5.2 m/s show the velocity field after. All flow conditions are non-reacting at $u_o=10$ m/s, $S=0.85$. Colorbar shows axial velocity normalized by bulk flow velocity.

Before the bifurcation point, the jet tilts slightly to the left with increased forcing amplitude, although the structure is fundamentally similar to that of the flow without acoustic forcing, seen in Figure 37. After the bifurcation point, the vortex breakdown bubble enlarges to over twice its original size, forcing the annular jet to an almost wall-jet-like configuration. This bifurcation phenomenon was highly repeatable. At higher

levels of acoustic forcing beyond the bifurcation the bubble becomes slightly bigger but the flow topology stays the same. This behavior was also observed at other forcing frequencies and configurations at high forcing amplitudes, but often exhibited a stochastic character and was not repeatable.

These results show that nonlinear effects can manifest themselves in two fundamentally different ways: both smoothly varying and nearly discontinuous dependencies of the flow field upon excitation amplitude. However, we were not able to isolate the controlling parameters governing which type of behavior could occur. For example, in the 800 Hz out-of-phase case, an abrupt bifurcation is observed. However, the corresponding transverse velocity fluctuations are nearly the same in the 400 Hz out-of-phase case where similar behavior was not seen.

The dependence of several other metrics of vortex bubble size and strength upon forcing characteristics were also analyzed. For example, the size of the bubble was measured using the distance between the edges of the recirculation zone as a function of downstream distance. The results of this analysis are similar to those discussed above, particularly the bifurcation behavior at 800 Hz out-of-phase forcing.

The strength of the vortex breakdown bubble was quantified in two ways. First, the circulation over each half of the bubble was calculated at each acoustic frequency, symmetry, and amplitude. Second, the radially-averaged recirculation strength of the bubble at each downstream location was calculated by integrating the axial velocity and normalizing it by the width of the recirculation region at that location. Both these measures showed very little response to the acoustic forcing, even at very high amplitudes, indicating that the strength of the vortex breakdown bubble did not change

dramatically with acoustic forcing. This result is not consistent with other studies discussed in the introduction [110, 122], as these studies considered jets without centerbodies. In annular jets with large centerbodies, like the configuration considered here, the boundary condition that results from the centerbody most likely impedes significant strengthening of the recirculation.

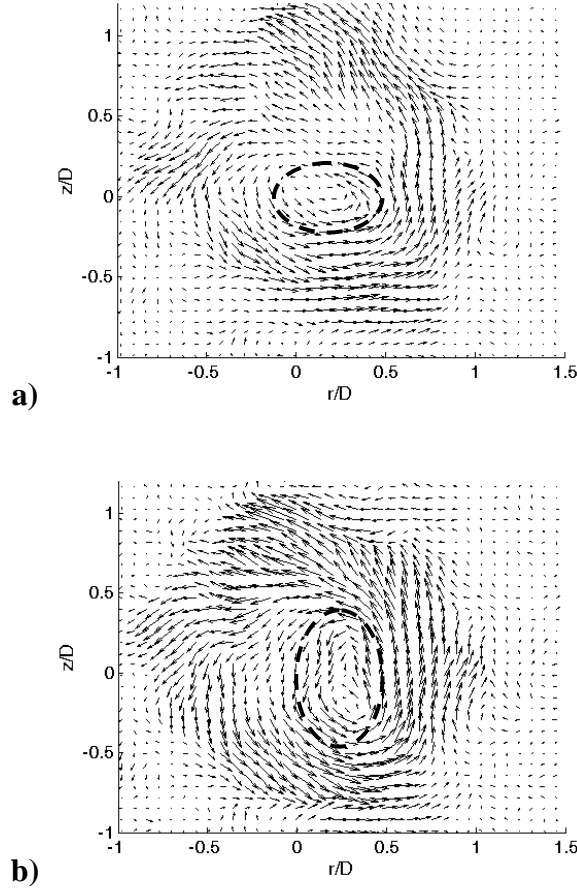
Dynamical response of flow to acoustic forcing, non-reacting flow

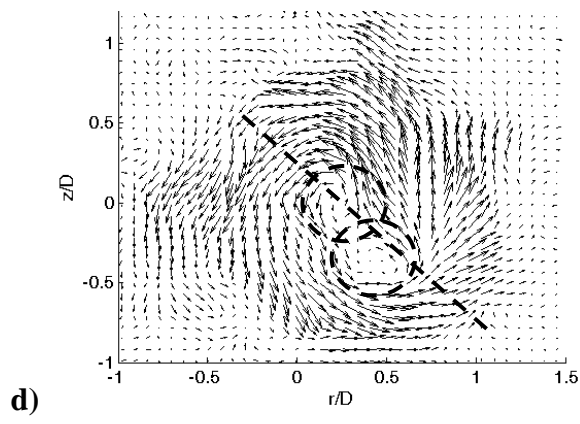
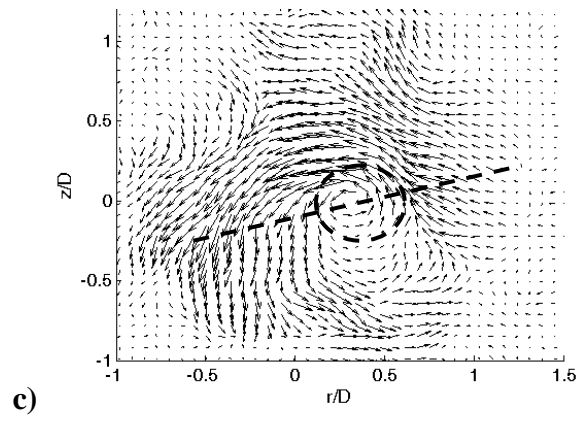
This section discusses the dynamical response of the flow to acoustic forcing at a variety of frequencies and amplitudes. Several types of responses are possible, particularly at high forcing amplitudes. First, the convectively unstable structures in the flow, the spanwise shear layers in particular, respond to the acoustic forcing even at very low amplitudes. These motions, however, are not the focus of this study, as discussed in the Introduction. The motion in the vortex breakdown region can also respond to the acoustic forcing. In this case, three types of response are possible: the self-excited motion can be enhanced, suppressed, or be unaffected by forcing and continue to oscillate independently of the acoustic forcing. In the case that it is suppressed, it is also possible that the instability could “lock-on” to the forcing frequency, resulting in similar motion of the structure, but now at the frequency of forcing. This phenomenon has been measured in bluff-body wakes [121], but was not seen in the current study.

As described above, the vortex breakdown bubble exhibits self-excited oscillations at low frequencies in the form of a precessing vortex core. These motions contain energy in several modes, but in particular the $m = -2$ and $m = -1$ modes, indicative of motion of the overall jet deformation and two coherent structures within the

jet recirculation zone. In this section, we present results on the dependence of these low frequency fluctuations as a function of forcing amplitude.

The presence of high amplitude acoustic forcing has a definite effect on the structure and modal content of the low frequency motion. An example of this shown in Figure 45 and Figure 46, where velocity fields for the low forcing amplitude and high forcing amplitude case at 400 Hz out-of-phase are shown, respectively. In both these cases, images were selected during similar parts of the cycle as those shown in the data in Figure 39 and the notional picture in Figure 40.





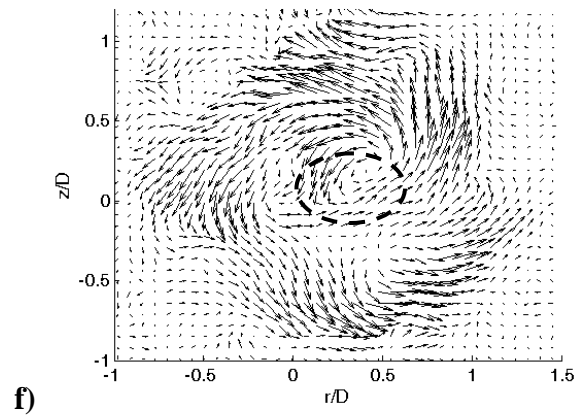
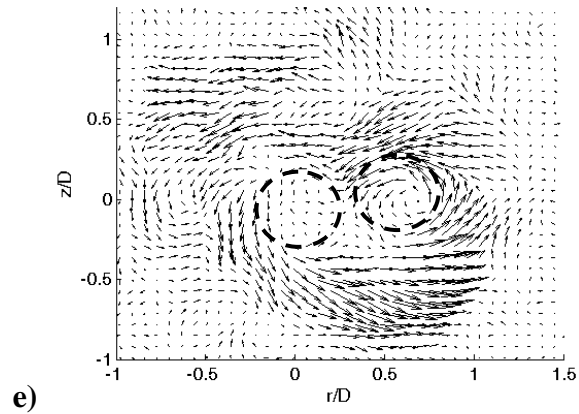
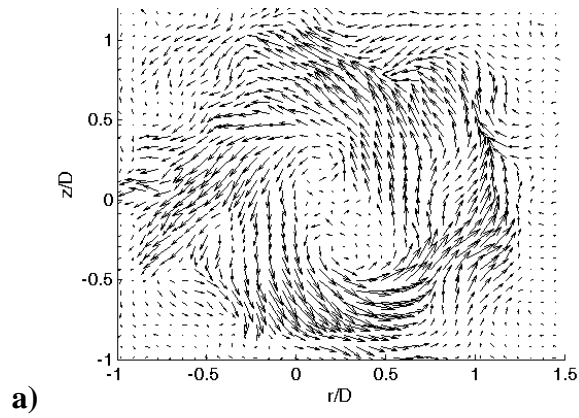
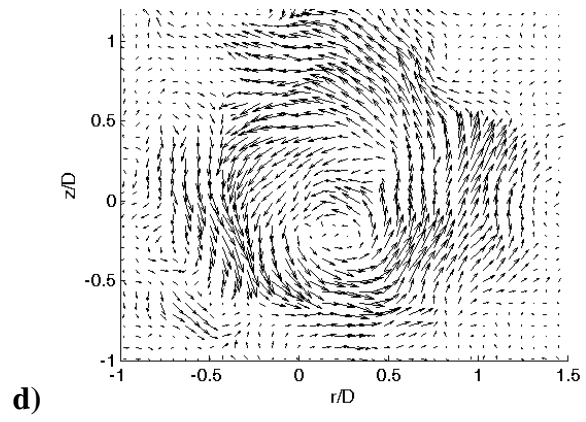
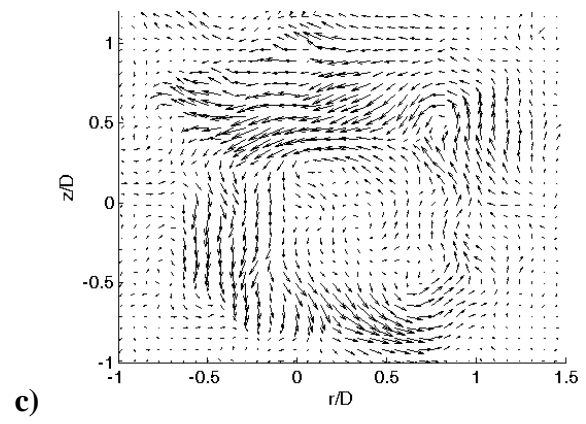
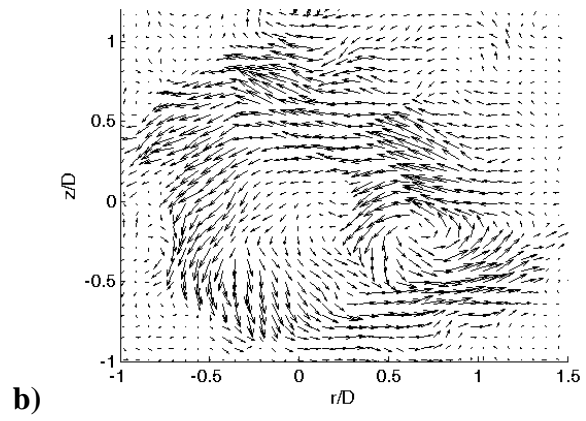


Figure 45. Precessing vortex core shown through the filtered velocity field in the

$r-\theta$ plane at $x/D=1$, for a non-reacting flow, 400 Hz out-of-phase forcing at

$$v'/\bar{u} = 0.1, u_o=10 \text{ m/s}, S=0.85.$$





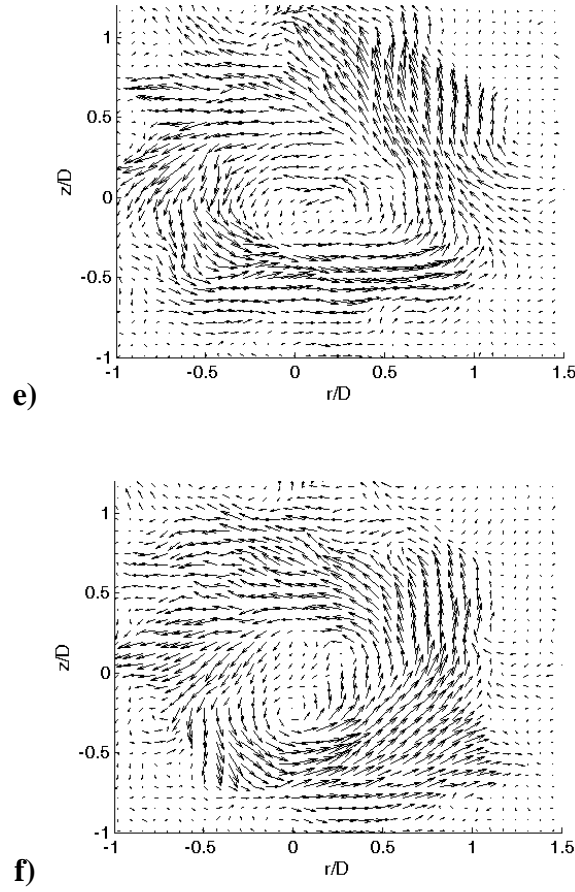


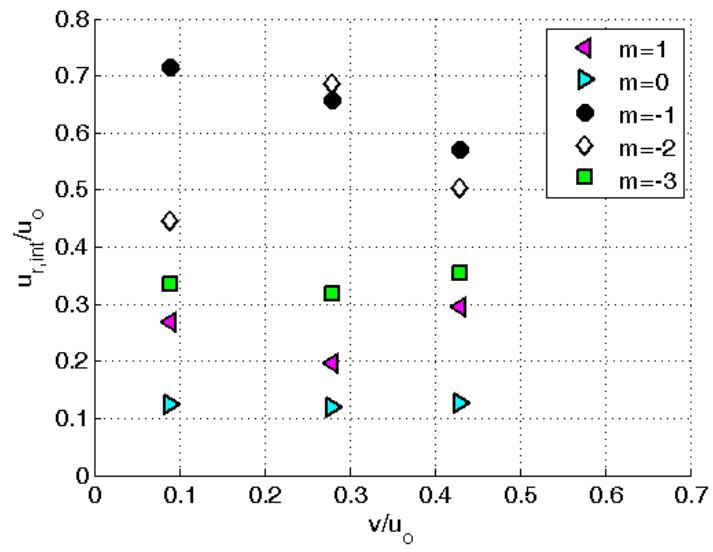
Figure 46. Precessing vortex core shown through the filtered velocity field in the $r-\theta$ plane at $x/D=1$, for a non-reacting flow, 400 Hz out-of-phase forcing at $v'/\bar{u} = 0.7$, $u_o=10$ m/s, $S=0.85$.

Figure 45 shows the cycle of the low frequency motion for the low amplitude forcing case at 400 Hz out-of-phase forcing. In this case, some of the same features seen in the unforced case are evident. For example, the inner coherent structures exist as a single structure through half the cycle (Figure 45a-c) and two structures through the remaining part of the cycle (Figure 45d-e). Despite that, the transit of these structures away from each other is less severe than in the unforced case, particularly when the jet is deformed along its bias axis as it is in Figure 39d in the unforced case. The overall jet

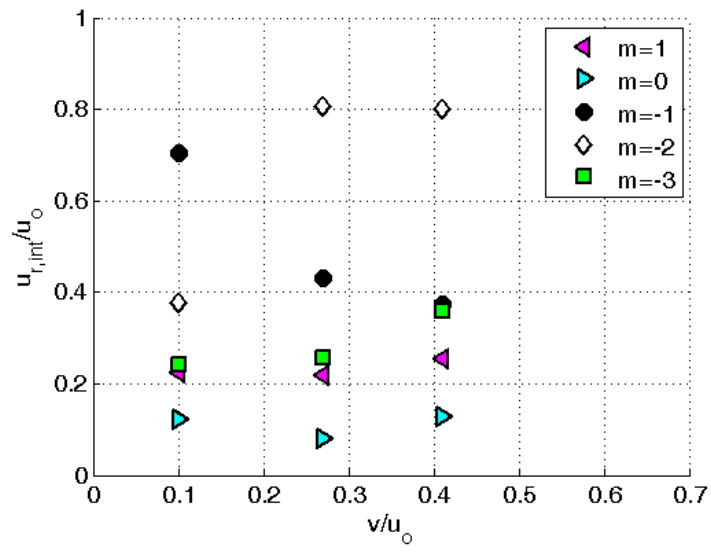
deformation still precesses around the center axis, as shown in Figure 45b-d, but the extent to which it deforms is less than in the unforced case. Additionally, the periodicity of these fluctuations begins to drift, causing significantly more uncertainty in the period of the cycle with acoustic forcing than without.

At the higher forcing amplitude, shown in Figure 46, the coherent motion of the fluctuation is highly altered. In this case, the coherent structures in the center of the recirculation zone appear to “merge” and “separate” as before, but do so in a much less regular fashion. Furthermore, the deformation of the overall jet structure is more irregular and aperiodic. While not shown here, these results are consistent with those seen at other forcing frequencies and forcing symmetries.

To quantify these changes, the integrated energy between 0 and 200 Hz (as shown in Figure 42) can be tracked as a function of forcing amplitude, mode number, radius from the centerline, forcing frequency, and forcing symmetry, meaning in-phase vs. out-of-phase forcing. Most importantly, the strength of mode $m = -1$ steadily decreases as the strength of mode $m = -2$ increases for increasing forcing amplitude for the out-of-phase cases only. This trend can be seen in Figure 47, which shows the strength of a number of modes at several forcing amplitudes for an out-of-phase forcing case.



a)



b)

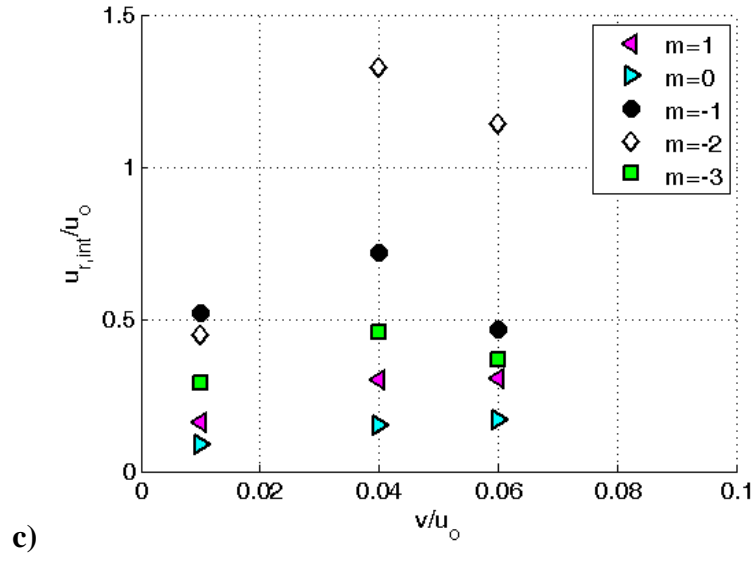
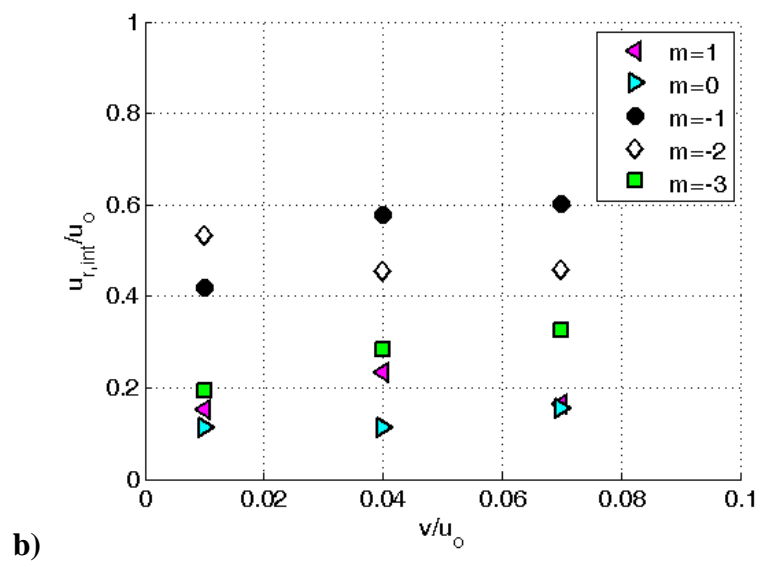
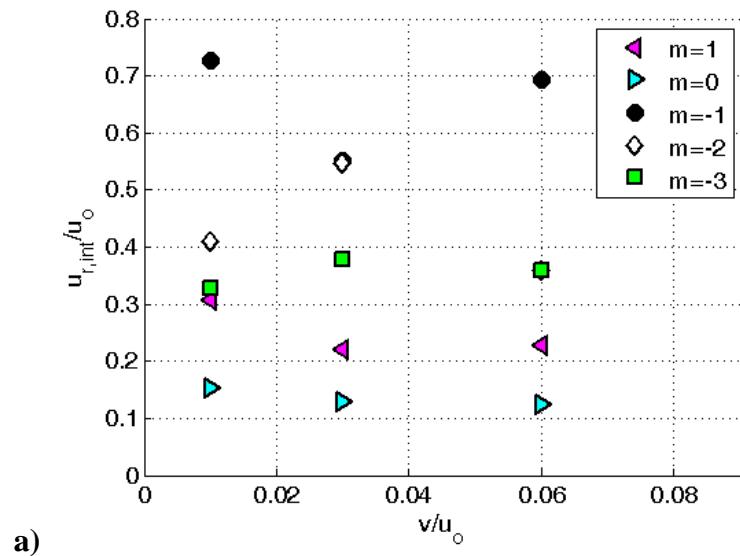


Figure 47. Mode strength for three forcing amplitudes at $r/D = 0.6$ for a) 400 Hz, b) 800 Hz, c) 1200 Hz out-of-phase forcing at $u_o=10$ m/s, $S=0.85$.

The same information is shown for an in-phase forcing case in Figure 48, where the amplitude of mode $m = -2$ has a lower amplitude.



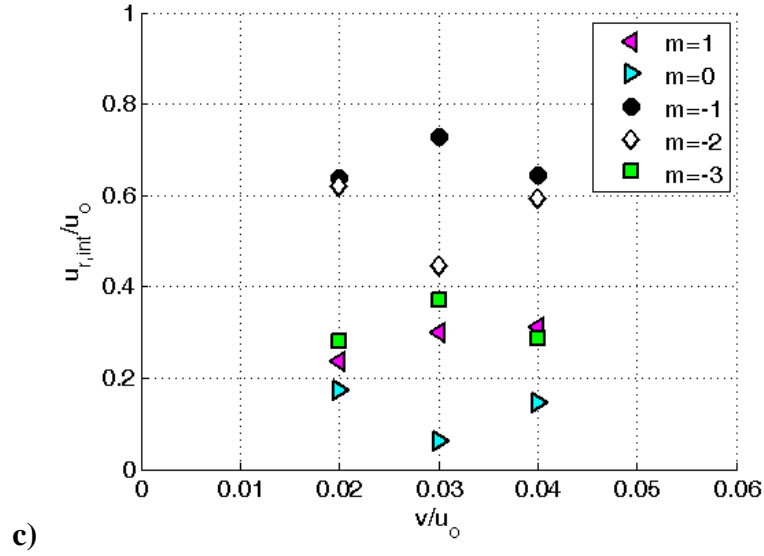


Figure 48. Mode strength for three forcing amplitudes at $r/D = 0.6$ a) 400 Hz, b) 800 Hz, c) 1200 Hz in-phase forcing at $u_o=10$ m/s, $S=0.85$. Note: mode $m = -2$ and $m = -3$ have very similar amplitudes at $v/u_o = 0.06$ in a) and the symbols overlap.

It is evident from Figure 47 that high amplitude, asymmetric acoustic forcing can have a significant effect on the structure of the swirling flow and the dynamical behavior of the vortex breakdown region. In the out-of-phase forcing cases, high amplitude acoustic forcing can suppress the mode $m = -1$, which describes the motion of the two coherent structures in the recirculation region, and enhance the $m = -2$ mode, which describes the motion of the overall jet deformation. This process can be seen at radii between $r/D = 0.4$ and $r/D = 0.9$, where the deformation motion of the jet is dominant. Visualization of this highly nonlinear process can be seen in the flow fields shown in Figure 46, where evidence of the coherent structures is scarce, but the overall deformation of the jet still exists.

In the in-phase case, the strength of the modes does not change substantially as a function of forcing amplitude. Additionally, the growth in the strength of mode $m = -2$ that was observed in the out-of-phase forcing case is not seen in the in-phase forcing cases. This may be indicative of the influence of acoustic forcing symmetry on the response of the flow. The out-of-phase forcing is asymmetric and adds energy to an asymmetric mode, while the in-phase, or symmetric, forcing case has less impact on the asymmetric mode energies.

These results should not be taken to imply that the flowfield is not responding to the forcing. In fact, the convectively unstable shear layers respond quite strongly to the excitation at the forcing frequency. To illustrate, Figure 49 shows the change in the total mode strength over the pertinent flow structures for the low frequency content compared to that at the forcing frequency. In this calculation, the energy in the low frequency content was integrated over both the frequency range from 0 to 200 Hz and the radii over which this low frequency motion dominates, $r/D = 0 - 0.6$. In the case of the shear layer response at the forcing frequency, the energy was integrated over the range of radii $r/D = 0.2 - 0.6$, the regions in which the inner and outer shear layer dominate. The fluctuation amplitude is normalized by the spectral integration width because of the significantly different spectral widths values used in the two plots.

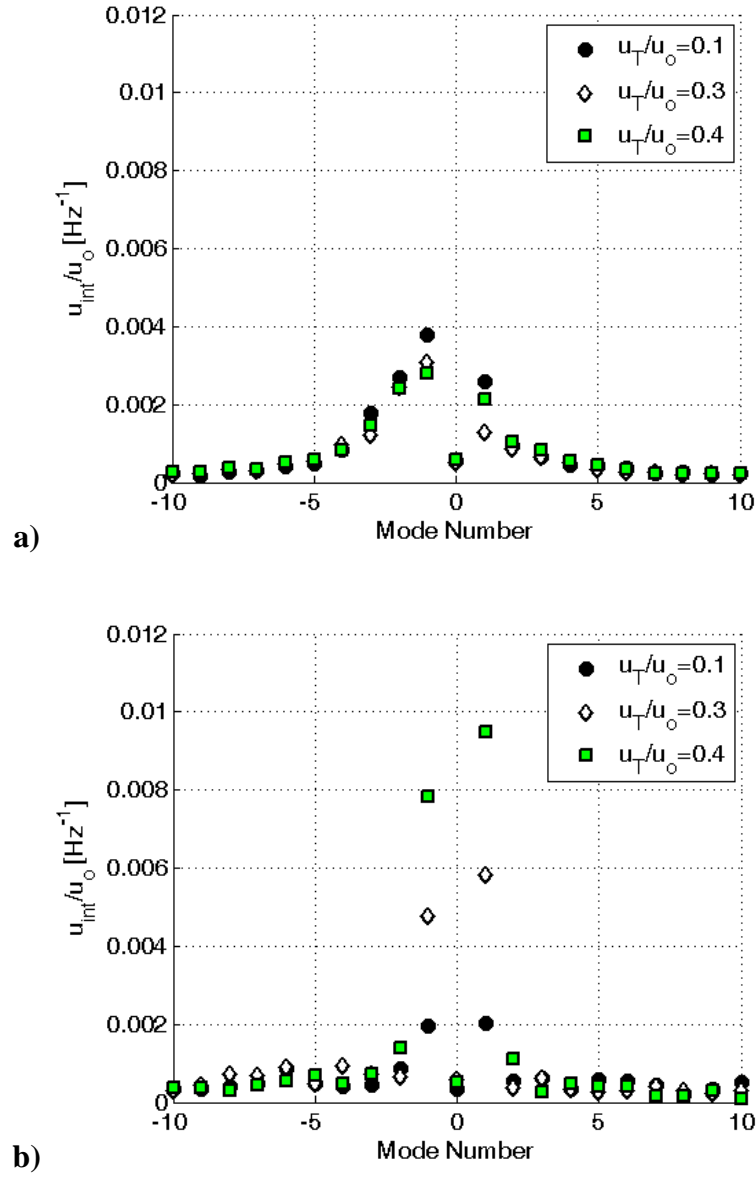


Figure 49. Modal energy distribution (per Hertz) for radially integrated a) low frequency motion below 200 Hz and b) motion at the forcing frequency, 400 Hz, for 400 Hz out-of-phase forcing at $u_o=10$ m/s, $S=0.85$.

It is evident from these two modal distributions that there is a fundamentally different process happening between the low frequency motion in the vortex core and the shear layer motions at the forcing frequency. In the case of the forcing frequency results,

the shear layers are responding in kind to the amplitude of the acoustic forcing, and a clear, monotonic growth of the helical $m = -1$ and $m = 1$ modes are present for this type of forcing. This is evident from the distribution of energy at the forcing frequency in modes $m = -1$ and $m = 1$ across each radial location; the energy peaks in the location so of the inner and outer shear layers. In this case, the amplitude of both modes at the highest forcing amplitude is roughly four times higher than that at the lowest amplitude, just as the highest amplitude of transverse acoustic forcing is four times that of the lowest.

In contrast, the precessing vortex core does not similarly respond to the acoustic forcing. In the case shown in Figure 49, the overall amplitude of the $m = -2$ mode stays relatively constant, while the amplitude of the $m = -1$ decreases by a factor of a third as the forcing amplitude increases by a factor of four. This behavior reflects the nature of the vortex breakdown region, the manifestation of an absolute instability, in that the response to high amplitude acoustic forcing is highly non-linear and relatively low amplitude. Further details contrasting the response of the absolutely unstable and convectively unstable structures are discussed in Chapter 5.

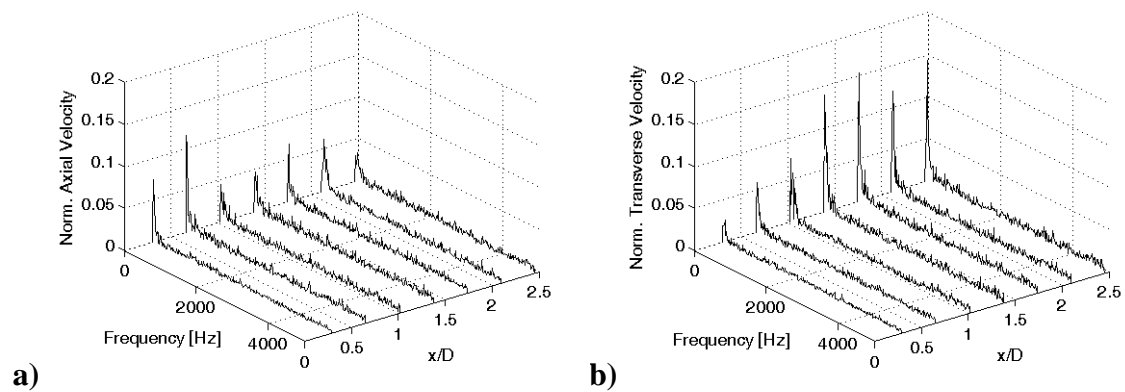
Reacting flow results

Many of the key phenomena discussed above are also observed in the reacting flow field and flame behavior. In this section, we highlight these observations and the important implications they have for understanding velocity-coupled flame response. Several reacting experimental conditions were considered, including flows with two geometric swirl numbers, 0.85 like the non-reacting data above, and 0.5. PIV data was

not taken in the $r-\theta$ plane for the reacting case. Although this data is later suggested as a recommendation for future work, care should be taken in its acquisition. Errors in PIV could arise from the variable index of refraction over the line of sight through the hot combustion products.

To start, Figure 19 shows the time-average velocity and vorticity field for the unforced, reacting annular swirling jet. Like the non-reacting data shown above, a clear vortex breakdown region exists along the centerline of the flow. There are two shear layers, an inner and an outer, and the flame is stabilized in the inner shear layer.

Example spectra of the velocity fluctuations along the jet centerline are shown in Figure 50. Like the non-reacting case, the narrowband fluctuations are found predominantly below 200 Hz and fluctuation amplitudes at the higher frequencies are quite low. Figure 50c-d shows a comparison of the reacting and non-reacting velocity spectra along the centerline at the point $x/D = 1$. Here, it is evident that the magnitude of low frequency fluctuation in the reacting case is lower than that in the non-reacting, possibly indicating that the presence of the flame damps the self-excited motion in the center recirculation region of the jet. The implications of this will be discussed at the end of this section.



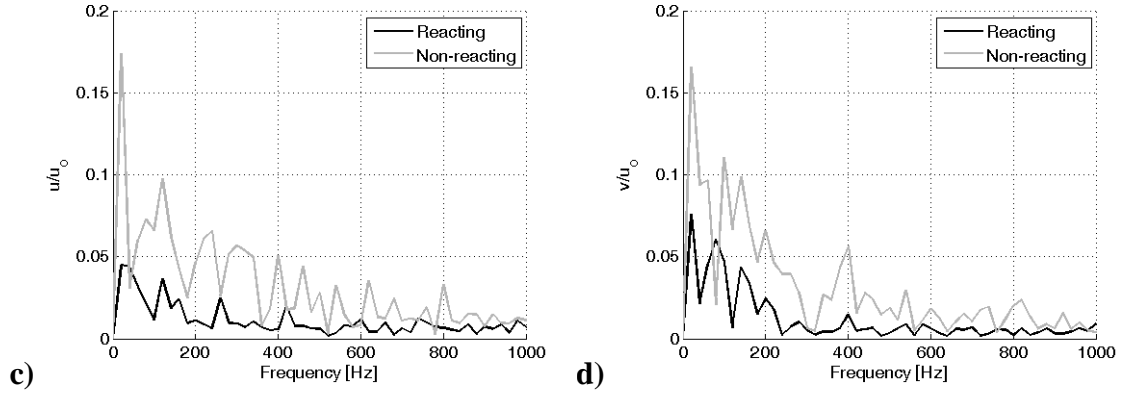


Figure 50. Spectra of normalized a) axial component and b) transverse component of velocity along the time-average centerline for reacting flow with no acoustic forcing, at $u_o=10$ m/s, $S=0.5$, and equivalence ratio of 0.9. Also shown is a comparison of the normalized non-reacting and reacting c) axial and d) transverse velocity fluctuations along the centerline of the flow field at $x/D = 1$.

Similar types of behavior are reflected in the time-average shape of the flame, measured as the time-average flame angle from the vertical as seen from flame luminescence data in Figure 51.

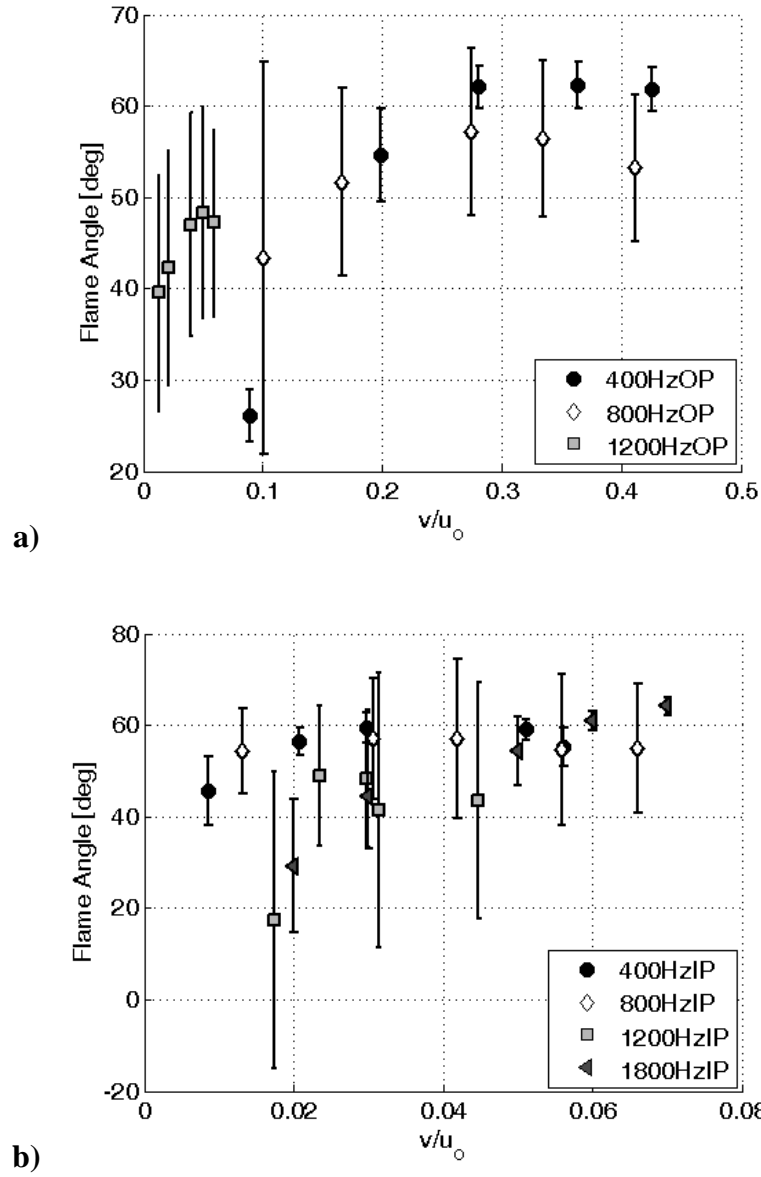


Figure 51. Dependence of time-average flame angle upon transverse acoustic forcing for a) out-of-phase and b) in-phase forcing for reacting flow at $u_o=10$ m/s, $S=0.5$, and equivalence ratio of 0.9.

Here, increases in the jet angle occur for several cases, including 400 Hz out-of-phase, 1200 Hz out-of-phase, and in particular, 1800 Hz in-phase. Significant changes in the flame shape are evident at 1800 Hz in-phase acoustic forcing, a result shown in

Figure 52. This figure shows time-average images of the flame at several forcing amplitudes. The spreading angle of these data is also shown in Figure 51b.

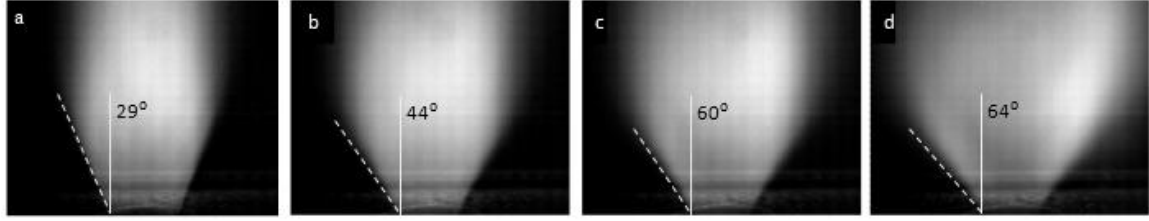


Figure 52. Line-of-sight overlays of 500 images of the flame at several forcing amplitudes a) 0.1 m/s, b) 0.5 m/s, c) 0.6 m/s and d) 0.7 m/s transverse velocity. Acoustic forcing is in-phase at 1800 Hz, flow velocity of 10 m/s, swirl number of 0.5, and equivalence ratio of 0.9.

This behavior has important implications for the amplitude of the flame heat release response to acoustic excitation. As was shown in Equation (10), the time-dependent behavior of the flame surface is a function of the time-average flame shape, given by the flame aspect ratio β . This stems from the fact that flames respond to velocity disturbances normal to their surface on an instantaneous basis, as is described in Equation (7). Changes in the angle of the flame relative to incident perturbations can change the amplitude of that dot-product, and hence the resulting flame response. In instances where the time-average flame angle can be changed significantly by acoustic forcing, as it is at 1800 Hz in-phase, then it is important to not only consider the unsteady flow field perturbing the flame, but also the sensitivity of the averaged flame position to the forcing.

Thus, the key effect of forcing on the vortex breakdown flow structures appears to be changes in its time-average character. The fluctuations in the vortex breakdown

region associated with the precessing vortex core seem to not be an important contributor to the flow fluctuations exciting the flame. Rather, previous studies by the authors [111] show that the bulk of the flame heat release fluctuation is the result of vortex rollup in the shear layers. This effect is shown in Figure 53, which shows line-of-site luminescence images of the flame under both out-of-phase and in-phase acoustic forcing at 400 Hz.

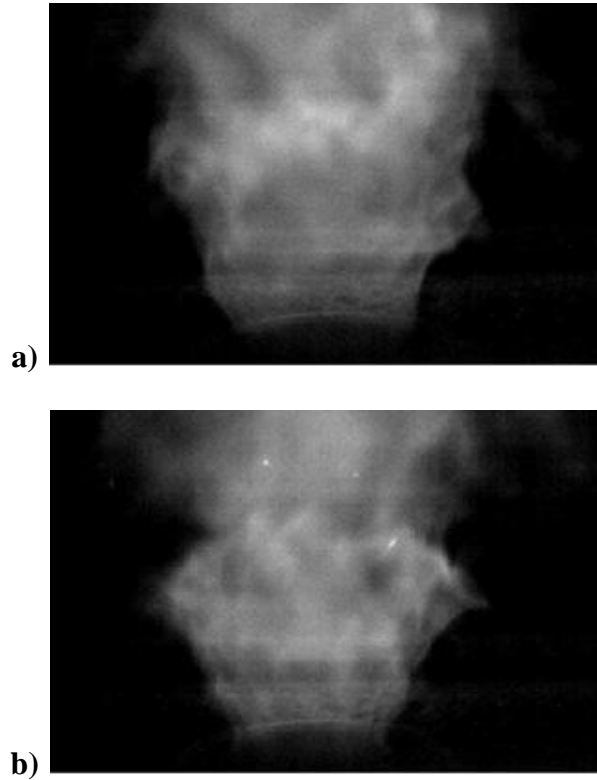


Figure 53. Flame luminescence images for 400 Hz a) out-of-phase and b) in-phase forcing conditions for a flow velocity of 10 m/s, swirl number of 0.5, and equivalence ratio of 0.9.

Figure 54 shows an example of the vorticity field calculated overlaid with a flame edge, calculated from the PIV Mie scattering image. The dark gray line indicates an approximate flame edge, determined using the sharp gradient in seeding density between high density reactants and low density products.

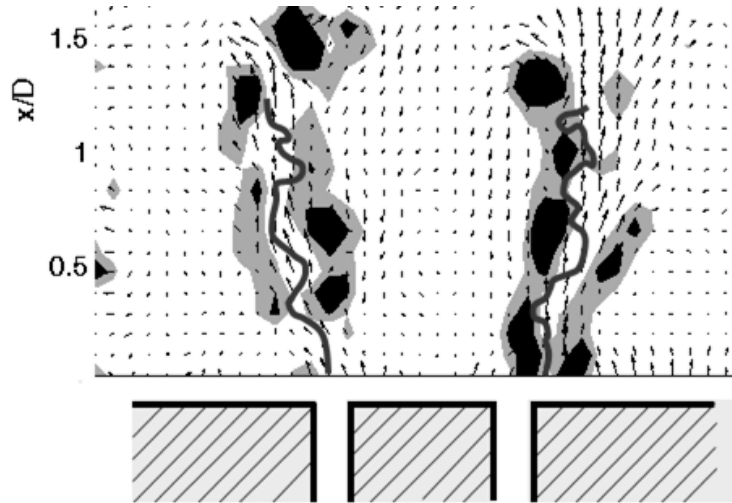


Figure 54. Absolute value of vorticity field showing the flame wrinkling due to inner shear layer rollup for 900 Hz out-of-phase at a flow velocity of 10 m/s, swirl number of 0.5, and equivalence ratio of 0.9.

As can be seen from these images, large-scale flame wrinkling is formed by motion in the inner shear layer, whose dynamics are influenced by the nature of the acoustic forcing. In the out-of-phase forcing case, the shear layer rolls up in a helical pattern, as is evident by the staggered vortices seen on either side of the flame in Figure 53a. In the in-phase, symmetric, forcing condition, large ring vortices roll up and disturb the flame in a symmetric way, as seen in Figure 53b. Both these motions lead to significant flame response at the forcing frequency, as the convectively unstable shear layer responds to the acoustic forcing at the forcing frequency.

There are two reasons for this. First, the flame lies directly in the shear layers and, so its motions are dominated by shear layer dynamics. Because of the convectively unstable nature of the shear layers, they respond quite strongly at the forcing frequency. Second, as shown above, the vortex breakdown bubble and its self excited motions

simply do not respond strongly to external forcing. For these reasons, it is evident that the precessing vortex core and other self-excited motions in the vortex breakdown region do not have a significant impact on overall flame response during even high amplitude acoustic forcing. The flame response is the result of motion in the convectively unstable shear layer and is affected very little by the dynamical structure of the vortex breakdown bubble.

These helical shear layer structures have been seen in LES simulation [130] in both the inner and outer shear layers. A typical result is pictured in Figure 55, which shows both a $r-x$ cut and a three-dimensional vorticity isocontour. The rollup of both shear layers is evident in the figure, as well as the complicated vortical motions in the recirculation zone.

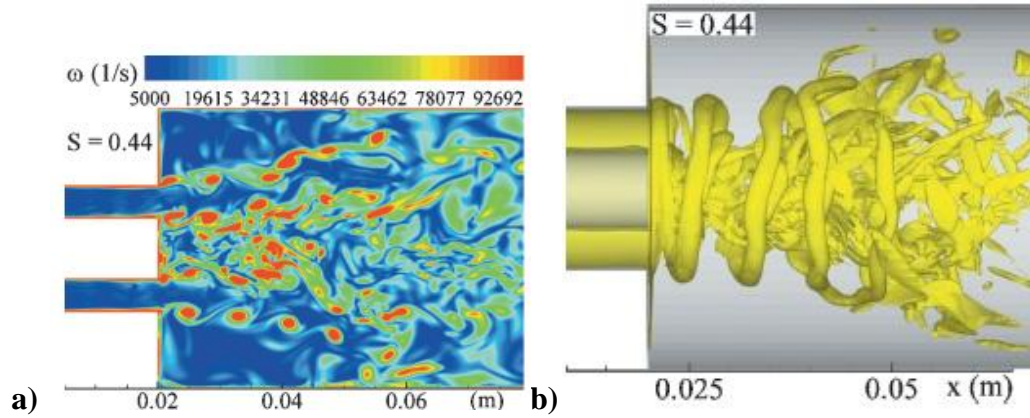


Figure 55. Vorticity in a swirling flow showing inner and outer shear layer vortex rollup for an a) $r-x$ cut and b) a three-dimensional vorticity isosurface at

$$\Omega = 75,000 s^{-1} \text{ [130].}$$

The results from this study show that high amplitude transverse acoustic forcing influences both the time-average and dynamic characteristics of the base flow of a

swirling annular jet. In these cases, high amplitude forcing can change the intrinsic behavior of the vortex breakdown structure, the manifestation of an absolute instability in the swirling jet. This result is consistent with our understanding of the characteristics of absolute instabilities.

We next consider several questions raised by this study. First, what effect does the symmetry of the acoustic forcing have on the response of the vortex breakdown region? Second, what parameters control monotonic versus bifurcation-type change in the flow field with acoustic forcing amplitude? Next, what role does frequency lock-on of the absolute instability play in a forced swirling flow with vortex breakdown? And finally, what does the observed behavior of the vortex breakdown region mean for flame response to high amplitude, transverse acoustic excitation? Each will be discussed further below.

Asymmetric forcing results in asymmetric flow response; this is a trend that has been observed in a variety of flows and forcing configurations. This has shown to be a key idea in our analysis of the response of the swirling jet shear layers, but what does it mean for the vortex breakdown bubble, and by extension, the base state? In shear layers, the response of these structures to symmetric versus asymmetric forcing fields is quite different. In the in-phase forcing case, a symmetric forcing configuration about the center plane of the experiment, the shear layers roll up into ring vortices on both the inner and outer edge of the annular jet, a symmetric response to a symmetric forcing condition. In the out-of-phase forcing case, the asymmetric forcing condition, the shear layers roll up into helical structures, an obviously asymmetric response to the asymmetric acoustic forcing.

Visual inspection of the flow field during transverse forcing experiments indicates that transverse forcing has a "bulk" effect on the flow, i.e., the flow sways side to side during out-of-phase forcing cases and stays rather stationary during in-phase forcing configurations. In this study, the vortex breakdown bubble displayed inherent dynamics in the absence of acoustic forcing, and the characteristics of this low frequency fluctuation were certainly altered in the presence of high amplitude acoustic forcing. Results presented here indicate that asymmetric forcing has more of an effect on the asymmetric instability modes, in particular mode $m = -2$. The mechanism by which this change in the behavior of the intrinsic characteristics was particular to the symmetry or type of acoustic forcing is a question that remains a topic for further investigation.

Second, it is important to consider the nature of the response of the vortex breakdown structure to high amplitude acoustics. In general, the time-average characteristics of the flow changes little with acoustic forcing; the width of the recirculation zone increases slightly with amplitude, pushing the annular jet and flame outwards from the centerline. The exception to this observation is the bifurcation case, 800 Hz out-of-phase forcing, which could not be reproduced here by longitudinal forcing. This sharp transition in state at very limited conditions seems to indicate that there are indeed different types of flow response behavior. This is consistent with the idea that absolutely unstable flows are intrinsically nonlinear because they are exhibiting limit cycle oscillations even in the absence of forcing. The bifurcation parameters for this type of behavior include frequency, amplitude of acoustic forcing, symmetry of forcing, among others that are not understood. Figure 56 summarizes the test cases that were analyzed and indicates where similar bifurcations in flow field were observed.

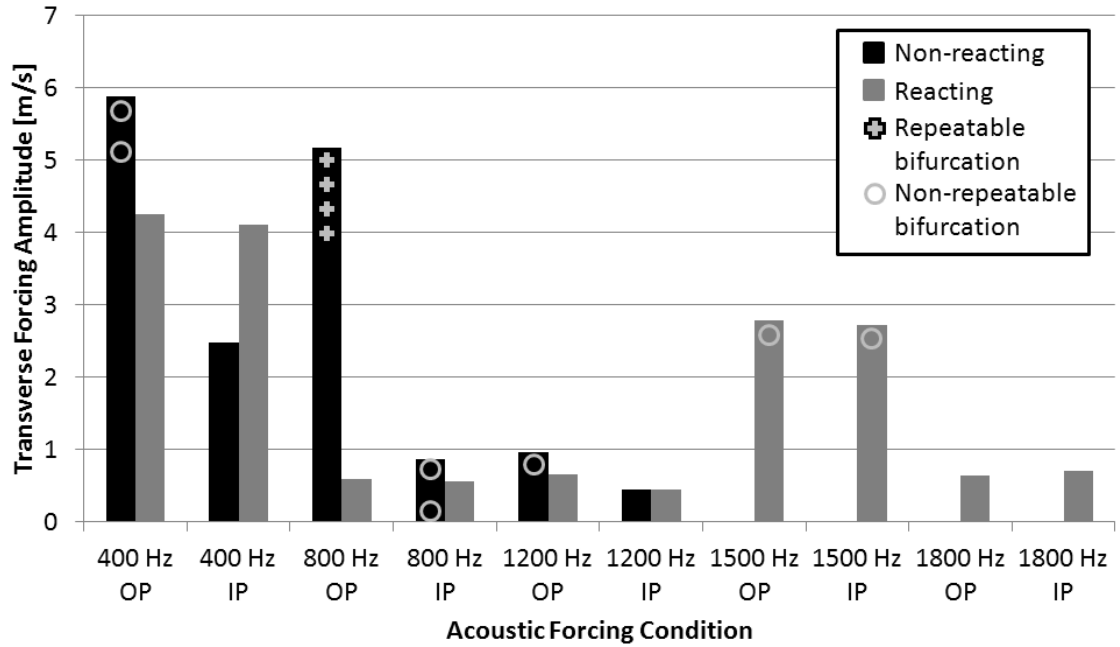


Figure 56. Acoustic parameter space for non-reacting and reacting test cases. Plus marks the location of reproducible bifurcation behavior, and circle marks the location of intermittent bifurcation behavior

Next, an interesting facet of acoustically forced flows, lock-in of absolute instabilities to the forcing frequency, has not been observed in this study. While the high amplitude acoustic forcing had an effect on the low frequency dynamics of the recirculation zone, this structure was altered but not locked-into the forcing frequency, as it sometimes is in other absolutely unstable flows. For example, studies have shown that the wake instability of bluff body wakes can be altered in the presence of high amplitude acoustic forcing [121].

Finally, the change in the "base state" of the flow will have a marked effect on the response of the flame during a combustion instability event. As described above, the dynamic behavior of the flame is dependent on both the time-average flame angle and the

fluctuating velocity field. While it is evident that several sources of fluctuating velocity stem from both the convectively unstable structures in the flow, such as shear layers, as well as the absolutely unstable structure investigated in this study, it is particularly interesting to see that the time-average shape of the flow, and as a result, the flame, can be so altered by the presence of high amplitude acoustic forcing. As in the 1800 Hz in-phase case, shown in Figure 52, where the flame angle flares out at high amplitudes of transverse acoustic forcing. This variation of time-averaged flow field with forcing amplitude must be captured to correctly predict the flame response to high amplitude acoustics.

CHAPTER 5

SHEAR LAYER DYNAMICS

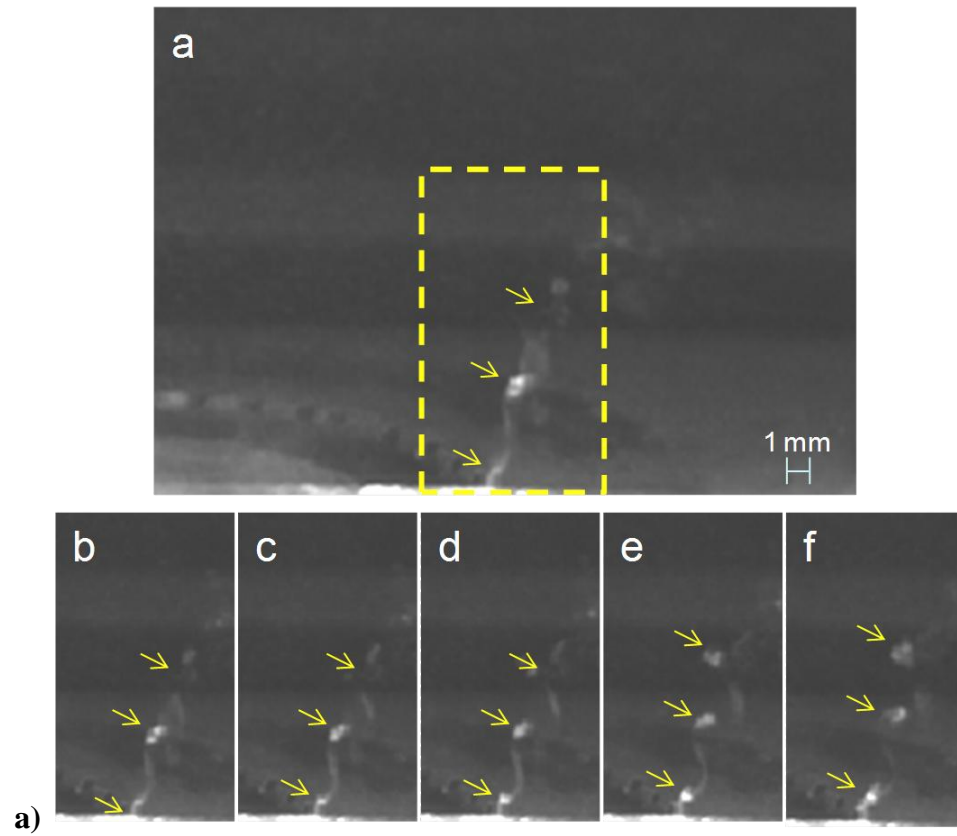
In the previous chapter, the response of the central recirculation zone, the result of the absolutely unstable swirling flow, to acoustic excitation of various frequencies, amplitudes, and symmetries was overviewed. In this chapter, the response of the convectively unstable shear layers structures and the resulting flame response are discussed. A variety of experimental techniques, including smoke visualization, flame visualization, and high-speed particle image velocimetry are used to describe the behavior of these structures. As discussed in the Introduction, these structures play a key role in understanding velocity-coupled flame response during transverse instabilities, and as such, a thorough treatment of this behavior is presented.

This chapter is organized as follows. First, an overview of the behavior of the unforced flow is outlined to provide a baseline for the forced flow experiments. Here, smoke visualization and PIV are used to describe the natural vortex rollup that results from the Kelvin-Helmholtz instability in the shear layers. Next, the response of the shear layers to acoustic forcing is described. In particular, an emphasis is placed on the differences between response of the flow to in-phase versus out-of-phase forcing. Data from smoke visualizations and PIV in several planes of view are presented. Finally, a discussion on the response of the flame to the shear layer motion is presented, again with emphasis on the role of acoustic field symmetry. Results from high-speed planar laser induced fluorescence (PLIF) and flame luminosity imaging are shown.

Behavior of the unforced flow

As described in the introduction, the shear layers are convectively unstable and as a result, display the Kelvin-Helmholtz instability. This instability, characterized by rollup of the shear layer into vortices that scale with the shear layer thickness, requires a constant disturbance source for this manifestation to continue. In the case of unforced flow, the incoming turbulence is more than enough broadband excitation to excite the shear layer, which then sheds vortices at a preferred frequency that scales with a Strouhal number of approximately $St = f\theta/u_o = 0.022$ according to linear, inviscid instability theory [94], where f is the preferred frequency, θ is the momentum thickness of the shear layer, and u_o is a characteristic velocity, in this case the jet bulk velocity.

This shear layer rollup happens in unforced swirling annular jets in both the inner and outer shear layers. Visualization of this effect is shown in Figure 57, which depicts a series of images of shear layer rollup in both the spanwise and streamwise inner shear layers taken 0.2 ms apart. Images a-f in Figure 57a show the rollup event of one vortex at the dump plane as another two convect downstream. In Figure 57b, images a-e show the rollup of a vortex in the streamwise shear layer in a series of images that were taken from the top of the combustor with the laser sheet placed at a distance of 6.5 mm downstream of the dump plane.



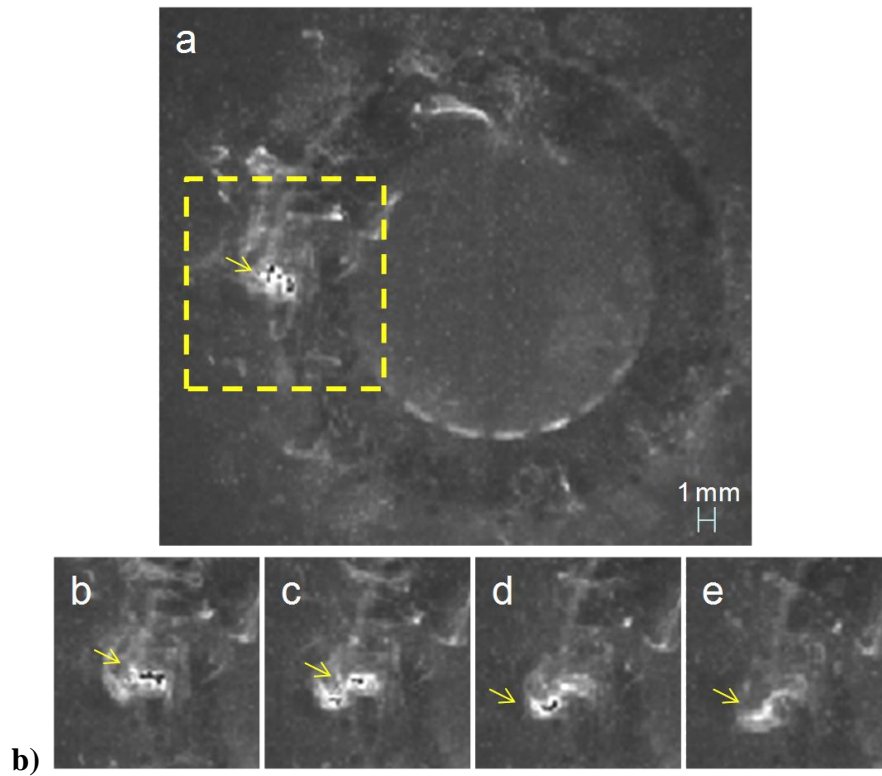


Figure 57. Instances of shear layer rollup in an unforced annular swirling jet in both the a) axial and b) azimuthal shear layers, with mean flow velocity of 10 m/s, swirl number of 0.85.

Figure 57a shows the spanwise shear layer rollup on the right-hand side of the nozzle. Small structures, approximately 1 mm across, roll up at the edge of the nozzle and convect downstream with the jet. Based on a mean flow speed of 10 m/s and the spacing of the vortices, the passage frequency is approximately 2500 Hz. Image b shows the beginning of the formation of a vortex in the outer shear layer. By image d the vortex has rolled up and begins to convect downstream. As it travels downstream, in images e-f, it also grows larger. It is clearly possible to see these fine-scale vortex rollup events in the outer shear layer. It is much more difficult to see these structures in the inner shear

layer as a result of the highly turbulent vortex breakdown region adjacent to the inner shear layer. Just as a vortex is formed, it is quickly deformed and diffused by the inner recirculation zone.

Figure 57b shows the streamwise shear layer rollup measured 6.5 mm downstream of the dump plane. These structures are significantly larger than the spanwise structures and can be seen to roll up as the flow rotates counter-clockwise. In the inner streamwise shear layer, the coherent structures are larger and more diffuse as a result of their interaction with the inner recirculation zone. The images shown in Figure 57b show the rollup of a vortex, indicated by a yellow arrow. It can be seen rolling up and convecting counter-clockwise through the series of images.

This natural shear layer rollup was also measured using high-speed PIV. Here, vorticity is used to visualize these coherent structures, and shedding in both the inner and outer shear layers is evident. Figure 58 shows a series of images of an unforced swirling jet taken 0.1 ms apart.

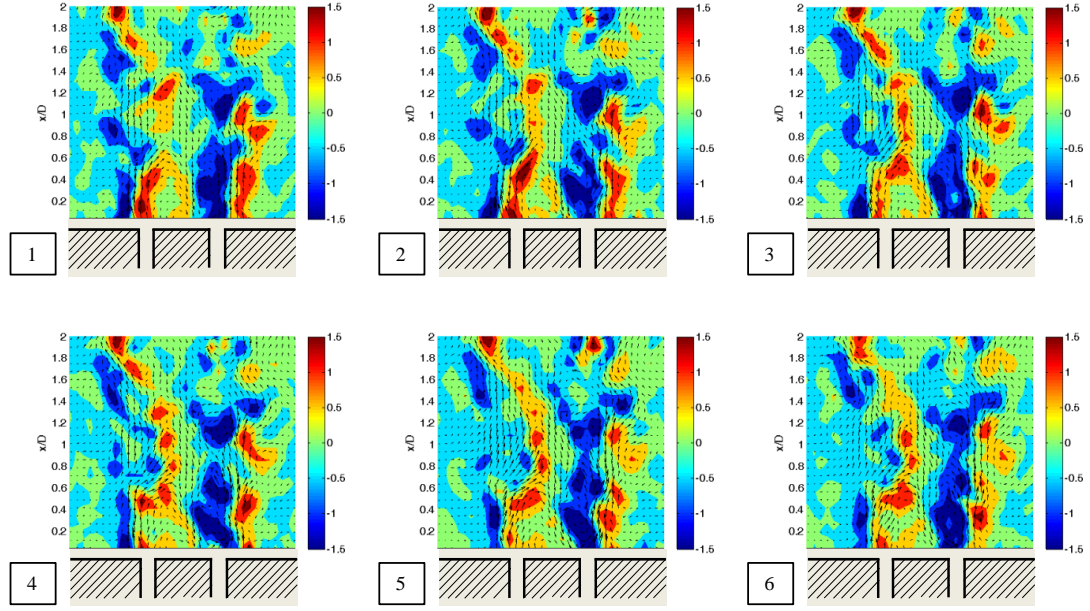


Figure 58. Six time instances of unforced, non-reacting jet flow show natural shear layer rollup, for $u_o=10$ and $S=0.85$. Normalized vorticity is shown in color; images are 0.1 ms apart.

These images show shedding of coherent structures in a highly turbulent flow field. This turbulence induces jitter in the structures, causing a random component to the initial shedding of the structures as well as their downstream evolution. This stems from both the random nature of the initial perturbation exciting the shear layer and the flow turbulence that buffets the structures as they convect downstream. As will be seen in a later section, this jitter is somewhat decreased in the case of acoustic forcing because the perturbation signal is clearly harmonic. The effect of flow turbulence on the downstream evolution of the structures is still seen, an effect that was described and quantified in detail for bluff-body flow fields by Shanbhogue [155].

Effect of acoustic forcing on shear layer dynamics

As discussed above, convectively unstable shear layers act as disturbance amplifiers and respond strongly to acoustic forcing. In this section, the response of the shear layers to acoustic forcing is discussed. This response was measured in two ways. First, a description of the velocity field in the r - x plane is described with support from both smoke visualization and high-speed PIV. Second, these effects were also measured in the r - θ plane and modal decompositions, described in Chapter 4, were used to understand the response of different modes to acoustic forcing. The results from these two studies, however, support a similar narrative about the behavior of these structures in the presence of acoustic forcing.

To first understand the response of a shear layer to acoustic excitation, the smoke system was used to visualize the response of the shear layer to transverse acoustic forcing. An important question is the mechanism through which the shear layer, which has its own most amplified frequency, responds to the excitation. As the shear layer is convectively unstable, it responds to the acoustic forcing, even at low amplitudes. Ho and Huang [156] have shown that forcing where $f_o \ll f_r$ leads to a phenomenon known as “collective interaction.” As illustrated by the sketch taken from Ho and Nossier [157] in Figure 59, the vortices interact so that in one region they are drawn together, further amplifying the induced flow field that causes their rotation around each other and coalescence. In the other region, they are pulled apart from each other. Also shown is a flow visualization from the present experiment of apparently the same phenomenon. Unlike the unforced case where the structures resulting from natural vortex shedding

were too small and weak to survive in the midst of the vortex breakdown bubble, these large collective interaction structures can be seen in the inner and outer shear layers.

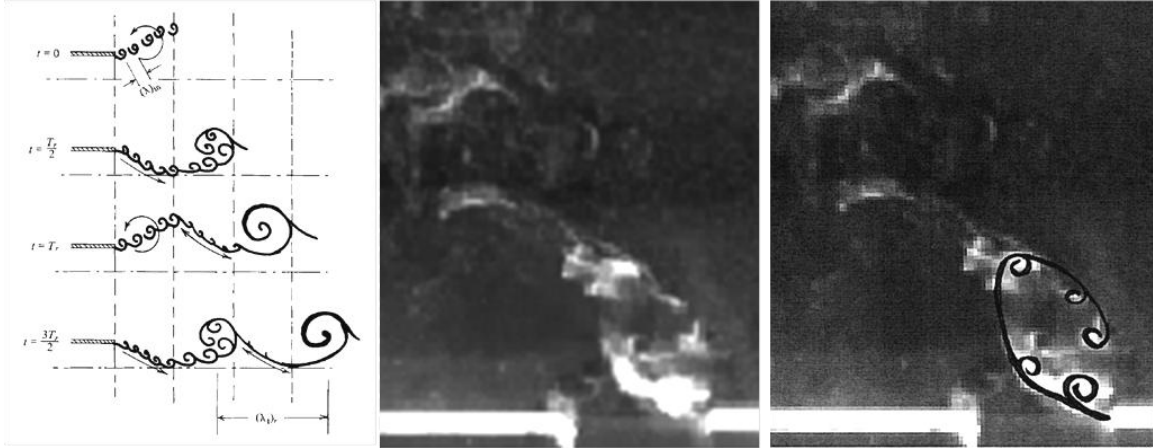


Figure 59. Collective interaction in shear layers from Ho and Nossier [157] (left) and from the current study (center and right) in the inner shear layer of the annular jet with acoustic forcing, out-of-phase forcing at 400 Hz at an amplitude of $v'/U_o=0.35$ and a bulk velocity of 10 m/s and swirl number of 0.85.

During a collective interaction event, several Kelvin-Helmholtz vortices rapidly merge and roll up into a larger structure whose passage frequency equals that of the excitation. In other words, an integer number of shear layer vortices with passage frequencies of approximately 2400 Hz merge into a larger vortex at a forcing frequency of 400 Hz. An example of such an event is shown in detail in Figure 60 and with less magnification in Figure 61. In Figure 60, what appears to be five smaller vortices, formed as a result of the Kelvin-Helmholtz instability, can be seen rolling into a larger structure, as described by Ho and Nossier [157] and shown in Figure 59. The time step between each image is 0.1 ms. Figure 61 shows the event with less magnification and

with larger time steps, 0.3 ms, and shows another collective interaction event, followed by the shedding of the large structure and its convection downstream, as also shown by Ho and Nossier [157] in Figure 59. This process is repeated once per acoustic cycle.

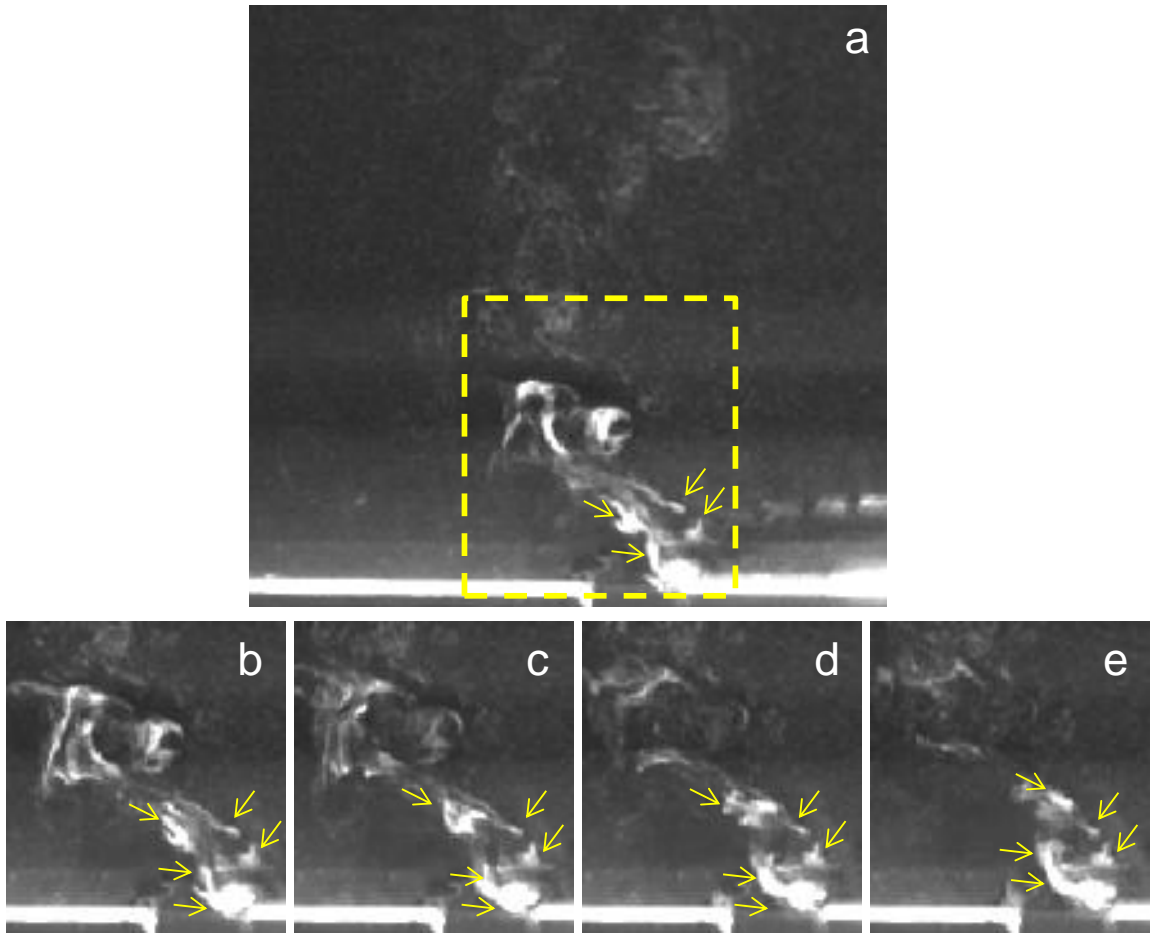


Figure 60. Collective interaction event in the inner shear layer with a bulk velocity of 10 m/s, swirl number of 0.85, and out-of-phase acoustic forcing at 400 Hz at an amplitude of $v'/U_o=0.35$.

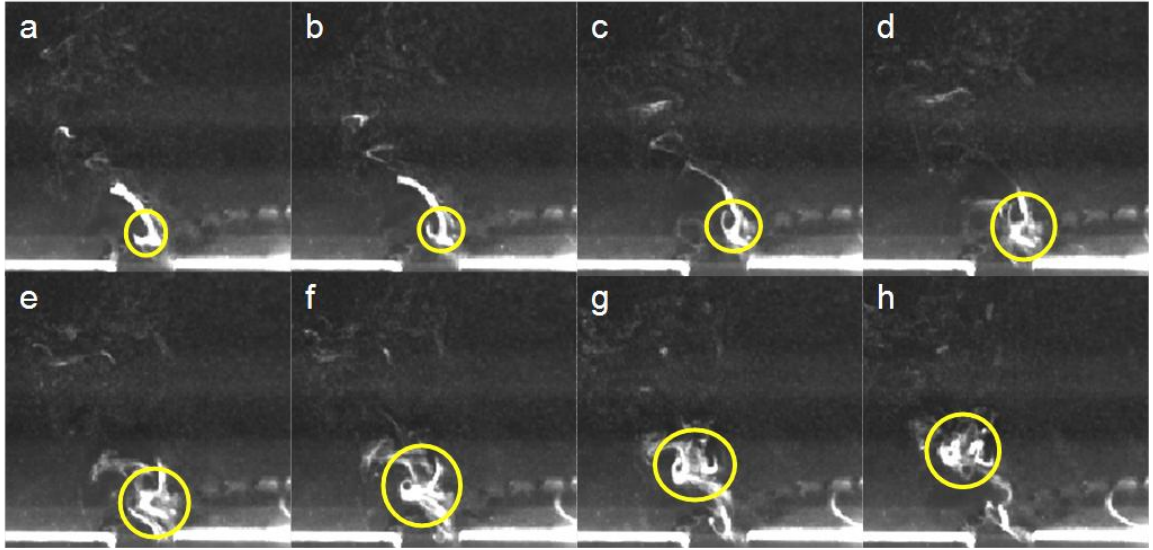


Figure 61. Collective interaction even showing the structure formation and separation at the same conditions as Figure 60. Each image is 0.3 ms apart.

Figure 62 shows this same event in the high-speed PIV data, circled in yellow. The PIV resolution is far too coarse to visualize the small shear layer vortices, but the larger merged vortical structure is evident, as shown in Figure 62. This field shows the velocity vectors superimposed on the out-of-plane vorticity, shown in the color bar on the right. The quantities plotted are the sum of the velocity and vorticity fluctuation at the forcing frequency and the mean at one instant of the acoustic cycle. The part of the cycle chosen corresponds to approximately the same moment in time as is shown in Figure 61g.

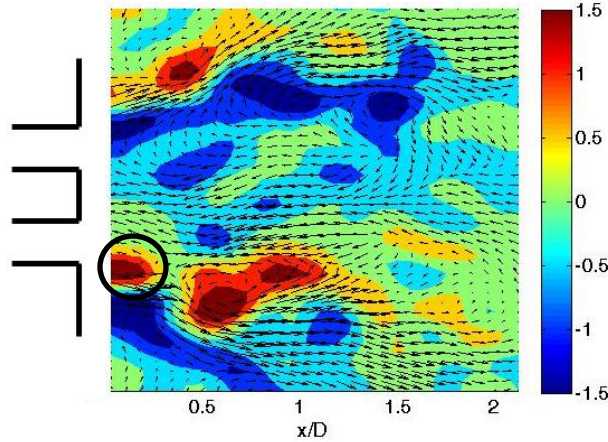


Figure 62. Collective interaction as seen in a velocity field from PIV for a non-reacting case at a bulk velocity of 10 m/s, swirl number of 0.85, and out-of-phase acoustic forcing at 400 Hz at an acoustic amplitude of $v'/U_o=0.35$. Structure from collective interaction is shown in the black circle.

The large-scale structure rotating in a clockwise direction at $r/D=0.5$ and $x/D=0.2$ is clearly evident in the figure. At $r/D=-0.5$ and $x/D=0.4$, an oppositely rotating structure is present in the inner shear layer and had been formed half a cycle before the one previously described. This structure is not as visible in the smoke image due to the rapid diffusion of the smoke.

The downstream evolution of these structures was not measurable using the smoke technique due to the quick diffusion of these structures downstream. Despite that, these measurements provide a baseline qualitative description of the collective interaction mechanism that is key to the formation of these structures. Next, the downstream evolution of these structures is addressed using data from high-speed PIV.

An issue that is inextricably linked with the response of the flow to acoustic forcing is the symmetry of the acoustic forcing. As described in the Introduction, flows

respond in-kind to the symmetry of the imposed acoustic field. In-phase forcing, a symmetric forcing condition, results in a symmetric response in the flow, at least initially. The out-of-phase forcing, an asymmetric forcing condition, results in an asymmetric response in the flow. This framework is overly simplistic in a swirling flow, though, because the base flow is inherently asymmetric due to the action of swirl. Previous studies [153] have shown that the most unstable modes of these flows have mode numbers of $|m| > 0$ and the $m = 0$ mode is hydrodynamically stable. This issue becomes integral to the understanding of the downstream evolution of the shear layer behavior, as will be discussed later.

In order to discuss the response of the shear layers, we look at the response of the flow at the forcing frequency. Here, a process referred to as harmonic reconstruction is used to quantify the motions only at one frequency. Since the high-speed PIV system produces time-resolved velocity fields, spectral analysis was used in much of this study. First, spectra were calculated for each point in space in the velocity and vorticity fields. To calculate the coherent fluctuations, the amplitude and phase of the Fourier transform of the velocity, $\hat{A}(x)$ and $\phi(x)$, were then used to harmonically reconstruct a time-domain flow field at the forcing frequency using the relation in Equation (14):

$$\hat{u}(\vec{x}, t) = \text{Re} \left[\hat{A}(\vec{x}) e^{-i(\omega t + \phi(\vec{x}))} \right] \quad (14)$$

“Hatted” variables, such as the velocity in Equation (14), are referred to as “harmonically reconstructed” quantities.

Two main conclusions can be drawn from the response of the flow at the forcing frequency. The first, a direct result of the nature of a standing acoustic field, is that the in-phase and out-of-phase forcing conditions result in very different acoustic velocity fluctuation amplitudes. As discussed above, in-phase, or symmetric, forcing results in an approximate velocity node along the centerline and hence very low amplitude acoustic velocity fluctuations in the region of the flow. Conversely, the out-of-phase, or asymmetric, forcing condition results in an approximate velocity anti-node and high amplitudes of acoustic velocity fluctuations. While these two conditions are part of the same acoustic field in an engine combustor geometry, the excitation amplitude they provide for the flow and flame are significantly different, and results in disparate flow response amplitudes.

The second effect stems directly from the symmetry of the acoustic forcing. As discussed above, asymmetric forcing results in asymmetric flow response; this is a trend that has been observed in a variety of flows and forcing configurations. This has shown to be a key idea in our analysis of the response of the swirling jet shear layers. The structures that most readily respond to acoustic forcing are the convectively unstable shear layers. As disturbance amplifiers, these structures respond strongly to acoustic forcing and are highly influenced by the symmetry of the acoustic field.

In shear layers, the response of these structures to symmetric versus asymmetric forcing fields is quite different. Figure 63 shows a notional sketch of a cross-section of the flow field. The figure shows three main features of the flow field in both the reacting and non-reacting flow. First, the center of the flow is dominated by the vortex breakdown bubble. On either side of the bubble is the annular jet column. The inner

shear layer, the region of shear between the jet column and the vortex breakdown region, and the outer shear layer, the region between the jet column and the ambient fluid, contain coherent vortices. These structures are formed as a result of fluctuating axial velocity at the nozzle, and the phase of the fluctuations on one edge with respect to the other edges determines the symmetry of the vorticity field.

Figure 63a shows the case of an asymmetric flow field, caused by out-of-phase acoustic forcing. Here, a helical pattern is created within each shear layer, resulting in a staggered vortex pattern in the plane formed by the laser sheet. Figure 63b shows an example of an axisymmetric flow field, where vortex rings propagate downstream from the inner and outer edges of the annulus. As they convect downstream, these structures deform and locally bend the jet column. In addition to the aforementioned processes, the transverse acoustic motion periodically shifts the flow field from side to side, shifting the angle of the jet column and the trajectories of the coherent structures.

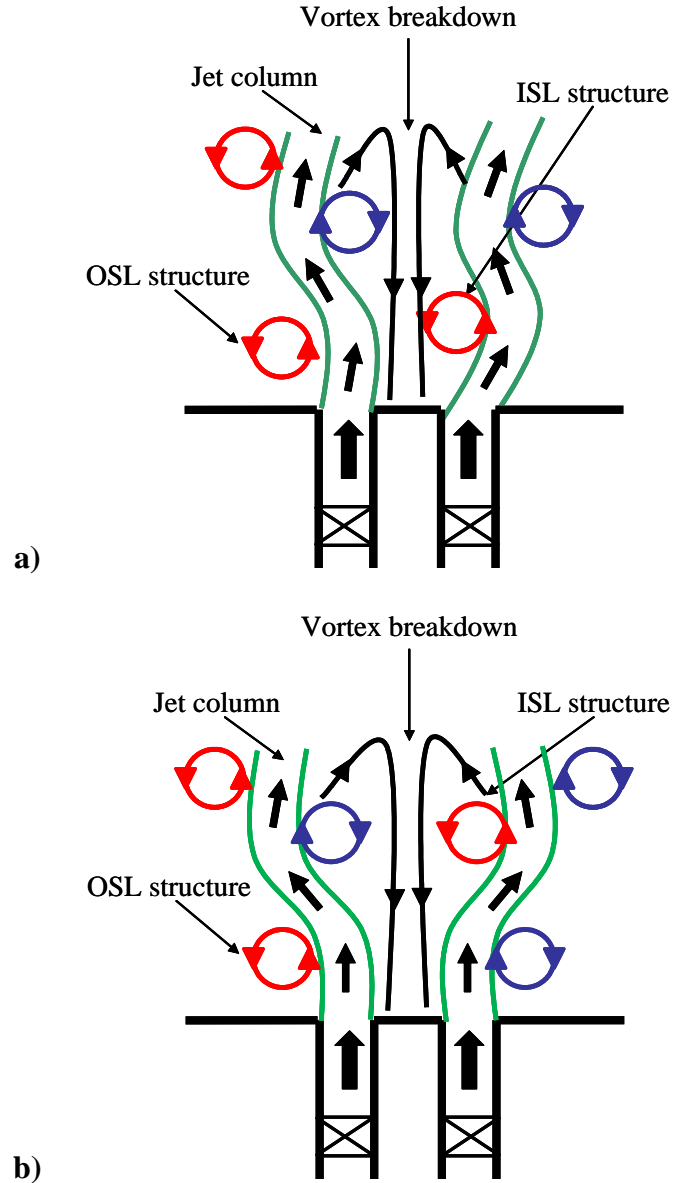


Figure 63. Notional picture of the flow field for a transversely forced swirling jet with a) out-of-phase and b) in-phase acoustic forcing. Coherent structures in the inner shear layer (ISL) and outer shear layer (OSL) travel downstream, bending the jet column as they pass.

In the in-phase forcing case, a symmetric forcing configuration about the center plane of the experiment, the shear layers roll up into ring vortices on both the inner and outer

edge of the annular jet, a symmetric response (the $m=0$ mode) at the dump plane to a symmetric forcing condition. In the out-of-phase forcing case, the asymmetric forcing condition, the shear layers roll up into helical structures, an obviously asymmetric response to the asymmetric acoustic forcing. The downstream evolution of these structures will be discussed later. Examples of this response are shown in Figure 64 and Figure 65 for several instances in time 0.83 ms apart.

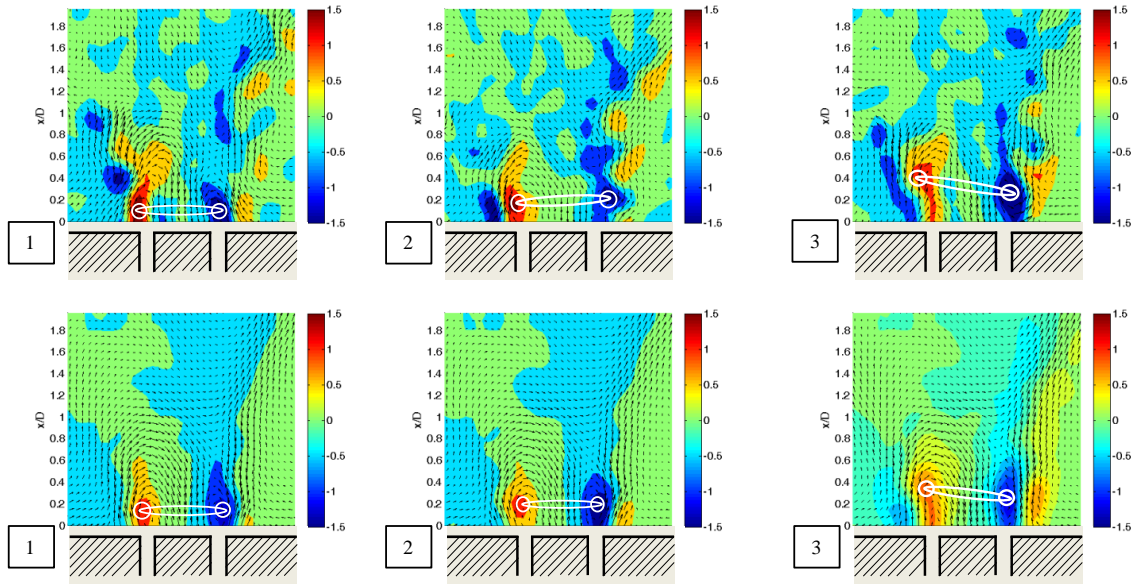


Figure 64. Comparison of instantaneous (top) and filtered (bottom) velocity at the forcing frequency for in-phase forcing at 400 Hz, non-reacting flow at $u_o=10$ m/s, $S=0.85$. White lines trace the vortex.

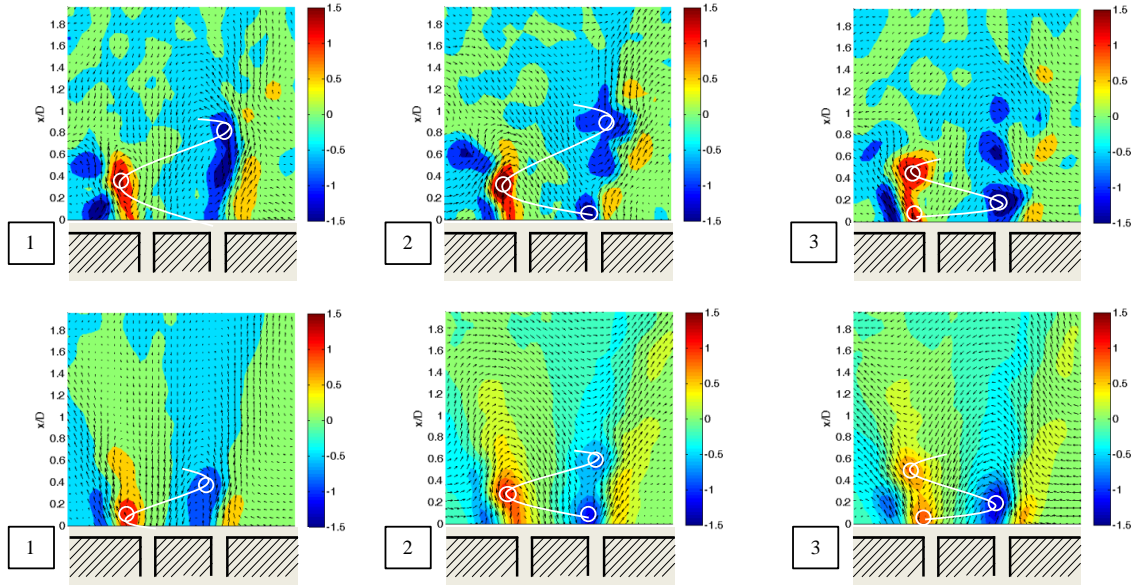


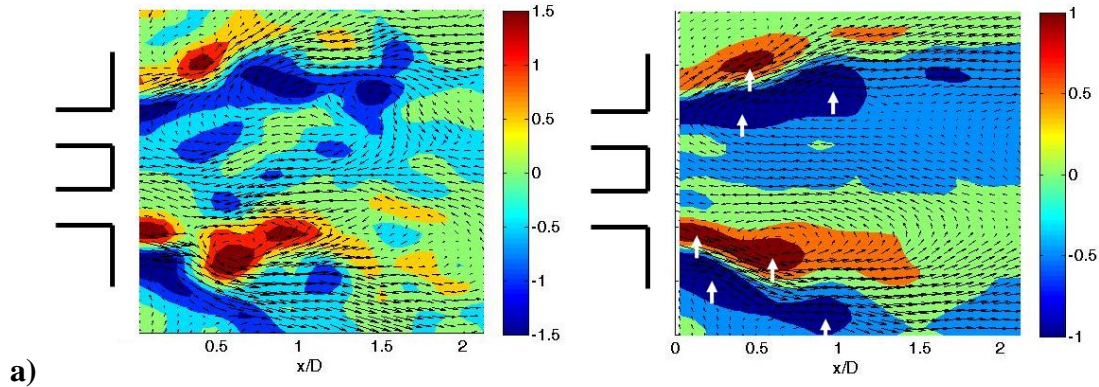
Figure 65. Comparison of instantaneous (top) and filtered (bottom) velocity at the forcing frequency for out-of-phase forcing at 400 Hz, non-reacting flow at $u_o=10$ m/s, $S=0.85$. White lines trace the vortex.

Here, in Figure 64 and Figure 65, both the instantaneous as well as the filtered velocity field at the forcing frequency is shown. This filtered velocity field is calculated by reconstructing the velocity field at the forcing frequency only. The filtered velocity is appropriate to show in this case because the shear layers are responding directly to the acoustics and further inspection and comparison of the instantaneous and filtered velocity and vorticity fields reveals great similarity.

It is clearly evident from the out-of-phase forcing case in Figure 65 that the response of the flow is asymmetric. Helical vortices are clearly seen in both the instantaneous and harmonically reconstructed flow fields. In the in-phase forcing cases, however, the symmetry of the flow response changes as a function of downstream distance. At the dump plane where the vortex is shed, corresponding to Image 1 in Figure 64, the ring vortex is clearly symmetric. As this vortex travels downstream, however, it begins to tilt. In Image 2 it tilts such that the right edge travels further

downstream fast, and in Image 3 it has rotated as well as convected downstream and now the opposite side is further downstream. This motion would come from the action of swirl, which is clearly present in both the instantaneous and harmonically reconstructed results. This issue will be discussed later in terms of modal decomposition results, which show the same behavior.

Similar results have been seen in reacting PIV results. The plots in Figure 66 show the filtered velocity and vorticity field by plotting the sum of the fluctuation of the vorticity at the forcing frequency and the mean vorticity. This calculation involves taking the FFT of the instantaneous velocity and vorticity at each point and harmonically reconstructing the signal at the forcing frequency, as described in Equation (14). This is effectively a filtering, or phase locking, process that captures only the motions at the forcing frequency, eliminating turbulent noise. This process also spatially smears out the instantaneous vorticity, due to cycle-cycle phase jitter in axial location of the vortical structures. Figure 66, like the notional pictures in Figure 63, shows the out-of-phase and in-phase velocity and vorticity fields for one phase of the acoustic cycle.



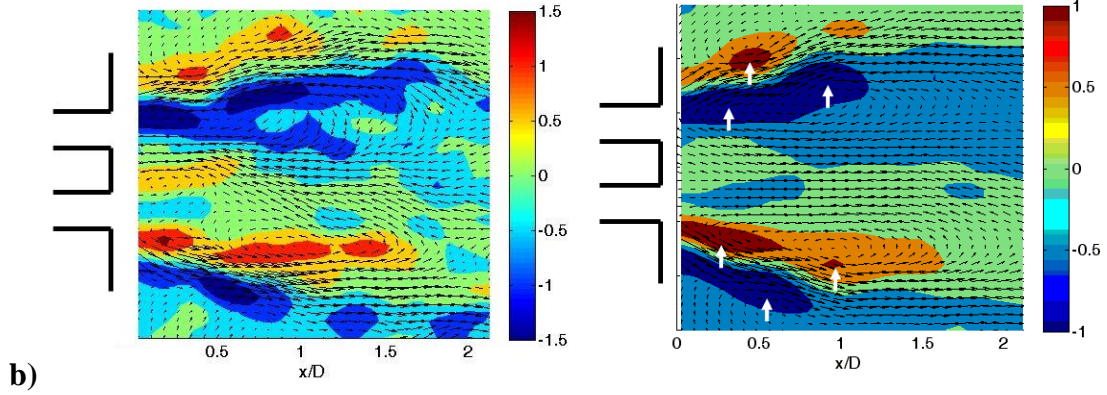


Figure 66. Normalized instantaneous (left) and filtered (right) velocity and vorticity field for a) out-of-phase and b) in-phase acoustic forcing for reacting flow at a bulk velocity of $U_o=10$ m/s and a forcing frequency of $f_o=400$ Hz.

In the out-of-phase forcing case, a pressure node is present along the centerline of the flow. The pressure fluctuations on either side of the node are out of phase, creating out-of-phase axial velocity fluctuations on either side of the nozzle. This asymmetry in the axial velocity fluctuations leads to an asymmetry in the vorticity field, which is evident in Figure 66a. For example, in the outer shear layer, the structure closest to the dump plane is on the right-hand side at $x/D=0.2$. The next shear layer structure is on the left-hand side at $x/D=0.5$. The final structure of significant strength in the outer shear layer is again on the right-hand side at $x/D=0.9$. This vortex structure suggests a helical vortex pattern in both the inner and outer shear layers, similar to LES simulations by García-Villalba and Frölich [158], shown in Figure 67.

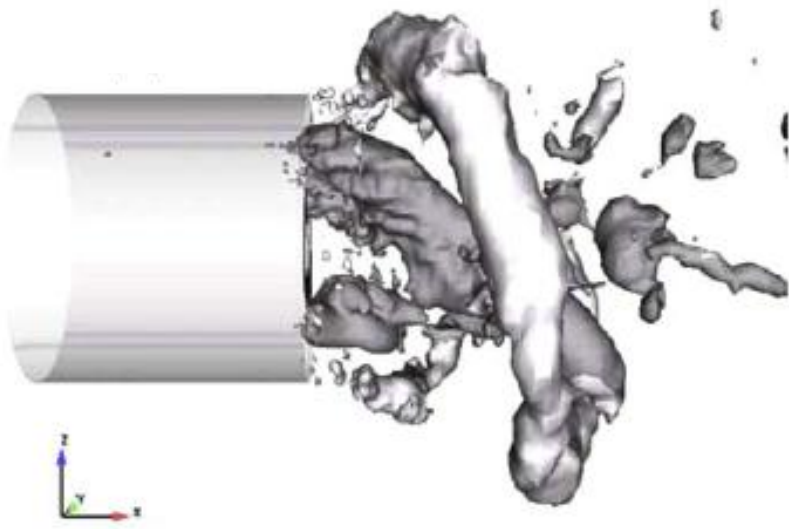


Figure 67. Snapshot of a helical shear layer instability in a swirling annular jet, used to visualize coherent structures from LES simulation [158] under longitudinal, self-excited oscillations.

In the in-phase forcing, the formation of structures in each shear layer is nominally axisymmetric. For example, the inner shear layer shows two sets of structures, one located at $x/D=0.3$ and one at $x/D=0.9$. The outer shear layer structures are also axisymmetric, but not aligned with the structures in the inner shear layer. Similar trends for both the in-phase and out-of-phase forcing are observed in the non-reacting cases as well.

The local behavior and downstream evolution of the shear layer structures appear qualitatively similar between the non-reacting and reacting cases, further emphasizing the point that heat release does not affect the basic mechanisms responsible for the appearance of unsteady flow structures in the shear layers that distort the flame. The major difference between the two is difference in dissipation rate of the vorticity. In the

reacting case, significant coherent structures are seen until $x/D=1$, where the coherent structures have decayed by $x/D=0.4$ in the non-reacting case.

Convection velocities of the vortex structures were estimated from the axial phase dependence of the vortical disturbances shown in Figure 68. These phases were calculated from the phase of the FFT at the forcing frequency along the inner and outer shear layers. The shear layer locations were estimated from the time-average vorticity magnitude maxima.

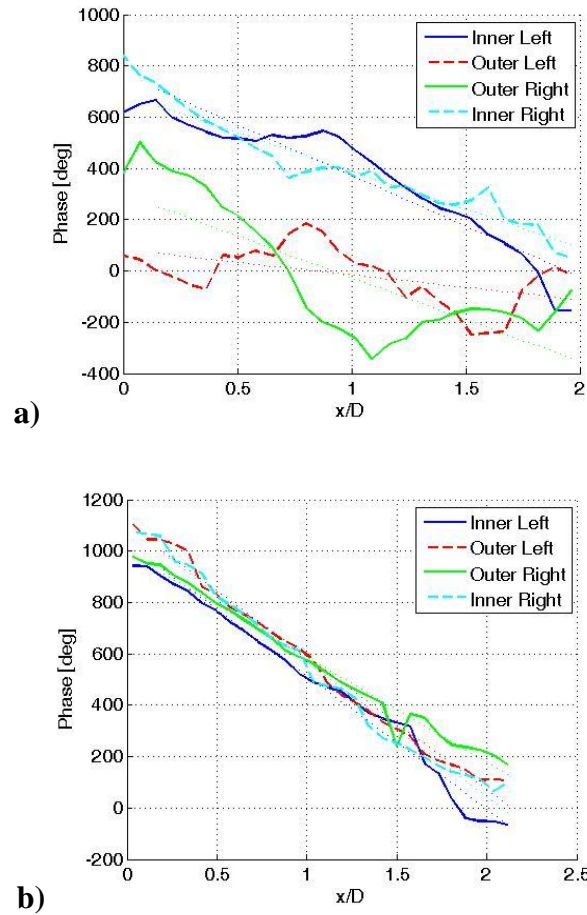


Figure 68. Phase of vorticity along shear layers for a) non-reacting and b) reacting flow at a bulk velocity of $U_o=10$ m/s and a forcing frequency of $f_o=400$ Hz out-of-phase.

Linear fits of the phase data were calculated as a function of downstream distance. The slope of this line was taken from the fit and used to calculate the convection velocity using the formula in Equation (15).

$$u_{c,v} = 2\pi f_o \frac{1}{\frac{d\phi}{dx}} \quad (15)$$

The convection speeds of the vorticity along the six lines of travel were calculated and averaged, leading to a value of 13 and 10 m/s for the non-reacting and reacting cases, respectively. Each convection speed falls within the range of convection speeds measured in non-swirling flows, which are $\sim 0.5U_o < u_{c,v} < \sim 1.5U_o$ [159]. Additionally, the phase between the disturbances traveling in the jets is shown in Table 2. The uncertainty in phase is ± 15 degrees.

Table 2. Average phase difference between vorticity disturbances in the left and right jet centers at several conditions at a bulk velocity of $U_o=10$ m/s and a forcing frequency of $f_o=400$ Hz.

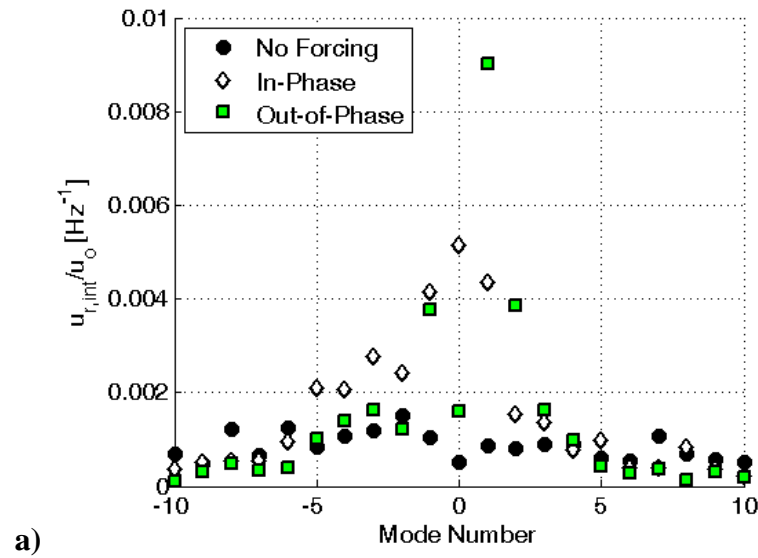
	Phase ($\pm 15^\circ$)
Non-reacting, Out-of-phase	20
Reacting, Out-of-phase	-50
Non-reacting, In-phase	100
Reacting, In-phase	130

These phase differences indicate the shape and symmetry of the disturbance field on either side of the nozzle. For example, the phases of the in- and out-of-phase reacting

cases are 130 and -50 degrees, respectively. This can be seen by looking at snapshots of the vorticity field at any point in time, shown in Figure 66.

The meaning of the -50 and 130 degree phase differences are evident from the plots in Figure 66. In Figure 66a, the out-of-phase forcing case, the vortical disturbances are non-axisymmetric. The plot in Figure 66b depicts the in-phase forcing case, which is roughly axisymmetric. Although the vortex pairs are slightly staggered, possibly because of the motion of the swirl, the 130 degree phase between the vorticity fluctuations on either side of the jet indicates that symmetric vortex rings are being formed.

Changes in the modal structure of the swirling flow are also evident between in-phase and out-of-phase forcing. Figure 69 shows the modal decomposition (integrated over all frequencies and radii between $r/D=0-1$) for the unforced, out-of-phase forcing, and in-phase forcing cases at high amplitude forcing at a downstream location of $x/D=0$. This location was chosen to capture the vortex rollup motion in the shear layers, as depicted in Figure 64 and Figure 65.



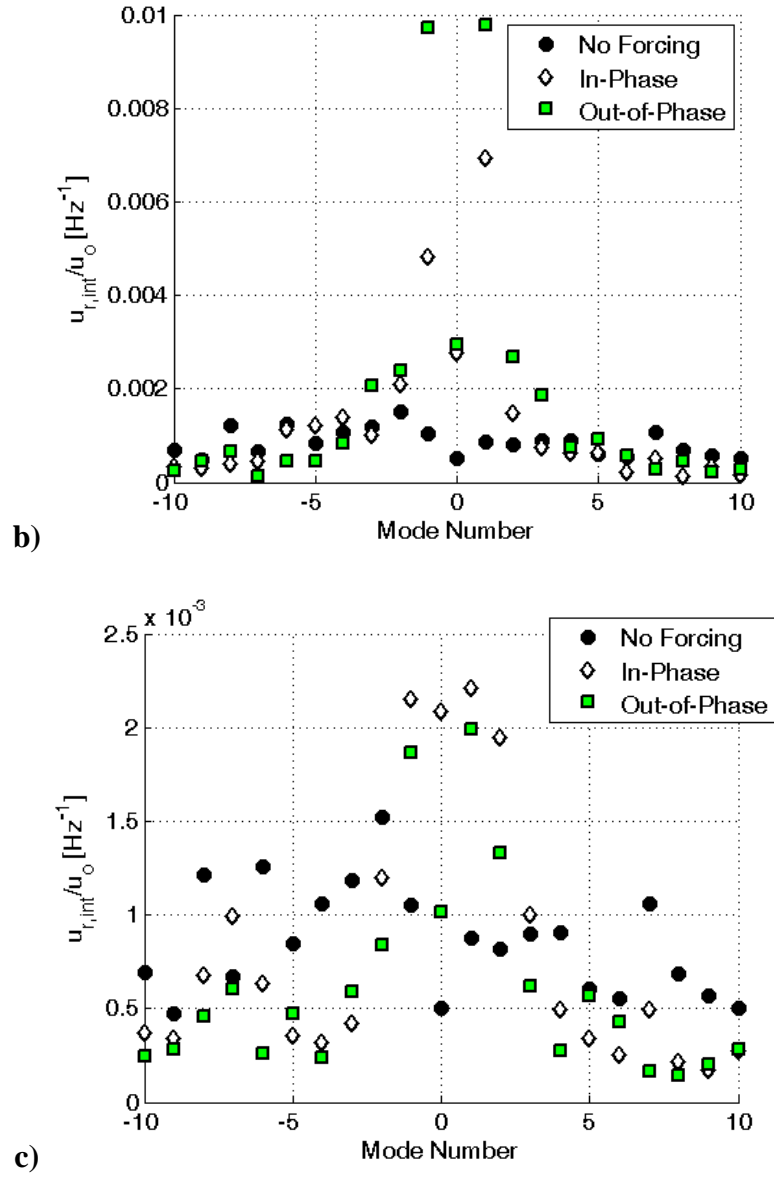


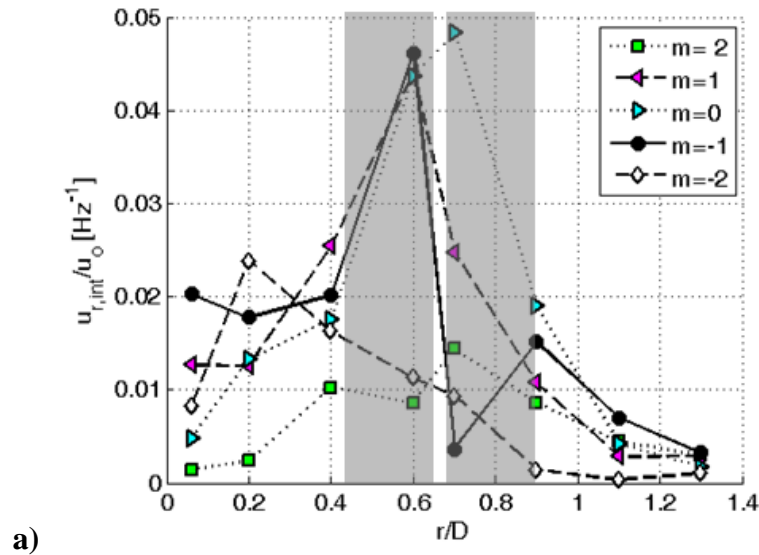
Figure 69. Distribution of mode amplitude at the forcing frequency integrated over radii $r/D=0-1$ plotted as a function of mode number at $x/D=0$ for a non-reacting, flow forced with a) 400 Hz, b) 800 Hz and c) 1200 Hz forcing at $u_o=10$ m/s, $S=0.85$.

Here, it is evident that different forcing configurations have different effects on the modal content of the flow. For example, out-of-phase forcing significantly amplifies modes $m = 1$, $m = 2$, and $m = -1$, two counter-swirling and a co-swirling helical modes,

respectively. The amplification of these two modes asymmetrically is indicative of the asymmetric response of the flow and the helical vortex in the shear layers. The strong $m=1$ mode represents the helical vortex shedding evident in the inner shear layer, as seen in Figure 65.

The in-phase forcing strongly amplifies the symmetric $m=0$ mode; this finding is congruent with the ring vortex shedding observed in the r - x view. Additionally, the $m=1$ and $m=-1$ modes are present at very similar amplitudes. In the inner shear layer region, between $r/D=0.2$ - 0.6 , the phase between the fluctuations at these two modes is zero within the uncertainty in phase estimation (15 degrees). The excitation of these two modes is also indicative of a symmetric response of the flow.

Additional information can be garnered from the radial distribution of fluctuation amplitude of each of these modes. Figure 70 shows the distribution of energy for in-phase and out-of-phase forcing, at the forcing frequency, for several mode numbers.



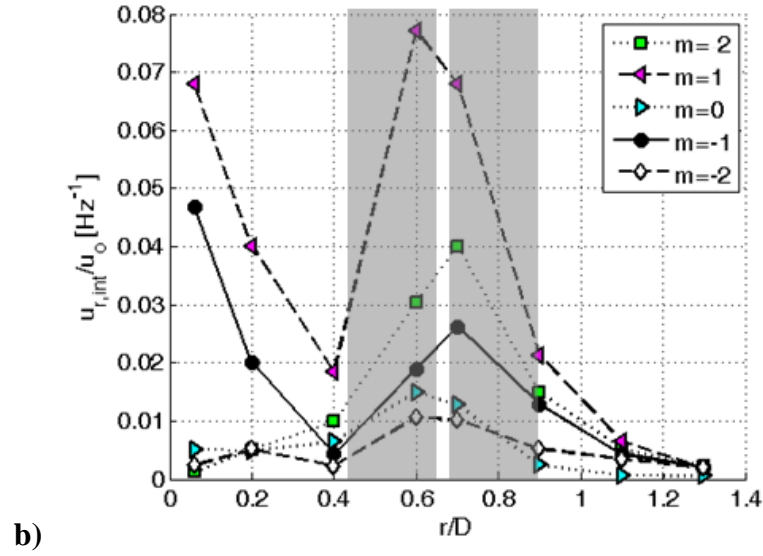
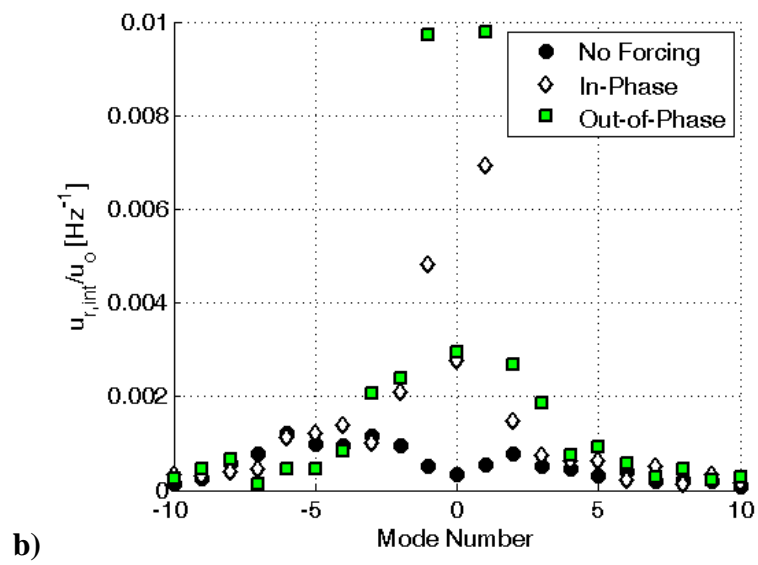
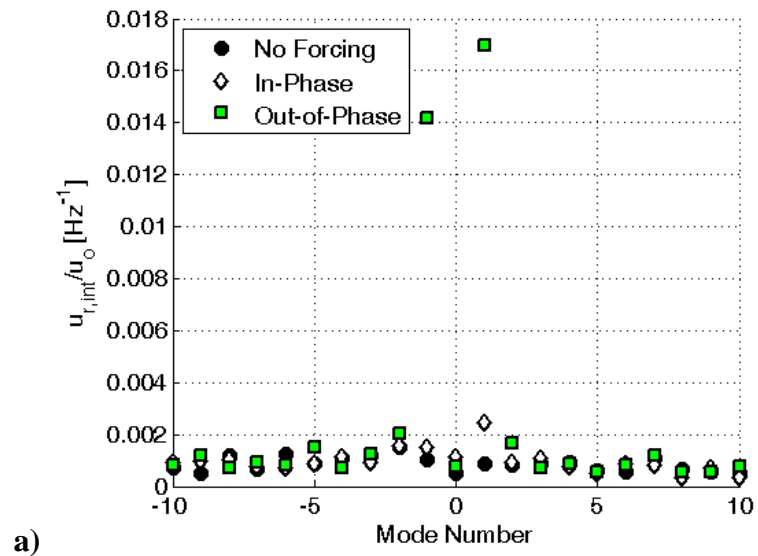


Figure 70. Distribution of mode amplitude at the forcing frequency plotted as a function radius for several mode numbers for a non-reacting, flow forced at 400 Hz
a) in-phase and b) out-of-phase forcing at $u_o=10$ m/s, $S=0.85$. Gray areas approximate the location of the inner and outer shear layers at $x/D=0$, where these data were taken.

In the out-of-phase forcing case, the dominant mode, $m=1$, is prevalent in the inner shear layer, as would be expected given their convectively unstable nature. This response is consistent with the helical response seen in the r - x view in Figure 65. In the in-phase forcing case, the response seems to focus in the inner shear layer for modes $m=-1$ and $m=1$, and in both the inner and outer shear layer for mode $m=0$.

Further downstream, however, the distribution of energy amongst the modes changes, as is shown in Figure 71. Here, the distribution of modal amplitude at a downstream location of $x/D=1$ is shown.



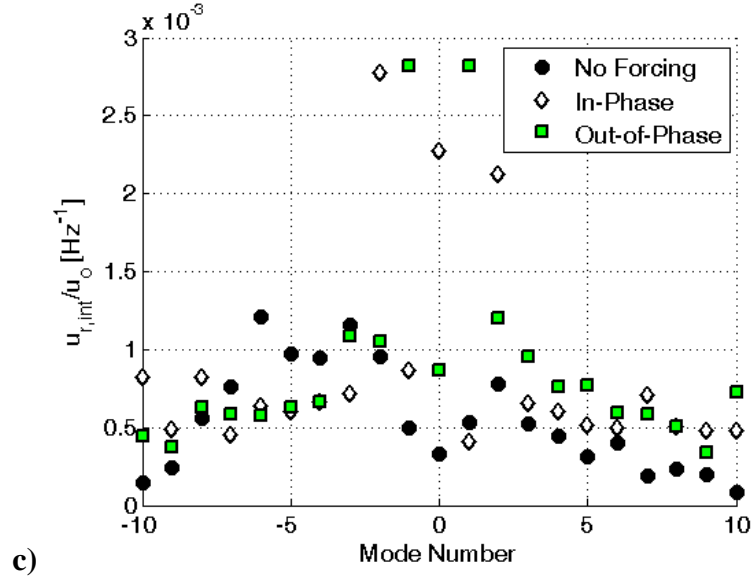


Figure 71. Distribution of mode amplitude at the forcing frequency integrated over radii $r/D=0-1$ plotted as a function of mode number at $x/D=1$ for a non-reacting, flow forced with 400 Hz forcing at $u_o=10$ m/s, $S=0.85$.

In this case, the effect of in-phase, symmetric forcing has been almost completely lost, manifesting as only a slight increase in the amplitude of modes $m=0$, $m=1$, and $m=-1$ over the unforced flow. This may be due to two factors. First, the action of swirl causes the ring vortices to tilt [75], introducing an inherent asymmetry in the flow structure downstream. Additionally, the $m=0$ mode is stable in a swirling jet. Theoretical analysis by several authors [153] indicates that asymmetric modes dominate for these flow profiles because of the action of swirl. Results from this analysis are shown in Figure 72.

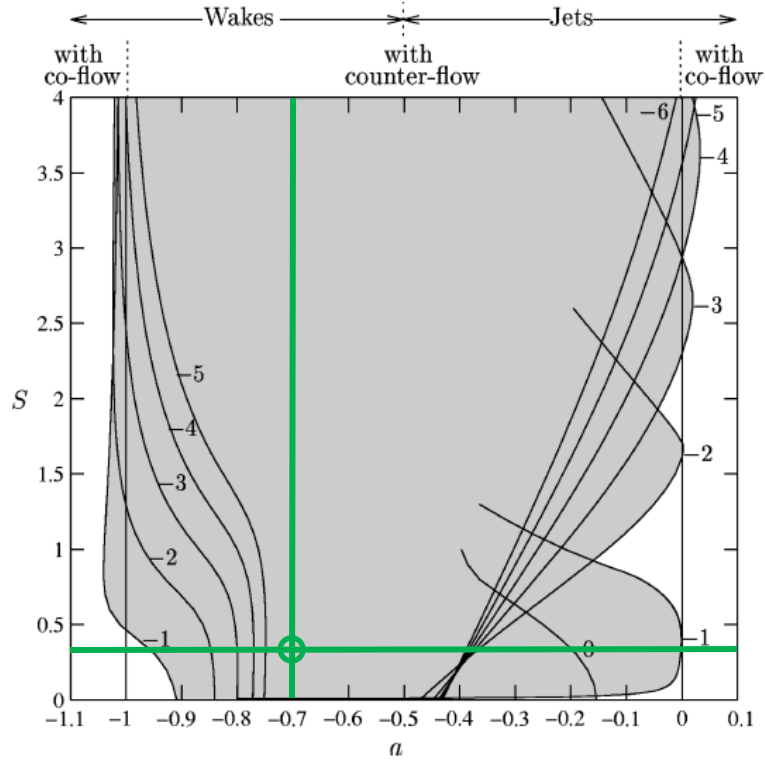


Figure 72. Swirling flow stability map as a function of swirl number (S) and backflow ratio (a) showing helical mode absolute (shaded region) and convective (white region) stability boundaries, from Loiseleux *et al.* [153]. Green lines indicate values of S and a for current flow field.

Figure 72 shows a stability calculation from Ref. [153] indicating the convective/absolute instability boundaries for a swirling flow; all mode numbers are convectively unstable. While the convective/absolute instability transition map does not directly explain the asymmetries observed in the in-phase forcing cases, it illustrates the stability tendencies of swirling flows and the dominance of asymmetric modes. Applying the formulation from Ref. [153], the location of the current flow field on this stability map was calculated. Figure 73 shows axial velocity profiles for three downstream

stations where r - θ data is available. In this way, the progress of the parameters a and S can be tracked as a function of downstream distance.

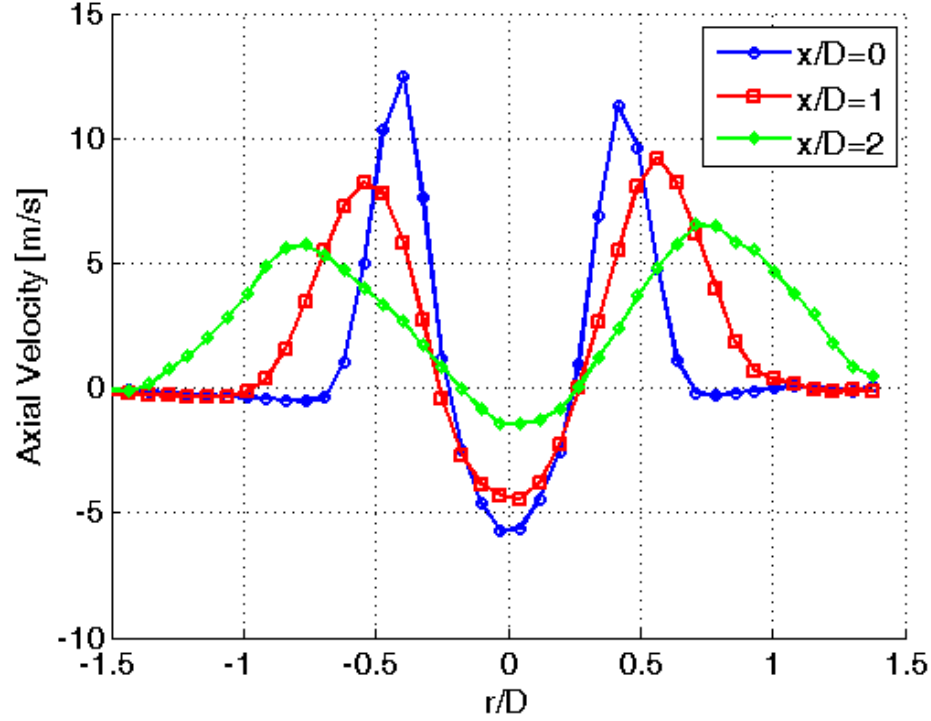


Figure 73. Time-average axial velocity profiles at three downstream stations for unforced flow at $u_o=10$ m/s and $S=0.85$.

Using these axial velocity profiles as well as the swirling flow profiles in Figure 20, estimations for the values of a and S have been calculated and are shown in Table 3 using the definitions in Equation (16).

$$a = \frac{U_\infty}{\Delta U} \quad (16)$$

$$S = \frac{\Omega R}{\Delta U}$$

Here, U_∞ is the mean axial flow velocity, ΔU is the velocity difference between the axial flow and the reverse flow in the vortex breakdown bubble, Ω is the solid body

rotation speed, and R is the radius of the core flow (in this case the reversed flow). Note that the definition of swirl number in the Loiseleux *et al.* formulation is very different from the geometric swirl number used in the current work; the geometric swirl number will have a greater value for the current profile as it does not account for the reverse flow in the vortex breakdown bubble as the Loiseleux *et al.* swirl number does.

Table 3. Value of swirling flow parameters from Loiseleux *et al.* formulation for stability calculation.

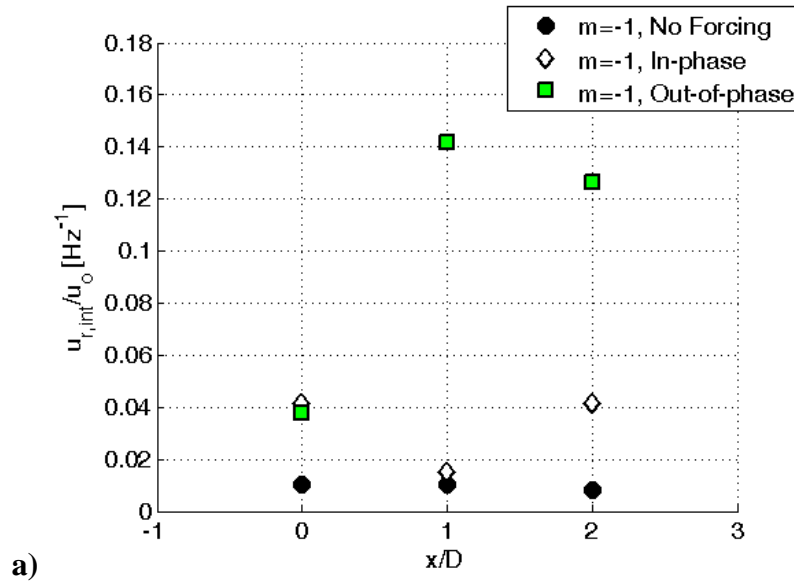
Downstream location	a	S
$x/D=0$	-0.7	0.3
$x/D=1$	-0.7	0.4
$x/D=2$	-0.7	0.4

As can be seen from Figure 72, marked with the values from Table 3, is that no symmetric mode is stable but several asymmetric modes are unstable. This further supports the observation that the symmetric vortex rings shed at the nozzle exit as a result of the symmetric forcing condition lose their symmetry with downstream distance as a result of the natural stability characteristics of the swirling flow.

In the out-of-phase forcing case, however, the amplitude of mode $m = -1$ has grown significantly, while the amplitude of mode $m = 1$ has also grown. The phase between the fluctuations at these two modes is close to zero (within the uncertainty of the phase calculation), but because the amplitudes are different, the resulting manifestation of these modes is a counter-swirling helix resulting from mode $m = 1$, as was seen at the $x/D=0$ station as well.

The strength of the helical shear layer instability is much higher at $x/D=0$, as can be seen in Figure 64, because the amplitude of mode $m=1$ is so much greater than that of any other mode number. At $x/D=1$, however, the strength of the shear layer vortex has decayed, and this is reflected in the similarity of the amplitudes of modes $m=-1$ and $m=1$. Additionally, theoretical analysis predict that the co-swirling mode, $m=-1$, is most unstable in swirling flow profiles of this type [75]. In this case, the response at $m=-1$ may be due to the natural instability of the jet, while the $m=1$ response of the jet stems from the acoustic forcing.

The downstream evolution of these mode strengths is shown in Figure 74.



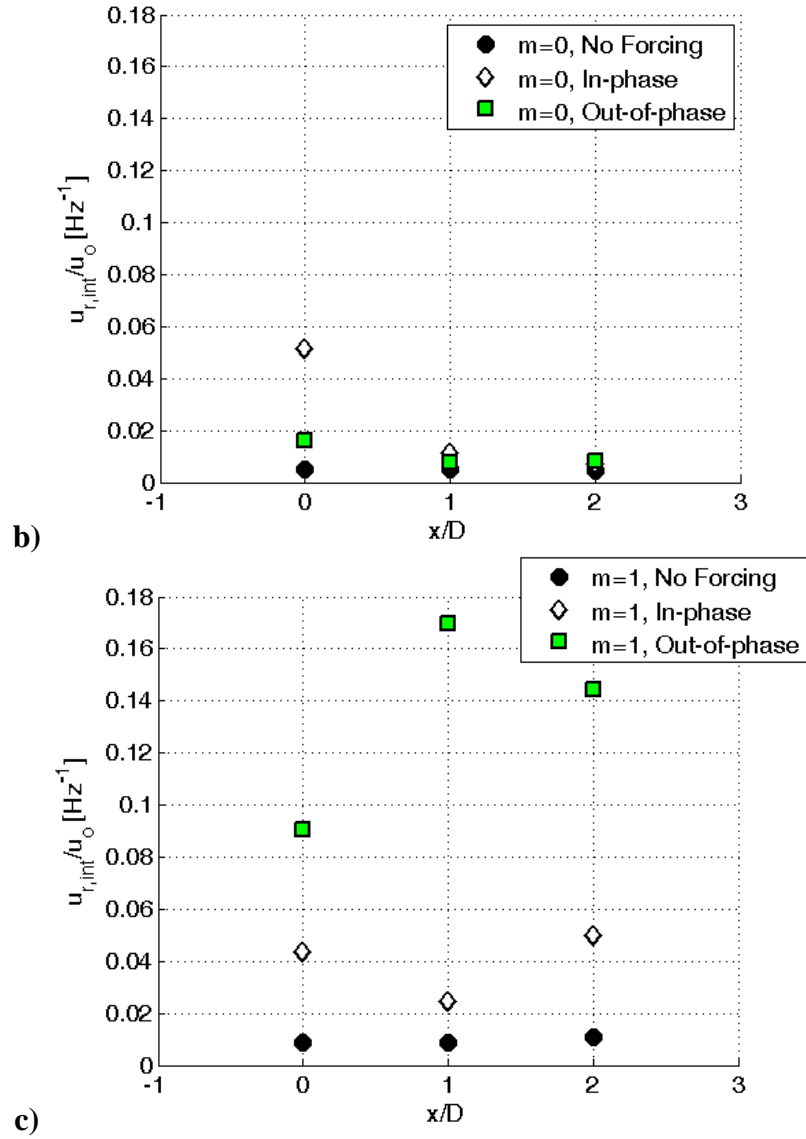


Figure 74. Amplitude of modes a) $m = -1$, b) $m = 0$, and c) $m = 1$ at the forcing frequency and integrated over $r/D=0-1$ for non-reacting flow in the $r-\theta$ plane for 400 Hz forcing at $u_o=10$ and $S=0.85$.

The downstream evolution of the three dominant modes at the forcing frequency can be seen in Figure 74. The trends that were qualitatively described in the $r-x$ plane in Figure 64 and Figure 65 can clearly be seen in the quantitative description of the motion using a spatial modal decomposition. In the in-phase forcing case, the symmetric $m = 0$

mode decays quickly downstream, as seen by the tilting of the vortex rings in the r - x plane. In the out-of-phase forcing case, both the $m = -1$ and $m = 1$ mode grow as a function of downstream distance, but combined their effect leads to a decay of amplitude of the helical mode after $x/D=1$. This is an important result that reflects the effect of the natural asymmetry of the swirling flow on the behavior of its hydrodynamically unstable structures in the presence of acoustic forcing.

This behavior is in contrast to the response of the low frequency motion, described in Chapter 4, to the various acoustic forcing conditions. Here, the response of the flow at the low frequency only, integrated from 0-200 Hz, is examined in order to capture the influence that acoustic forcing can have on the intrinsically occurring motions. As described with reference to Figure 39, the swirling jet has two main motions, a jet column deformation that is described by the $m = -2$ mode, and a pair of coherent structures described by the $m = -1$ mode. In this section, we use modal decomposition to see the effect of the symmetry of forcing. Again, we consider motions at a downstream distance of $x/D=1$, where the most vigorous recirculation zone motion is located.

First, the spectral content of several of these modes is shown in Figure 75. Here, peaks at 400 Hz are evident in both the out-of-phase and in-phase high amplitude forcing cases, although to a much lesser extent in the in-phase forcing condition. Modes $m = -2$, $m = -1$, and for the out-of-phase forcing case, $m = 1$, have significant low frequency content.

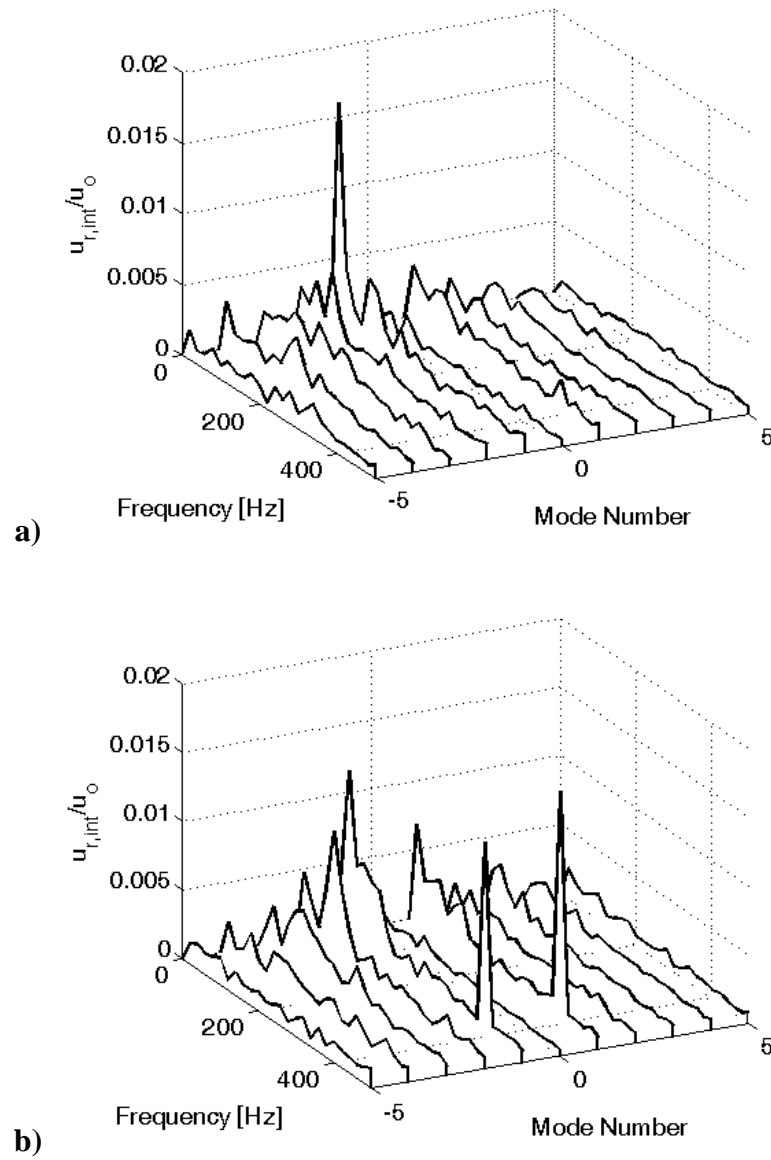


Figure 75. Spectra of several mode numbers integrated over radius and frequency in the $r-\theta$ plane at $x/D=1$, for a non-reacting, flow forced at 400 Hz a) in-phase and b) out-of-phase at $u_o=10$ m/s, $S=0.85$.

Figure 76 shows the response of the low frequency content to high amplitude acoustic forcing. Here, the in-phase and out-of-phase results are compared against the

unforced results; each mode coefficient is integrated between 0-200 Hz and radially between $r/D=0-1$.

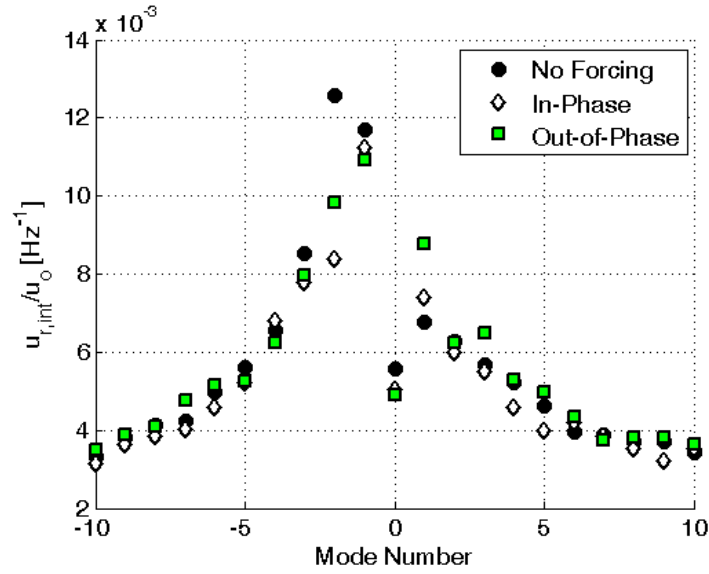


Figure 76. Distribution of mode amplitude at the low frequencies integrated over radii $r/D=0-1$ plotted as a function of mode number at $x/D=1$ for a non-reacting, flow forced with 400 Hz forcing at $u_o=10$ m/s, $S=0.85$.

Here again, it is evident that different forcing symmetries have different effects on the modal content of the velocity fluctuations. In both the in-phase and out-of-phase forcing cases, high amplitude forcing decreases the amplitude of the self-excited behavior at modes $m = -2$ and $m = -1$, but adds energy to the mode $m = 1$. The magnitude to which these effects take hold is dissimilar, particular in the variation in strength of mode $m = -2$.

One final comment on the response of the convectively unstable shear layers to acoustic forcing is the relative amplitude of the acoustic velocity fluctuations and the resulting vortical velocity fluctuations. The amplitude of this coupling, described by the $F_{L\omega}$ and $F_{T\omega}$ pathways outlined in Figure 6, has important implications for modeling and

the determination of which velocity-coupling pathways are necessary to include in a reduced order model. This type of decomposition, an acoustic/vortical decomposition, is also a useful way to categorize the disturbance types in this complex velocity disturbance field.

This data considers the unsteady disturbance field characteristics, as opposed to the total instantaneous/filtered field structure detailed earlier. There are fundamental differences between the appearance of the unsteady flow structures as visualized by their instantaneous and fluctuating values. For example, the location and characteristics of vortical structures can look fundamentally different between the two, and conclusions about topological flow features should probably only be drawn from the total, instantaneous or filtered field characteristics. That said, the unsteady flame response is closely linked to these fluctuating quantities. In this section, we look only at the fluctuating quantities, by subtracting the time-average behavior, to more carefully investigate the behavior of the different velocity disturbances in the flow field.

Surface plots of the amplitude of both the velocity and vorticity fluctuations show interesting results. Figure 77, Figure 78, and Figure 79 show the amplitude of the axial velocity, transverse velocity, and vorticity fluctuations at the forcing frequency, respectively, for both non-reacting and reacting flow.

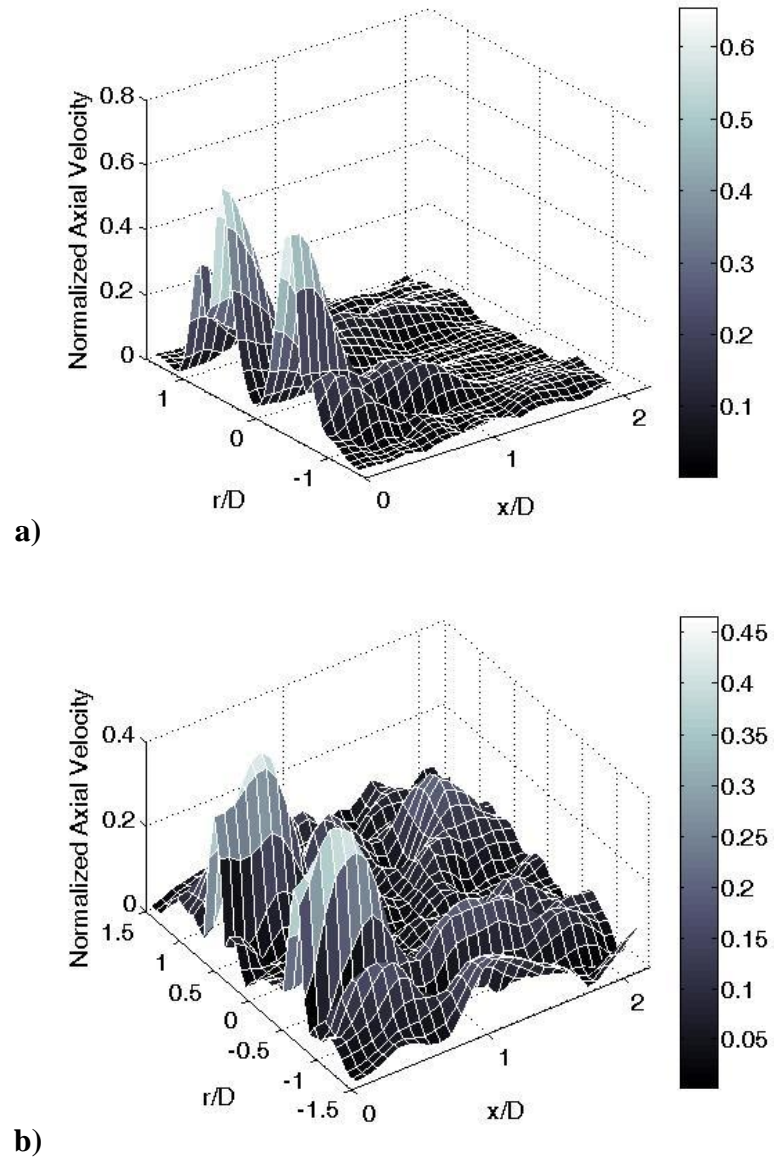


Figure 77. Normalized amplitude of axial velocity fluctuations for a) non-reacting and b) reacting flow at the forcing frequency at a bulk velocity of $u_o=10$ m/s and a forcing frequency of $f_o=400$ Hz out-of-phase.

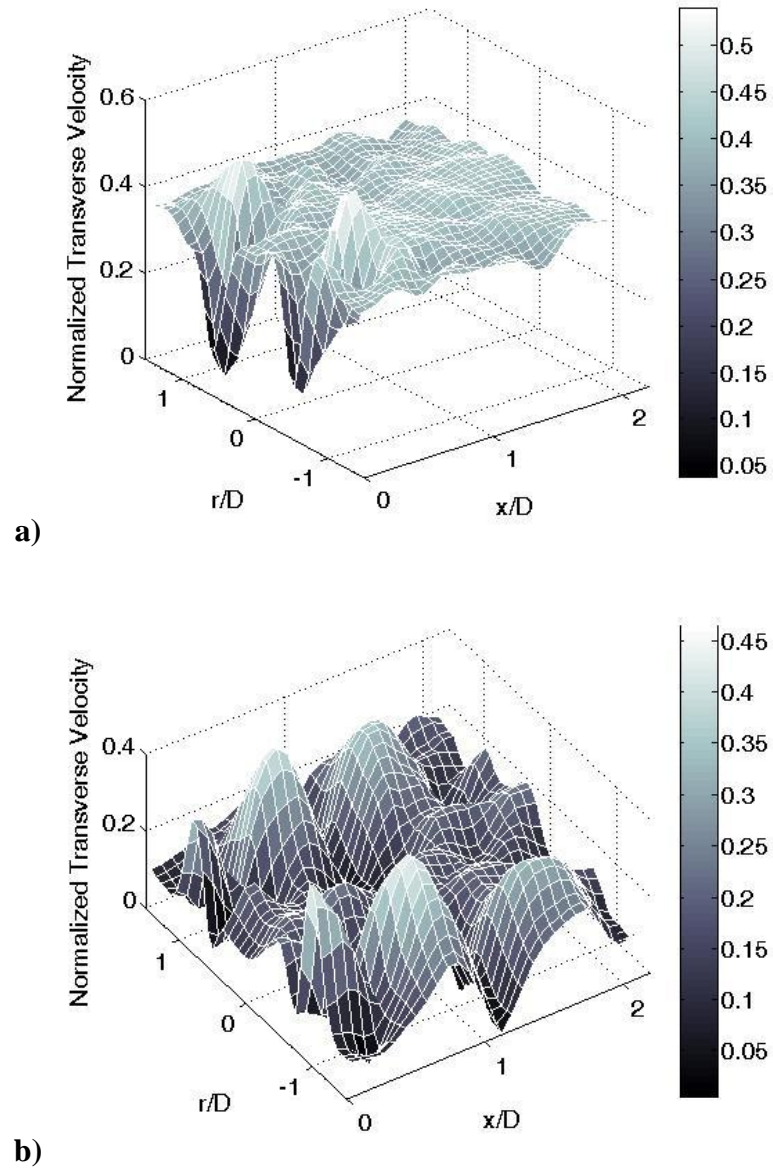


Figure 78. Normalized amplitude of transverse velocity fluctuations for a) non-reacting and b) reacting flow at the forcing frequency at a bulk velocity of $u_o=10$ m/s and a forcing frequency of $f_o=400$ Hz out-of-phase.

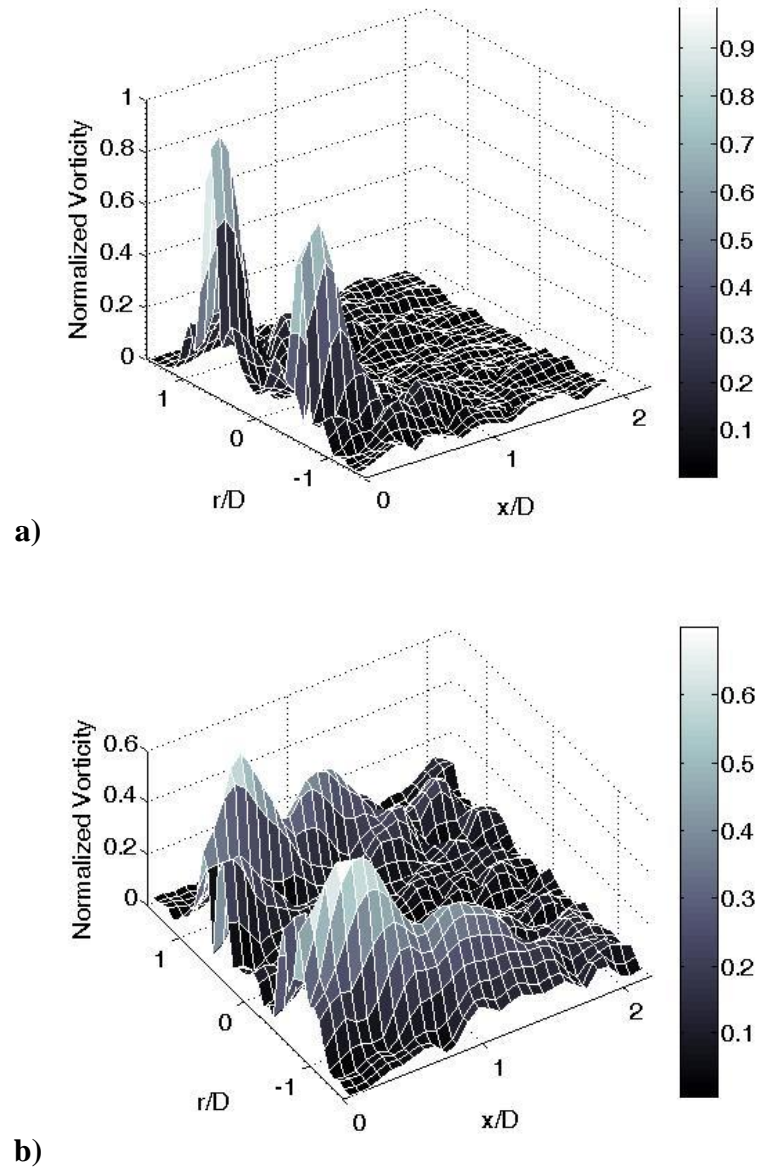


Figure 79. Normalized amplitude of vorticity fluctuations for a) non-reacting and b) reacting flow at the forcing frequency at a bulk velocity of $u_o=10$ m/s and a forcing frequency of $f_o=400$ Hz out-of-phase.

One of the most prominent features of these plots is the highly non-monotonic characteristics of the unsteady velocity field, suggesting cancellation phenomenon. For example, in Figure 78b, which shows the transverse velocity fluctuations at the forcing

frequency for a reacting case, the fluctuation amplitude peaks at approximately $x/D=0$, decreases to a minimum value at $x/D=0.3$, and then increases until a downstream distance of $x/D=0.6$ where it again peaks and decreases.

While both the axial and transverse velocity fluctuation fields show the interference phenomenon, there is another important factor that differentiates these two types of fluctuations. The transverse velocity fluctuation surface, shown in Figure 78, has a constant offset across the field. This offset is a result of the acoustic velocity fluctuations, which are of nearly constant amplitude across the field of view for the out-of-phase forcing case shown. Conversely, there is no offset of the axial velocity surfaces, indicating that there are no longitudinal acoustics in the flow field downstream of the immediate nozzle exit. Thus, longitudinal acoustics are important in the immediate vicinity of the nozzle, but these fluctuations do not contribute in any significant way farther into the combustor.

It is hypothesized that the non-monotonic spatial dependence of velocity amplitude is due to the simultaneous presence of both acoustic and vortical velocity disturbances. This can be shown by constructing a simple model of the unsteady transverse velocity field, with disturbances propagating at two different axial phase speeds. The input parameters for this model are the initial amplitude of each wave (A_1 and A_2), the decay rate (α) and convection speed ($u_{c,v}$) of the vortical disturbance, and the phase (ϕ) between the two disturbance types, see Equation (17).

$$\begin{aligned} u_{acoustic} &= A_1 e^{-i(\omega t + \phi)} \\ u_{vortical} &= A_2 e^{-i\omega(t - x/u_{c,v})} e^{-\alpha x} \end{aligned} \tag{17}$$

The convection velocity of the vortical wave was estimated from the mean of the velocities calculated from Equation (17). The decay rate was then calculated by fitting an exponential to the decay of time-average vorticity as a function of downstream distance, the results of which can be seen in Figure 80. This was done for both the non-reacting and the reacting case.

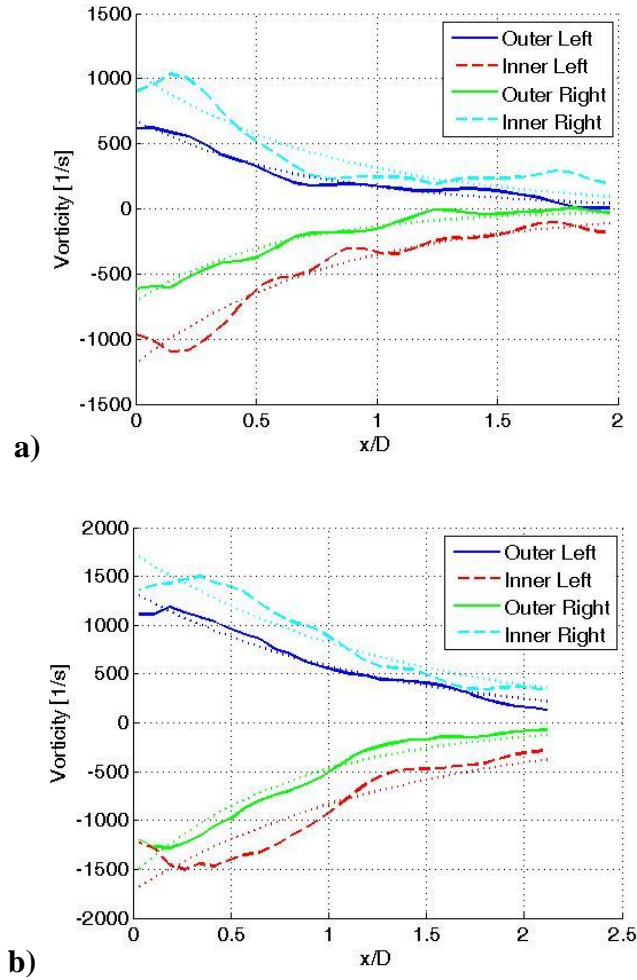


Figure 80. Time-average vorticity in shear layers for the a) non-reacting and b) reacting cases at a bulk velocity of $u_o=10$ m/s and a forcing frequency of $f_o=400$ Hz

out-of-phase. Dotted lines indicate exponential curve fits to calculate decay rates with downstream distance.

The parameters for the acoustic wave were less straightforward to extract from experimental data and were used as fit parameters to match the data. The parameters used in the model for both the non-reacting and reacting cases are shown in Table 4

Table 4. Two-wave model conditions for non-reacting and reacting cases at 400 Hz out-of-phase acoustic forcing and 10 m/s bulk flow velocity.

	Non-reacting	Reacting
A_1	0.3	0.25
ϕ	$\pi/6$	$\pi/4$
A_2	0.3	0.25
α [1/m]	43	27
$u_{c,v}$ [m/s]	13	10

The results of both the data and the model in the non-reacting and reacting cases are as shown in Figure 81 through Figure 83.

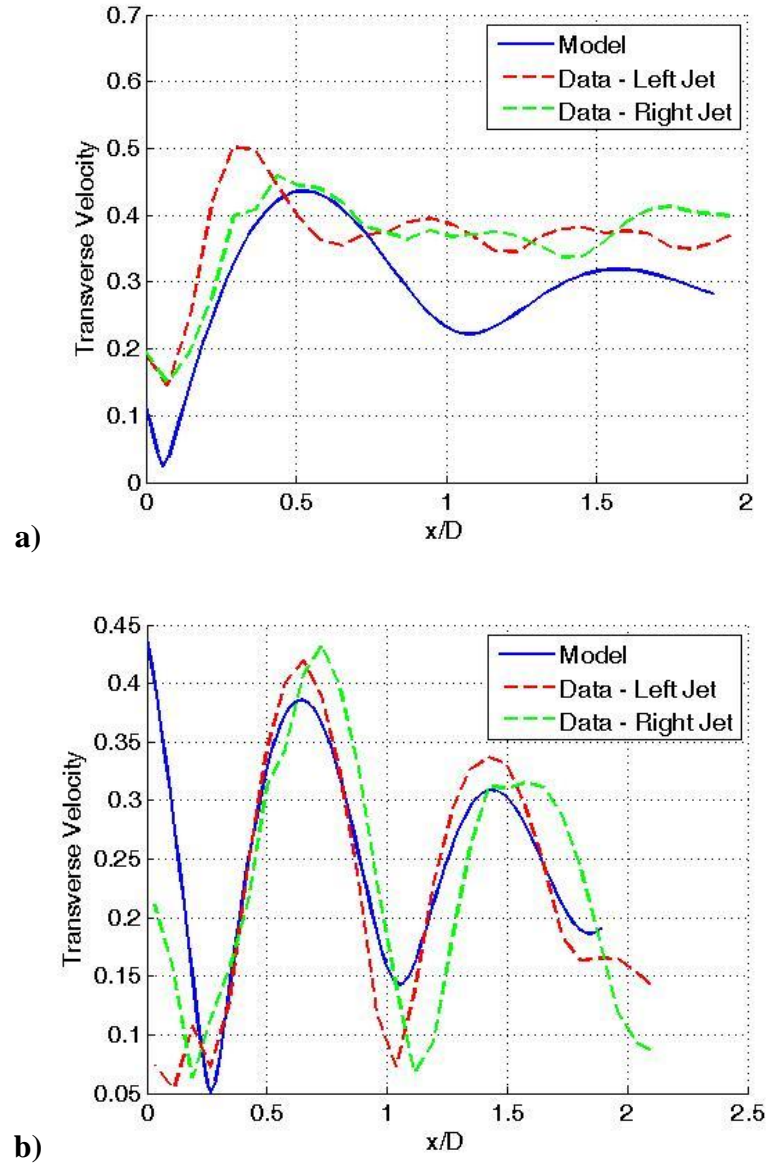


Figure 81. Comparison of transverse velocity fluctuation amplitude in left and right jet of the a) non-reacting and b) reacting data and the two-wave interaction model.

The bulk velocity was $u_o=10$ m/s and the forcing frequency was $f_o=400$ Hz out-of-phase.

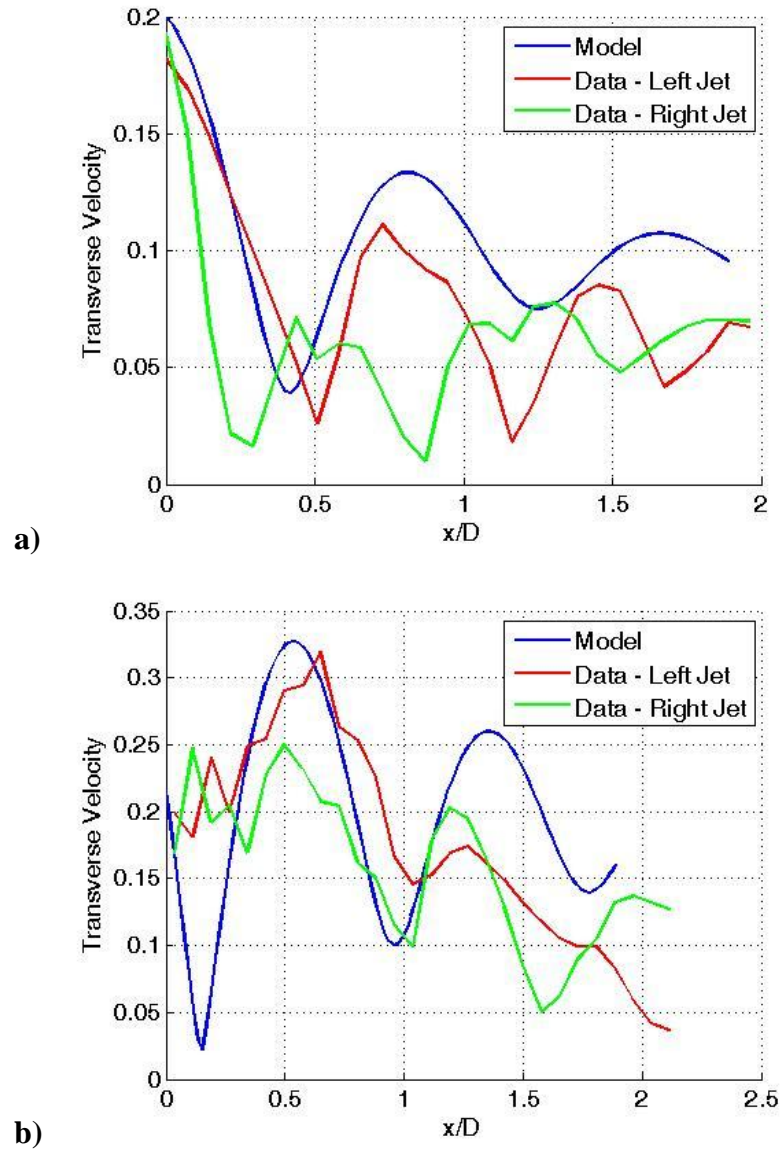


Figure 82. Comparison of transverse velocity fluctuation amplitude in left and right jet of the a) non-reacting and b) reacting data and the two-wave interaction model. The bulk velocity was $u_o=10$ m/s and the forcing frequency was $f_o=400$ Hz in-phase.

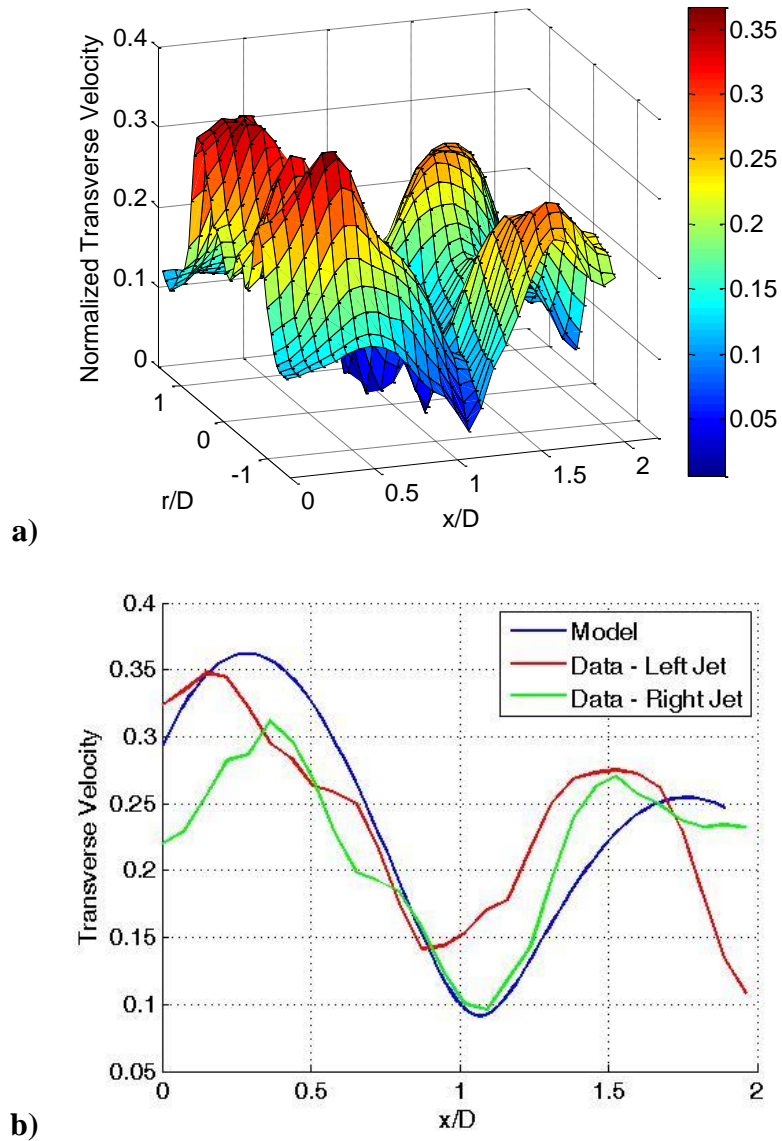


Figure 83. Comparison of transverse velocity fluctuation amplitude in left and right jet of the non-reacting data and the two-wave interaction model. The bulk velocity was $u_o=40$ m/s, non-reacting flow and the forcing frequency was $f_o=400$ Hz in-phase.

Here, a) shows the amplitude of transverse fluctuations over the entire flow field, while b) shows the cuts at the jet centers as above.

As can be seen from Figure 81 through Figure 83, the results of the data and the model align reasonably well for a variety of forcing and flow conditions. A critical

feature of these graphs is the peak spacing in the interference pattern, which is only a function of the difference in acoustic and vortical phase velocities. This peak spacing is captured quite well in the model, which is significant since the fitted parameters did not impact this result.

An important implication of this model is that the amplitudes of the acoustic and vortical wave are essentially the same. For example, both the acoustic and vortical fluctuations in the reacting case, shown in Figure 81b, are 25% of the bulk flow velocity. This result has important implications on flame response modeling, as models often assume that it is the vortical disturbances that dominate the flame response [160]. These results show that the acoustic and vortical disturbances have comparable magnitudes. This result reinforces the complexity of disturbance field and while the mechanisms do have causal relationships, as shown in Figure 6, they co-exist and combine to create a complex disturbance field.

These results also speak to the amplitude and phase of $F_{T\omega}$, the transfer function that describes the relationship between the transverse acoustic motion and the vortex rollup at the nozzle, as shown in Figure 6. The ratio of the amplitudes, A_1 and A_2 , gives the magnitude of the transfer function at this particular forcing frequency, while the phase between the two disturbances, Φ , is the phase of the transfer function at the forcing frequency. Note that this results suggests then, that $F_{T\omega} \sim 1$.

Response of the flame to shear layer motion

As discussed in the Introduction, the motivation for this comprehensive study of the vortical response of the flow was to understand the mechanisms by which flame area

fluctuations are created. This wrinkling can be measured in several ways, including Mie scattering from PIV images, as seen in Figure 54, planar laser induced fluorescence (PLIF), as seen in Figure 9, and high-speed imaging of flame luminescence, which was used extensively in this study as a qualitative method of describing flame response. For reference, a series of images from high-speed PLIF is shown in Figure 84, which shows a complicated wrinkling of the flame that stems from both coherent as well as turbulent motions. In this case, a helical shear layer response created a helical wrinkle on the flame that can be seen as a series of staggered wrinkles on this cut of the flame surface, which is located at the line between light and dark in this type of image.

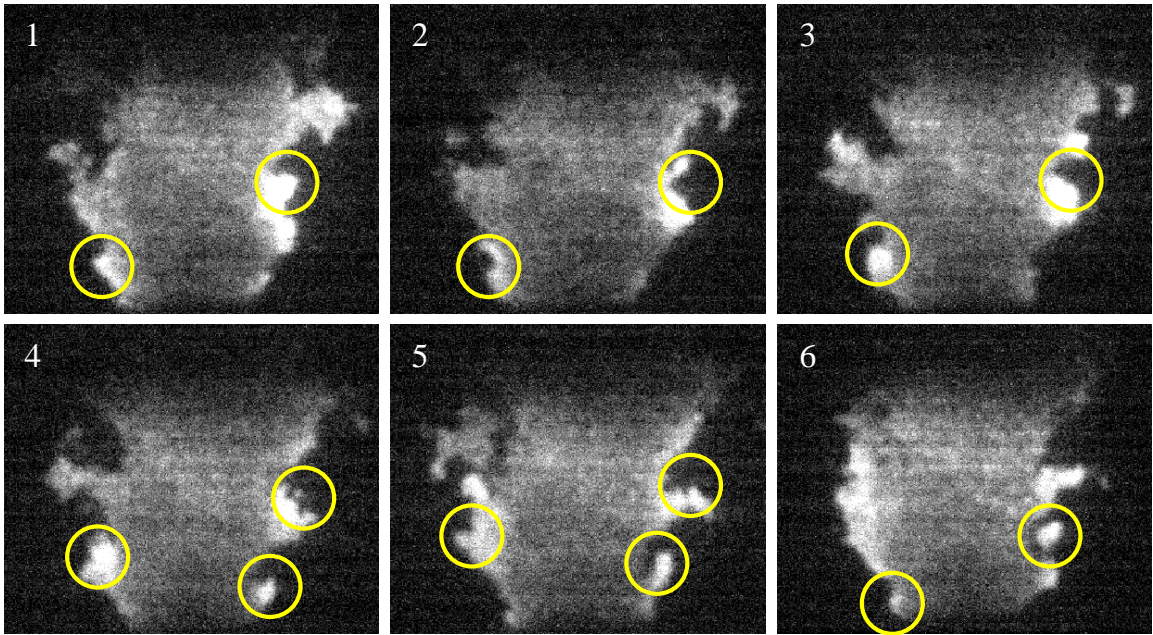
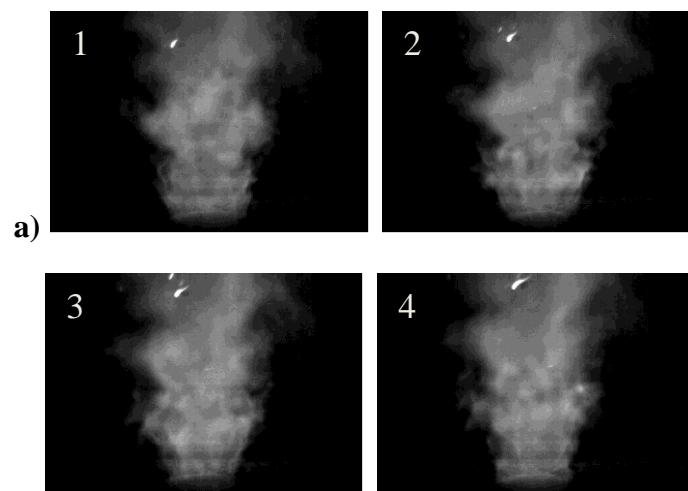


Figure 84. Time series of OH PLIF images showing centerbody stabilized swirl flame forced at 400 Hz out-of-phase, $u_o=10$ m/s, $S=0.5$, $\phi=0.9$. Yellow circles indicate locations of flame wrinkling due to vortex rollup in a helical pattern.

As will be discussed in the suggestions for future work in Chapter 6, simultaneous measurement of the velocity and flame edge will help elucidate cause and effect

relationships between the velocity field and resulting flame response. In this study, evidence of flame wrinkling, and in particular the effect of forcing symmetry, was investigated using high-speed flame luminescence imaging. Here, the difference in the vortical response of the flow field between symmetric (in-phase) and asymmetric (out-of-phase) forcing has been shown to have a significant effect on the character of the flame response. This can be seen in flame luminescence imaging, examples of which are shown in Figure 85.



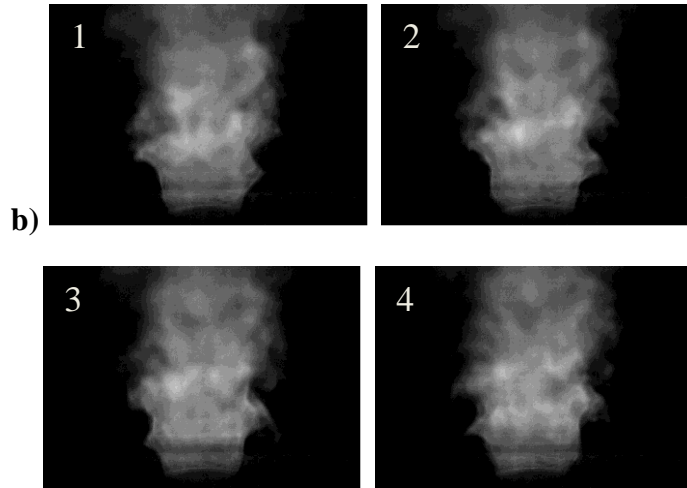


Figure 85. Examples of flame response, via luminescence imaging, for a) in-phase (symmetric) and b) out-of-phase (asymmetric) forcing conditions for a flow velocity of 10 m/s, swirl number of 0.5, and equivalence ratio of 0.9. Images are 0.6 ms apart in each filmstrip.

In these images, it is evident that the flame wrinkling changes with acoustic field symmetry. For asymmetric forcing, an asymmetric, helical pattern exists on the flame, while in the symmetric forcing case, a symmetric ring vortex creates axisymmetric wrinkles on the flame surface, at least near the flame base. The differences in flow response that create this flame response effect are the motivating factors for this work.

Each of these results – smoke visualization, high-speed PIV, high-speed PLIF, and high-speed flame luminescence imaging – have shown the importance of the excitation of the convectively unstable shear layer by transverse acoustic forcing. Additionally, the symmetry of the acoustic field plays a large role in the hydrodynamic response of the flow. A symmetric forcing condition results in an initially symmetric flow response, while asymmetric forcing results in asymmetric flow response; these differences in flow response result in similarly phased flame wrinkling response.

However, the natural asymmetry of the swirling flow influences the downstream propagation and symmetry of these shear layer structures. The once symmetric response of the shear layer due to in-phase forcing becomes asymmetric as the rings tilt due to the action of swirl.

CHAPTER 6

CONCLUSIONS AND RECOMMENDATIONS

In this chapter, the overall contributions of the work presented in this thesis are outlined. Here, the results of this study are placed in context of the overall field of combustion instability research and the applications of this work towards improvement of low emissions combustor operation and design. Additionally, recommendations for further work are put forward for future consideration.

Summary of contributions

This work has provided two significant contributions to the field of combustion instability research. In addition, it has provided a large archival data set that should be used for future analysis and comparison with modeling efforts. This section will highlight the two fundamental contributions; Appendix A contains a catalog of data obtained over the course of this study as well as examples of each data set.

Formulation of velocity-coupled flame response description

The first major contribution of this work is the formulation of a velocity-coupled flame response description for flames undergoing transverse instability. The velocity coupled pathway description is shown again in Figure 86.

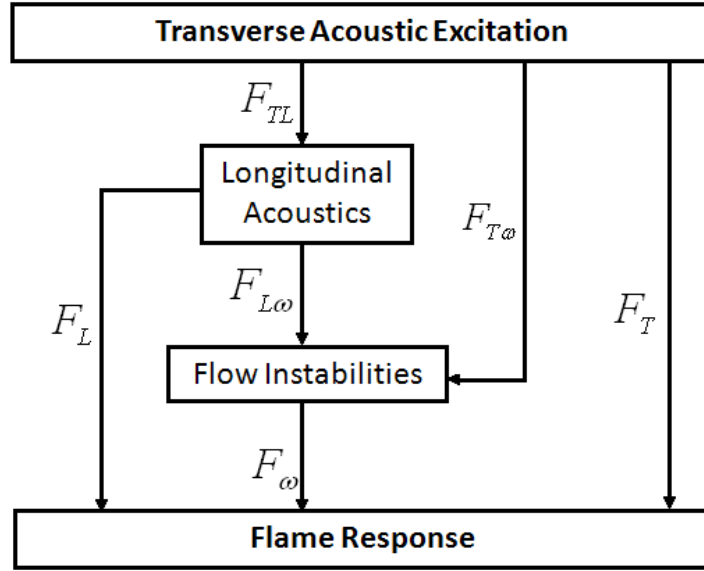


Figure 86. Velocity disturbance mechanisms in a transversely forced flame.

As discussed in the Introduction, the response of flames to transverse excitation is fundamentally different than that to longitudinal excitation. Several issues highlight this distinction. First, the variation in acoustic mode structure between nozzles has a significant impact on the way transverse instabilities are understood and modeled for full engine configurations. As described with reference to Figure 3, the transverse acoustic mode shape for both can and annular combustor systems results in a variable excitation amplitude and symmetry across the nozzles. It is for this reason that a variety of acoustic frequencies, amplitudes, and symmetries were considered in this study. They ranged across frequencies of $f = 400$ to 1800 Hz, transverse acoustic forcing amplitudes of $v'/u_o = 0.01$ to 0.5 , and both velocity node and pressure node standing wave forcing conditions.

Next, the natural asymmetry of the acoustic field produces significantly different flow and flame response than in the symmetric, longitudinally forced case. This fact was

particularly pertinent in the shear layer response of the flow and the resulting flame sheet motion imposed by these structures. It was shown that asymmetric forcing, out-of-phase forcing with a velocity anti-node along the centerline of the flow, resulted in asymmetric response of the swirling annular jet. In this way, helical vortices were shed in both the inner and outer shear layers, and helical flame wrinkling was observed. Conversely, it was also shown that symmetric forcing, in-phase forcing with a pressure anti-node along the centerline of the flow, resulted in initially symmetric response of the shear layers. Ring vortices were shed at the inner and outer edge of the nozzle annulus and corresponding flame wrinkles were observed. As these structures travel downstream, however, the symmetry is lost due to the naturally asymmetric nature of the flow; this is manifested in two ways. First, the swirling component of the flow adds a natural asymmetry and causes the vortex rings to tilt. Additionally, the symmetric $m = 0$ mode is stable for swirling flows and as such, excitation of this mode does not result in appreciable response downstream of the dump plane.

Third, transverse forcing produces more pathways for flame excitation than its longitudinal counterpart, particularly in the coupling between the transverse acoustic field in the combustor and the longitudinal acoustic field in the nozzle. While the direct transverse acoustic excitation of the flame is often negligible, the occurrence of coupling between the transverse and longitudinal acoustic modes can lead to heightened flame response. The transverse acoustic mode can couple with the longitudinal mode in the nozzle near a nozzle natural frequency. This coupling, however, is dependent on the relative geometries and resultant natural modes of the combustor and swirler nozzle, as well as the nozzle acoustic impedance, which is a function of nozzle blockage ratio, flow

velocity, and gas temperature. It is for this reason that the response of flames to transverse excitation is inextricably linked to the geometry of the system. This result is extremely important going forward in the application of the current results; results such as flame response amplitude and phase cannot necessarily be translated from one combustor geometry to another. This result was the first experimental validation of this phenomenon for gas turbine architectures, following the LES work of Staffelbach *et al.* [25].

Finally, the relative contribution of these various pathways can change dramatically as a function of acoustic frequency, amplitude, symmetry, and flow structure. Foundations of quantifying these relative contributions were made in the current study. For example, measurements of F_{TL} , the transverse to longitudinal transfer function, were made to show the relative contribution of the transverse versus longitudinal acoustic pathways in the velocity-coupled flame response mechanism. Additionally, trends of when this velocity transfer function would have amplitudes significantly above or below unity were discussed for further application to various combustor geometries. Another example was the decomposition of the flow field into the acoustic and vortical components, resulting in approximations for the velocity transfer functions $F_{T\omega}$ and $F_{L\omega}$, the acoustic to vortical velocity transfer functions describing relative amplitudes and phases of acoustic and vortical velocity fluctuations in the overall disturbance field. Here, it was shown that the acoustic and vortical contributions from the shear layers have similar amplitudes and must be considered in a description of the overall velocity disturbance field.

Description of response of swirling flow to transverse forcing based on flow stability

The second contribution of this work is a description of the response of a swirling flow, both reacting and non-reacting, to transverse acoustic fields by using hydrodynamic stability concepts as a basis for understanding the response of the flow. This is particularly important in the case of swirling flows because there are several flow structures with different stability characteristics. The swirling jet itself is absolutely unstable, which results in vortex breakdown and a large recirculation zone along the centerline of the flow. This structure is the largest feature of the flow and defines the overall flow geometry and resultant flame shape in a reacting flow field. There are also two shear layers, stemming from both the inner and outer edge of the annular jet nozzle, that are convectively unstable.

Absolutely unstable flows act as self-excited oscillators, displaying intrinsic oscillations even in the face of low amplitude acoustic forcing. Only at high amplitudes of acoustic forcing can the dynamics and overall structure of the manifestation of the absolute instability be altered. This was measured in this study by investigating both the time-average and dynamical response of the vortex breakdown bubble to transverse acoustic forcing of varying amplitudes. At low amplitudes, the overall structure of the bubble did not change and the dynamical behavior of the vortex core was only slightly altered. At high amplitudes of excitation, though, significant changes of the both the time-average and dynamical behavior of the flow was measured. The time-average characteristics were shown to have two types of response to high amplitude acoustics; the appearance of either behavior was dependent on the frequency, symmetry, and amplitude of the acoustic forcing. While a gradual change in flame angle was measured at several

frequencies with increasing amplitude, a bifurcation-type change in the vortex breakdown bubble structure was measured in the non-reacting flow field at certain forcing conditions. This can have a significant implication for the flame response, as the flame responds to velocity fluctuations normal to its surface. As the time-average shape of the flame changes, the amplitude of the normal component of the velocity field can also change.

Alternatively, the convectively unstable structures, in particular the shear layers, act as disturbance amplifiers and respond to even low levels of acoustic forcing for both non-reacting and reacting flow. The symmetry of the response of these structures is particularly interesting and pertinent to the case of transverse instabilities in annular gas turbine combustor geometries. Here, the flow response between symmetric and asymmetric transverse acoustic fields manifested as shedding of ring and helical vortices, respectively. Despite that, the natural asymmetry of the flow plays a role in the downstream evolution of these structures, resulting in a baseline asymmetric response that cannot be altered even at high amplitudes of symmetric acoustic forcing.

In the discussion of the shear layer dynamics, both non-reacting and reacting data were used to describe these dynamics with some equivalence. While the presence of a flame can certainly change the shape and dynamics of the vortex breakdown bubble, the overall dynamics of the shear layers remain unchanged in the presence of the flame. This does not mean that the results are quantitatively the same between a reacting and non-reacting case, but instead that the fundamental coupling mechanisms and behavior of acoustically driven shear layers remain the same between these two cases.

The contribution of this portion of the work is not only the insight gained through these studies, but also the establishment of a methodology that first considers the hydrodynamic stability characteristics of different flow structures within a flow field when investigating its response to acoustic forcing. Going forward, this type of methodology will be quite important for understanding more complex flow fields in real combustor architectures.

Recommendations for future work

Several recommendations for future work naturally follow the results of the current study. These are detailed in this section.

First, a more extensive characterization of the flow field, particularly in the r - θ plane, is required to complete the archival data set produced in this work. Focus should be placed on comparison of the response of the flow at various downstream locations for longitudinal versus transverse forcing to measure the excitation of different spatial modes with a variety of forcing configurations. Also, both velocity and flame data should be collected for the reacting case in this plane of view. High-speed PLIF can be used to measure flame response at various downstream distances, although simple chemiluminescence imaging in the r - θ plane would help determine the response of the flame to various acoustic forcing conditions, as has been done by Hauser *et al.* [28].

Additionally, simultaneous measurements of the velocity field and flame could help establish a causal link between velocity field fluctuations and flame motion. Both simultaneous PIV and PLIF, and PIV and chemiluminescence will help to further our understanding of the velocity-coupled response of flames to transverse acoustic fields.

Additionally, simultaneous PIV and PLIF can help measure the influence of the flame on the flow field. In this way, changes in vortex breakdown structure due to exothermicity, or variation in shear layer vortex strength with flame location can be measured and quantified with these simultaneous measurements. These results will help the development of better models for reacting swirling flows.

Next, in addition to flame imaging as described above, more thorough measurements of flame transfer functions should be done to both complete the current data set for a variety of forcing amplitudes and build a more comprehensive database for reduced order model development and validation. A more thorough investigation of amplitude effects on flame transfer functions could be used to compare these results with similar measurements made on longitudinally forced flames [50].

Finally, the investigation of multiple flames in the current combustor geometry should be undertaken to further mimic the flow and flame boundary conditions in an annular gas turbine combustor. As described in Chapter 2, great care was taken in designing the current experiment so that it would faithfully mimic the acoustic and flow boundary conditions in an annular combustor; the transverse acoustic mode shape and high aspect ratio combustor geometry help to meet this goal. The natural next step in this research is to investigate the flow and flame response with multiple flames. The current combustor geometry supports up to five nozzles, allowing for the investigation of five flames simultaneously. The additional understand of the physics introduced by flame-flame interactions, particularly in a transversely forced situation where acoustic particle velocity forces the flow side to side, would help in the development of better frameworks of understanding and reduced order models for these instabilities. Extensive velocity

measurements would also help build an understanding of the effect that adjacent swirling jets have on flow structure, an effect that has been insufficiently measured by other authors [161]. Additionally, these data could be very useful in validating computation models of full combustor flow simulations.

Overall, the goal of this study was to develop a wealth of understanding of the response of swirling flows and flames to transverse acoustic excitation for application to gas turbine combustor geometries. It is the wish of the author that this work not only increases our academic understanding, but also be considered in the design and operation of low emissions gas turbine engines in the future.

APPENDIX A

TECHNICAL DRAWINGS OF COMBUSTOR

Details of combustor

This section shows several technical drawings pertinent to the boundary conditions of the combustor geometry. First, Figure 87 shows an isoview of the combustor without the speaker tubes. Here, the exit boundary condition as well as the dump plane are evident. The exit boundary has five 2” holes where the center one has been covered by a window. This window was present for all data described in this study and was required to shield the PIV sheet optic located directly above from hot products and seeding particles.

Details of the exit and entry boundary conditions are shown in Figure 88, Figure 89, and Figure 90. Below, further details of the experimental systems are outlined.

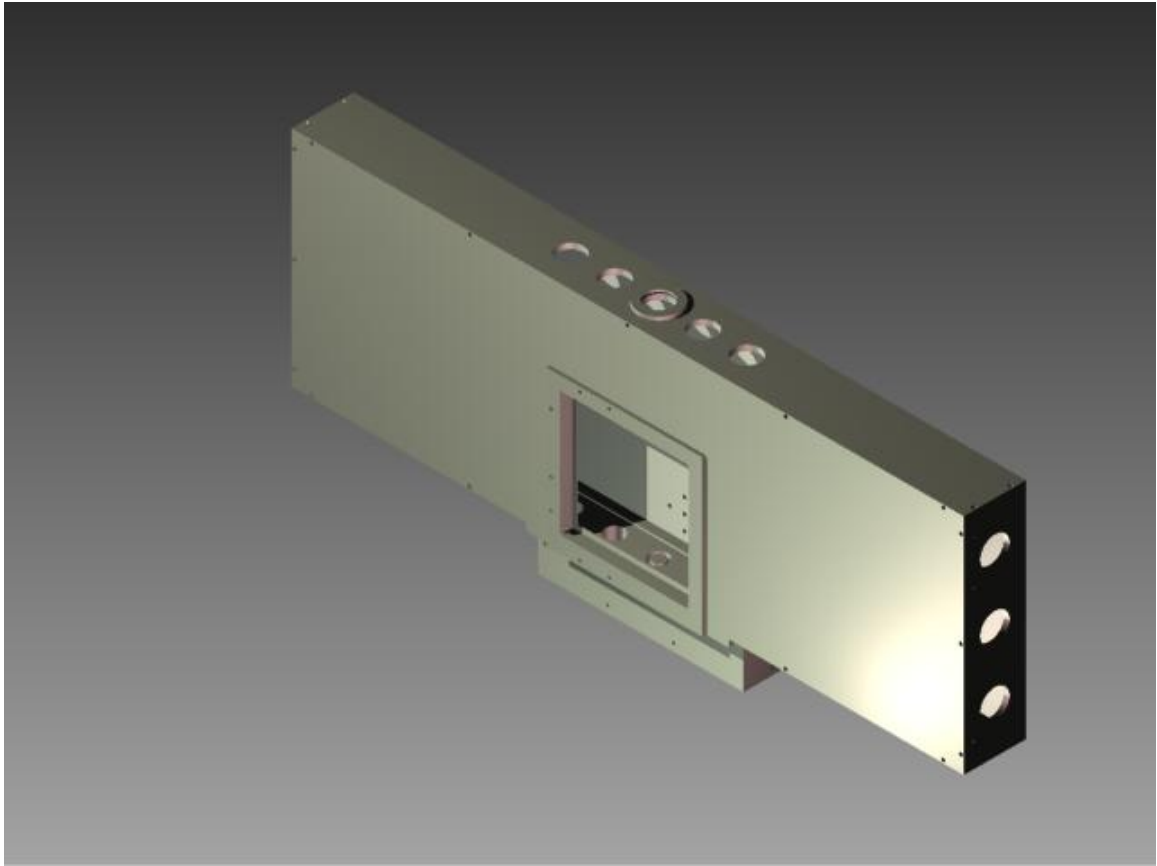


Figure 87. Isovview of combustor

Note: The vertically aligned holes are microphone ports.

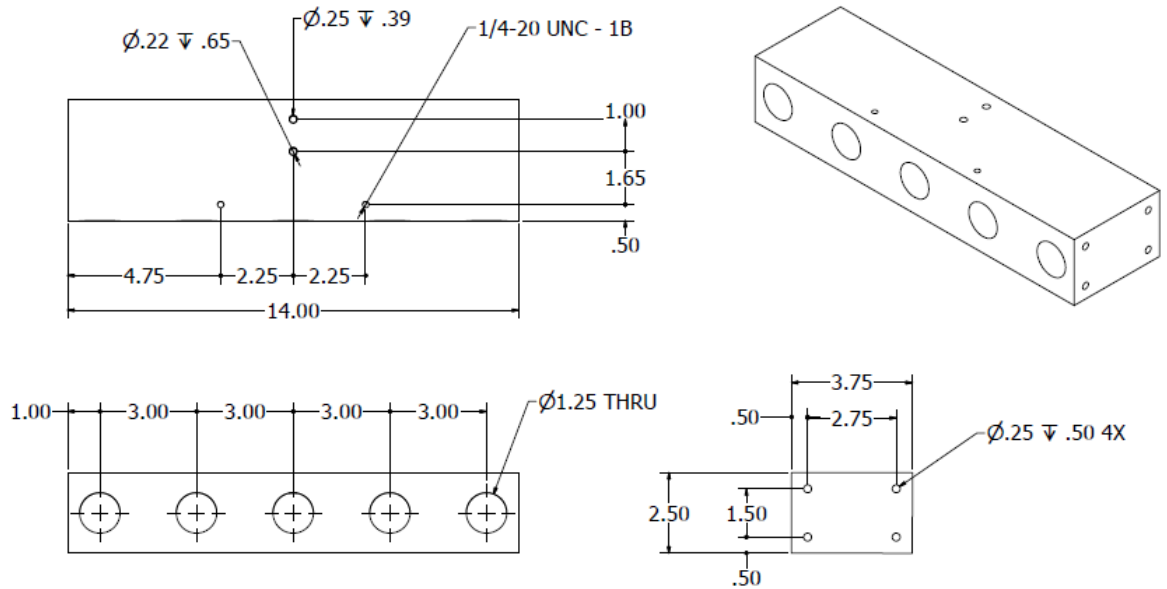


Figure 88. Details of the swirler box at the dump plane.

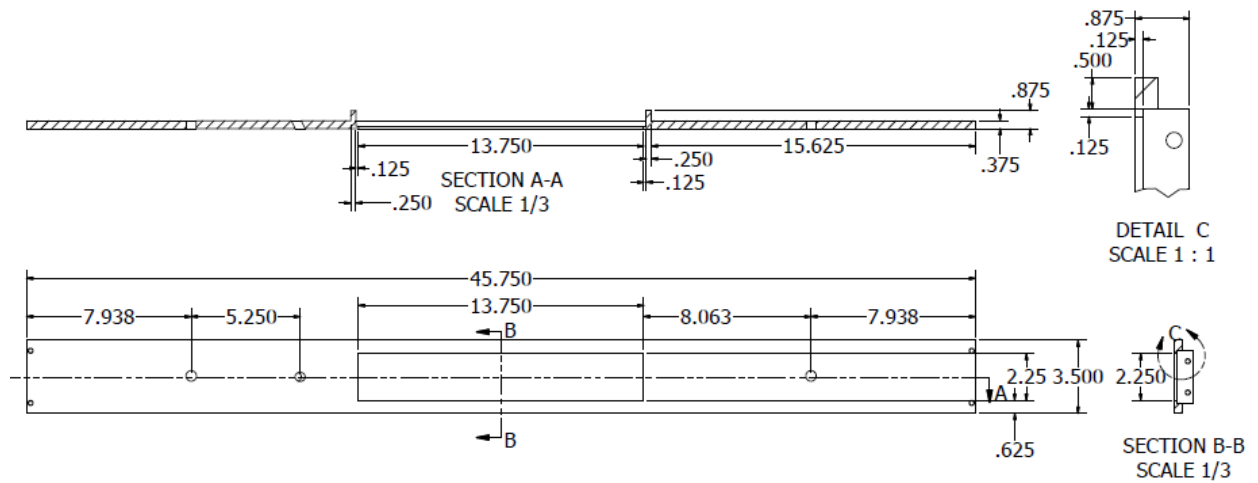


Figure 89. Details of the dump plane around the swirler box. Includes two unused air ports (left- and right-most holes) as well as port for hydrogen torch igniter. Swirler box mates with this part in the notched section detailed in the upper right of the figure.

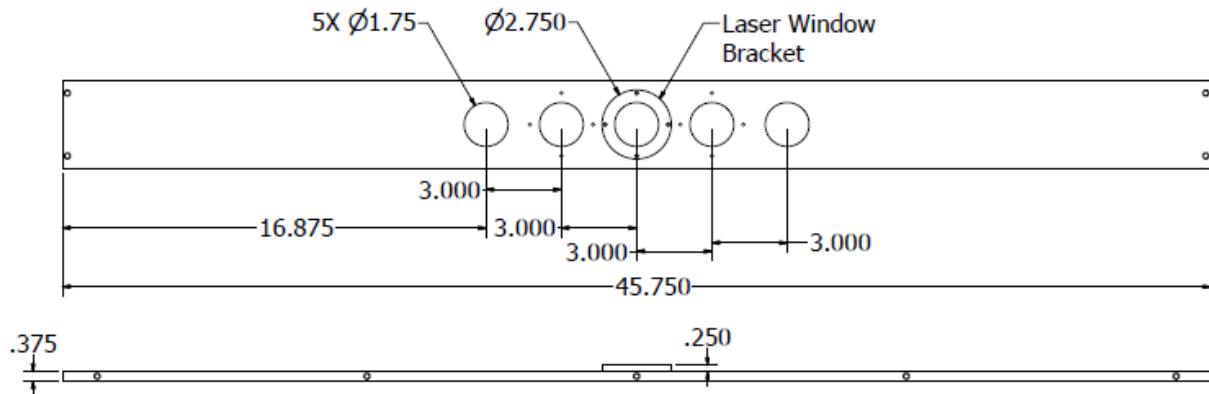


Figure 90. Details of the exit plane, including location of laser window and laser window bracket.

Details of acoustic driving system

Speaker tubes

- 6 tubes
- Length of 1 meter
- Constructed of 2" carbon steel pipe

Sound system

- Function generator
 - Tectronix AFG 3022
- Amplifiers
 - AE Techron LVC 608 linear amp, dual channel
- Speakers
 - Galls SK144
 - 100 W driver (120 dB of sound at 10')

Details of flow system

Flow path

- Air line – 125 psig supply
 - 2” carbon steel, Schedule 40 pipe
 - Regulator
 - Set pressure: 20 psig
 - Max pressure: 200 psig
 - Gate valve
 - Orifice plate
 - Beta ratio – 0.27552
 - Orifice bore diameter – 0.5695”
 - Differential pressure transducers
 - Omega PX771A
 - 1-5 Vdc output
 - Range: 0 – 300 inH₂O
 - Static pressure transducer
 - Dwyer Series 626
 - 0-5 Vdc output
 - Range: 0-30 psig
- Gas line – 25 psig supply
 - 1.5” carbon steel, Schedule 40 pipe
 - ASCO Solenoid valve
 - ½” Swagelok needle valve
 - Orifice plate
 - Beta ratio – 0.23671
 - Orifice bore diameter – 0.1472”
 - Differential pressure transducer
 - Omega PX771A
 - 1-5 Vdc output

- Range: 0 – 300 inH₂O
- Static pressure transducer
 - Dwyer Series 626
 - 0-5 Vdc output
 - Range: 0-30 psig

APPENDIX B

TECHNICAL DRAWINGS OF SWIRLER

Two swirlers were used during these series of tests. The first has a turning angle of 45° and results in a geometric swirl number of 0.85, as is shown in Figure 91. The second has a turning angle of 30° and results in a geometric swirl number of 0.5, as shown in Figure 92.

Note: The swirler blades are turned at a 45° degree angle.

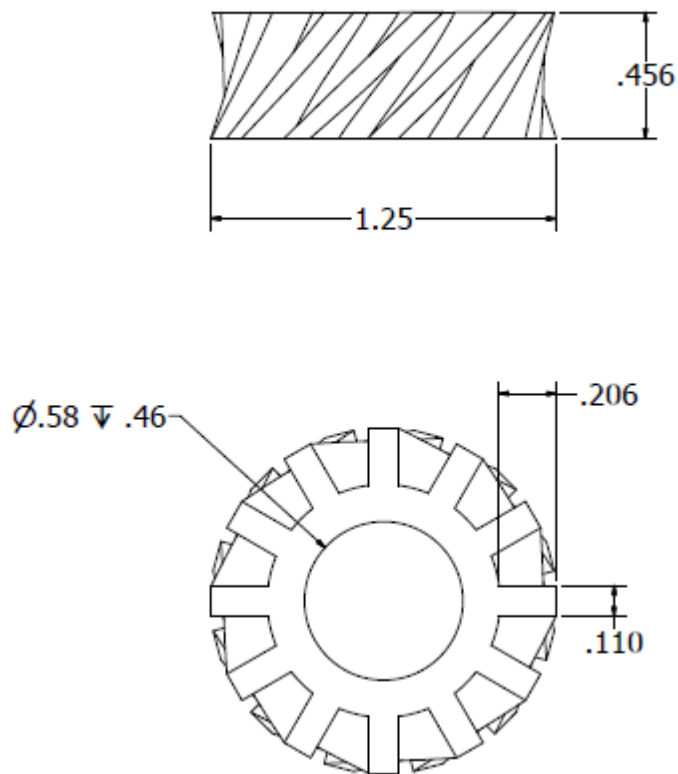


Figure 91. Drawing of 45° swirler.

Note: The swirler blades are turned at a 30 degree angle.

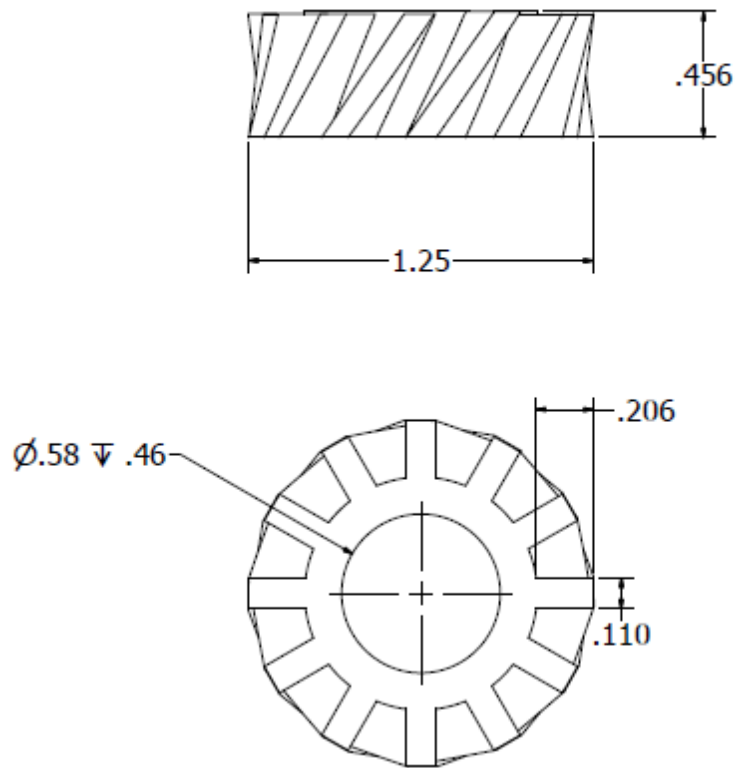


Figure 92. Drawing of 30° swirler.

APPENDIX C

DETAILS OF SMOKE SYSTEM

The smoke was created by heating olive oil in a carbon steel smoker, shown in Figure 93. Entering air was controlled with a gate valve for optimal smoke rate. The oil was heated with a propane torch placed on the side of the smoker as indicated.

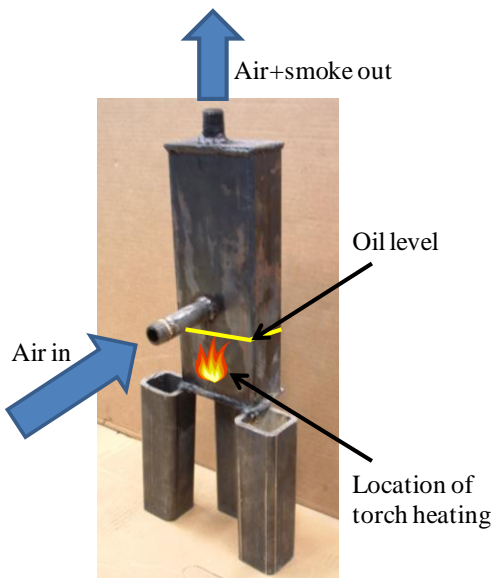


Figure 93. Olive oil smoke production device with air-in port, flow exit port, and indications for the location of torch heating and optimal oil level.

This configuration produced very high rates of smoke production in the inner shear layer, but very little in the outer. For inner shear layer smoke delivery, smoke was piped through a hollow centerbody with 20 1 mm holes drilled obliquely from the centerbody edge into the smoke reservoir in the center. This piece is shown in Figure 94.

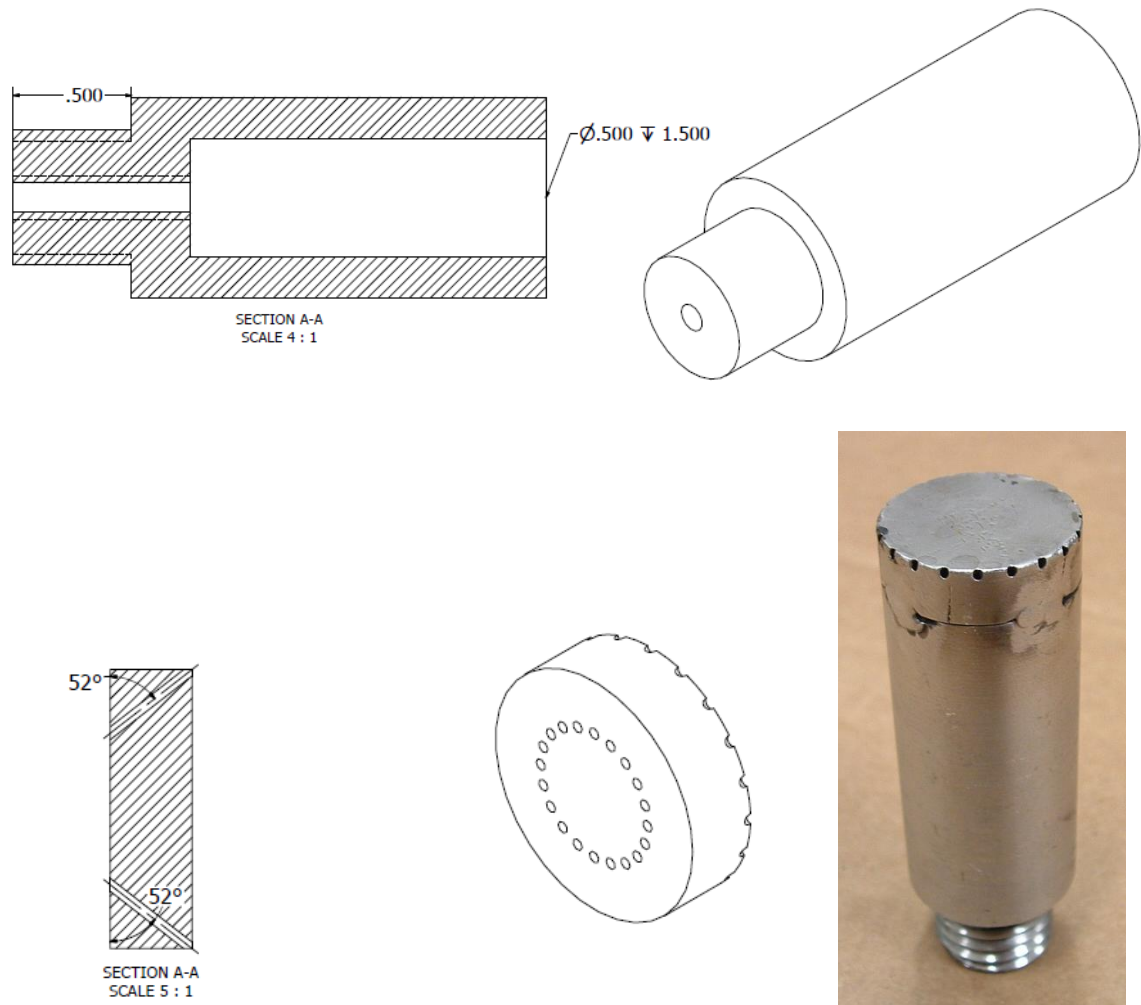


Figure 94. Specifications on the inner shear layer smoke delivery system.

A similar reservoir system was used for the outer shear layer. A PVC dump plane was constructed with an elliptical smoke reservoir on all sides of the swirler cavity. A top plate with holes drilled obliquely from the reservoir to the outer annulus edge was attached to the top and allowed for delivery of the smoke. The plenum specifications are shown in Figure 95.

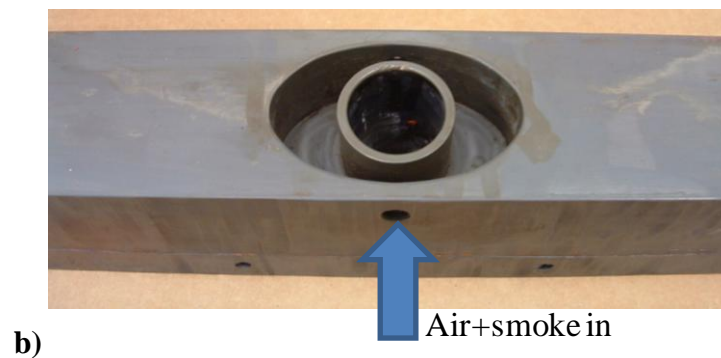
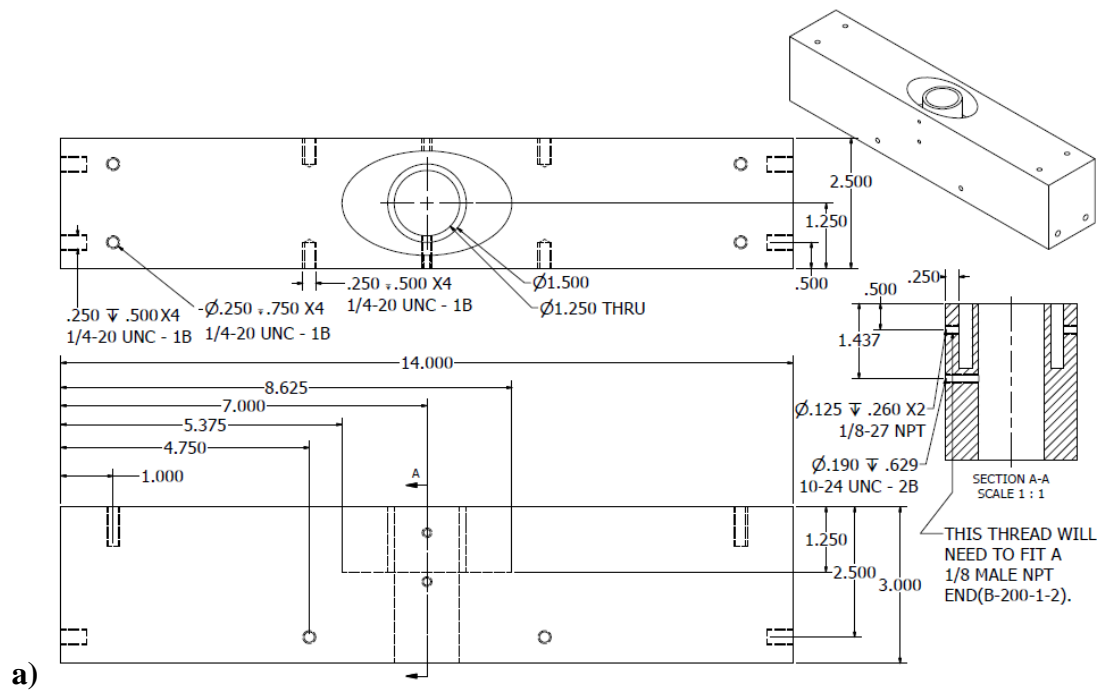


Figure 95. Specifications for the outer shear layer smoke delivery with a) technical drawings, b) plenum configuration, and c) outer shear layer smoke delivery holes.

Later on, a different smoke delivery system was attempted, using woodchips soaked in water as the smoke-creating agent, with little success. The smoke quality of the initial experiments could not be repeated and it is recommended by the author that both a new smoke creation and delivery system be designed for future testing if necessary.

APPENDIX D

OVERVIEW OF EXPERIMENTAL DATA

Table 5. Overview of PIV data sets.

	Diagnostic	Diagnostic details	Reacting?	Swirl number	u_bulk [m/s]	Phi	Frequency [Hz]	Amplitude [mV]	Symmetry
1	PIV	r-x cut	Non-reacting	0.85	10				
2	PIV	r-x cut	Non-reacting	0.85	10		400	100	out-of-phase
3	PIV	r-x cut	Non-reacting	0.85	10		400	200	out-of-phase
4	PIV	r-x cut	Non-reacting	0.85	10		400	300	out-of-phase
5	PIV	r-x cut	Non-reacting	0.85	10		400	400	out-of-phase
6	PIV	r-x cut	Non-reacting	0.85	10		400	500	out-of-phase
7	PIV	r-x cut	Non-reacting	0.85	10		400	600	out-of-phase
8	PIV	r-x cut	Non-reacting	0.85	10		400	700	out-of-phase
9	PIV	r-x cut	Non-reacting	0.85	10		400	800	out-of-phase
10	PIV	r-x cut	Non-reacting	0.85	10		400	900	out-of-phase
11	PIV	r-x cut	Non-reacting	0.85	10		400	1000	out-of-phase
12	PIV	r-x cut	Non-reacting	0.85	10		400	1100	out-of-phase
13	PIV	r-x cut	Non-reacting	0.85	10		400	1200	out-of-phase
14	PIV	r-x cut	Non-reacting	0.85	10		400	1300	out-of-phase
15	PIV	r-x cut	Non-reacting	0.85	10		400	1400	out-of-phase
16	PIV	r-x cut	Non-reacting	0.85	10		400	1500	out-of-phase
17	PIV	r-x cut	Non-reacting	0.85	10		400	100	in-phase
18	PIV	r-x cut	Non-reacting	0.85	10		400	200	in-phase
19	PIV	r-x cut	Non-reacting	0.85	10		400	300	in-phase
20	PIV	r-x cut	Non-reacting	0.85	10		400	400	in-phase
21	PIV	r-x cut	Non-reacting	0.85	10		400	500	in-phase
22	PIV	r-x cut	Non-reacting	0.85	10		400	600	in-phase
23	PIV	r-x cut	Non-reacting	0.85	10		400	700	in-phase
24	PIV	r-x cut	Non-reacting	0.85	10		400	800	in-phase
25	PIV	r-x cut	Non-reacting	0.85	10		400	900	in-phase
26	PIV	r-x cut	Non-reacting	0.85	10		400	1000	in-phase
27	PIV	r-x cut	Non-reacting	0.85	10		400	1100	in-phase
28	PIV	r-x cut	Non-reacting	0.85	10		400	1200	in-phase
29	PIV	r-x cut	Non-reacting	0.85	10		400	1300	in-phase
30	PIV	r-x cut	Non-reacting	0.85	10		400	1400	in-phase
31	PIV	r-x cut	Non-reacting	0.85	10		400	1500	in-phase
32	PIV	r-x cut	Non-reacting	0.85	10		800	100	out-of-phase
33	PIV	r-x cut	Non-reacting	0.85	10		800	200	out-of-phase
34	PIV	r-x cut	Non-reacting	0.85	10		800	300	out-of-phase
35	PIV	r-x cut	Non-reacting	0.85	10		800	400	out-of-phase
36	PIV	r-x cut	Non-reacting	0.85	10		800	500	out-of-phase
37	PIV	r-x cut	Non-reacting	0.85	10		800	600	out-of-phase

38	PIV	r-x cut	Non-reacting	0.85	10		800	700	out-of-phase
39	PIV	r-x cut	Non-reacting	0.85	10		800	800	out-of-phase
40	PIV	r-x cut	Non-reacting	0.85	10		800	900	out-of-phase
41	PIV	r-x cut	Non-reacting	0.85	10		800	1000	out-of-phase
42	PIV	r-x cut	Non-reacting	0.85	10		800	1100	out-of-phase
43	PIV	r-x cut	Non-reacting	0.85	10		800	1200	out-of-phase
44	PIV	r-x cut	Non-reacting	0.85	10		800	1300	out-of-phase
45	PIV	r-x cut	Non-reacting	0.85	10		800	1400	out-of-phase
46	PIV	r-x cut	Non-reacting	0.85	10		800	1500	out-of-phase
47	PIV	r-x cut	Non-reacting	0.85	10		800	100	in-phase
48	PIV	r-x cut	Non-reacting	0.85	10		800	200	in-phase
49	PIV	r-x cut	Non-reacting	0.85	10		800	300	in-phase
50	PIV	r-x cut	Non-reacting	0.85	10		800	400	in-phase
51	PIV	r-x cut	Non-reacting	0.85	10		800	500	in-phase
52	PIV	r-x cut	Non-reacting	0.85	10		800	600	in-phase
53	PIV	r-x cut	Non-reacting	0.85	10		800	700	in-phase
54	PIV	r-x cut	Non-reacting	0.85	10		800	800	in-phase
55	PIV	r-x cut	Non-reacting	0.85	10		800	900	in-phase
56	PIV	r-x cut	Non-reacting	0.85	10		800	1000	in-phase
57	PIV	r-x cut	Non-reacting	0.85	10		800	1100	in-phase
58	PIV	r-x cut	Non-reacting	0.85	10		800	1200	in-phase
59	PIV	r-x cut	Non-reacting	0.85	10		800	1300	in-phase
60	PIV	r-x cut	Non-reacting	0.85	10		800	1400	in-phase
61	PIV	r-x cut	Non-reacting	0.85	10		800	1500	in-phase
62	PIV	r-x cut	Non-reacting	0.85	10		1200	100	out-of-phase
63	PIV	r-x cut	Non-reacting	0.85	10		1200	200	out-of-phase
64	PIV	r-x cut	Non-reacting	0.85	10		1200	300	out-of-phase
65	PIV	r-x cut	Non-reacting	0.85	10		1200	400	out-of-phase
66	PIV	r-x cut	Non-reacting	0.85	10		1200	500	out-of-phase
67	PIV	r-x cut	Non-reacting	0.85	10		1200	600	out-of-phase
68	PIV	r-x cut	Non-reacting	0.85	10		1200	700	out-of-phase
69	PIV	r-x cut	Non-reacting	0.85	10		1200	800	out-of-phase
70	PIV	r-x cut	Non-reacting	0.85	10		1200	900	out-of-phase
71	PIV	r-x cut	Non-reacting	0.85	10		1200	1000	out-of-phase
72	PIV	r-x cut	Non-reacting	0.85	10		1200	1100	out-of-phase
73	PIV	r-x cut	Non-reacting	0.85	10		1200	1200	out-of-phase
74	PIV	r-x cut	Non-reacting	0.85	10		1200	1300	out-of-phase
75	PIV	r-x cut	Non-reacting	0.85	10		1200	1400	out-of-phase
76	PIV	r-x cut	Non-reacting	0.85	10		1200	1500	out-of-phase
77	PIV	r-x cut	Non-reacting	0.85	10		1200	100	in-phase
78	PIV	r-x cut	Non-reacting	0.85	10		1200	200	in-phase
79	PIV	r-x cut	Non-reacting	0.85	10		1200	300	in-phase
80	PIV	r-x cut	Non-reacting	0.85	10		1200	400	in-phase
81	PIV	r-x cut	Non-reacting	0.85	10		1200	500	in-phase
82	PIV	r-x cut	Non-reacting	0.85	10		1200	600	in-phase
83	PIV	r-x cut	Non-reacting	0.85	10		1200	700	in-phase
84	PIV	r-x cut	Non-reacting	0.85	10		1200	800	in-phase
85	PIV	r-x cut	Non-reacting	0.85	10		1200	900	in-phase
86	PIV	r-x cut	Non-reacting	0.85	10		1200	1000	in-phase
87	PIV	r-x cut	Non-reacting	0.85	10		1200	1100	in-phase

88	PIV	r-x cut	Non-reacting	0.85	10		1200	1200	in-phase
89	PIV	r-x cut	Non-reacting	0.85	10		1200	1300	in-phase
90	PIV	r-x cut	Non-reacting	0.85	10		1200	1400	in-phase
91	PIV	r-x cut	Non-reacting	0.85	10		1200	1500	in-phase
92	PIV	r-x cut	Non-reacting	0.85	15		400	1000	out-of-phase
93	PIV	r-x cut	Non-reacting	0.85	15		400	1000	in-phase
94	PIV	r-x cut	Non-reacting	0.85	20		400	1000	out-of-phase
95	PIV	r-x cut	Non-reacting	0.85	20		400	1000	in-phase
96	PIV	r-x cut	Non-reacting	0.85	40		400	1000	out-of-phase
97	PIV	r-x cut	Non-reacting	0.85	40		400	1000	in-phase
98	PIV	r-x cut	Non-reacting	0.85	15		800	1000	out-of-phase
99	PIV	r-x cut	Non-reacting	0.85	15		800	1000	in-phase
100	PIV	r-x cut	Non-reacting	0.85	20		800	1000	out-of-phase
101	PIV	r-x cut	Non-reacting	0.85	20		800	1000	in-phase
102	PIV	r-x cut	Non-reacting	0.85	40		800	1000	out-of-phase
103	PIV	r-x cut	Non-reacting	0.85	40		800	1000	in-phase
104	PIV	r-x cut	Non-reacting	0.85	15		1200	1000	out-of-phase
105	PIV	r-x cut	Non-reacting	0.85	15		1200	1000	in-phase
106	PIV	r-x cut	Non-reacting	0.85	20		1200	1000	out-of-phase
107	PIV	r-x cut	Non-reacting	0.85	20		1200	1000	in-phase
108	PIV	r-x cut	Non-reacting	0.85	40		1200	1000	out-of-phase
109	PIV	r-x cut	Non-reacting	0.85	40		1200	1000	in-phase
110	PIV	r-x cut, zoom	Non-reacting	0.85	10				
111	PIV	r-x cut, zoom	Non-reacting	0.85	20				
112	PIV	r-x cut, zoom	Non-reacting	0.85	10		400	1000	out-of-phase
113	PIV	r-x cut, zoom	Non-reacting	0.85	10		400	1000	in-phase
114	PIV	r-x cut, zoom	Non-reacting	0.85	20		400	1000	out-of-phase
115	PIV	r-x cut, zoom	Non-reacting	0.85	20		400	1000	in-phase
116	PIV	r-x cut, zoom	Non-reacting	0.85	10		800	1000	out-of-phase
117	PIV	r-x cut, zoom	Non-reacting	0.85	10		800	1000	in-phase
118	PIV	r-x cut, zoom	Non-reacting	0.85	20		800	1000	out-of-phase
119	PIV	r-x cut, zoom	Non-reacting	0.85	20		800	1000	in-phase
120	PIV	r-x cut, zoom	Non-reacting	0.85	10		1200	1000	out-of-phase
121	PIV	r-x cut, zoom	Non-reacting	0.85	10		1200	1000	in-phase
122	PIV	r-x cut, zoom	Non-reacting	0.85	20		1200	1000	out-of-phase
123	PIV	r-x cut, zoom	Non-reacting	0.85	20		1200	1000	in-phase
124	PIV	r-x cut	Reacting	0.85	10	0.9			
125	PIV	r-x cut	Reacting	0.85	10	0.9	400	1000	out-of-phase
126	PIV	r-x cut	Reacting	0.85	10	0.9	400	1000	in-phase
127	PIV	r-x cut	Reacting	0.85	10	0.9	800	1000	out-of-phase

128	PIV	r-x cut	Reacting	0.85	10	0.9	800	1000	in-phase
129	PIV	r-x cut	Reacting	0.85	10	0.9	1200	1000	out-of-phase
130	PIV	r-x cut	Reacting	0.85	10	0.9	1200	1000	in-phase
131	PIV	r-x cut	Non-reacting	0.5	10				
132	PIV	r-x cut	Non-reacting	0.5	10		100	300	out-of-phase
133	PIV	r-x cut	Non-reacting	0.5	10		100	350	out-of-phase
134	PIV	r-x cut	Non-reacting	0.5	10		100	400	out-of-phase
135	PIV	r-x cut	Non-reacting	0.5	10		100	450	out-of-phase
136	PIV	r-x cut	Non-reacting	0.5	10		200	300	out-of-phase
137	PIV	r-x cut	Non-reacting	0.5	10		200	350	out-of-phase
138	PIV	r-x cut	Non-reacting	0.5	10		200	400	out-of-phase
139	PIV	r-x cut	Non-reacting	0.5	10		200	450	out-of-phase
140	PIV	r-x cut	Non-reacting	0.5	10		300	250	out-of-phase
141	PIV	r-x cut	Non-reacting	0.5	10		300	300	out-of-phase
142	PIV	r-x cut	Non-reacting	0.5	10		300	350	out-of-phase
143	PIV	r-x cut	Non-reacting	0.5	10		300	400	out-of-phase
144	PIV	r-x cut	Non-reacting	0.5	10		400	150	out-of-phase
145	PIV	r-x cut	Non-reacting	0.5	10		400	150	out-of-phase
146	PIV	r-x cut	Non-reacting	0.5	10		400	200	out-of-phase
147	PIV	r-x cut	Non-reacting	0.5	10		400	250	out-of-phase
148	PIV	r-x cut	Non-reacting	0.5	10		500	200	out-of-phase
149	PIV	r-x cut	Non-reacting	0.5	10		500	250	out-of-phase
150	PIV	r-x cut	Non-reacting	0.5	10		500	300	out-of-phase
151	PIV	r-x cut	Non-reacting	0.5	10		500	300	out-of-phase
152	PIV	r-x cut	Non-reacting	0.5	10		500	350	out-of-phase
153	PIV	r-x cut	Non-reacting	0.5	10		500	350	out-of-phase
154	PIV	r-x cut	Non-reacting	0.5	10		500	400	out-of-phase
155	PIV	r-x cut	Non-reacting	0.5	10		500	450	out-of-phase
156	PIV	r-x cut	Non-reacting	0.5	10		500	500	out-of-phase
157	PIV	r-x cut	Non-reacting	0.5	10		500	600	out-of-phase
158	PIV	r-x cut	Non-reacting	0.5	10		600	250	out-of-phase
159	PIV	r-x cut	Non-reacting	0.5	10		600	300	out-of-phase
160	PIV	r-x cut	Non-reacting	0.5	10		600	350	out-of-phase
161	PIV	r-x cut	Non-reacting	0.5	10		600	400	out-of-phase
162	PIV	r-x cut	Non-reacting	0.5	10		600	500	out-of-phase
163	PIV	r-x cut	Non-reacting	0.5	10		600	550	out-of-phase
164	PIV	r-x cut	Non-reacting	0.5	10		600	600	out-of-phase
165	PIV	r-x cut	Non-reacting	0.5	10		600	650	out-of-phase
166	PIV	r-x cut	Non-reacting	0.5	10		600	700	out-of-phase
167	PIV	r-x cut	Non-reacting	0.5	10		600	900	out-of-phase
168	PIV	r-x cut	Non-reacting	0.5	10		700	250	out-of-phase
169	PIV	r-x cut	Non-reacting	0.5	10		700	300	out-of-phase
170	PIV	r-x cut	Non-reacting	0.5	10		700	400	out-of-phase
171	PIV	r-x cut	Non-reacting	0.5	10		700	450	out-of-phase
172	PIV	r-x cut	Non-reacting	0.5	10		700	600	out-of-phase
173	PIV	r-x cut	Non-reacting	0.5	10		900	250	out-of-phase
174	PIV	r-x cut	Non-reacting	0.5	10		900	300	out-of-phase
175	PIV	r-x cut	Non-reacting	0.5	10		900	400	out-of-phase
176	PIV	r-x cut	Non-reacting	0.5	10		900	450	out-of-phase
177	PIV	r-x cut	Non-reacting	0.5	10		900	600	out-of-phase

178	PIV	r-x cut	Non-reacting	0.5	10		1000	600	out-of-phase
179	PIV	r-x cut	Non-reacting	0.5	10		1000	800	out-of-phase
180	PIV	r-x cut	Non-reacting	0.5	10		1000	900	out-of-phase
181	PIV	r-x cut	Non-reacting	0.5	10		1000	1000	out-of-phase
182	PIV	r-x cut	Non-reacting	0.5	10		1000	1100	out-of-phase
183	PIV	r-x cut	Non-reacting	0.5	10		1100	200	out-of-phase
184	PIV	r-x cut	Non-reacting	0.5	10		1100	300	out-of-phase
185	PIV	r-x cut	Non-reacting	0.5	10		1100	400	out-of-phase
186	PIV	r-x cut	Non-reacting	0.5	10		1100	400	out-of-phase
187	PIV	r-x cut	Non-reacting	0.5	10		1100	450	out-of-phase
188	PIV	r-x cut	Non-reacting	0.5	10		1100	500	out-of-phase
189	PIV	r-x cut	Non-reacting	0.5	10		1100	800	out-of-phase
190	PIV	r-x cut	Non-reacting	0.5	10		1100	900	out-of-phase
191	PIV	r-x cut	Non-reacting	0.5	10		1100	1000	out-of-phase
192	PIV	r-x cut	Non-reacting	0.5	10		1100	1100	out-of-phase
193	PIV	r-x cut	Non-reacting	0.5	10		1200	1500	out-of-phase
194	PIV	r-x cut	Non-reacting	0.5	10		1200	1600	out-of-phase
195	PIV	r-x cut	Non-reacting	0.5	10		1200	1700	out-of-phase
196	PIV	r-x cut	Non-reacting	0.5	10		1200	1800	out-of-phase
197	PIV	r-x cut	Non-reacting	0.5	10		1200	1900	out-of-phase
198	PIV	r-x cut	Non-reacting	0.5	10		1200	2000	out-of-phase
199	PIV	r-x cut	Non-reacting	0.5	10		1300	200	out-of-phase
200	PIV	r-x cut	Non-reacting	0.5	10		1300	300	out-of-phase
201	PIV	r-x cut	Non-reacting	0.5	10		1300	400	out-of-phase
202	PIV	r-x cut	Non-reacting	0.5	10		1300	500	out-of-phase
203	PIV	r-x cut	Non-reacting	0.5	10		1300	550	out-of-phase
204	PIV	r-x cut	Non-reacting	0.5	10		1300	600	out-of-phase
205	PIV	r-x cut	Non-reacting	0.5	10		1300	700	out-of-phase
206	PIV	r-x cut	Non-reacting	0.5	10		1400	200	out-of-phase
207	PIV	r-x cut	Non-reacting	0.5	10		1400	300	out-of-phase
208	PIV	r-x cut	Non-reacting	0.5	10		1400	350	out-of-phase
209	PIV	r-x cut	Non-reacting	0.5	10		1400	400	out-of-phase
210	PIV	r-x cut	Non-reacting	0.5	10		1400	400	out-of-phase
211	PIV	r-x cut	Non-reacting	0.5	10		1400	450	out-of-phase
212	PIV	r-x cut	Non-reacting	0.5	10		1400	500	out-of-phase
213	PIV	r-x cut	Non-reacting	0.5	10		1400	600	out-of-phase
214	PIV	r-x cut	Non-reacting	0.5	10		1400	650	out-of-phase
215	PIV	r-x cut	Non-reacting	0.5	10		1400	700	out-of-phase
216	PIV	r-x cut	Non-reacting	0.5	10		1400	800	out-of-phase
217	PIV	r-x cut	Non-reacting	0.5	10		1500	700	out-of-phase
218	PIV	r-x cut	Non-reacting	0.5	10		1500	750	out-of-phase
219	PIV	r-x cut	Non-reacting	0.5	10		1500	800	out-of-phase
220	PIV	r-x cut	Non-reacting	0.5	10		1500	900	out-of-phase
221	PIV	r-x cut	Non-reacting	0.5	10		1500	1100	out-of-phase
222	PIV	r-x cut	Non-reacting	0.5	10		1500	1100	out-of-phase
223	PIV	r-x cut	Non-reacting	0.5	10		1500	1200	out-of-phase
224	PIV	r-x cut	Non-reacting	0.5	10		1500	1200	out-of-phase
225	PIV	r-x cut	Non-reacting	0.5	10		1500	1300	out-of-phase
226	PIV	r-x cut	Non-reacting	0.5	10		1500	1300	out-of-phase
227	PIV	r-x cut	Non-reacting	0.5	10		1600	300	out-of-phase

228	PIV	r-x cut	Non-reacting	0.5	10		1600	300	out-of-phase
229	PIV	r-x cut	Non-reacting	0.5	10		1600	350	out-of-phase
230	PIV	r-x cut	Non-reacting	0.5	10		1600	350	out-of-phase
231	PIV	r-x cut	Non-reacting	0.5	10		1600	400	out-of-phase
232	PIV	r-x cut	Non-reacting	0.5	10		1600	700	out-of-phase
233	PIV	r-x cut	Non-reacting	0.5	10		1600	750	out-of-phase
234	PIV	r-x cut	Non-reacting	0.5	10		1600	800	out-of-phase
235	PIV	r-x cut	Non-reacting	0.5	10		1600	800	out-of-phase
236	PIV	r-x cut	Non-reacting	0.5	10		1600	850	out-of-phase
237	PIV	r-x cut	Non-reacting	0.5	10		1600	900	out-of-phase
238	PIV	r-x cut	Non-reacting	0.5	10		1600	900	out-of-phase
239	PIV	r-x cut	Non-reacting	0.5	10		1700	600	out-of-phase
240	PIV	r-x cut	Non-reacting	0.5	10		1700	700	out-of-phase
241	PIV	r-x cut	Non-reacting	0.5	10		1700	900	out-of-phase
242	PIV	r-x cut	Non-reacting	0.5	10		1700	950	out-of-phase
243	PIV	r-x cut	Non-reacting	0.5	10		1700	1000	out-of-phase
244	PIV	r-x cut	Non-reacting	0.5	10		1700	1100	out-of-phase
245	PIV	r-x cut	Non-reacting	0.5	10		1700	1200	out-of-phase
246	PIV	r-x cut	Non-reacting	0.5	10		1700	1300	out-of-phase
247	PIV	r-x cut	Non-reacting	0.5	10		1700	1400	out-of-phase
248	PIV	r-x cut	Non-reacting	0.5	10		1800	700	out-of-phase
249	PIV	r-x cut	Non-reacting	0.5	10		1800	700	out-of-phase
250	PIV	r-x cut	Non-reacting	0.5	10		1800	750	out-of-phase
251	PIV	r-x cut	Non-reacting	0.5	10		1800	750	out-of-phase
252	PIV	r-x cut	Non-reacting	0.5	10		1800	800	out-of-phase
253	PIV	r-x cut	Non-reacting	0.5	10		1800	900	out-of-phase
254	PIV	r-x cut	Non-reacting	0.5	10		1800	950	out-of-phase
255	PIV	r-x cut	Non-reacting	0.5	10		1800	1000	out-of-phase
256	PIV	r-x cut	Non-reacting	0.5	10		1800	1100	out-of-phase
257	PIV	r-x cut	Non-reacting	0.5	10		1800	1200	out-of-phase
258	PIV	r-x cut	Non-reacting	0.5	10		1800	1300	out-of-phase
259	PIV	r-x cut	Non-reacting	0.5	10		1800	1400	out-of-phase
260	PIV	r-x cut	Non-reacting	0.5	10		1900	1100	out-of-phase
261	PIV	r-x cut	Non-reacting	0.5	10		1900	1150	out-of-phase
262	PIV	r-x cut	Non-reacting	0.5	10		1900	1200	out-of-phase
263	PIV	r-x cut	Non-reacting	0.5	10		1900	1300	out-of-phase
264	PIV	r-x cut	Non-reacting	0.5	10		1900	2000	out-of-phase
265	PIV	r-x cut	Non-reacting	0.5	10		2000	1100	out-of-phase
266	PIV	r-x cut	Non-reacting	0.5	10		2000	1150	out-of-phase
267	PIV	r-x cut	Non-reacting	0.5	10		2000	1200	out-of-phase
268	PIV	r-x cut	Non-reacting	0.5	10		2000	1300	out-of-phase
269	PIV	r-x cut	Non-reacting	0.5	10		2000	2000	out-of-phase
270	PIV	r-x cut	Reacting	0.5	10	0.9			
271	PIV	r-x cut	Reacting	0.5	10	0.9	400	250	out-of-phase
272	PIV	r-x cut	Reacting	0.5	10	0.9	500	250	out-of-phase
273	PIV	r-x cut	Reacting	0.5	10	0.9	600	400	out-of-phase
274	PIV	r-x cut	Reacting	0.5	10	0.9	700	600	out-of-phase
275	PIV	r-x cut	Reacting	0.5	10	0.9	800	200	out-of-phase
276	PIV	r-x cut	Reacting	0.5	10	0.9	900	600	out-of-phase
277	PIV	r-x cut	Reacting	0.5	10	0.9	1000	1100	out-of-phase

278	PIV	r-x cut	Reacting	0.5	10	0.9	1100	500	out-of-phase
279	PIV	r-x cut	Reacting	0.5	10	0.9	1200	1800	out-of-phase
280	PIV	r-x cut	Reacting	0.5	10	0.9	1300	600	out-of-phase
281	PIV	r-x cut	Reacting	0.5	10	0.9	1400	500	out-of-phase
282	PIV	r-x cut	Reacting	0.5	10	0.9	1500	1300	out-of-phase
283	PIV	r-x cut	Reacting	0.5	10	0.9	1600	750	out-of-phase
284	PIV	r-x cut	Reacting	0.5	10	0.9	1700	1100	out-of-phase
285	PIV	r-x cut	Reacting	0.5	10	0.9	400	250	in-phase
286	PIV	r-x cut	Reacting	0.5	10	0.9	500	250	in-phase
287	PIV	r-x cut	Reacting	0.5	10	0.9	600	400	in-phase
288	PIV	r-x cut	Reacting	0.5	10	0.9	700	600	in-phase
289	PIV	r-x cut	Reacting	0.5	10	0.9	800	200	in-phase
290	PIV	r-x cut	Reacting	0.5	10	0.9	900	600	in-phase
291	PIV	r-x cut	Reacting	0.5	10	0.9	1000	1100	in-phase
292	PIV	r-x cut	Reacting	0.5	10	0.9	1100	500	in-phase
293	PIV	r-x cut	Reacting	0.5	10	0.9	1200	1800	in-phase
294	PIV	r-x cut	Reacting	0.5	10	0.9	1300	600	in-phase
295	PIV	r-x cut	Reacting	0.5	10	0.9	1400	500	in-phase
296	PIV	r-x cut	Reacting	0.5	10	0.9	1500	1300	in-phase
297	PIV	r-x cut	Reacting	0.5	10	0.9	1600	750	in-phase
298	PIV	r-x cut	Reacting	0.5	10	0.9	1700	1100	in-phase
299	PIV	r-x cut	Reacting	0.5	10	0.9	1800	1100	in-phase
300	PIV	r-x cut	Non-reacting	0.5	10				
301	PIV	r-x cut	Non-reacting	0.5	10		400	400	longitudinal
302	PIV	r-x cut	Non-reacting	0.5	10		400	600	longitudinal
303	PIV	r-x cut	Non-reacting	0.5	10		400	800	longitudinal
304	PIV	r-x cut	Non-reacting	0.5	10		400	1200	longitudinal
305	PIV	r-x cut	Non-reacting	0.5	10		400	1000	longitudinal
306	PIV	r-x cut	Non-reacting	0.5	10		400	1400	longitudinal
307	PIV	r-x cut	Non-reacting	0.5	10		800	400	longitudinal
308	PIV	r-x cut	Non-reacting	0.5	10		800	600	longitudinal
309	PIV	r-x cut	Non-reacting	0.5	10		800	800	longitudinal
310	PIV	r-x cut	Non-reacting	0.5	10		800	1200	longitudinal
311	PIV	r-x cut	Non-reacting	0.5	10		800	1000	longitudinal
312	PIV	r-x cut	Non-reacting	0.5	10		800	1400	longitudinal
313	PIV	r-x cut	Non-reacting	0.5	10		1200	400	longitudinal
314	PIV	r-x cut	Non-reacting	0.5	10		1200	600	longitudinal
315	PIV	r-x cut	Non-reacting	0.5	10		1200	800	longitudinal
316	PIV	r-x cut	Non-reacting	0.5	10		1200	1200	longitudinal
317	PIV	r-x cut	Non-reacting	0.5	10		1200	1000	longitudinal
318	PIV	r-x cut	Non-reacting	0.5	10		1200	1400	longitudinal
319	PIV	r-x cut	Non-reacting	0.85	10				
320	PIV	r-x cut	Non-reacting	0.85	10		400	1000	longitudinal
321	PIV	r-x cut	Non-reacting	0.85	10		400	2000	longitudinal
322	PIV	r-x cut	Non-reacting	0.85	10		400	3000	longitudinal
323	PIV	r-x cut	Non-reacting	0.85	10		400	4000	longitudinal
324	PIV	r-x cut	Non-reacting	0.85	10		800	1000	longitudinal
325	PIV	r-x cut	Non-reacting	0.85	10		800	2000	longitudinal
326	PIV	r-x cut	Non-reacting	0.85	10		800	3000	longitudinal
327	PIV	r-x cut	Non-reacting	0.85	10		800	4000	longitudinal

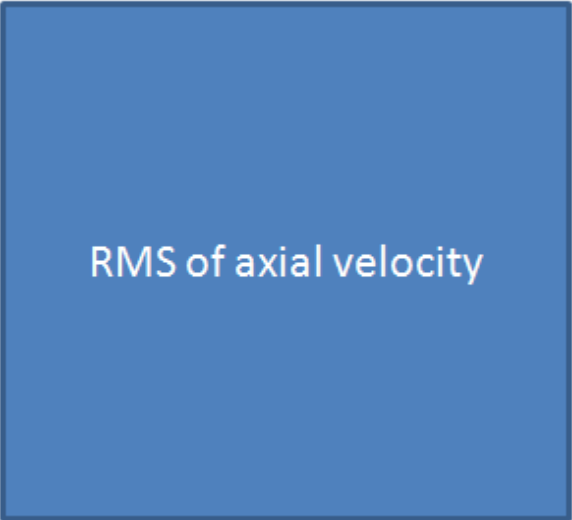
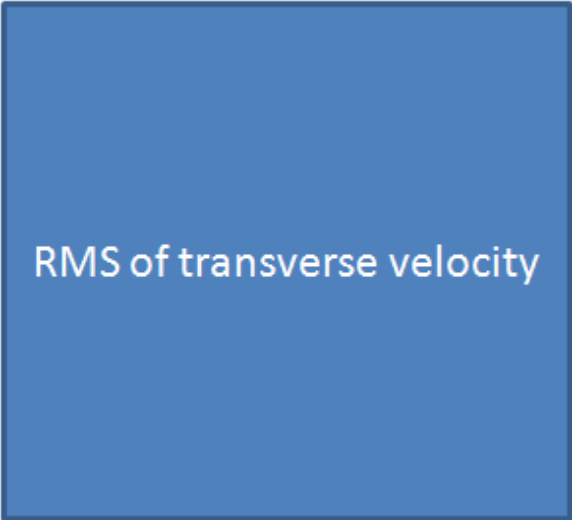
328	PIV	r-x cut	Non-reacting	0.85	10		800	5000	longitudinal
329	PIV	r-x cut	Non-reacting	0.85	10		800	6000	longitudinal
330	PIV	r-x cut	Non-reacting	0.85	10		800	7000	longitudinal
331	PIV	r-x cut	Non-reacting	0.85	10		800	8000	longitudinal
332	PIV	r-x cut	Non-reacting	0.85	10		800	9000	longitudinal
333	PIV	r-x cut	Non-reacting	0.85	10		800	10000	longitudinal
328	PIV	r-x cut	Non-reacting	0.85	10		1200	1000	longitudinal
329	PIV	r-x cut	Non-reacting	0.85	10		1200	2000	longitudinal
330	PIV	r-x cut	Non-reacting	0.85	10		1200	3000	longitudinal
331	PIV	r-x cut	Non-reacting	0.85	10		1200	4000	longitudinal
332	PIV	r-theta, 0D	Non-reacting	0.85	10				
333	PIV	r-theta, 0D	Non-reacting	0.85	10		400	100	out-of-phase
334	PIV	r-theta, 0D	Non-reacting	0.85	10		400	200	out-of-phase
335	PIV	r-theta, 0D	Non-reacting	0.85	10		400	300	out-of-phase
336	PIV	r-theta, 0D	Non-reacting	0.85	10		400	400	out-of-phase
337	PIV	r-theta, 0D	Non-reacting	0.85	10		400	500	out-of-phase
338	PIV	r-theta, 0D	Non-reacting	0.85	10		400	600	out-of-phase
339	PIV	r-theta, 0D	Non-reacting	0.85	10		400	700	out-of-phase
340	PIV	r-theta, 0D	Non-reacting	0.85	10		400	800	out-of-phase
341	PIV	r-theta, 0D	Non-reacting	0.85	10		400	900	out-of-phase
342	PIV	r-theta, 0D	Non-reacting	0.85	10		400	1000	out-of-phase
343	PIV	r-theta, 0D	Non-reacting	0.85	10		400	1100	out-of-phase
344	PIV	r-theta, 0D	Non-reacting	0.85	10		400	100	in-phase
345	PIV	r-theta, 0D	Non-reacting	0.85	10		400	200	in-phase
346	PIV	r-theta, 0D	Non-reacting	0.85	10		400	300	in-phase
347	PIV	r-theta, 0D	Non-reacting	0.85	10		400	400	in-phase
348	PIV	r-theta, 0D	Non-reacting	0.85	10		400	500	in-phase
349	PIV	r-theta, 0D	Non-reacting	0.85	10		400	600	in-phase
350	PIV	r-theta, 0D	Non-reacting	0.85	10		400	700	in-phase
351	PIV	r-theta, 0D	Non-reacting	0.85	10		400	800	in-phase
352	PIV	r-theta, 0D	Non-reacting	0.85	10		400	900	in-phase
353	PIV	r-theta, 0D	Non-reacting	0.85	10		400	1000	in-phase
354	PIV	r-theta, 0D	Non-reacting	0.85	10		400	1100	in-phase
355	PIV	r-theta, 0D	Non-reacting	0.85	10		800	200	out-of-phase
356	PIV	r-theta, 0D	Non-reacting	0.85	10		800	600	out-of-phase
357	PIV	r-theta, 0D	Non-reacting	0.85	10		800	1000	out-of-phase
358	PIV	r-theta, 0D	Non-reacting	0.85	10		800	200	in-phase
359	PIV	r-theta, 0D	Non-reacting	0.85	10		800	600	in-phase
360	PIV	r-theta, 0D	Non-reacting	0.85	10		800	1000	in-phase
361	PIV	r-theta, 0D	Non-reacting	0.85	10		1200	200	out-of-phase
362	PIV	r-theta, 0D	Non-reacting	0.85	10		1200	600	out-of-phase
363	PIV	r-theta, 0D	Non-reacting	0.85	10		1200	1000	out-of-phase
364	PIV	r-theta, 0D	Non-reacting	0.85	10		1200	200	in-phase
365	PIV	r-theta, 0D	Non-reacting	0.85	10		1200	600	in-phase
366	PIV	r-theta, 0D	Non-reacting	0.85	10		1200	1000	in-phase
367	PIV	r-theta, 0D	Non-reacting	0.85	10		1500	200	out-of-phase
368	PIV	r-theta, 0D	Non-reacting	0.85	10		1500	600	out-of-phase
369	PIV	r-theta, 0D	Non-reacting	0.85	10		1500	1000	out-of-phase
370	PIV	r-theta, 0D	Non-reacting	0.85	10		1500	200	in-phase
371	PIV	r-theta, 0D	Non-reacting	0.85	10		1500	600	in-phase

372	PIV	r-theta, 0D	Non-reacting	0.85	10		1500	1000	in-phase
373	PIV	r-theta, 0D	Non-reacting	0.85	10		1800	100	out-of-phase
374	PIV	r-theta, 0D	Non-reacting	0.85	10		1800	200	out-of-phase
375	PIV	r-theta, 0D	Non-reacting	0.85	10		1800	300	out-of-phase
376	PIV	r-theta, 0D	Non-reacting	0.85	10		1800	400	out-of-phase
377	PIV	r-theta, 0D	Non-reacting	0.85	10		1800	500	out-of-phase
378	PIV	r-theta, 0D	Non-reacting	0.85	10		1800	600	out-of-phase
379	PIV	r-theta, 0D	Non-reacting	0.85	10		1800	700	out-of-phase
380	PIV	r-theta, 0D	Non-reacting	0.85	10		1800	800	out-of-phase
381	PIV	r-theta, 0D	Non-reacting	0.85	10		1800	900	out-of-phase
382	PIV	r-theta, 0D	Non-reacting	0.85	10		1800	1000	out-of-phase
383	PIV	r-theta, 0D	Non-reacting	0.85	10		1800	1100	out-of-phase
384	PIV	r-theta, 0D	Non-reacting	0.85	10		1800	100	in-phase
385	PIV	r-theta, 0D	Non-reacting	0.85	10		1800	200	in-phase
386	PIV	r-theta, 0D	Non-reacting	0.85	10		1800	300	in-phase
387	PIV	r-theta, 0D	Non-reacting	0.85	10		1800	400	in-phase
388	PIV	r-theta, 0D	Non-reacting	0.85	10		1800	500	in-phase
389	PIV	r-theta, 0D	Non-reacting	0.85	10		1800	600	in-phase
390	PIV	r-theta, 0D	Non-reacting	0.85	10		1800	700	in-phase
391	PIV	r-theta, 0D	Non-reacting	0.85	10		1800	800	in-phase
392	PIV	r-theta, 0D	Non-reacting	0.85	10		1800	900	in-phase
393	PIV	r-theta, 0D	Non-reacting	0.85	10		1800	1000	in-phase
394	PIV	r-theta, 0D	Non-reacting	0.85	10		1800	1100	in-phase
395	PIV	r-theta, 1D	Non-reacting	0.85	10				
396	PIV	r-theta, 1D	Non-reacting	0.85	10		400	200	out-of-phase
397	PIV	r-theta, 1D	Non-reacting	0.85	10		400	600	out-of-phase
398	PIV	r-theta, 1D	Non-reacting	0.85	10		400	1000	out-of-phase
399	PIV	r-theta, 1D	Non-reacting	0.85	10		400	200	in-phase
400	PIV	r-theta, 1D	Non-reacting	0.85	10		400	600	in-phase
401	PIV	r-theta, 1D	Non-reacting	0.85	10		400	1000	in-phase
402	PIV	r-theta, 1D	Non-reacting	0.85	10		800	200	out-of-phase
403	PIV	r-theta, 1D	Non-reacting	0.85	10		800	600	out-of-phase
404	PIV	r-theta, 1D	Non-reacting	0.85	10		800	1000	out-of-phase
405	PIV	r-theta, 1D	Non-reacting	0.85	10		800	200	in-phase
406	PIV	r-theta, 1D	Non-reacting	0.85	10		800	600	in-phase
407	PIV	r-theta, 1D	Non-reacting	0.85	10		800	1000	in-phase
408	PIV	r-theta, 1D	Non-reacting	0.85	10		1200	200	out-of-phase
409	PIV	r-theta, 1D	Non-reacting	0.85	10		1200	600	out-of-phase
410	PIV	r-theta, 1D	Non-reacting	0.85	10		1200	1000	out-of-phase
411	PIV	r-theta, 1D	Non-reacting	0.85	10		1200	200	in-phase
412	PIV	r-theta, 1D	Non-reacting	0.85	10		1200	600	in-phase
413	PIV	r-theta, 1D	Non-reacting	0.85	10		1200	1000	in-phase
414	PIV	r-theta, 1D	Non-reacting	0.85	10		1500	200	out-of-phase
415	PIV	r-theta, 1D	Non-reacting	0.85	10		1500	600	out-of-phase
416	PIV	r-theta, 1D	Non-reacting	0.85	10		1500	1000	out-of-phase
417	PIV	r-theta, 1D	Non-reacting	0.85	10		1500	200	in-phase
418	PIV	r-theta, 1D	Non-reacting	0.85	10		1500	600	in-phase
419	PIV	r-theta, 1D	Non-reacting	0.85	10		1500	1000	in-phase
420	PIV	r-theta, 1D	Non-reacting	0.85	10		1800	200	out-of-phase
421	PIV	r-theta, 1D	Non-reacting	0.85	10		1800	600	out-of-phase

422	PIV	r-theta, 1D	Non-reacting	0.85	10		1800	1000	out-of-phase
423	PIV	r-theta, 1D	Non-reacting	0.85	10		1800	200	in-phase
424	PIV	r-theta, 1D	Non-reacting	0.85	10		1800	600	in-phase
425	PIV	r-theta, 1D	Non-reacting	0.85	10		1800	1000	in-phase
426	PIV	r-theta, 2D	Non-reacting	0.85	10				
427	PIV	r-theta, 2D	Non-reacting	0.85	10		400	200	out-of-phase
428	PIV	r-theta, 2D	Non-reacting	0.85	10		400	600	out-of-phase
429	PIV	r-theta, 2D	Non-reacting	0.85	10		400	1000	out-of-phase
430	PIV	r-theta, 2D	Non-reacting	0.85	10		400	200	in-phase
431	PIV	r-theta, 2D	Non-reacting	0.85	10		400	600	in-phase
432	PIV	r-theta, 2D	Non-reacting	0.85	10		400	1000	in-phase
433	PIV	r-theta, 2D	Non-reacting	0.85	10		800	200	out-of-phase
434	PIV	r-theta, 2D	Non-reacting	0.85	10		800	600	out-of-phase
435	PIV	r-theta, 2D	Non-reacting	0.85	10		800	1000	out-of-phase
436	PIV	r-theta, 2D	Non-reacting	0.85	10		800	200	in-phase
437	PIV	r-theta, 2D	Non-reacting	0.85	10		800	600	in-phase
438	PIV	r-theta, 2D	Non-reacting	0.85	10		800	1000	in-phase
439	PIV	r-theta, 2D	Non-reacting	0.85	10		1200	200	out-of-phase
440	PIV	r-theta, 2D	Non-reacting	0.85	10		1200	600	out-of-phase
441	PIV	r-theta, 2D	Non-reacting	0.85	10		1200	1000	out-of-phase
442	PIV	r-theta, 2D	Non-reacting	0.85	10		1200	200	in-phase
443	PIV	r-theta, 2D	Non-reacting	0.85	10		1200	600	in-phase
444	PIV	r-theta, 2D	Non-reacting	0.85	10		1200	1000	in-phase
445	PIV	r-theta, 2D	Non-reacting	0.85	10		1500	200	out-of-phase
446	PIV	r-theta, 2D	Non-reacting	0.85	10		1500	600	out-of-phase
447	PIV	r-theta, 2D	Non-reacting	0.85	10		1500	1000	out-of-phase
448	PIV	r-theta, 2D	Non-reacting	0.85	10		1500	200	in-phase
449	PIV	r-theta, 2D	Non-reacting	0.85	10		1500	600	in-phase
450	PIV	r-theta, 2D	Non-reacting	0.85	10		1500	1000	in-phase
451	PIV	r-theta, 2D	Non-reacting	0.85	10		1800	200	out-of-phase
452	PIV	r-theta, 2D	Non-reacting	0.85	10		1800	600	out-of-phase
453	PIV	r-theta, 2D	Non-reacting	0.85	10		1800	1000	out-of-phase
454	PIV	r-theta, 2D	Non-reacting	0.85	10		1800	200	in-phase
455	PIV	r-theta, 2D	Non-reacting	0.85	10		1800	600	in-phase
456	PIV	r-theta, 2D	Non-reacting	0.85	10		1800	1000	in-phase

The following pages show examples of the PIV data set that span the entire range of data taken. The first three pages act as a key to explain the formatting of each of these examples. The instantaneous images are taken 0.1 ms apart.

	Diagnostic	Diagnostic details	Reacting?	Swirl number	u_bulk [m/s]	Phi	Frequency [Hz]	Amplitude [mV]	Symmetry
1	PIV								



Fluctuation
amplitude at
forcing frequency
– transverse
velocity

Fluctuation
amplitude at
forcing frequency
– axial velocity

Fluctuation
amplitude at
forcing frequency
– vorticity

Spectra of
reference
velocities

Spectrum of
centerline
transverse
velocity

Spectrum of
centerline axial
velocity

Instantaneous
plot of vorticity
contour and
velocity vectors

Instantaneous
plot of vorticity
contour and
velocity vectors

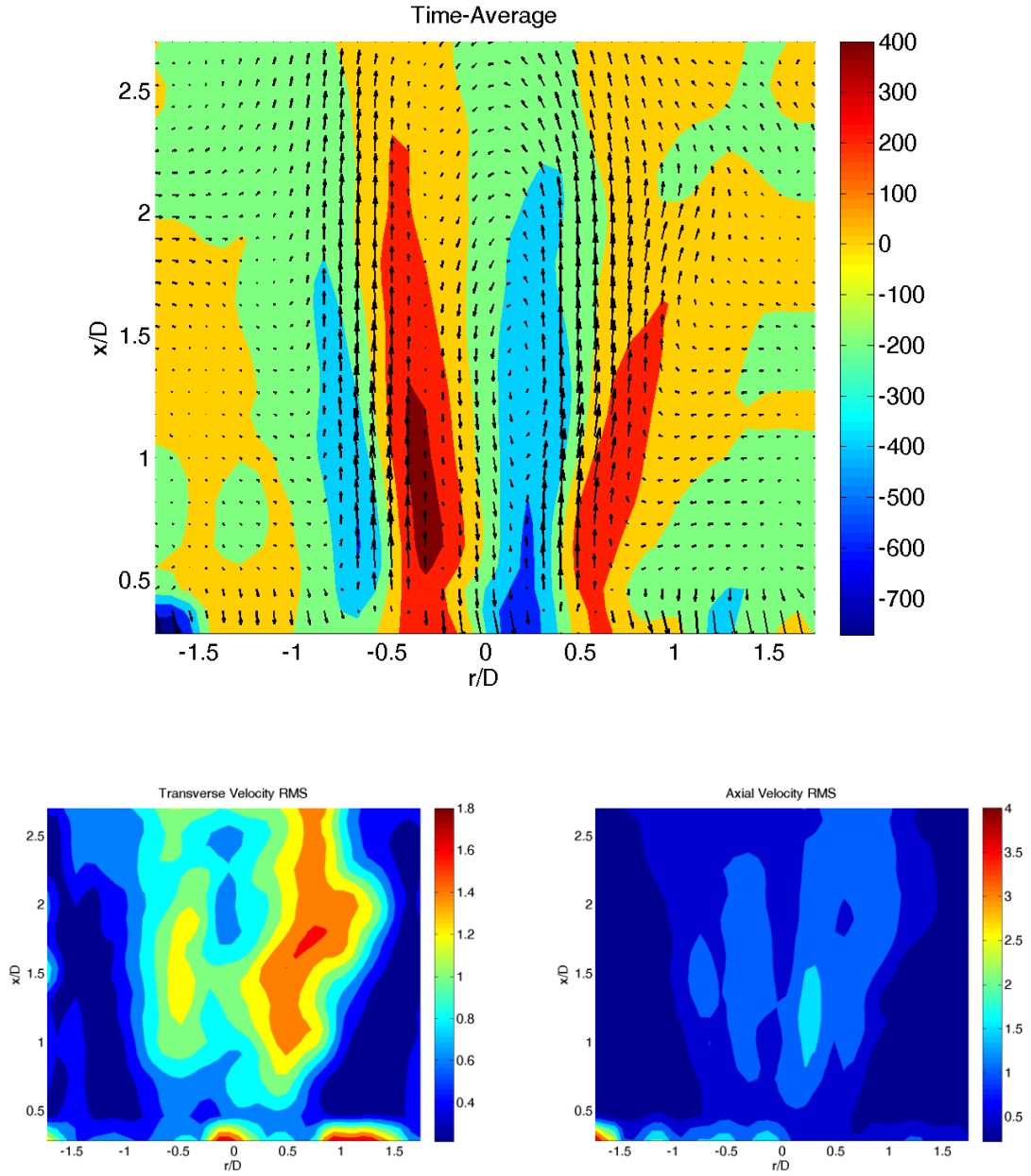
Instantaneous
plot of vorticity
contour and
velocity vectors

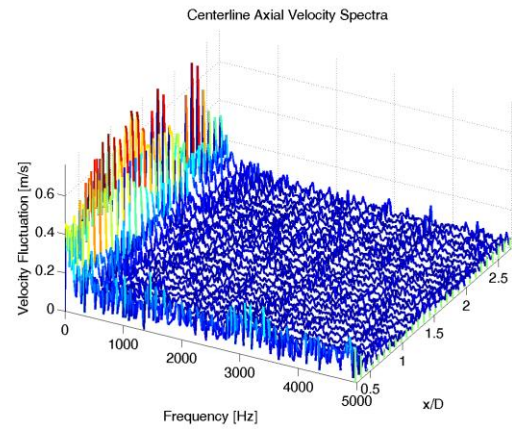
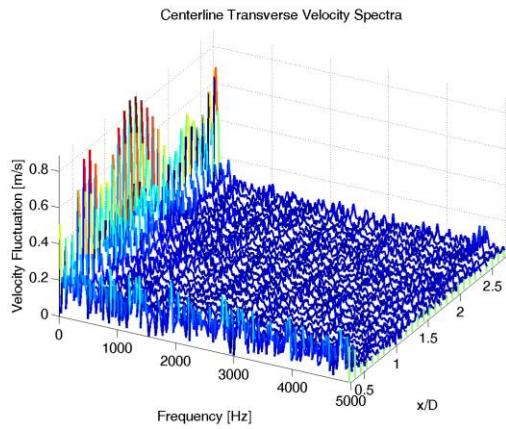
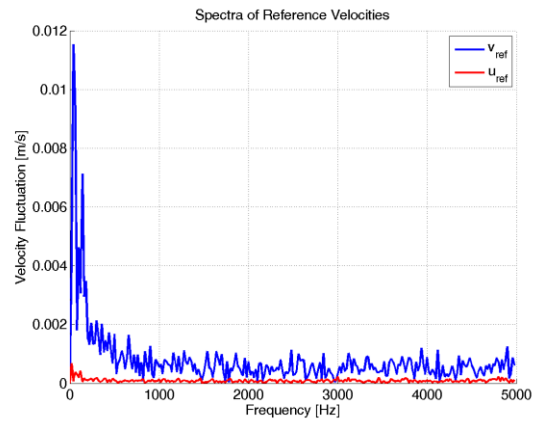
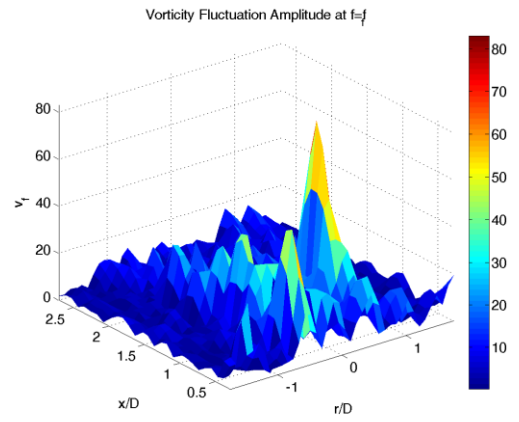
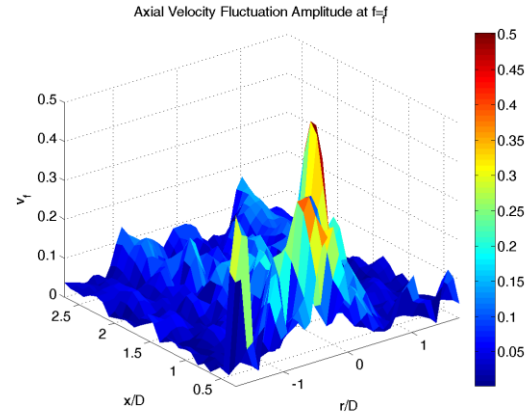
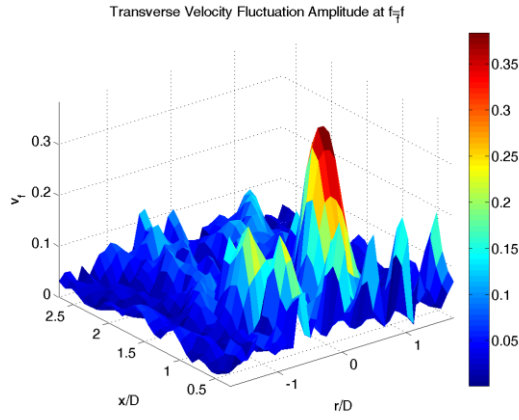
Instantaneous
plot of vorticity
contour and
velocity vectors

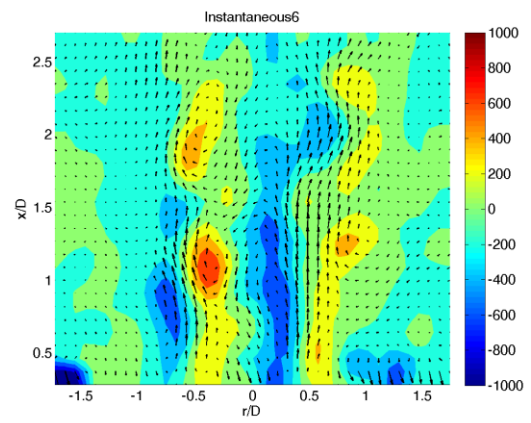
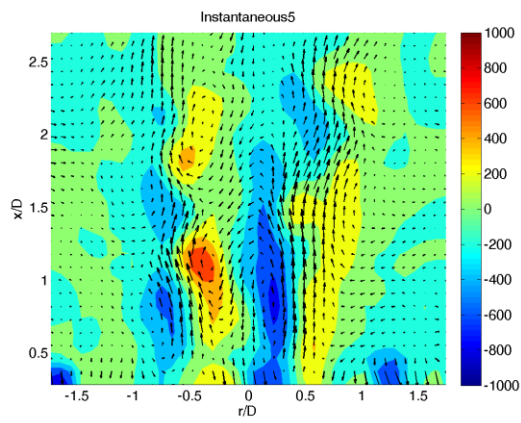
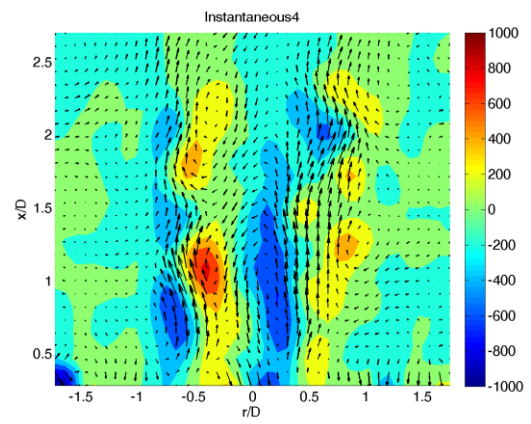
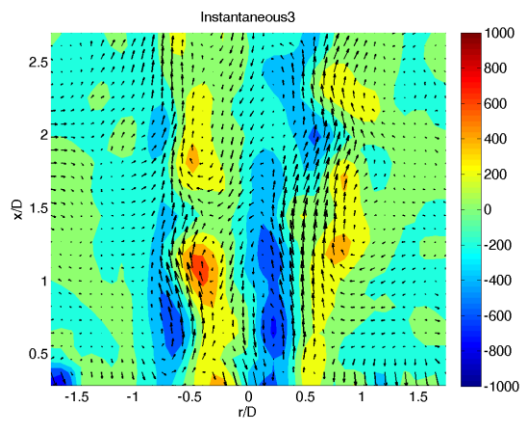
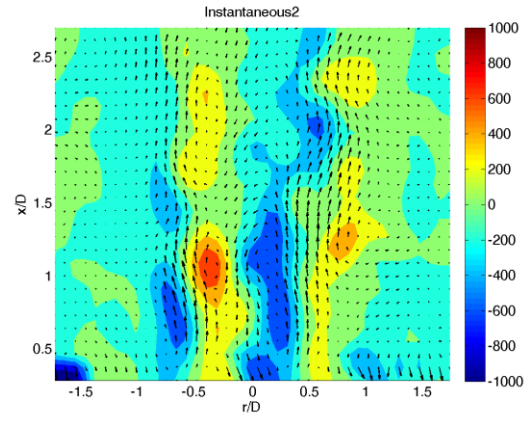
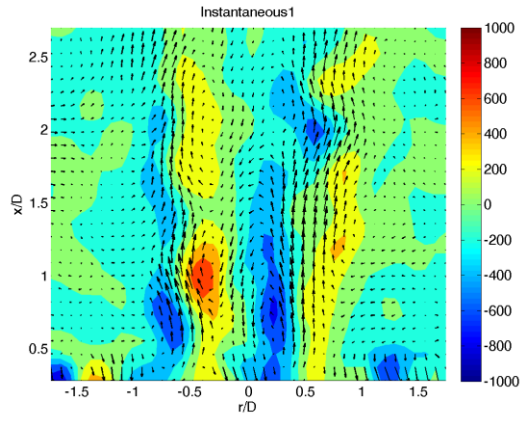
Instantaneous
plot of vorticity
contour and
velocity vectors

Instantaneous
plot of vorticity
contour and
velocity vectors

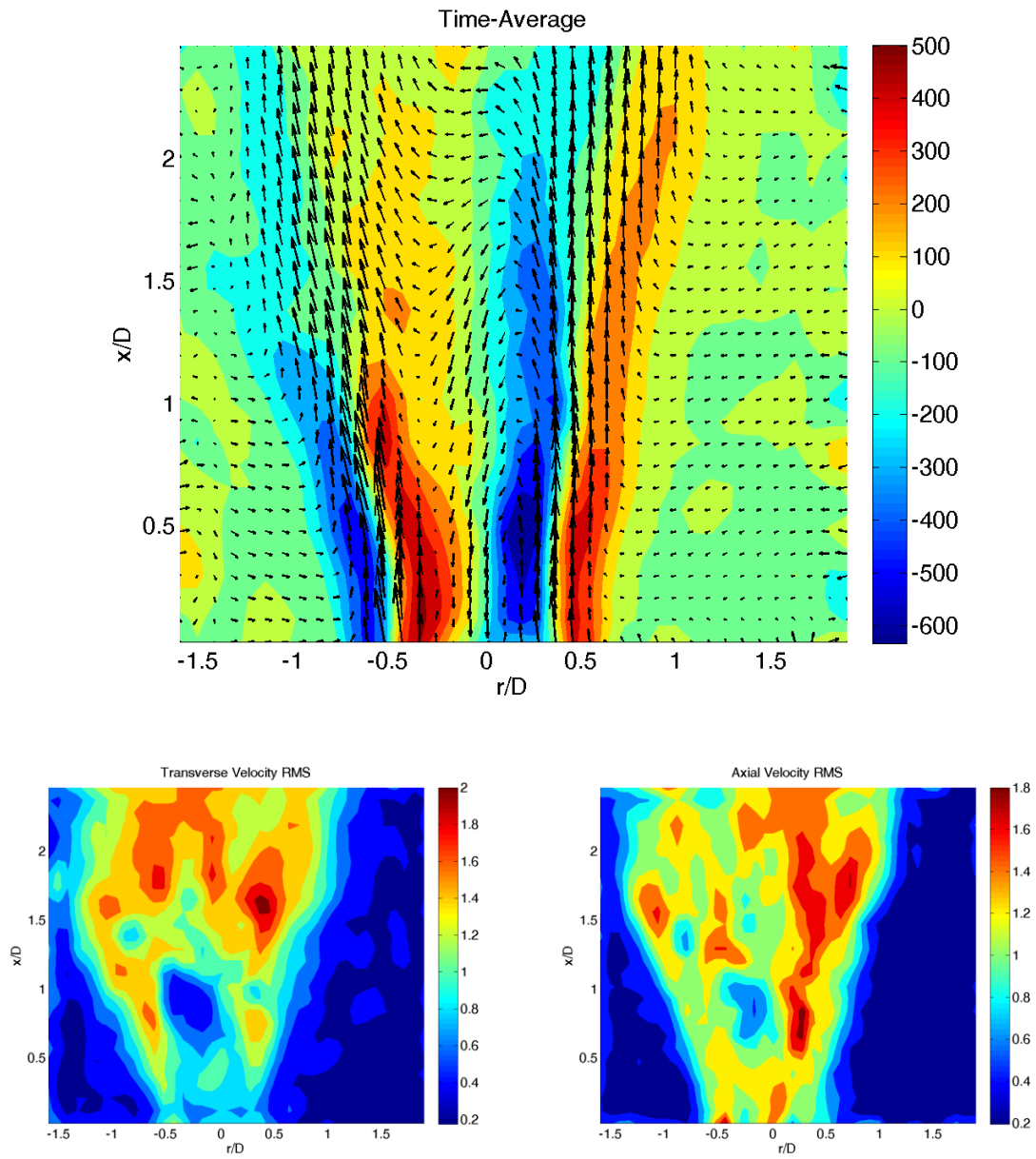
	Diagnostic	Diagnostic details	Reacting?	Swirl number	u_{bulk} [m/s]	Phi	Frequency [Hz]	Amplitude [mV]	Symmetry
1	PIV	r-x cut	Non-reacting	0.5	10		400	1400	Longitudinal

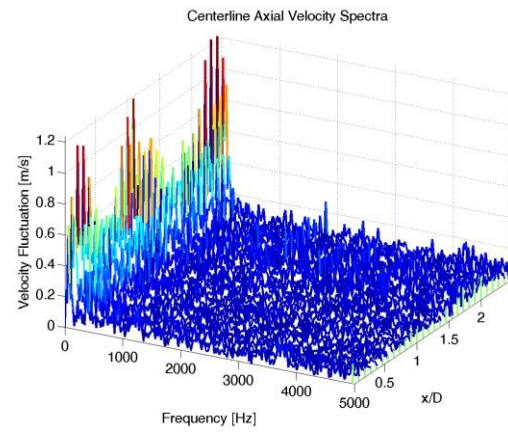
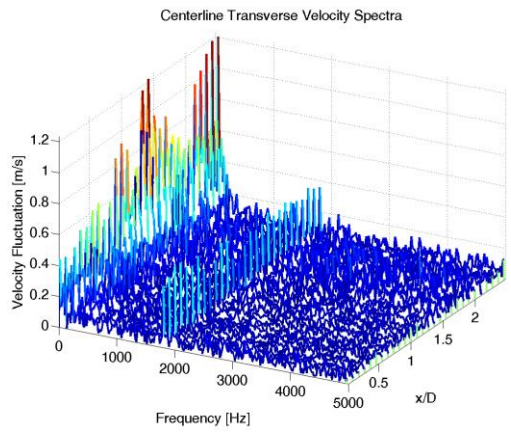
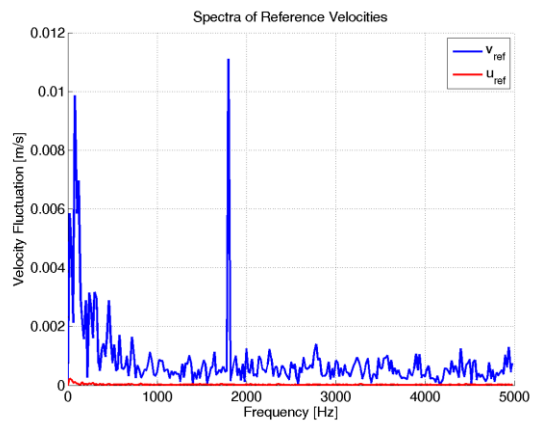
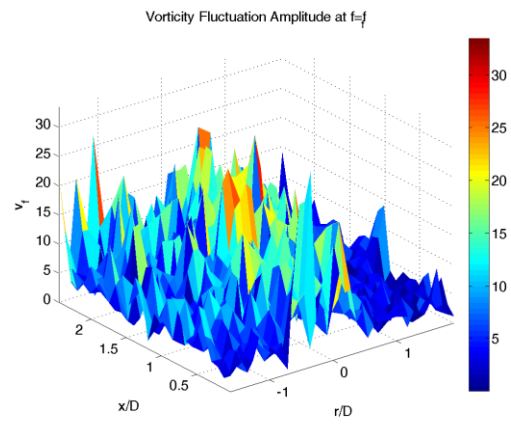
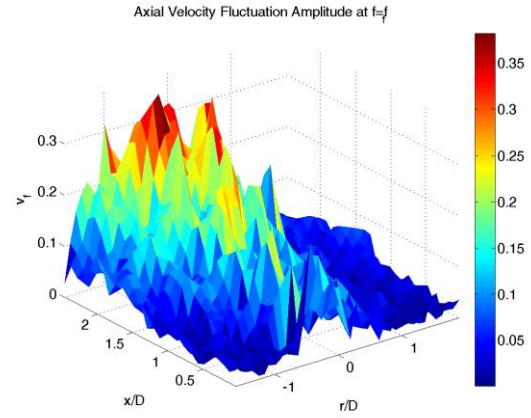
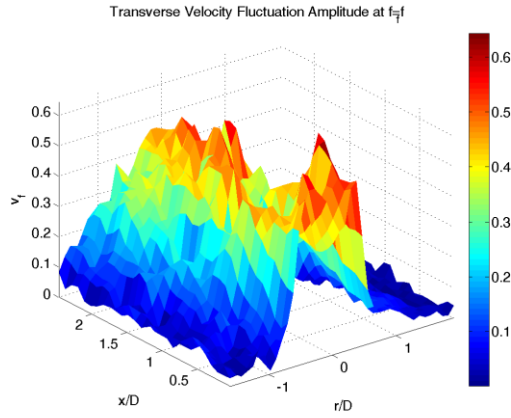


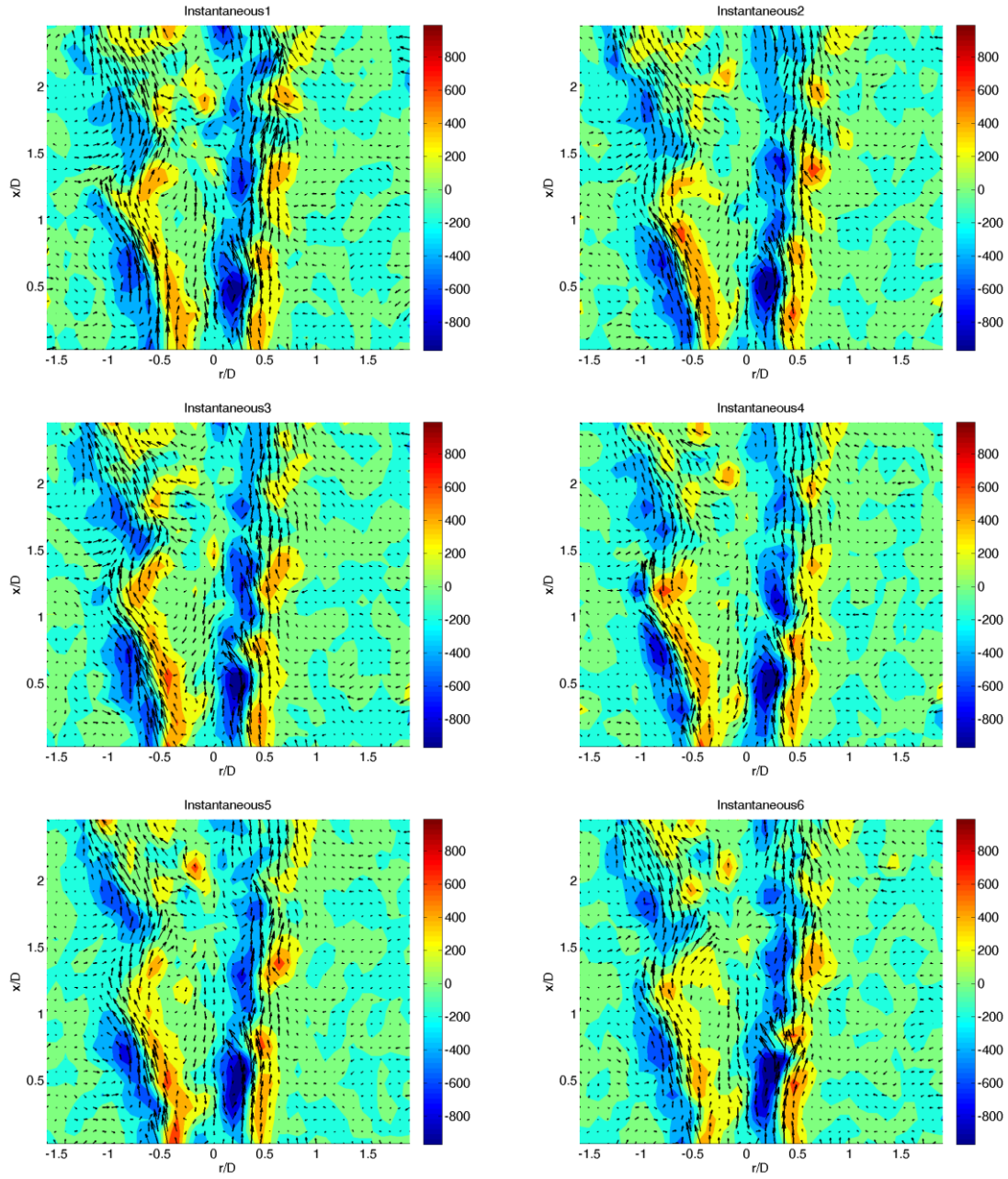




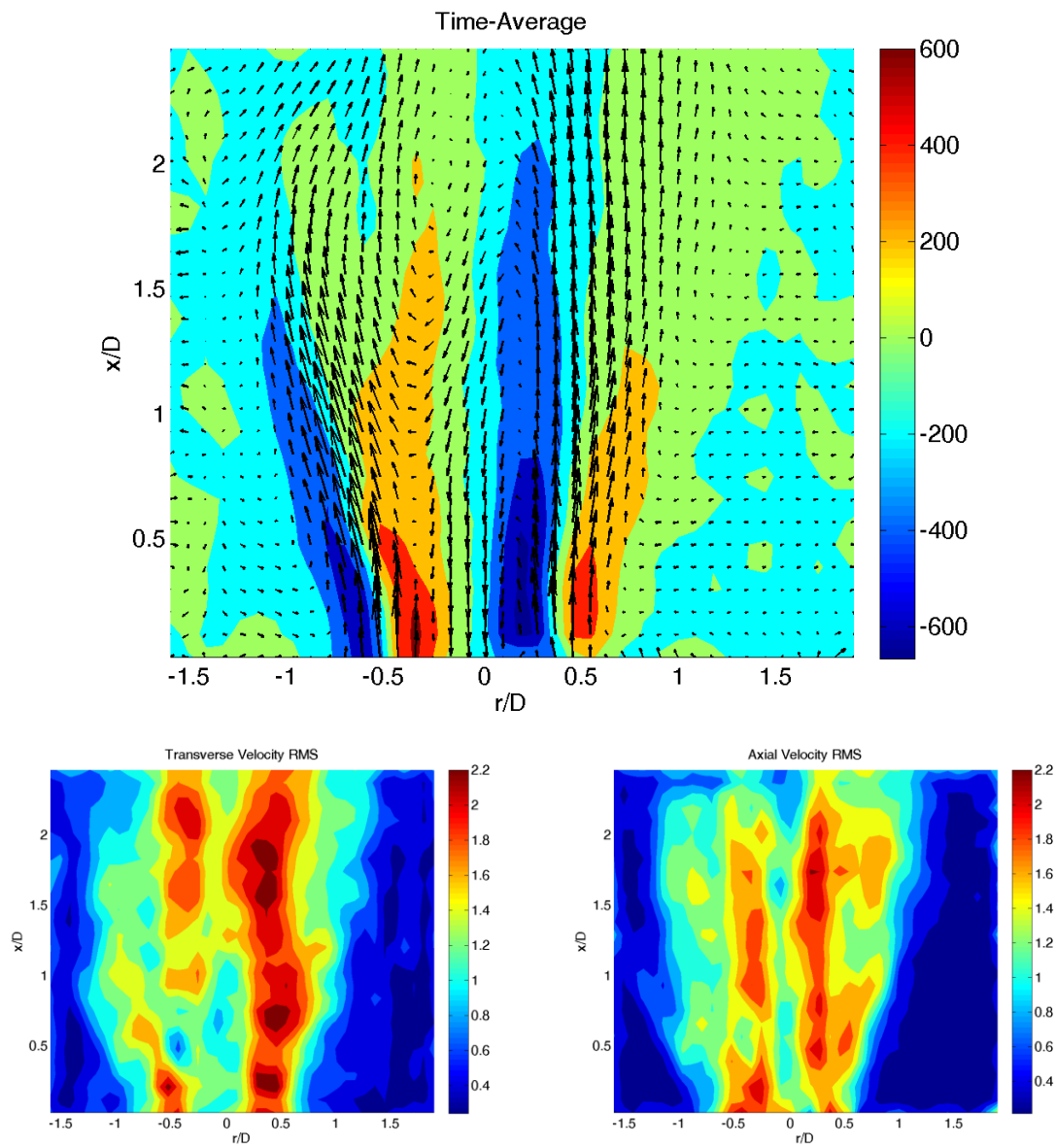
	Diagnostic	Diagnostic details	Reacting?	Swirl number	u_bulk [m/s]	Phi	Frequency [Hz]	Amplitude [mV]	Symmetry
1	PIV	r-x cut	Non-reacting	0.5	10		1800	1400	out-of-phase

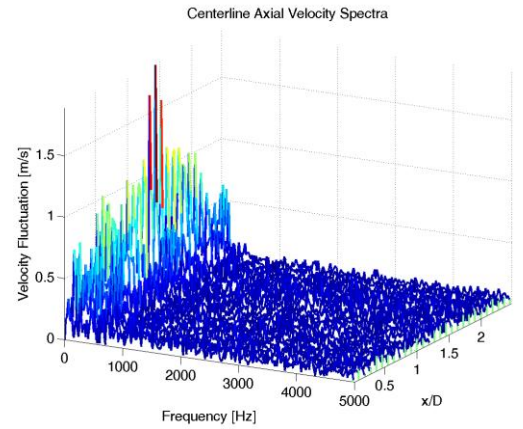
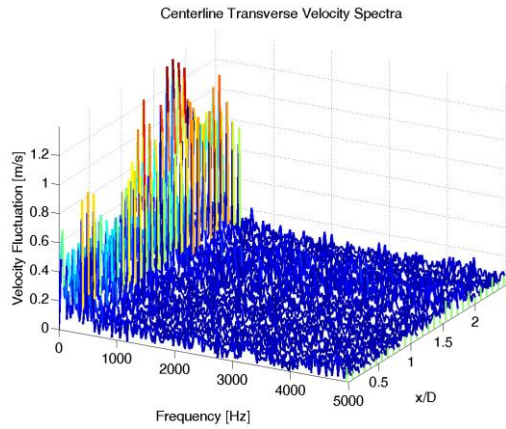
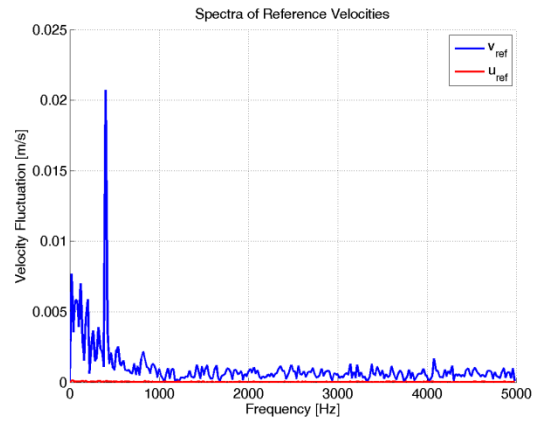
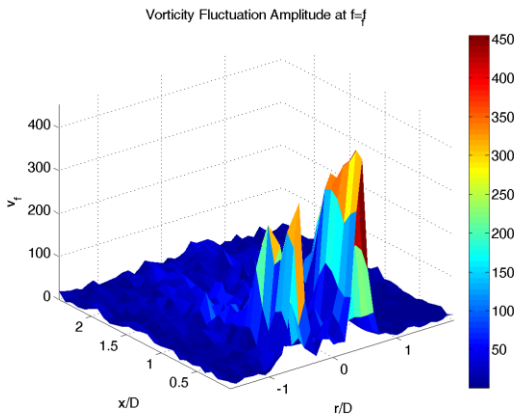
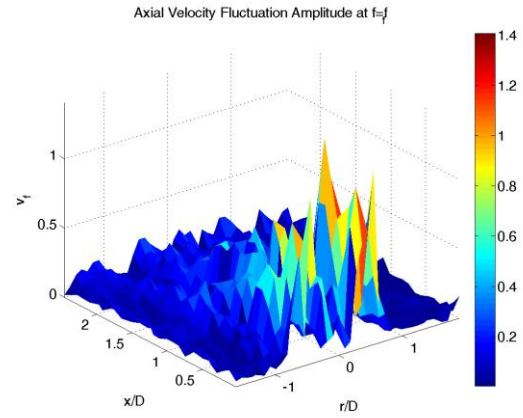
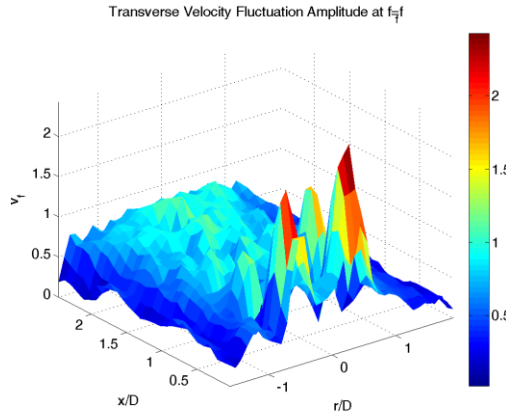


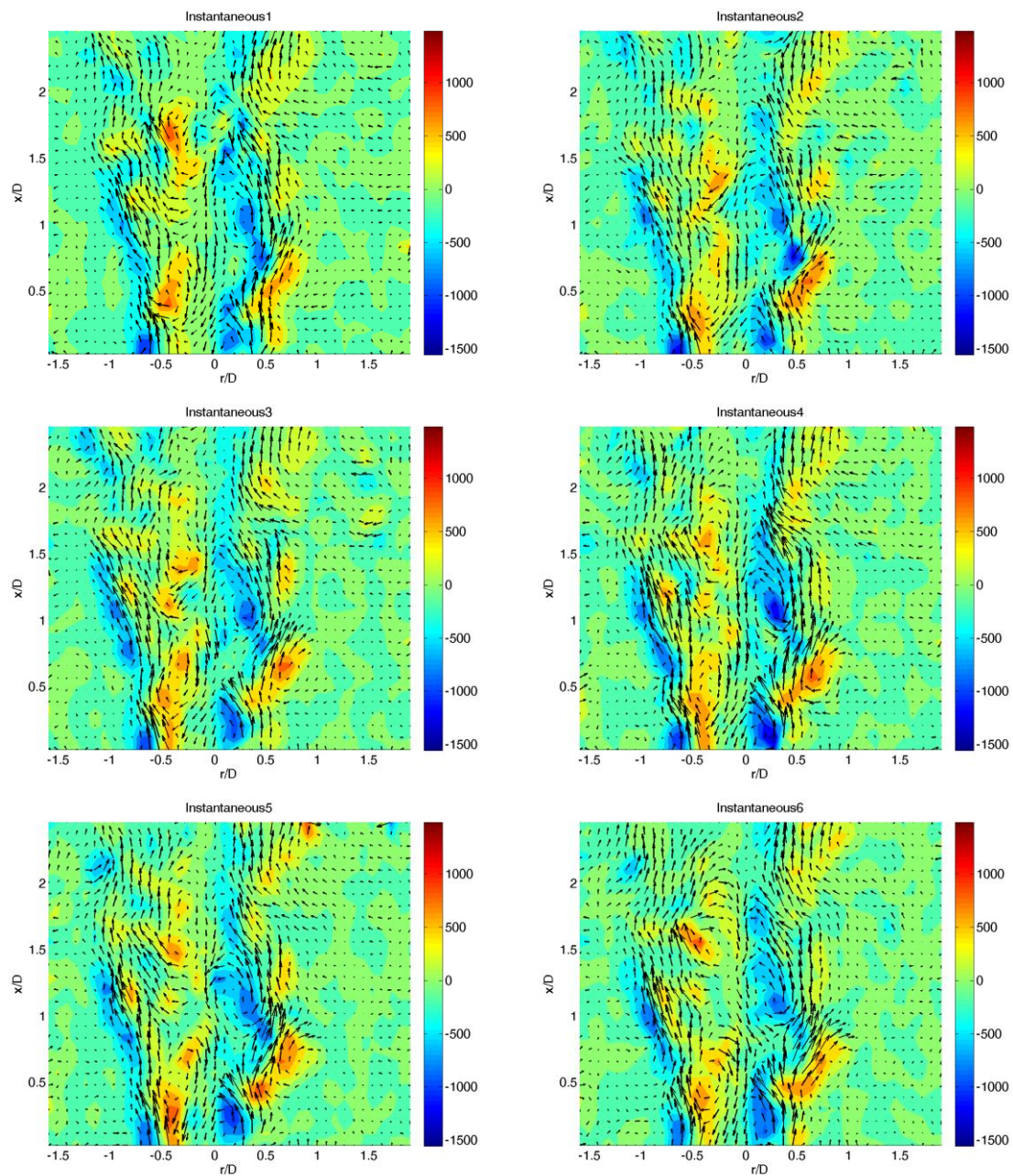




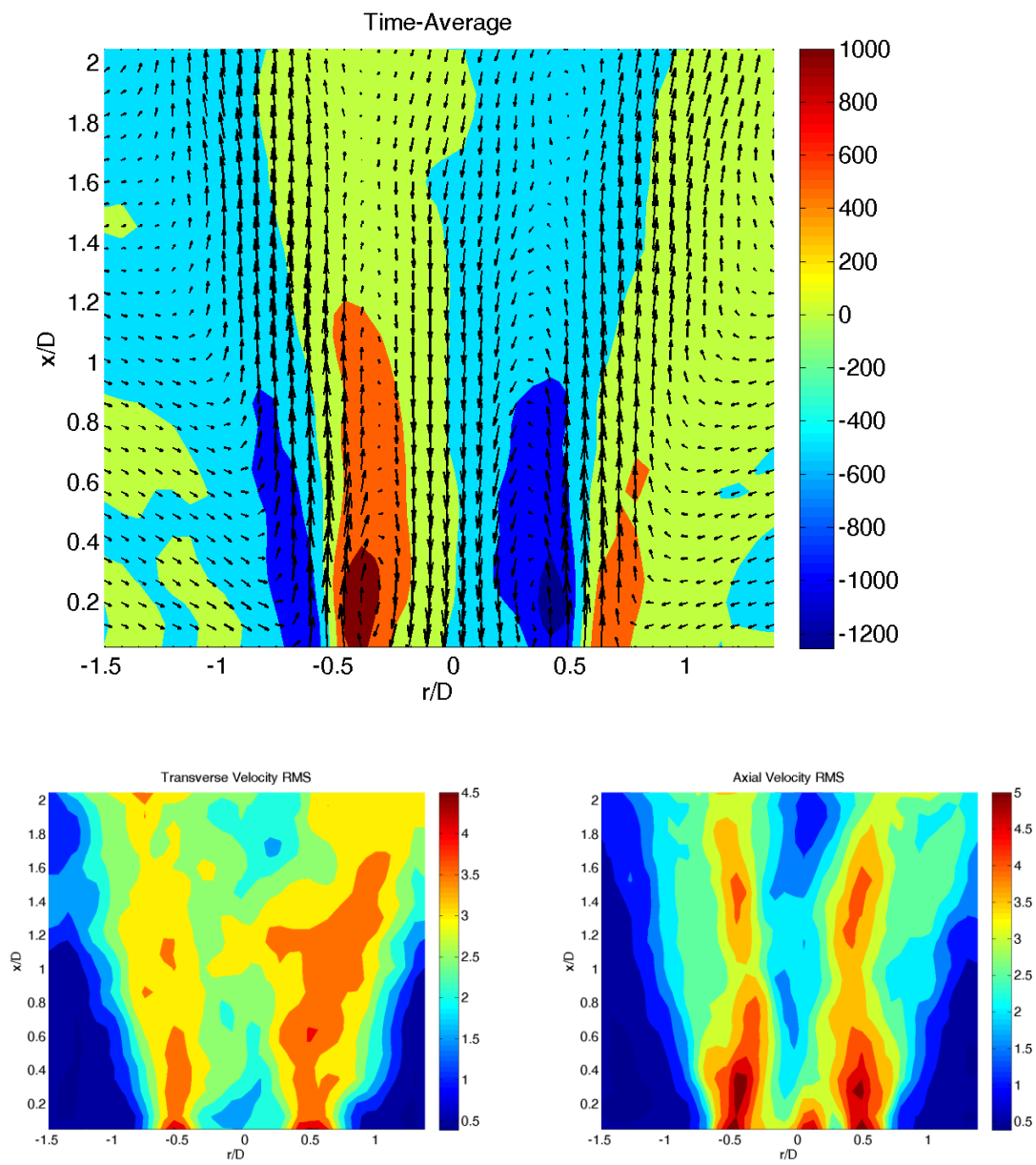
	Diagnostic	Diagnostic details	Reacting?	Swirl number	u_bulk [m/s]	Phi	Frequency [Hz]	Amplitude [mV]	Symmetry
1	PIV	r-x cut	Non-reacting	0.5	10		400	250	out-of-phase

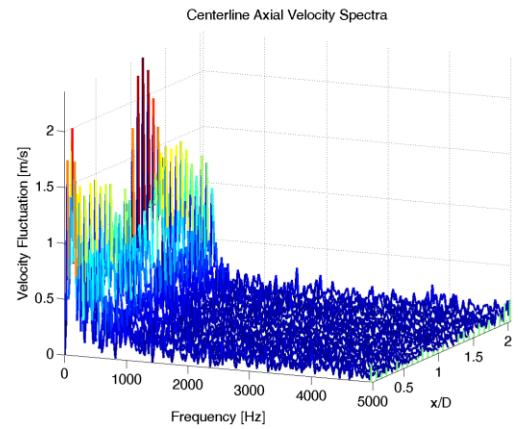
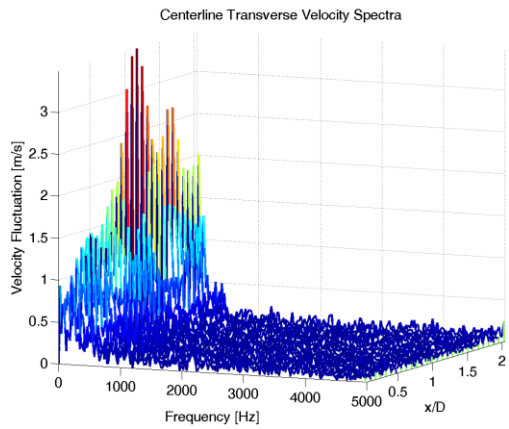
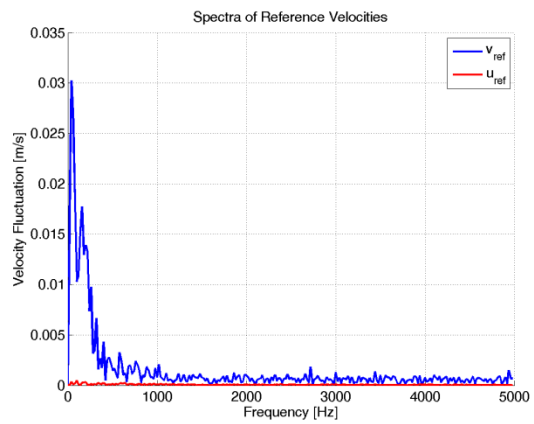
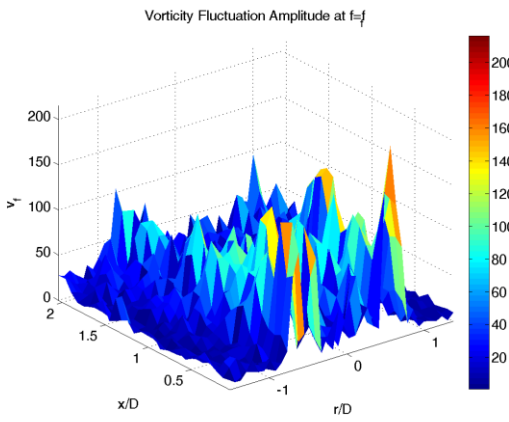
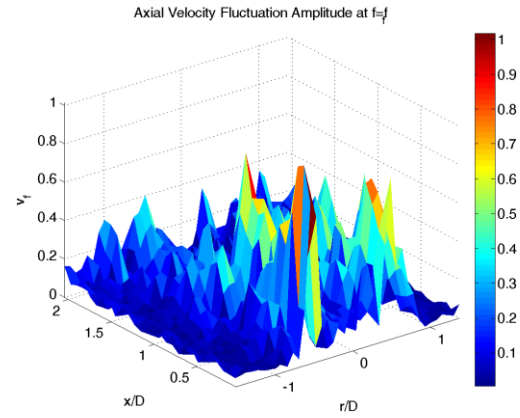
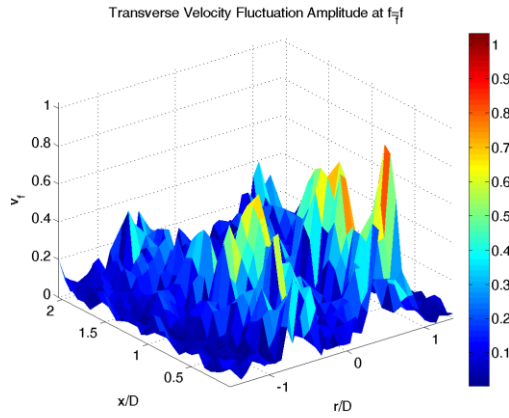


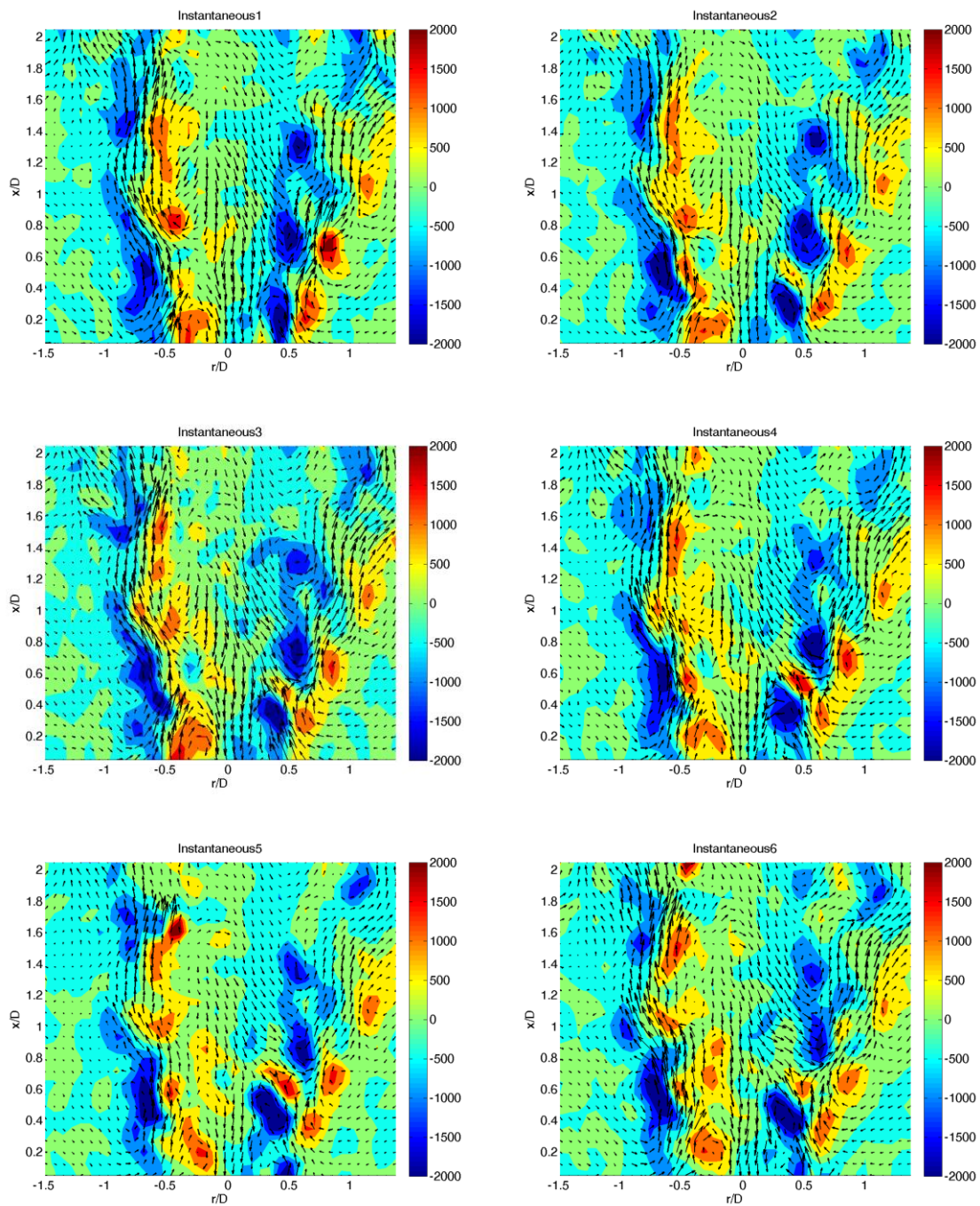




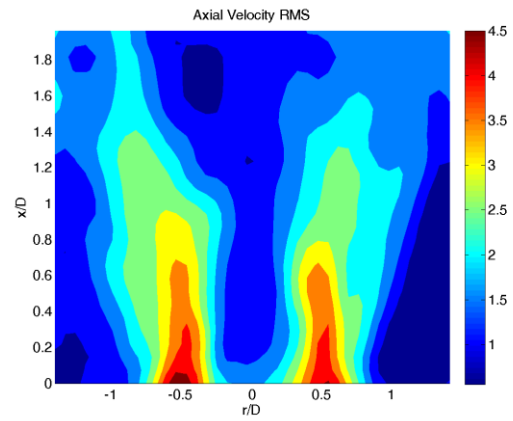
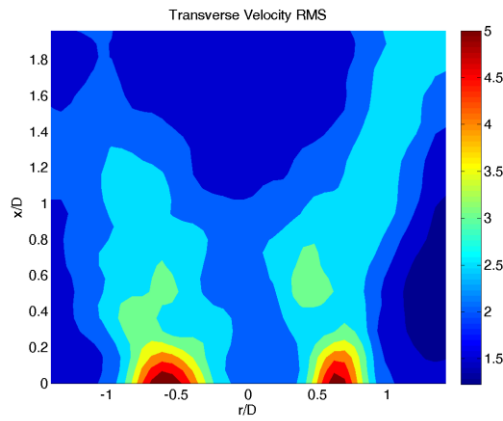
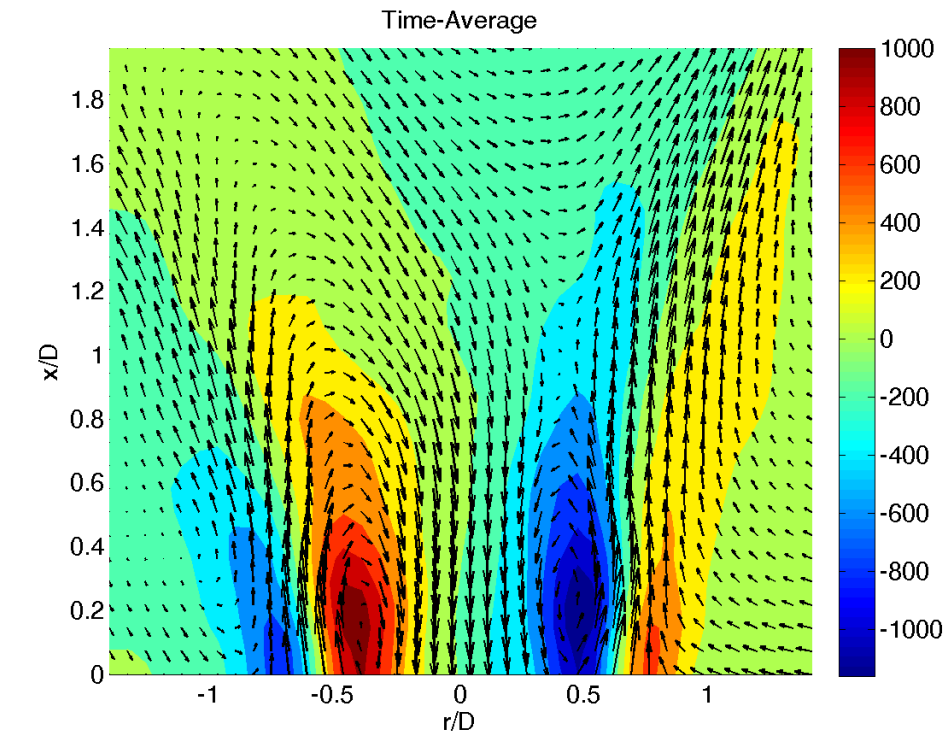
	Diagnostic	Diagnostic details	Reacting?	Swirl number	u_bulk [m/s]	Phi	Frequency [Hz]	Amplitude [mV]	Symmetry
1	PIV	r-x cut	Non-reacting	0.85	10		800	10000	Longitudinal

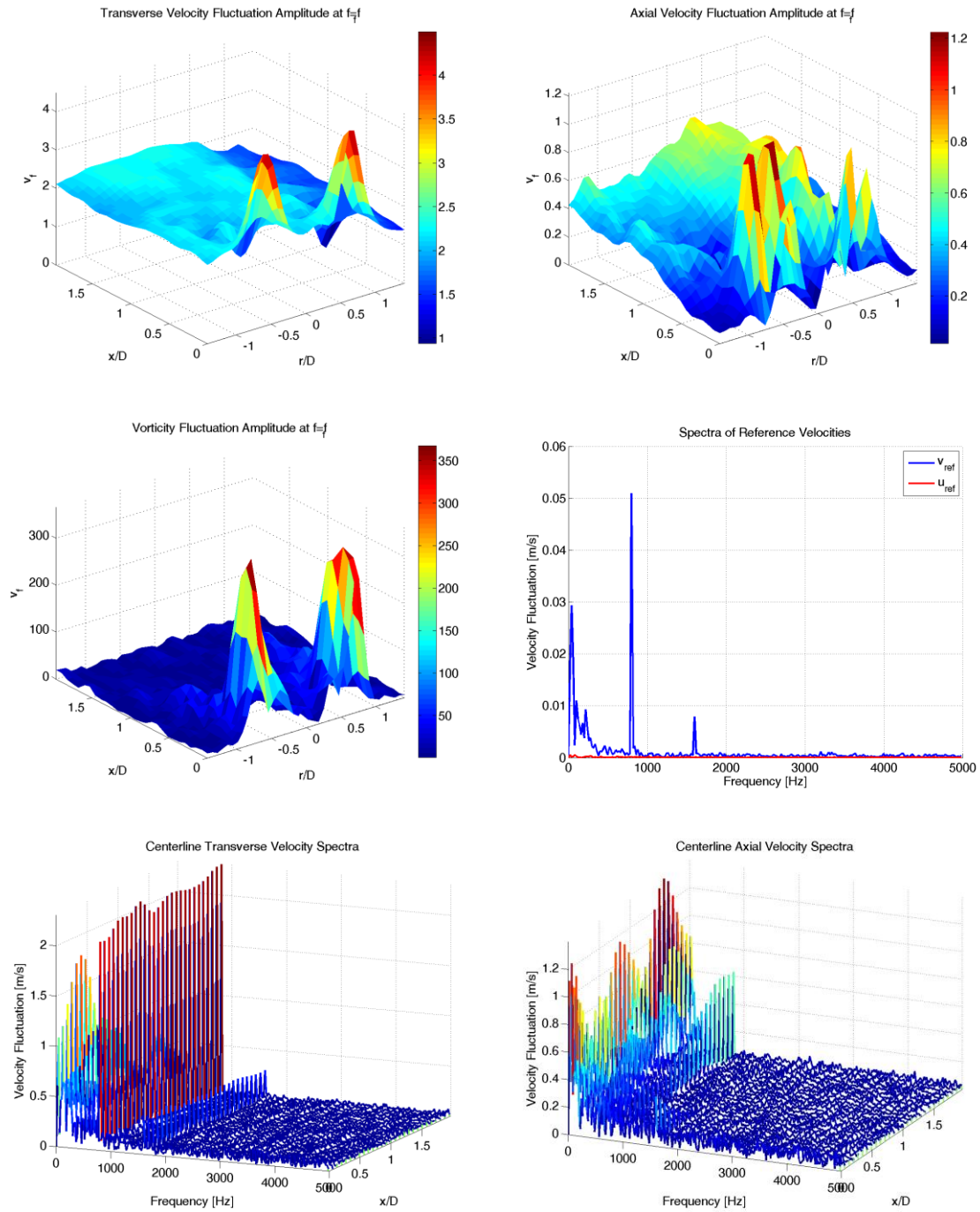


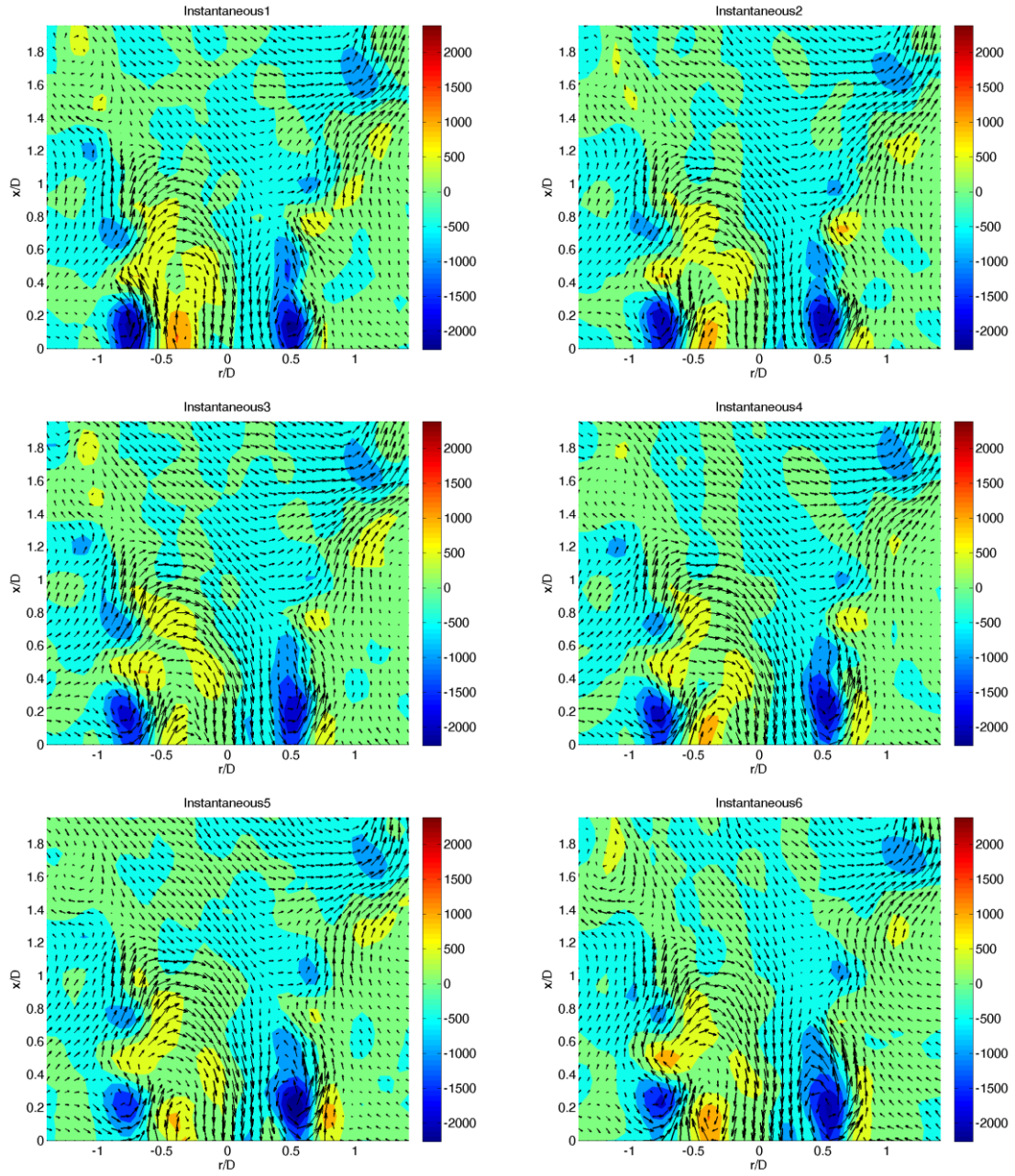




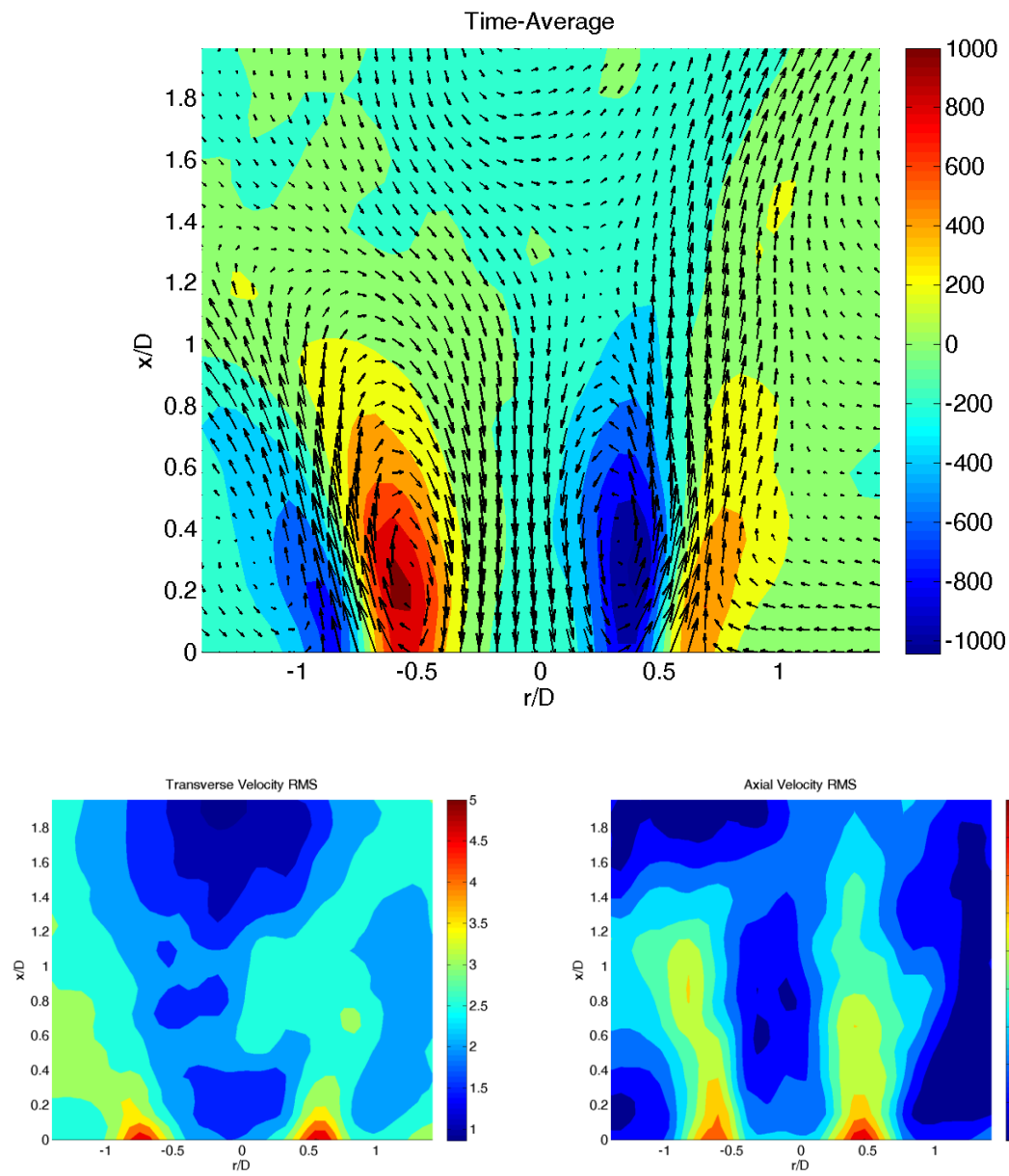
	Diagnostic	Diagnostic details	Reacting?	Swirl number	u_bulk [m/s]	Phi	Frequency [Hz]	Amplitude [mV]	Symmetry
1	PIV	r-x cut	Non-reacting	0.85	10		800	600	out-of-phase

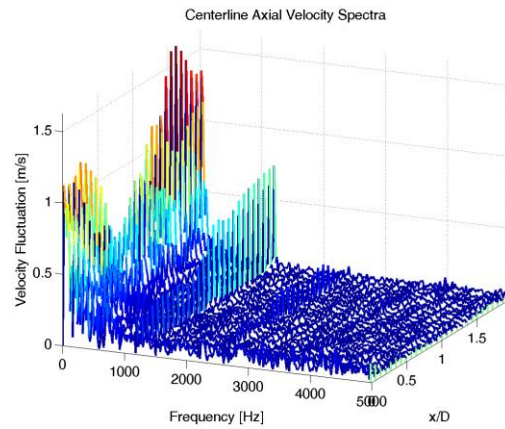
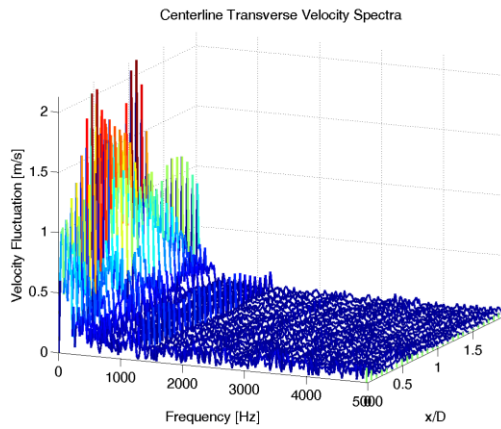
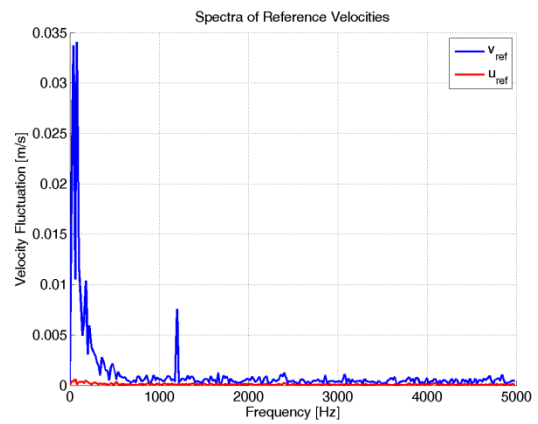
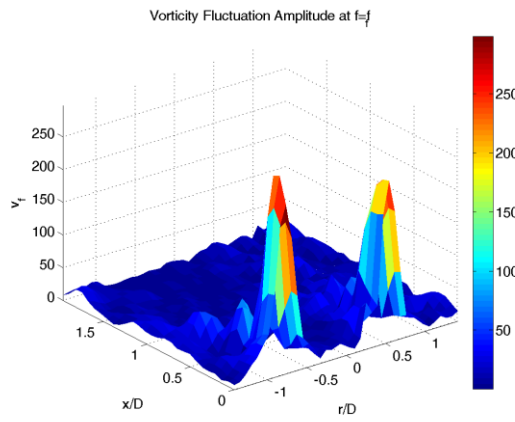
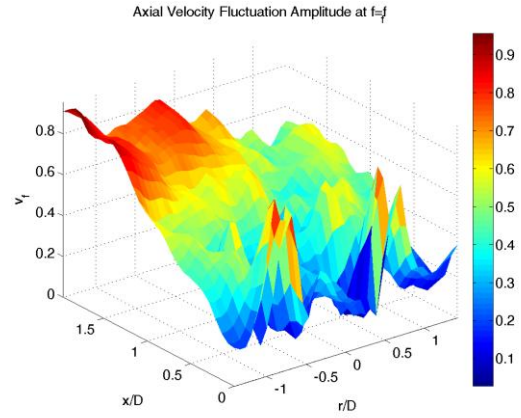
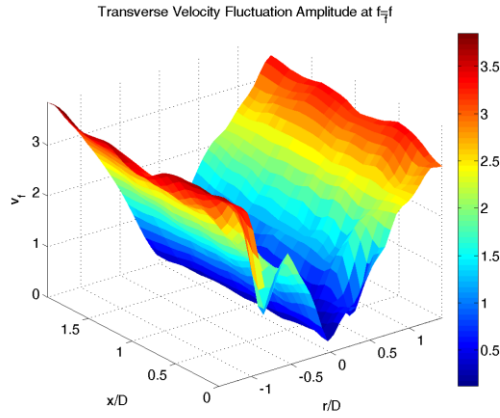


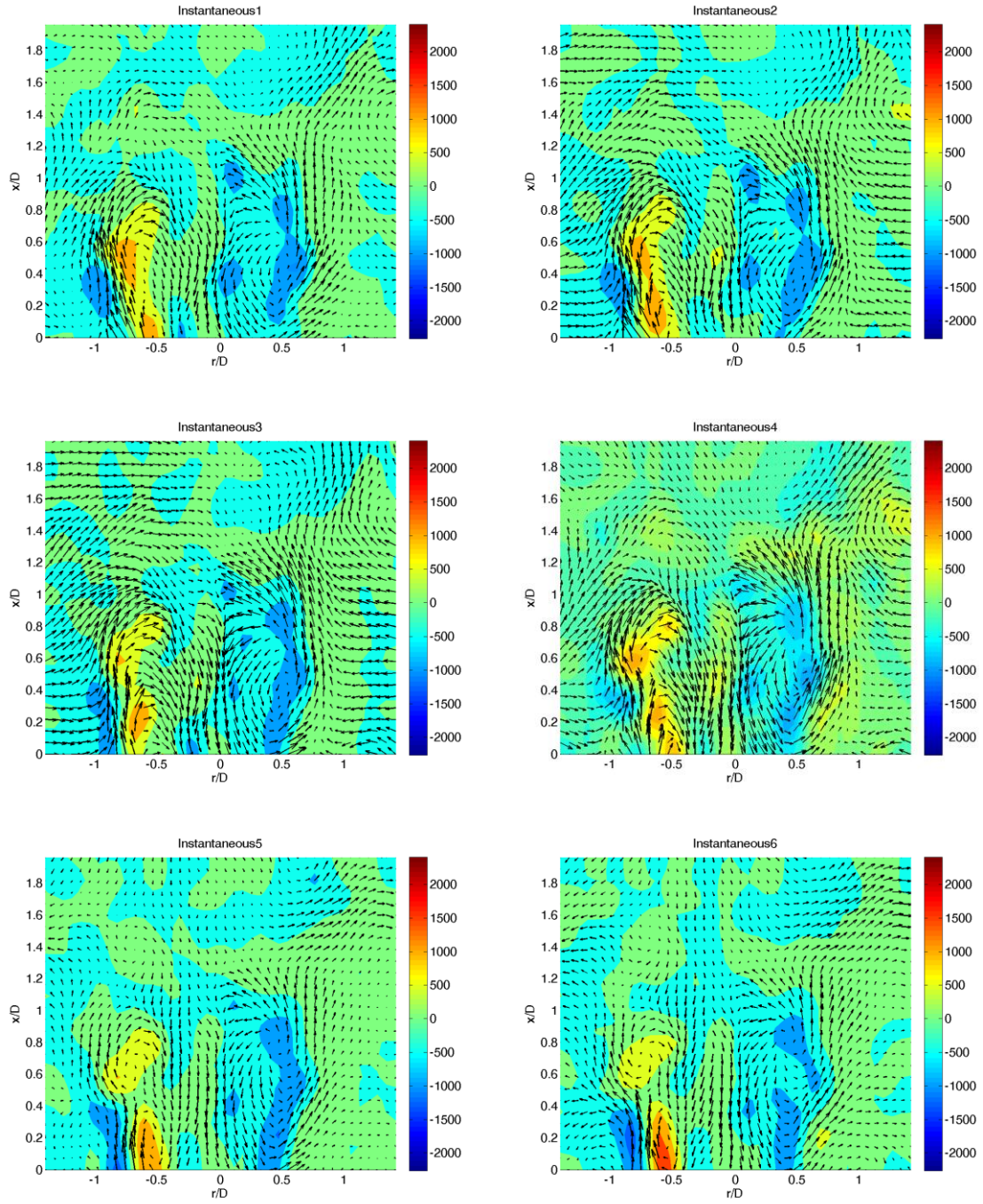




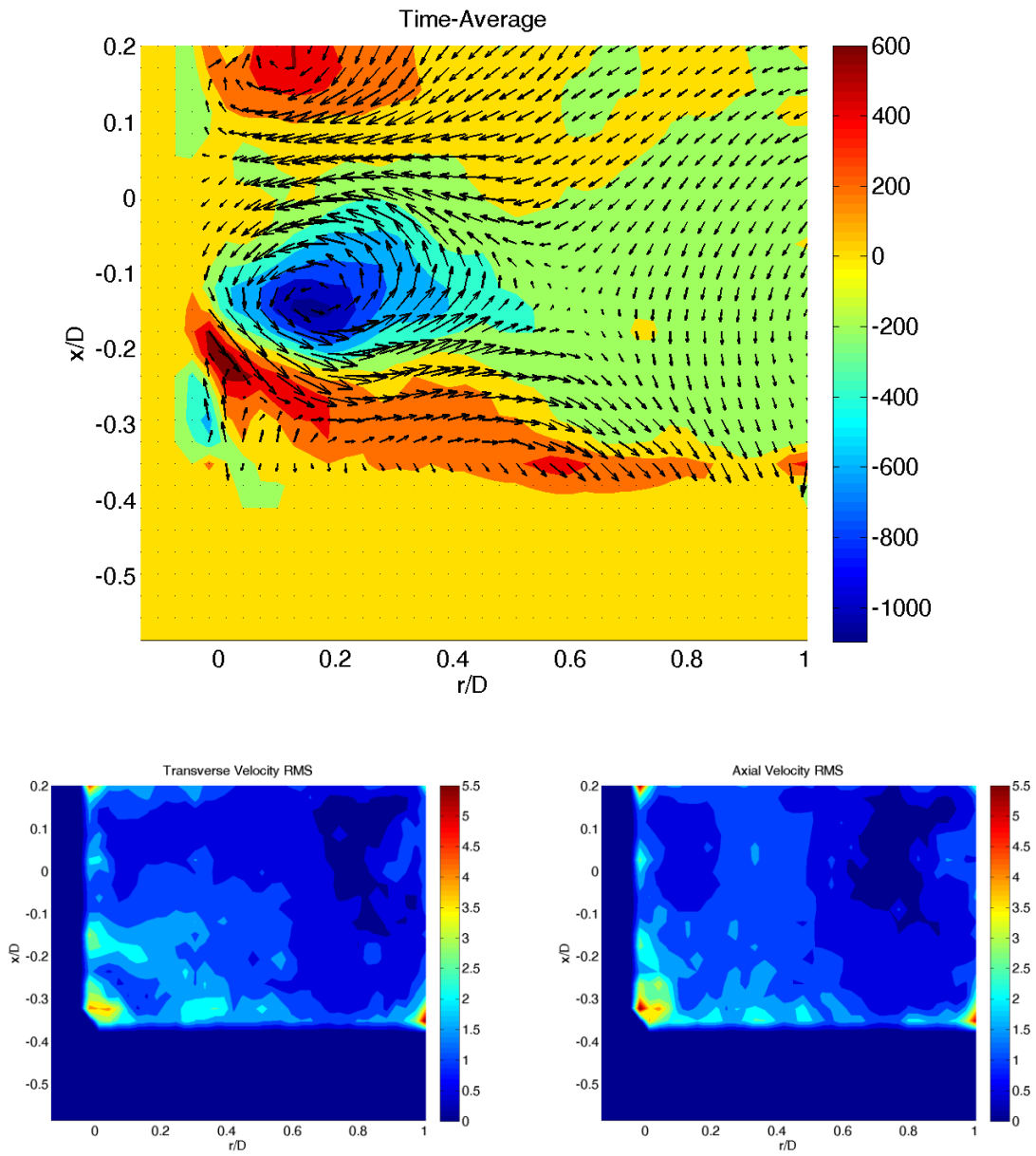
	Diagnostic	Diagnostic details	Reacting?	Swirl number	u_bulk [m/s]	Phi	Frequency [Hz]	Amplitude [mV]	Symmetry
1	PIV	r-x cut	Non-reacting	0.85	10		1200	1100	in-phase

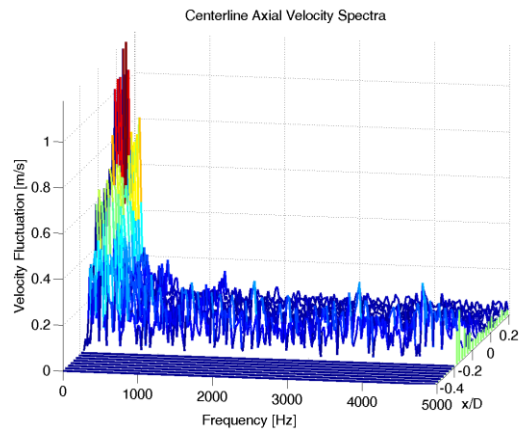
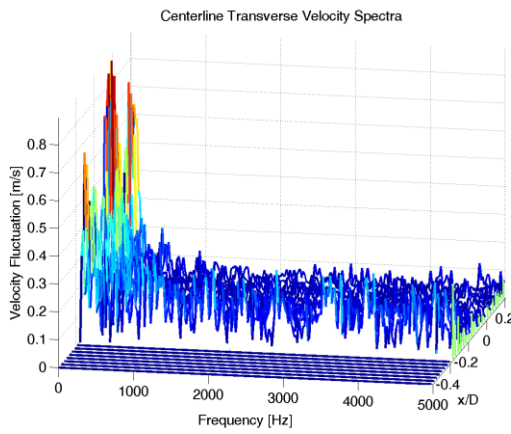
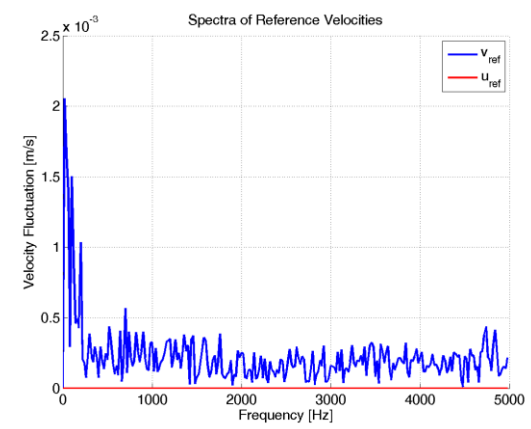
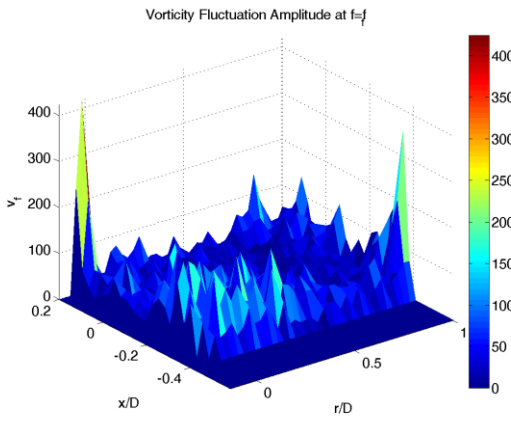
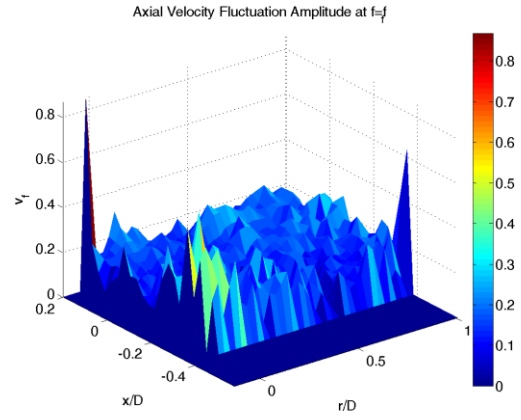
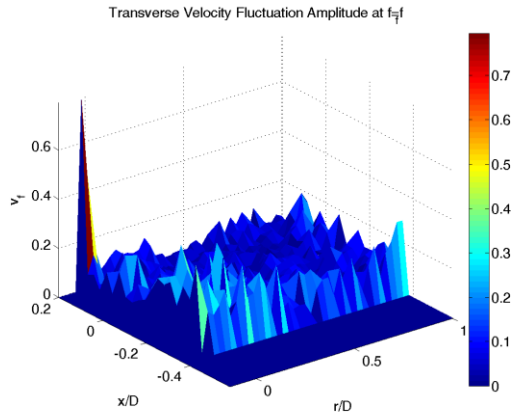


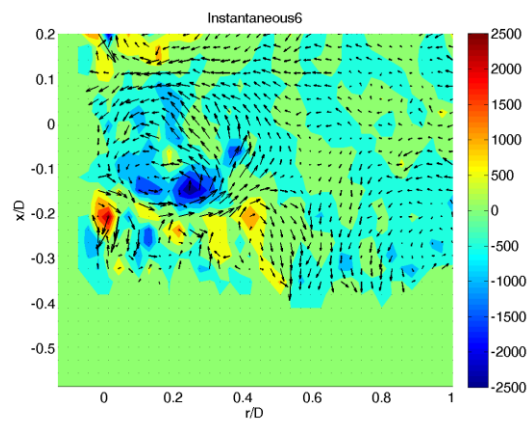
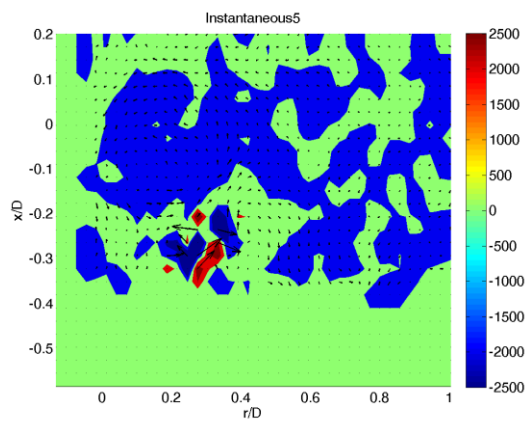
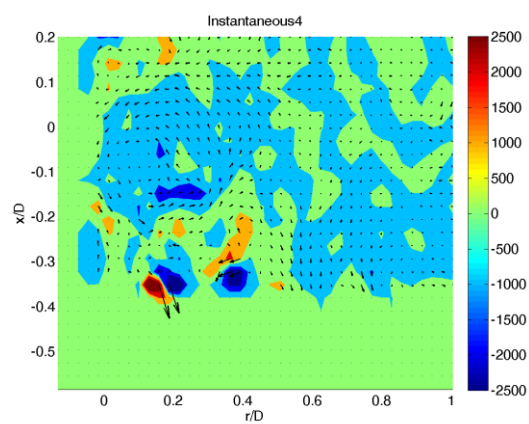
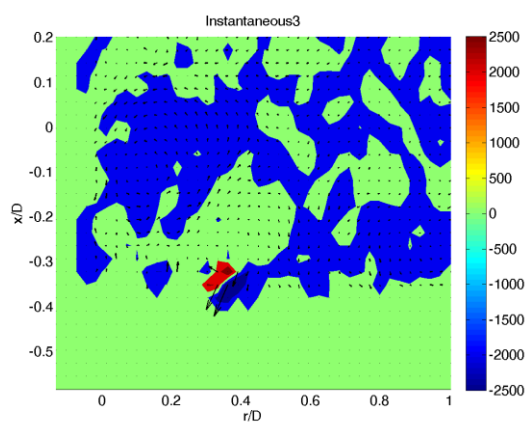
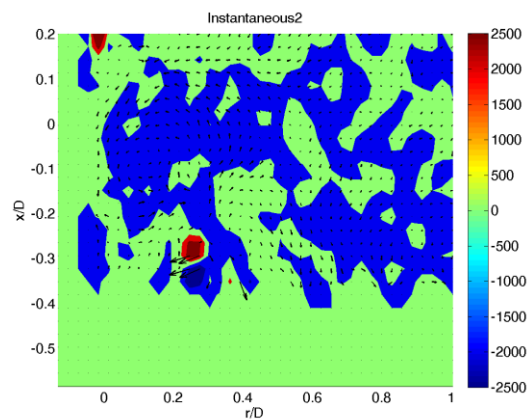
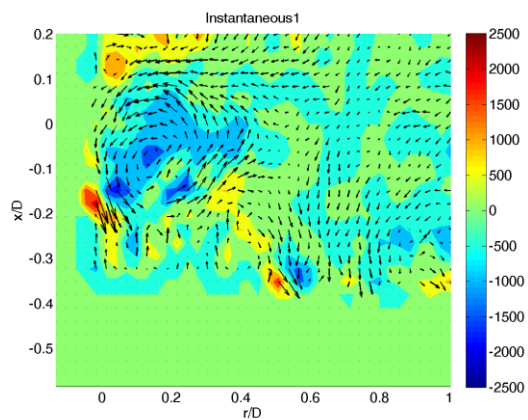




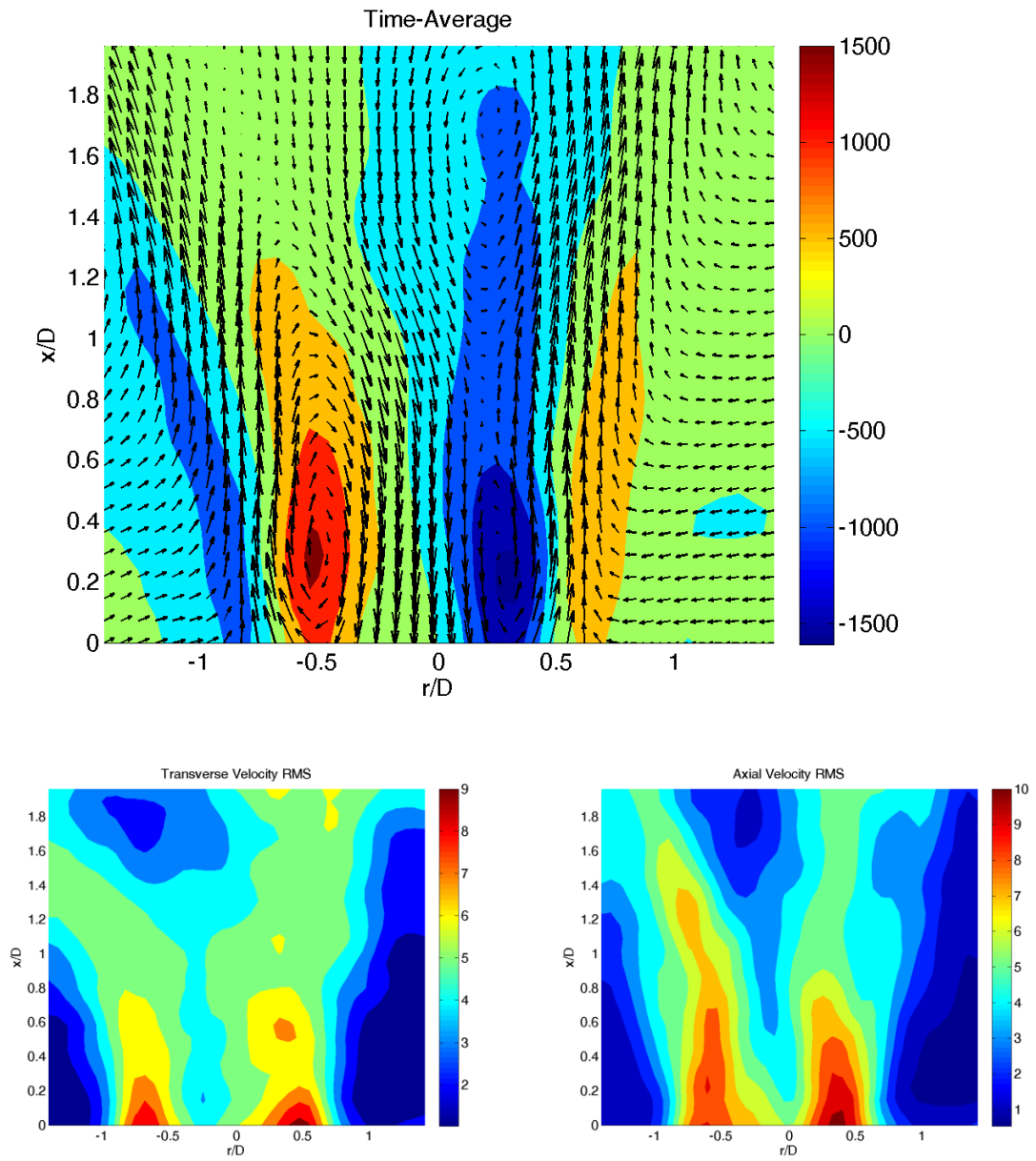
	Diagnostic	Diagnostic details	Reacting?	Swirl number	u_bulk [m/s]	Phi	Frequency [Hz]	Amplitude [mV]	Symmetry
1	PIV	r-x cut zoom	Non-reacting	0.85	10		1200	1000	out-of-phase

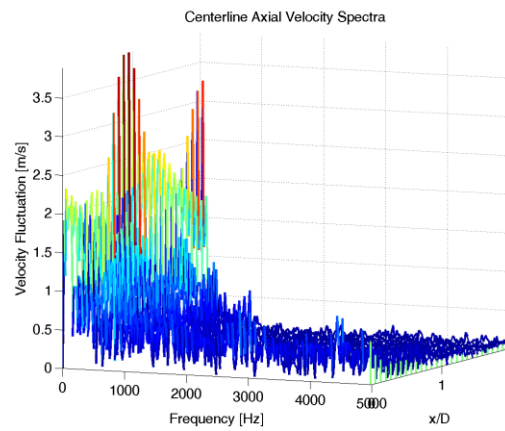
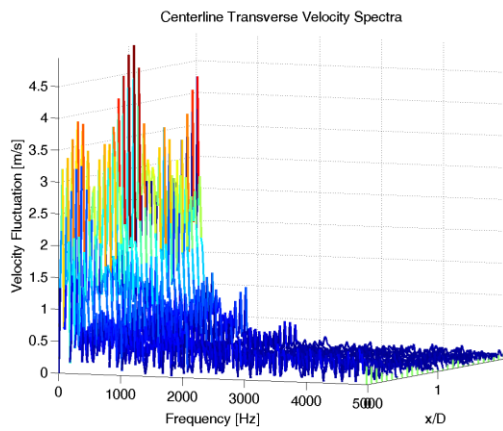
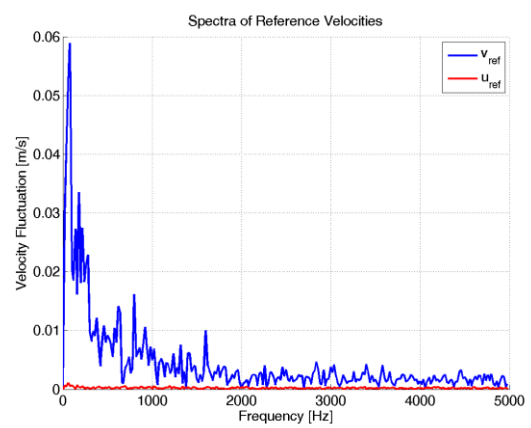
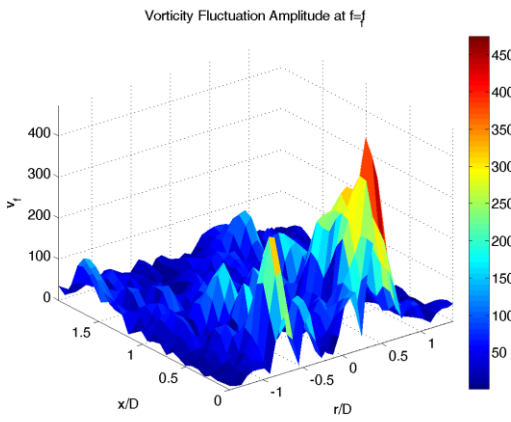
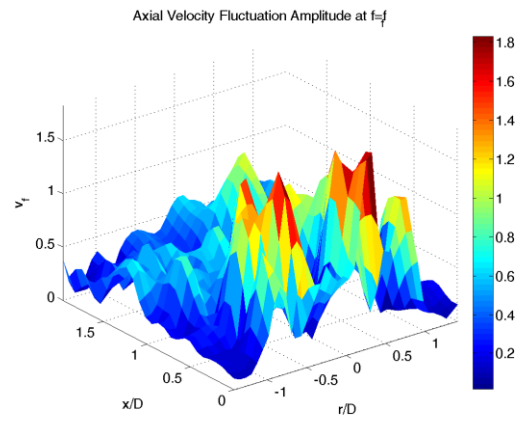
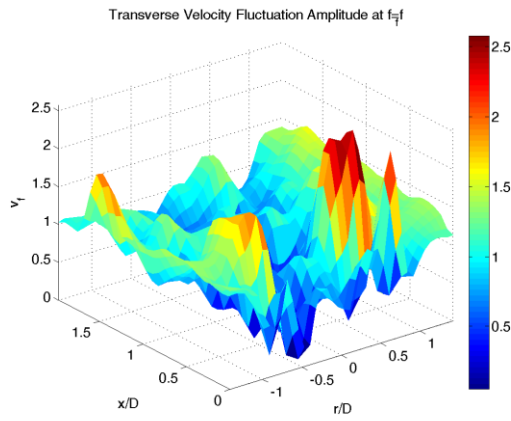


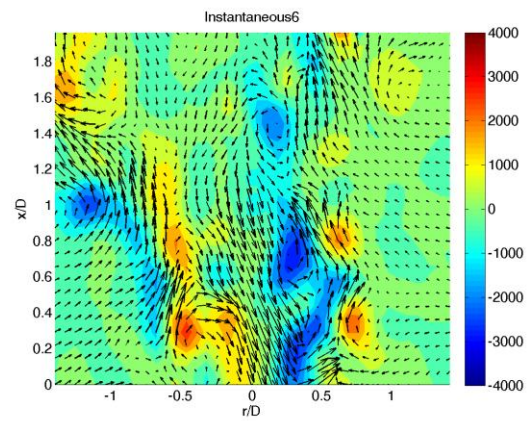
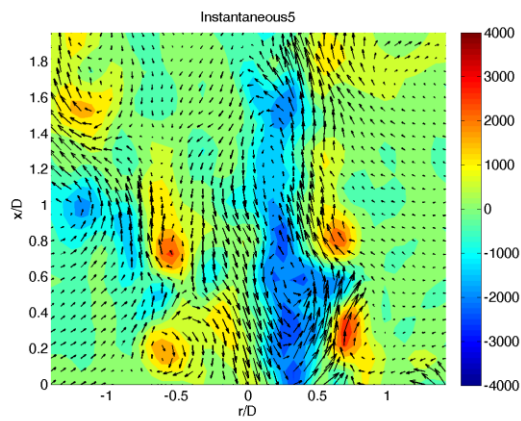
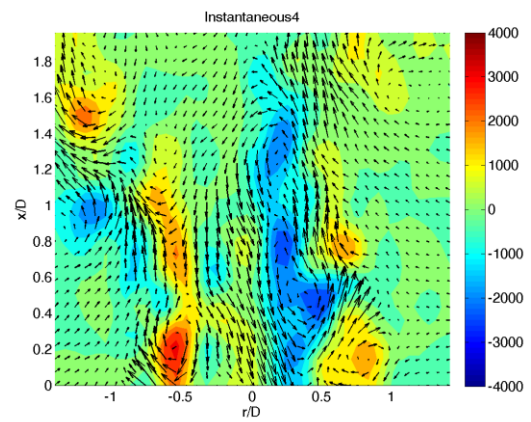
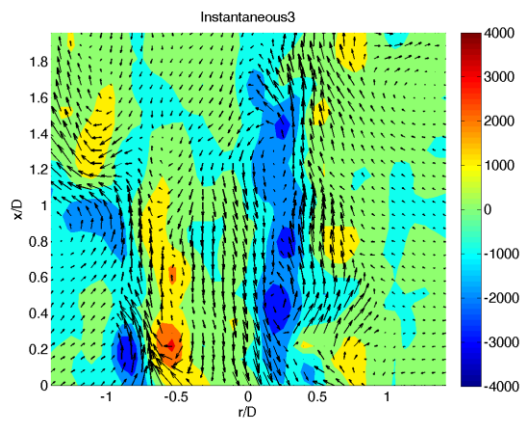
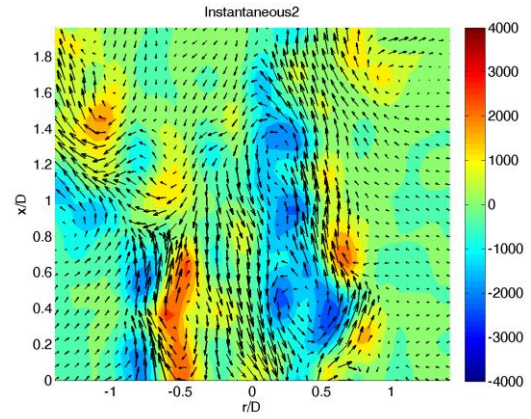
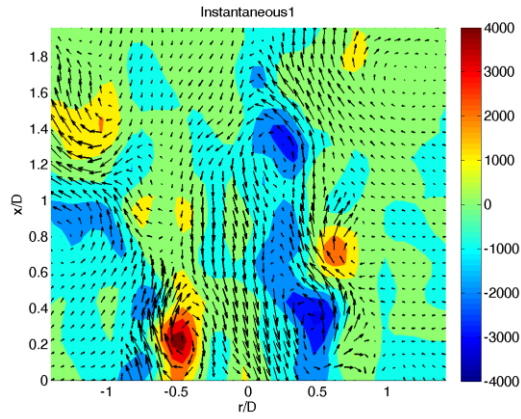




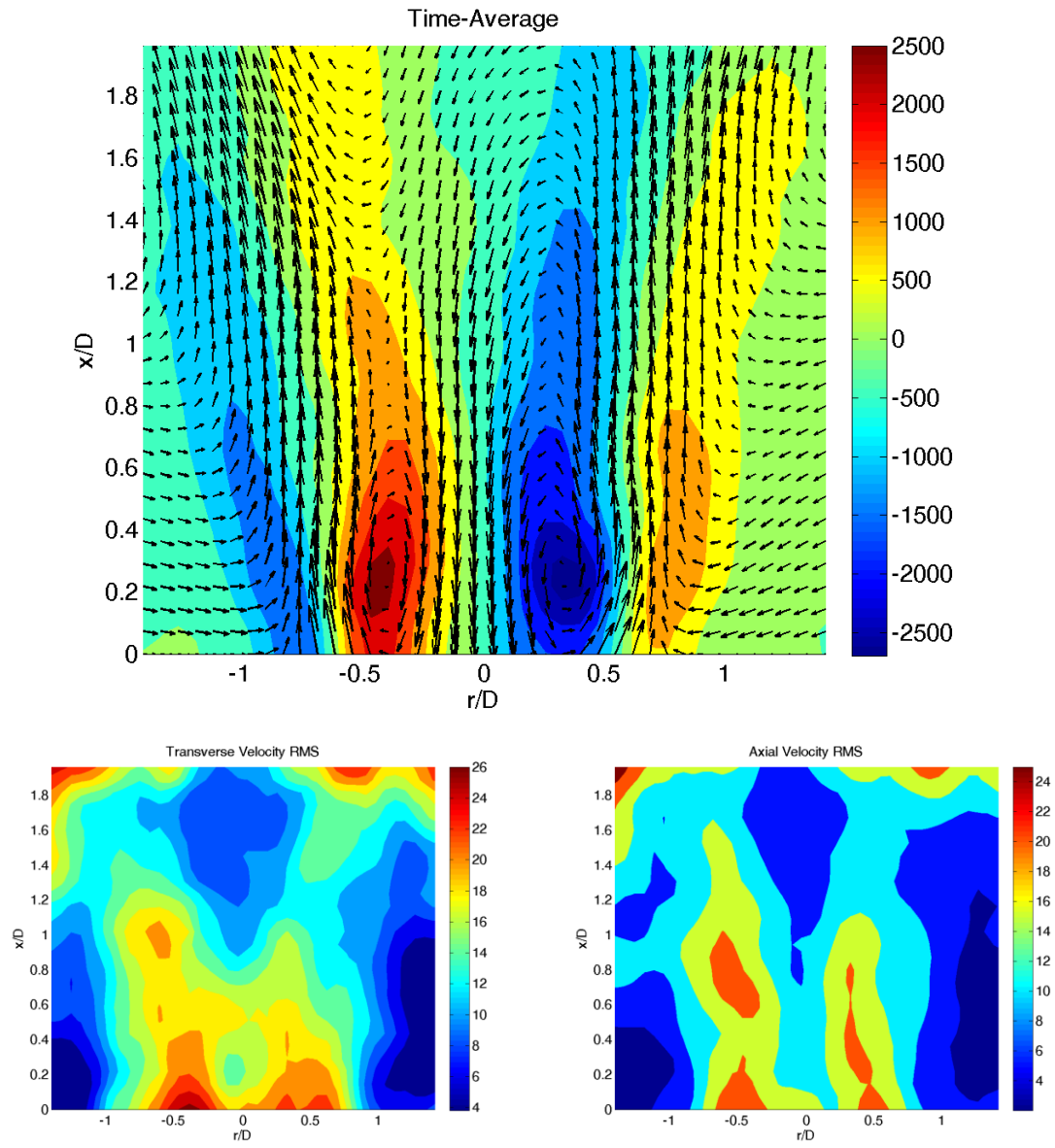
	Diagnostic	Diagnostic details	Reacting?	Swirl number	u_bulk [m/s]	Phi	Frequency [Hz]	Amplitude [mV]	Symmetry
1	PIV	r-x cut	Non-reacting	0.85	20		800	1000	in-phase

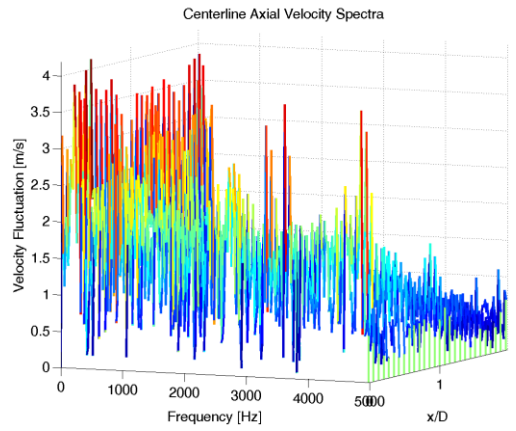
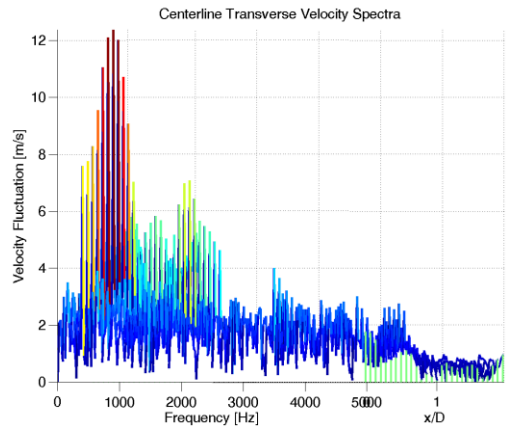
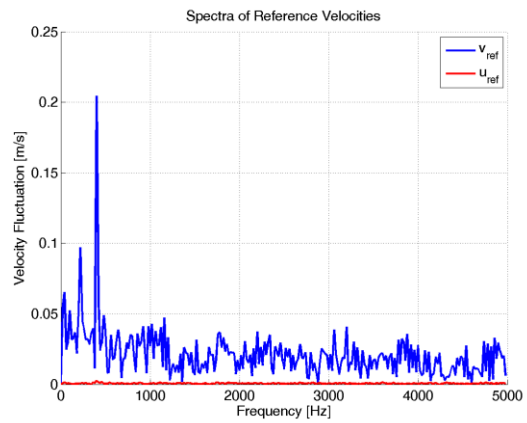
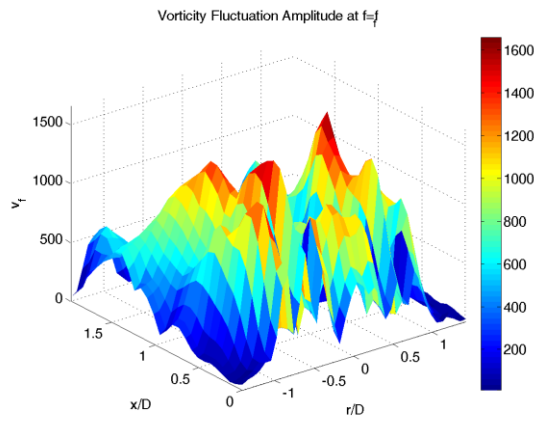
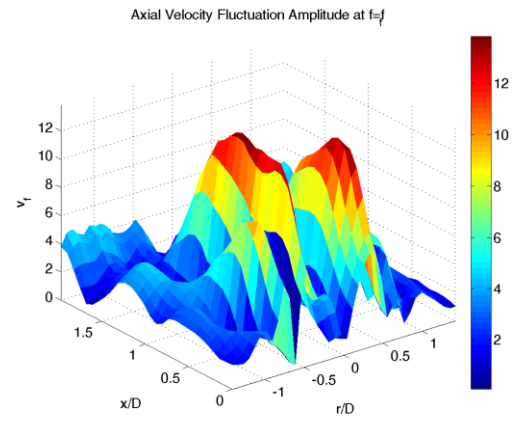
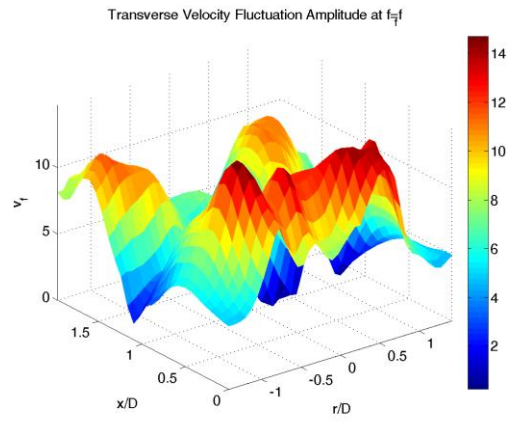


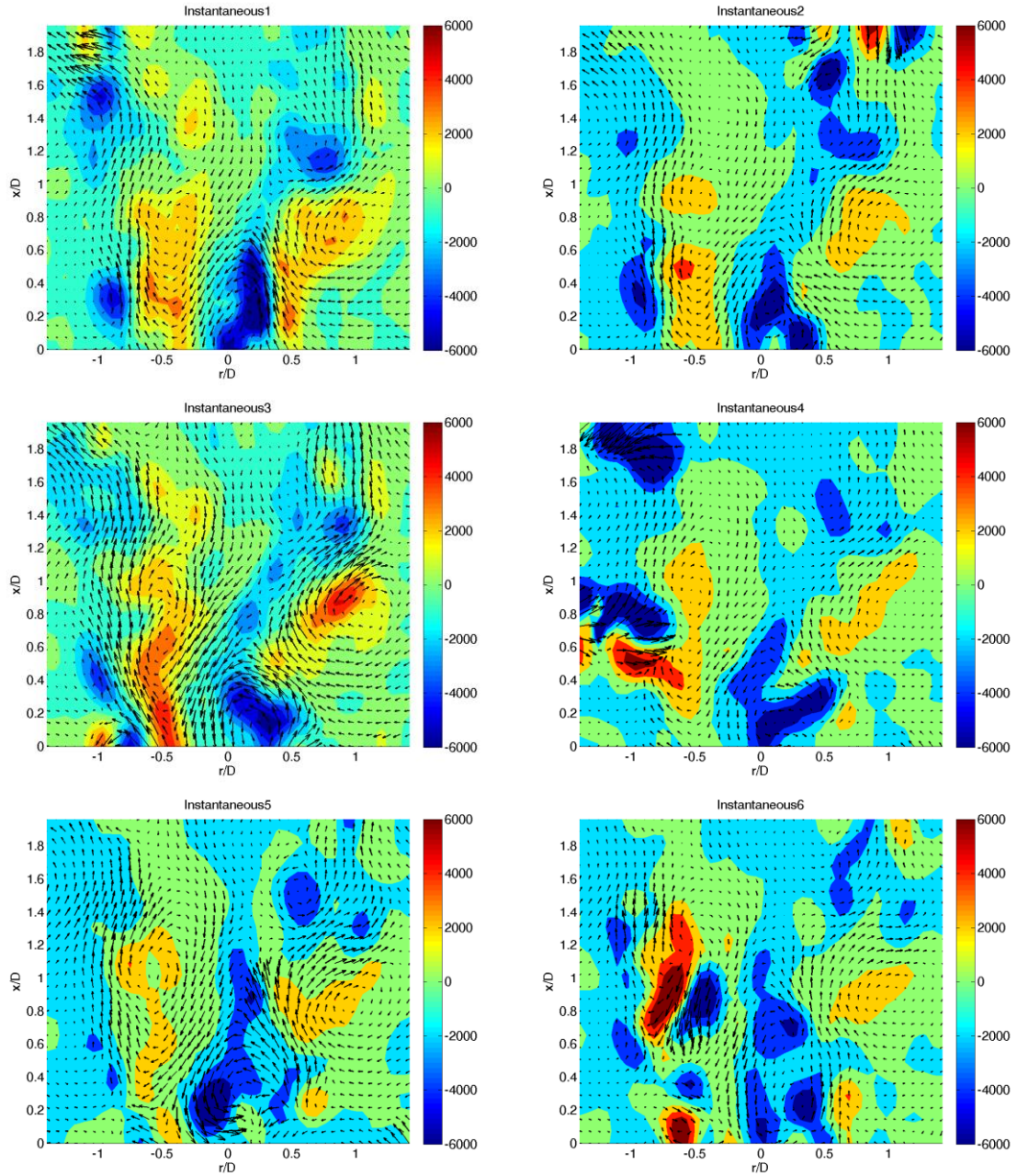




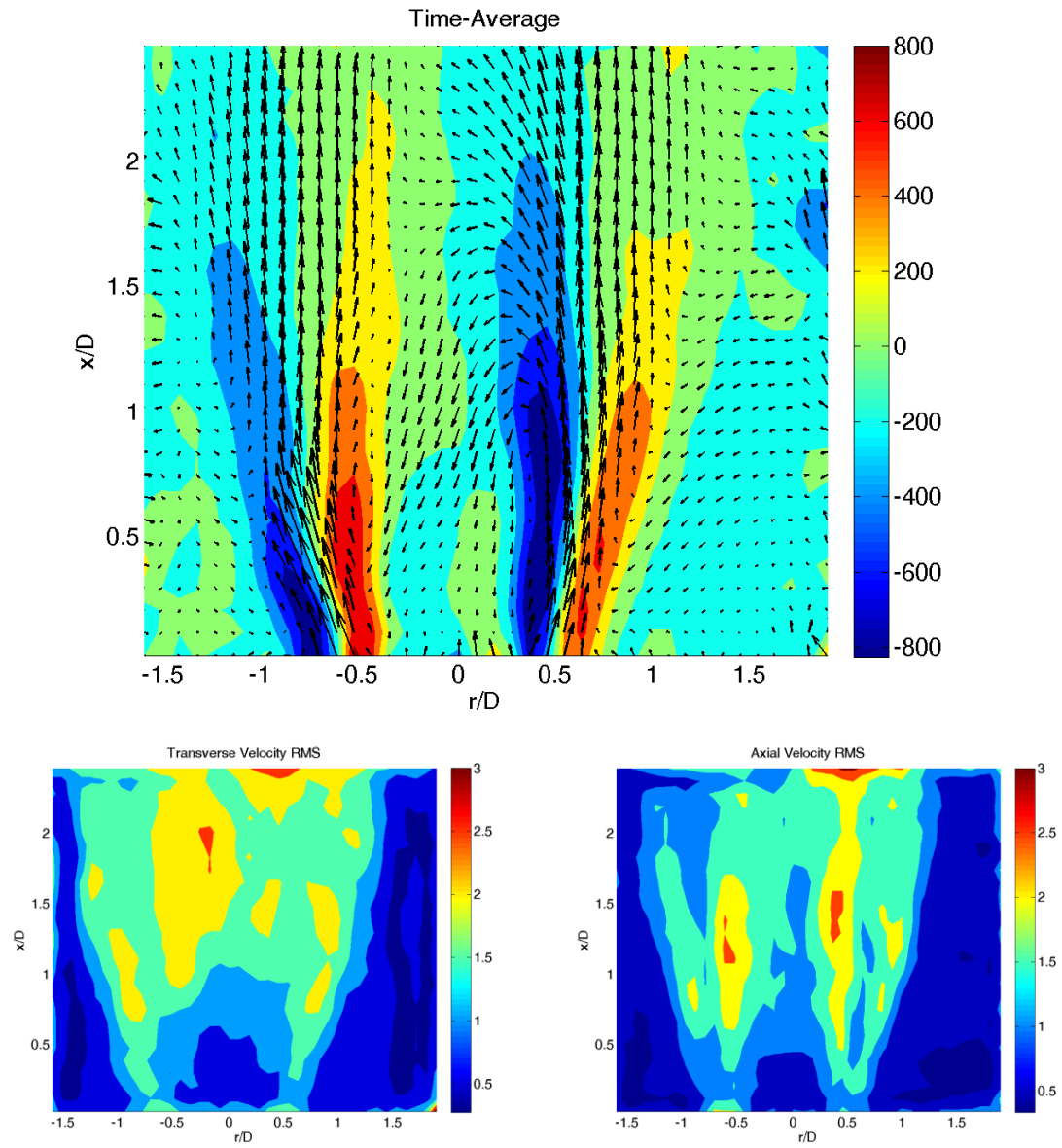
	Diagnostic	Diagnostic details	Reacting?	Swirl number	u_bulk [m/s]	Phi	Frequency [Hz]	Amplitude [mV]	Symmetry
1	PIV	r-x cut	Non-reacting	0.85	40		400	1000	out-of-phase

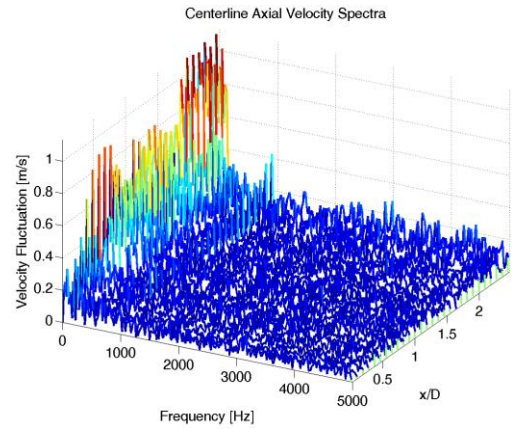
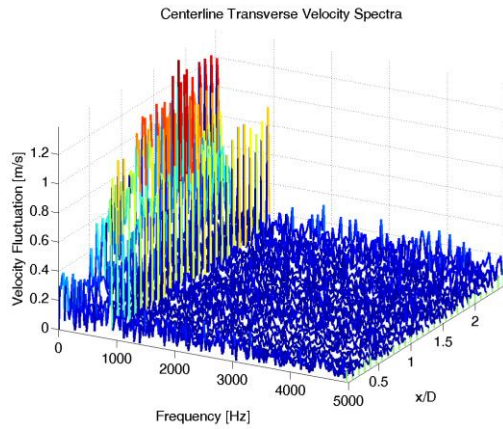
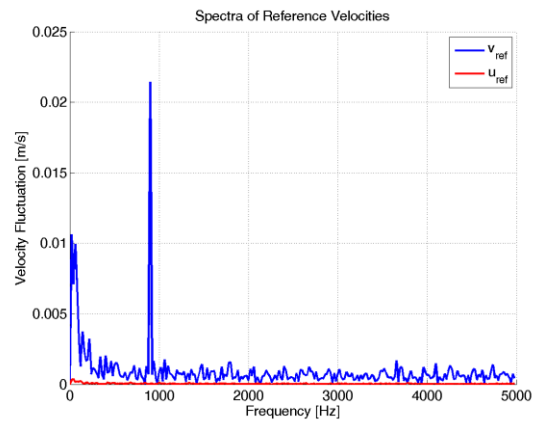
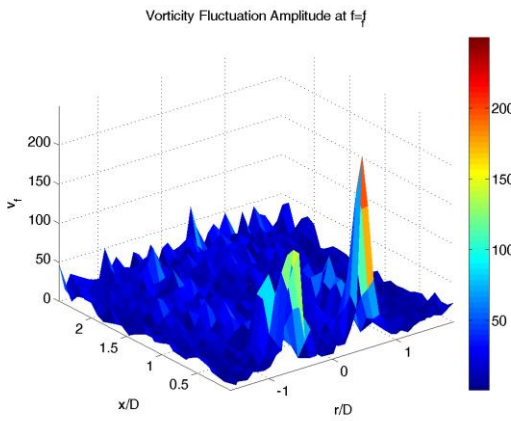
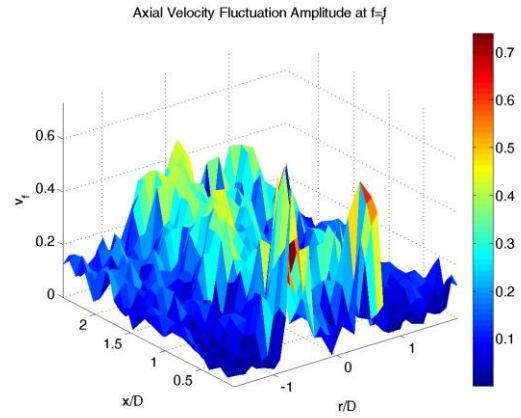
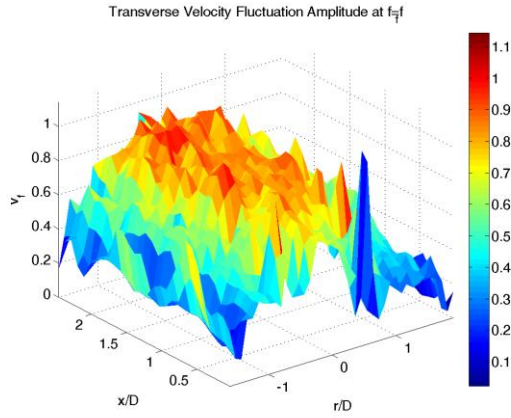


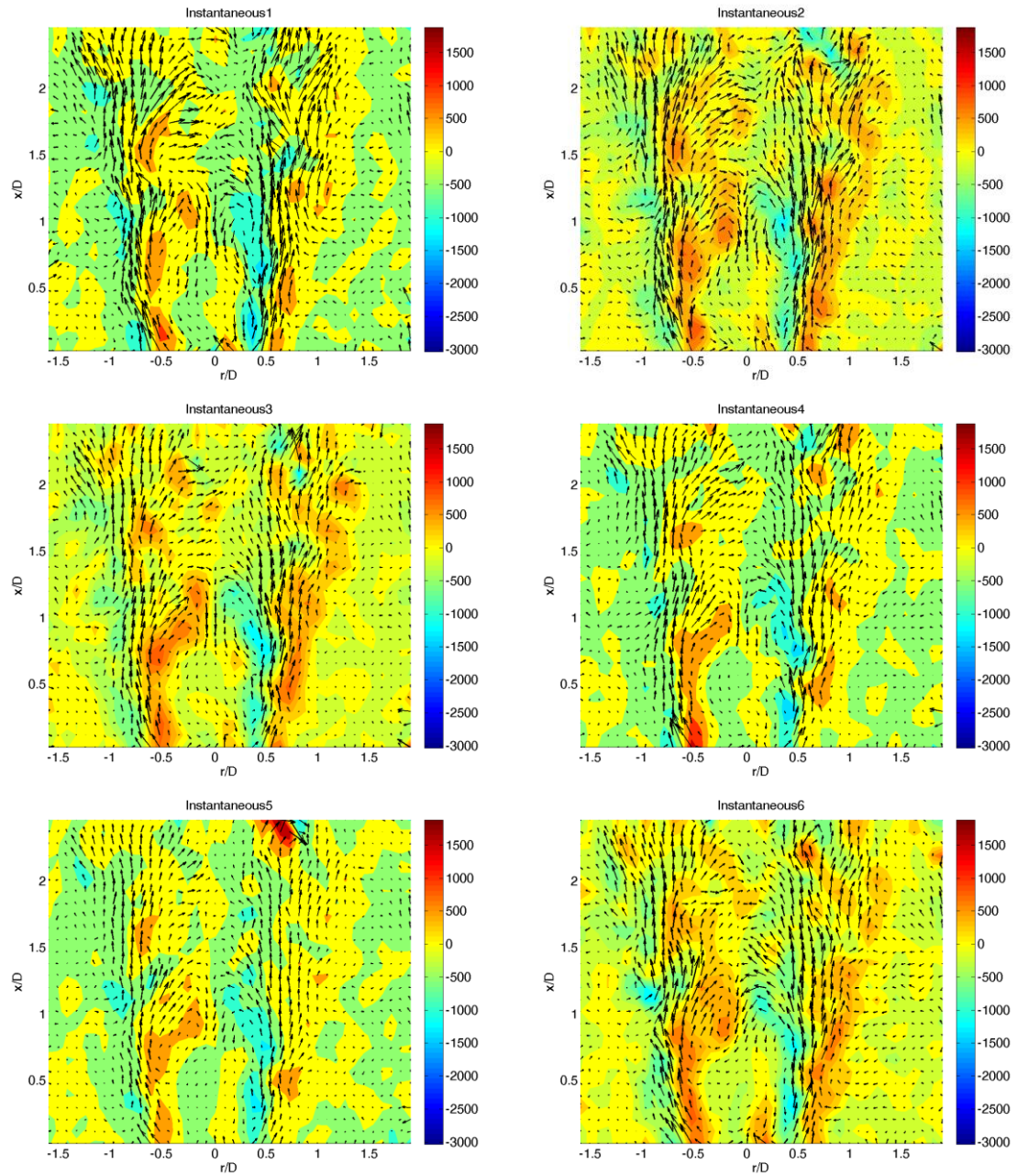




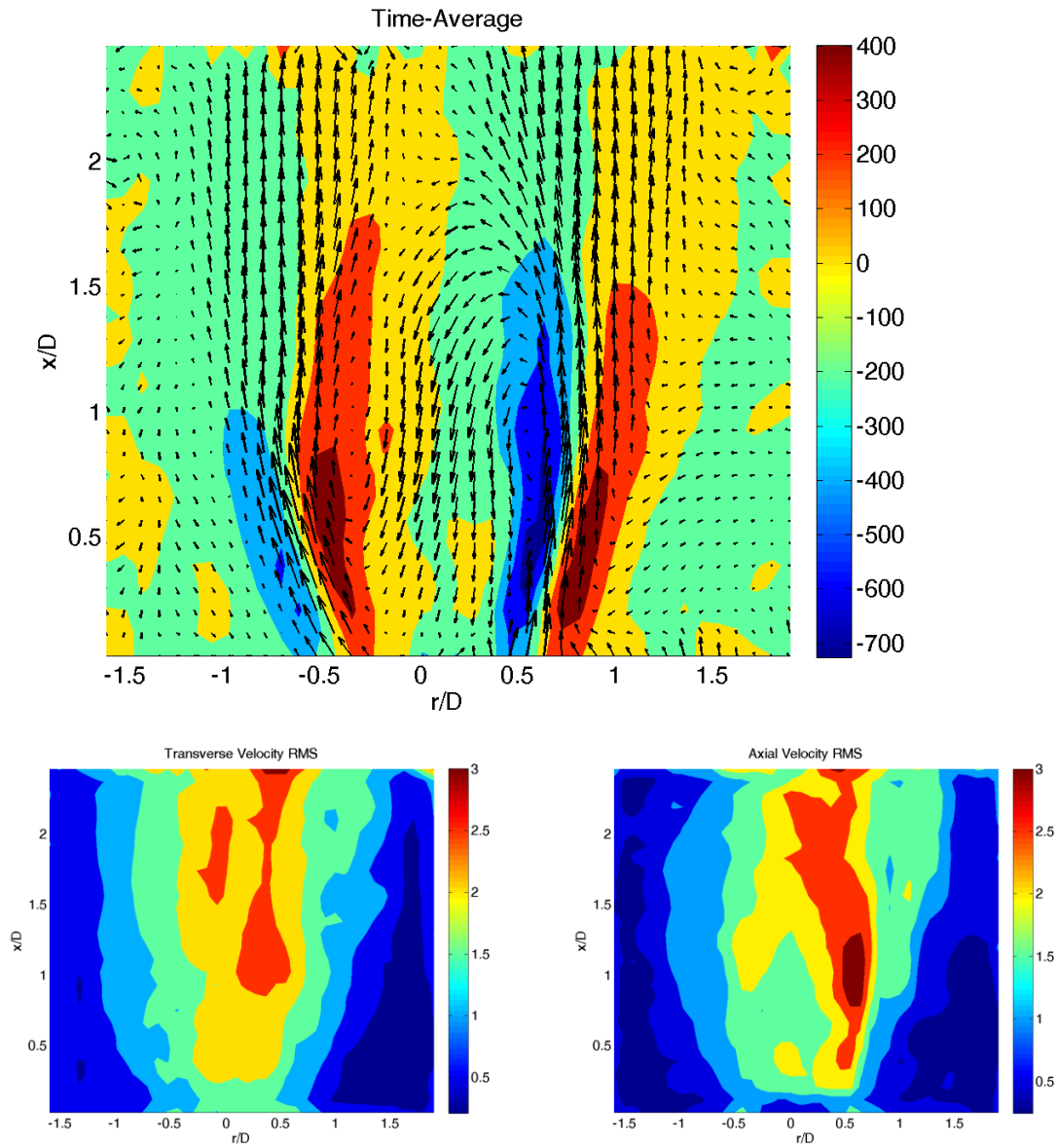
	Diagnostic	Diagnostic details	Reacting?	Swirl number	u_bulk [m/s]	Phi	Frequency [Hz]	Amplitude [mV]	Symmetry
1	PIV	r-x cut	Reacting	0.5	10		900	600	out-of-phase

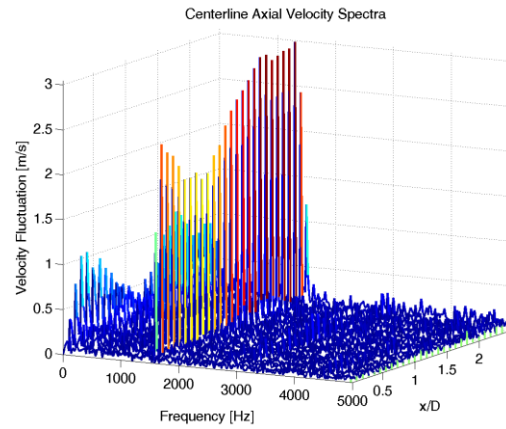
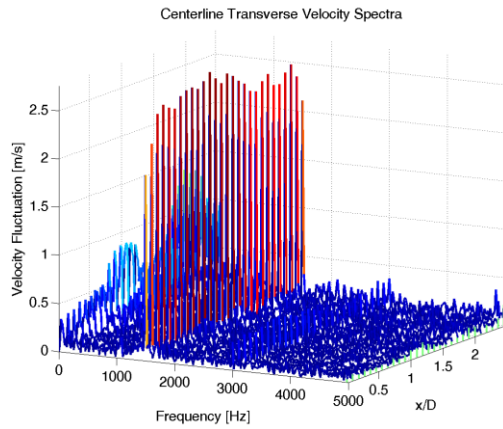
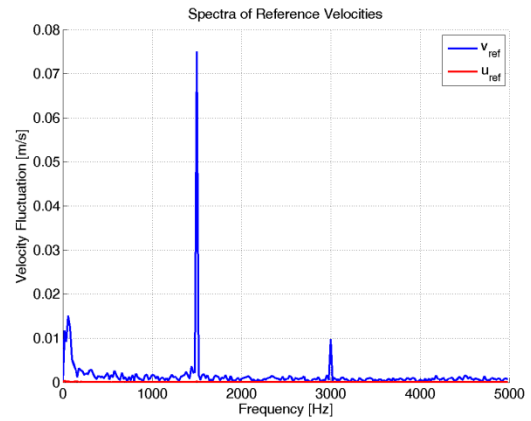
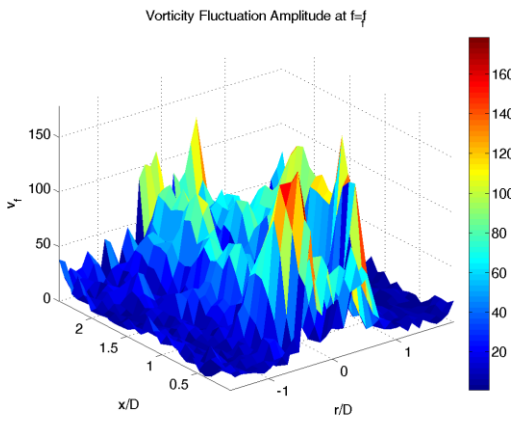
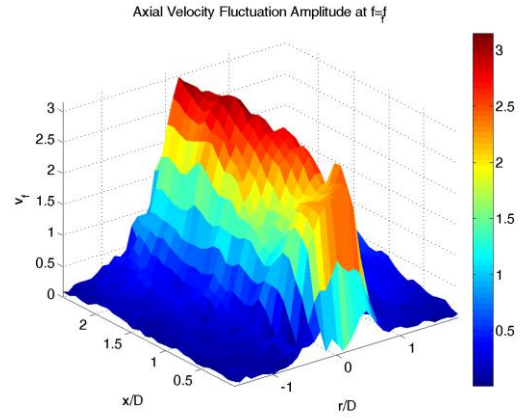
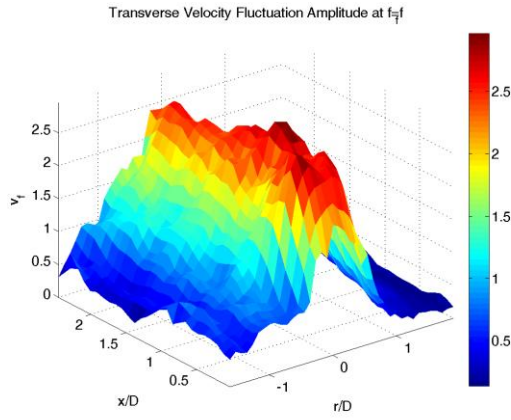


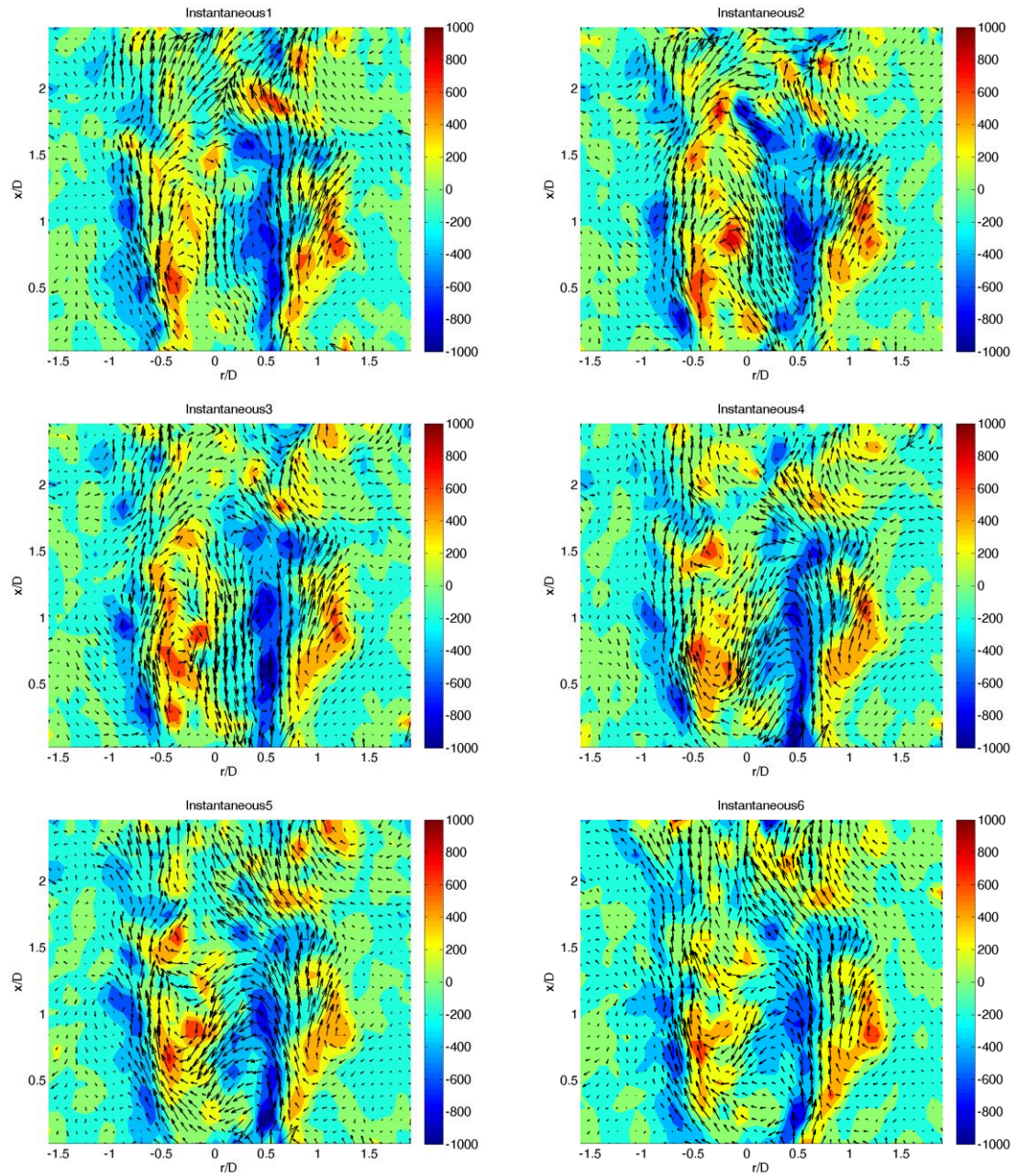




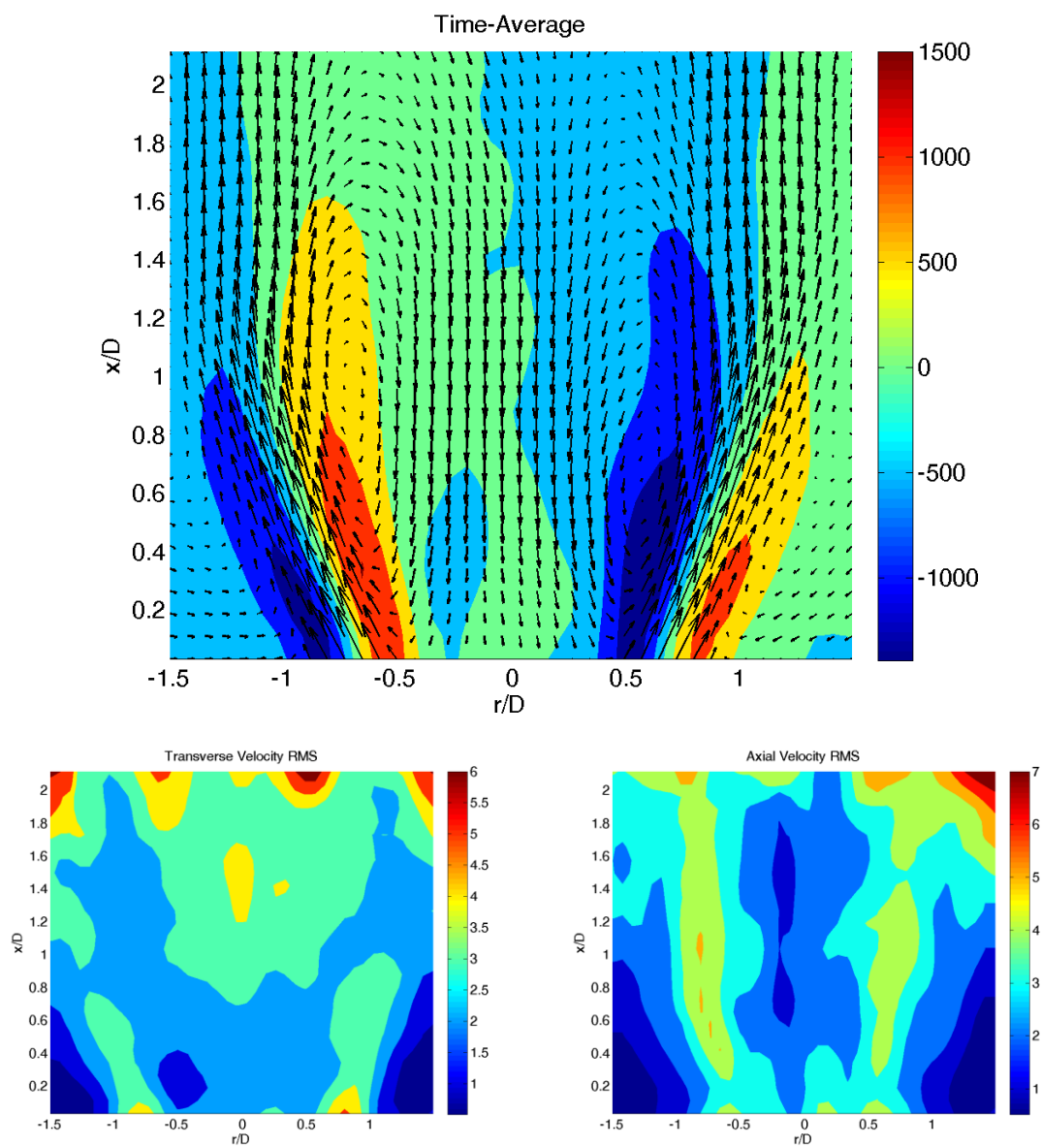
	Diagnostic	Diagnostic details	Reacting?	Swirl number	u_bulk [m/s]	Phi	Frequency [Hz]	Amplitude [mV]	Symmetry
1	PIV	r-x cut	Reacting	0.5	10		1500	1300	in-phase

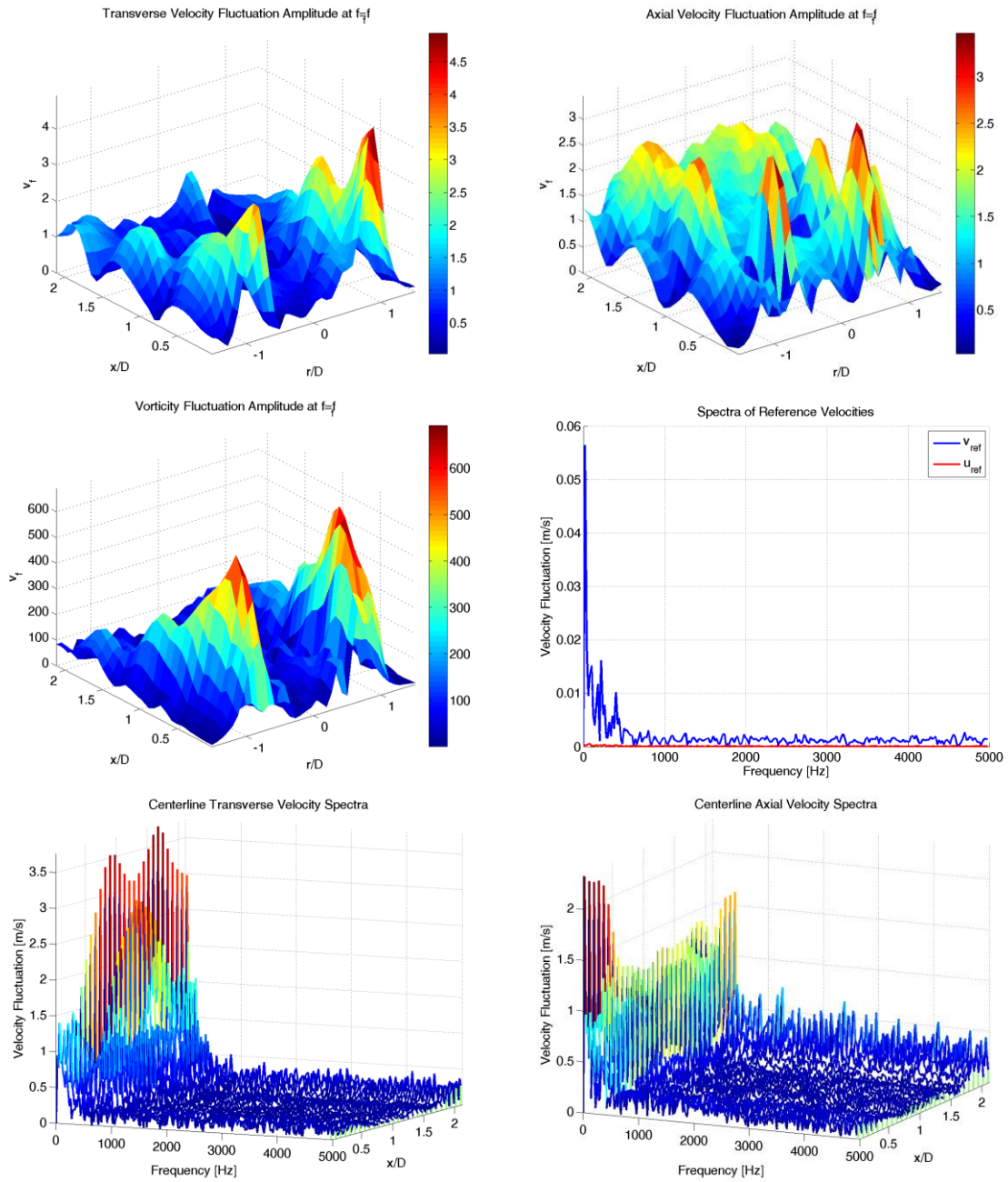


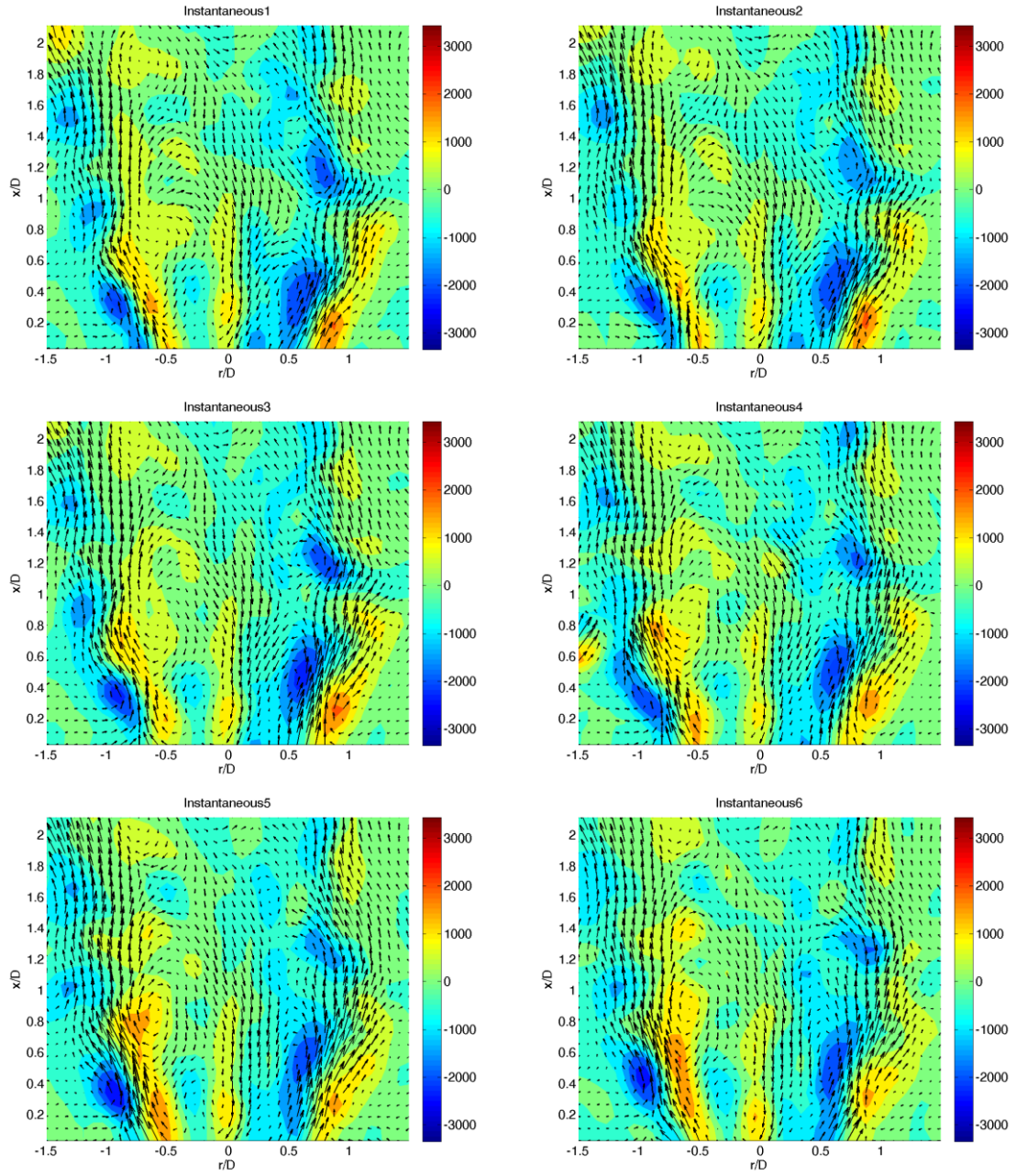




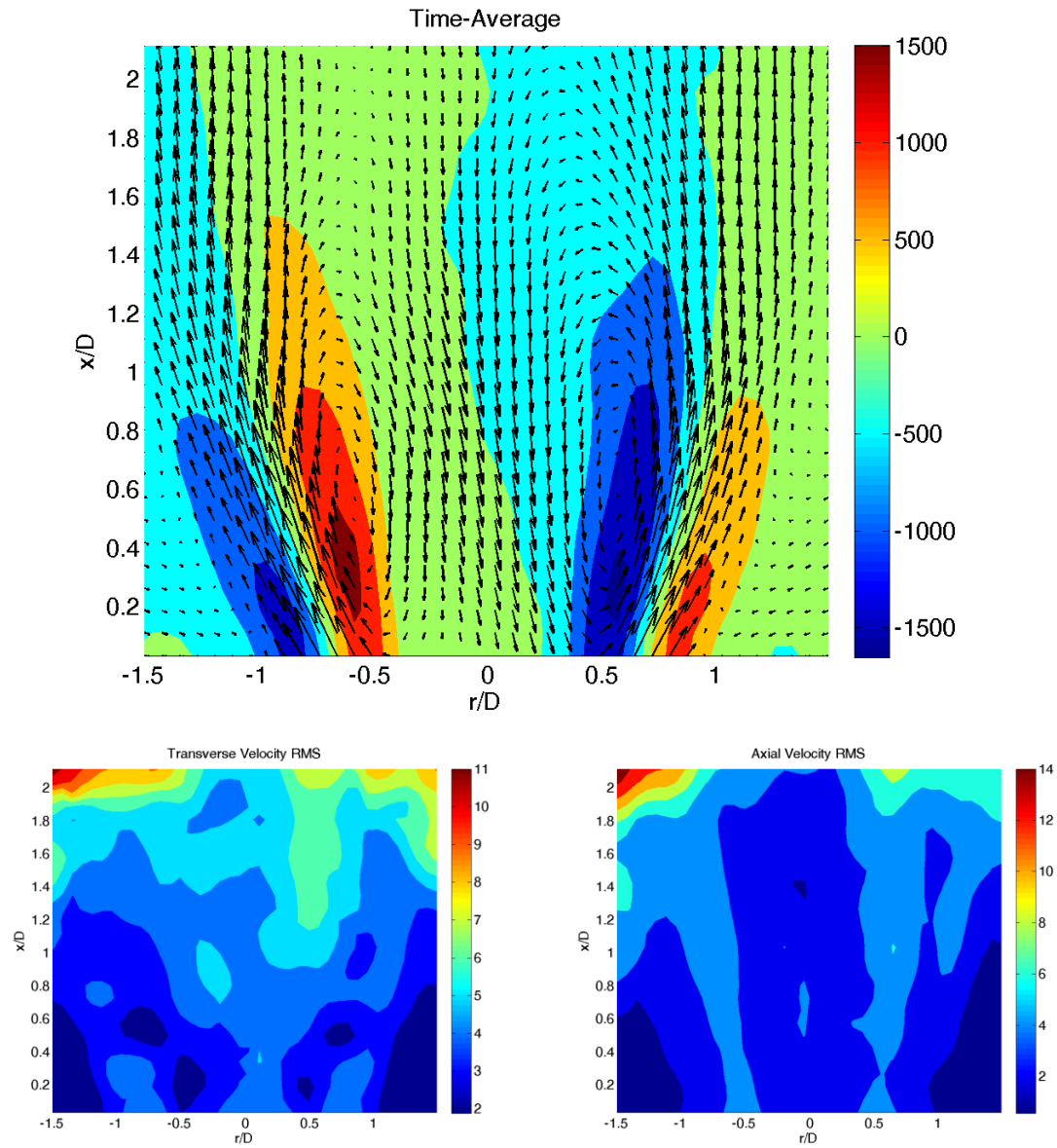
	Diagnostic	Diagnostic details	Reacting?	Swirl number	u_bulk [m/s]	Phi	Frequency [Hz]	Amplitude [mV]	Symmetry
1	PIV	r-x cut	Reacting	0.85	10		400	1000	in-phase

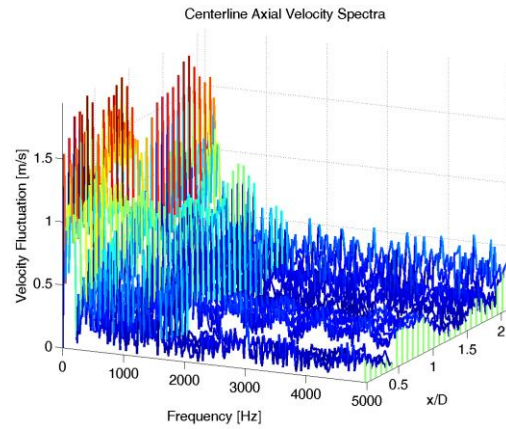
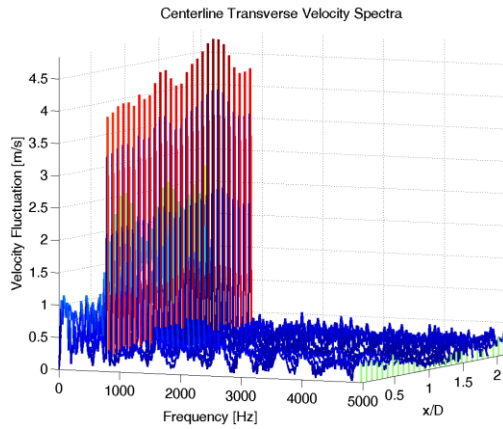
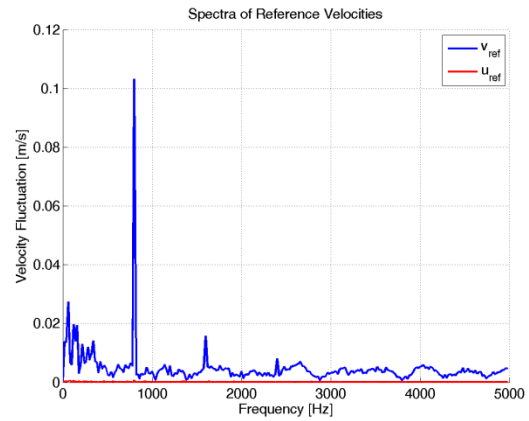
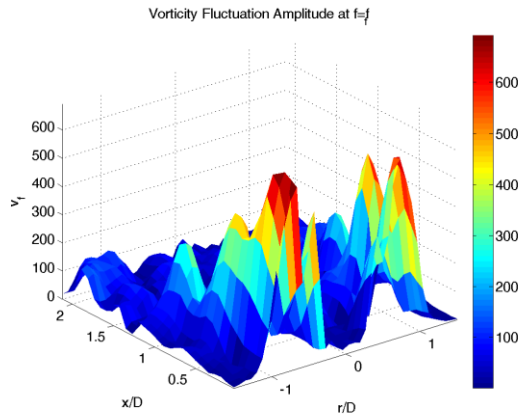
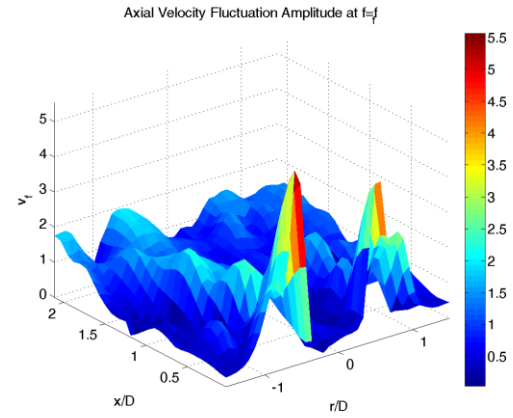
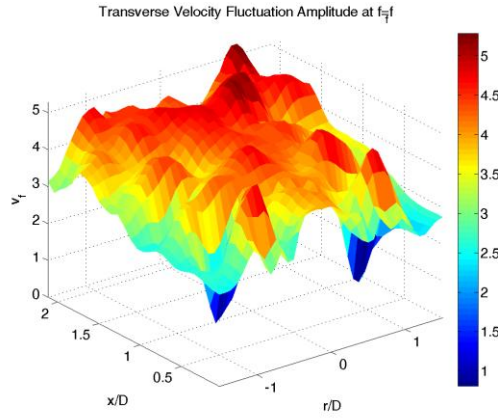


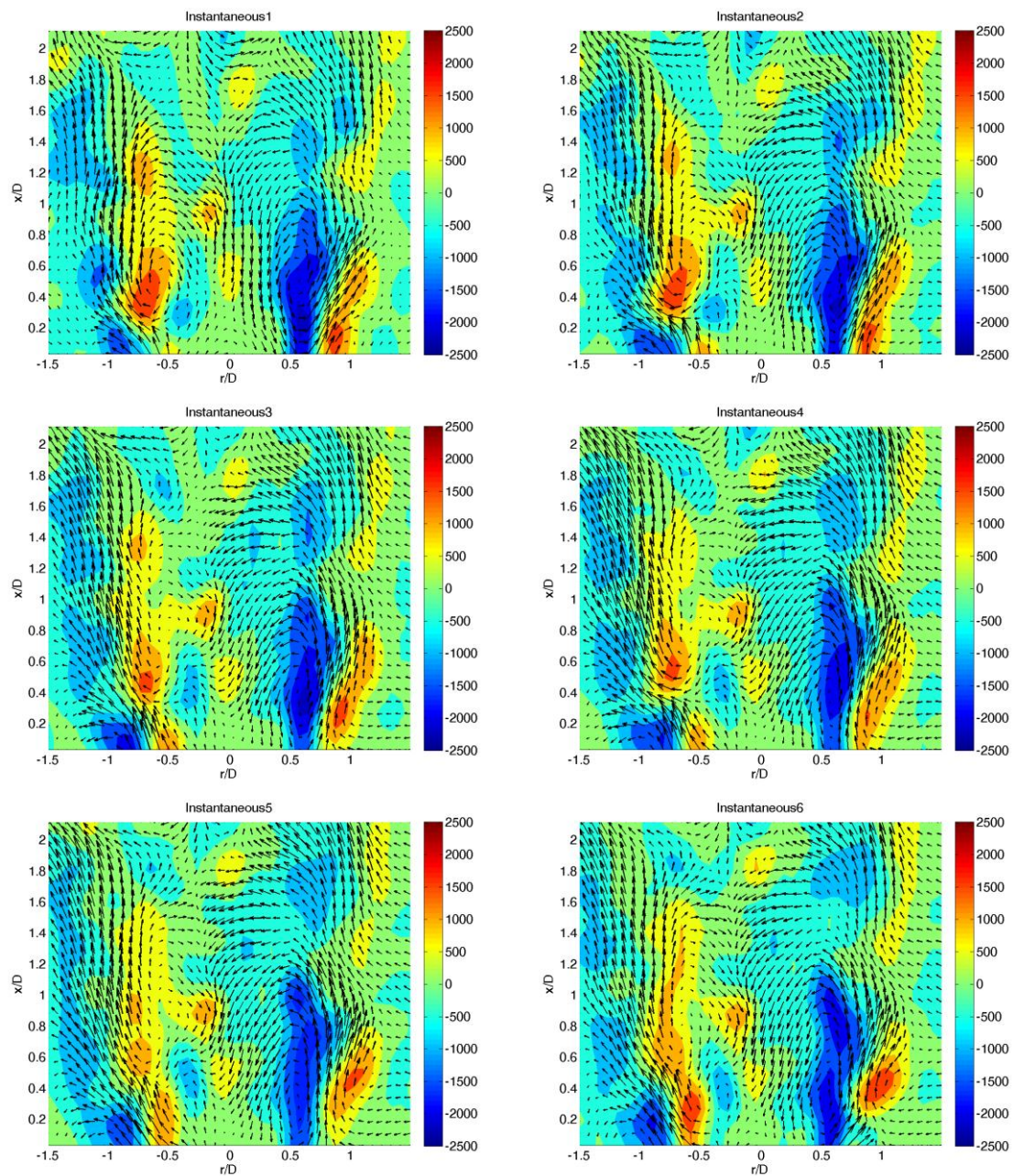




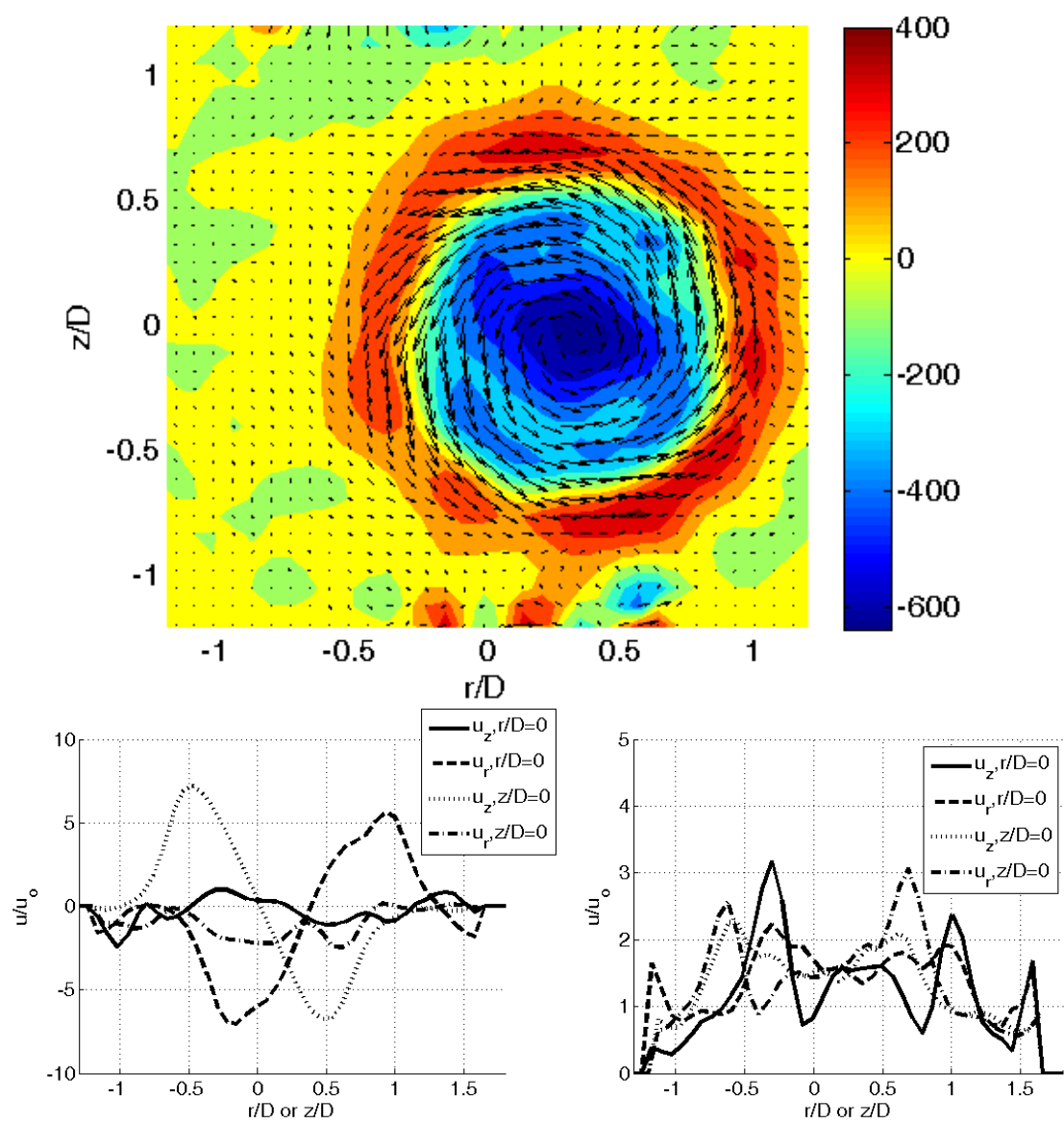
	Diagnostic	Diagnostic details	Reacting?	Swirl number	u_bulk [m/s]	Phi	Frequency [Hz]	Amplitude [mV]	Symmetry
1	PIV	r-x cut	Reacting	0.85	10		800	1000	out-of-phase

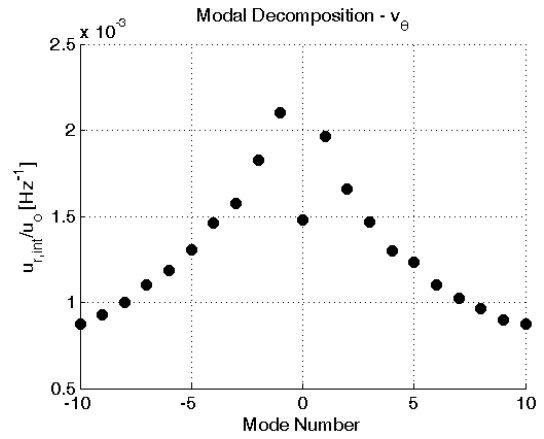
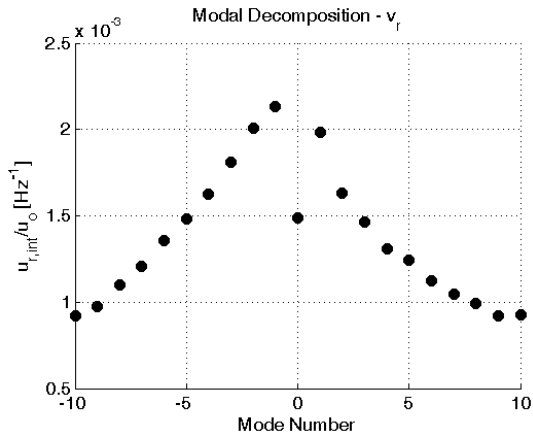
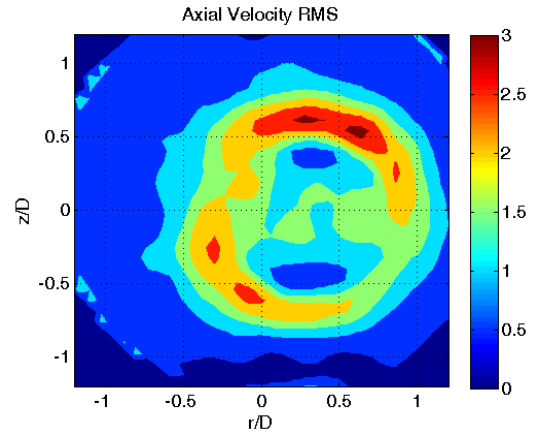
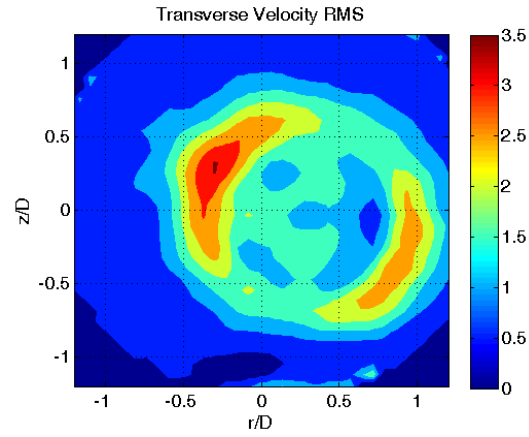


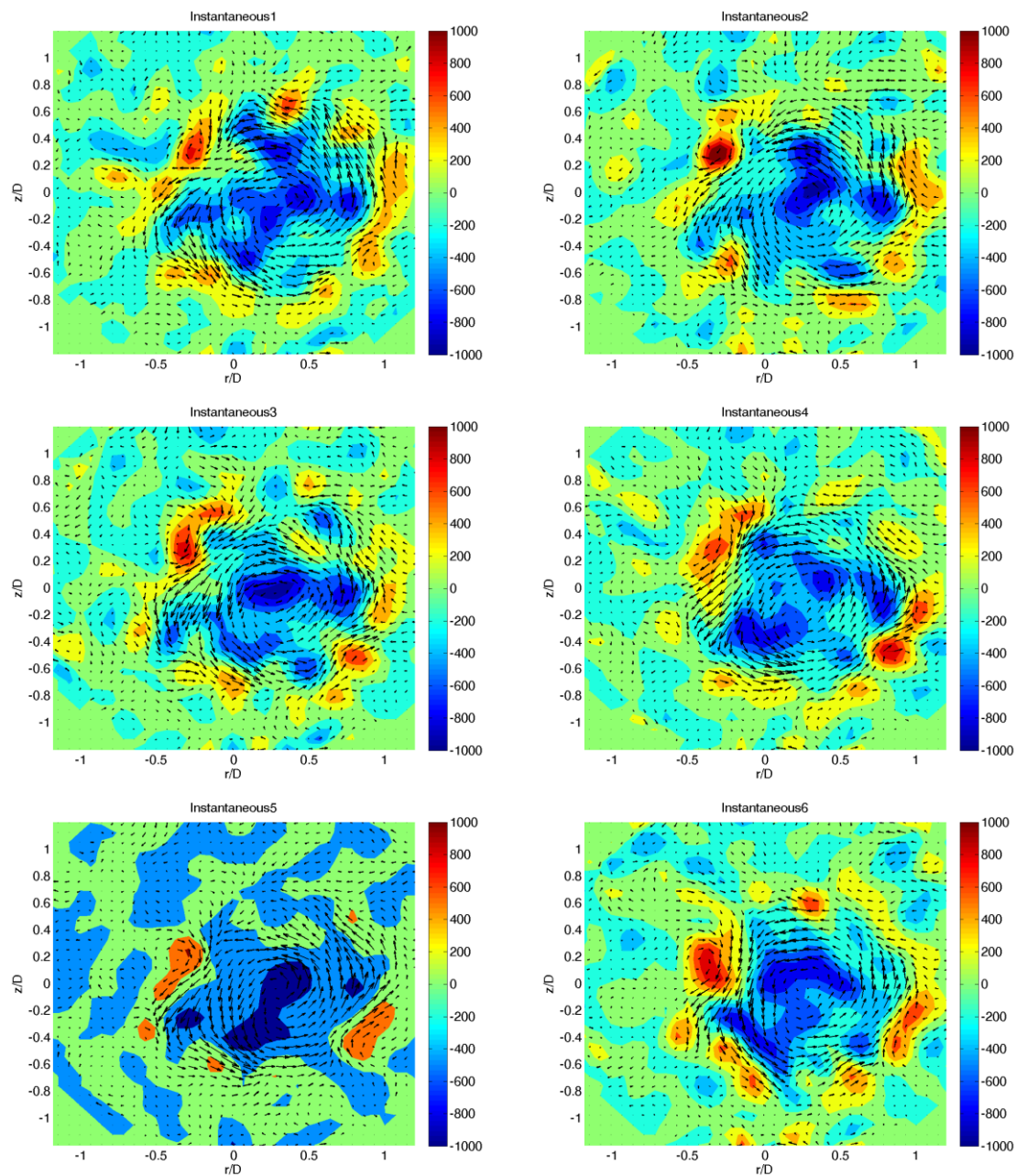




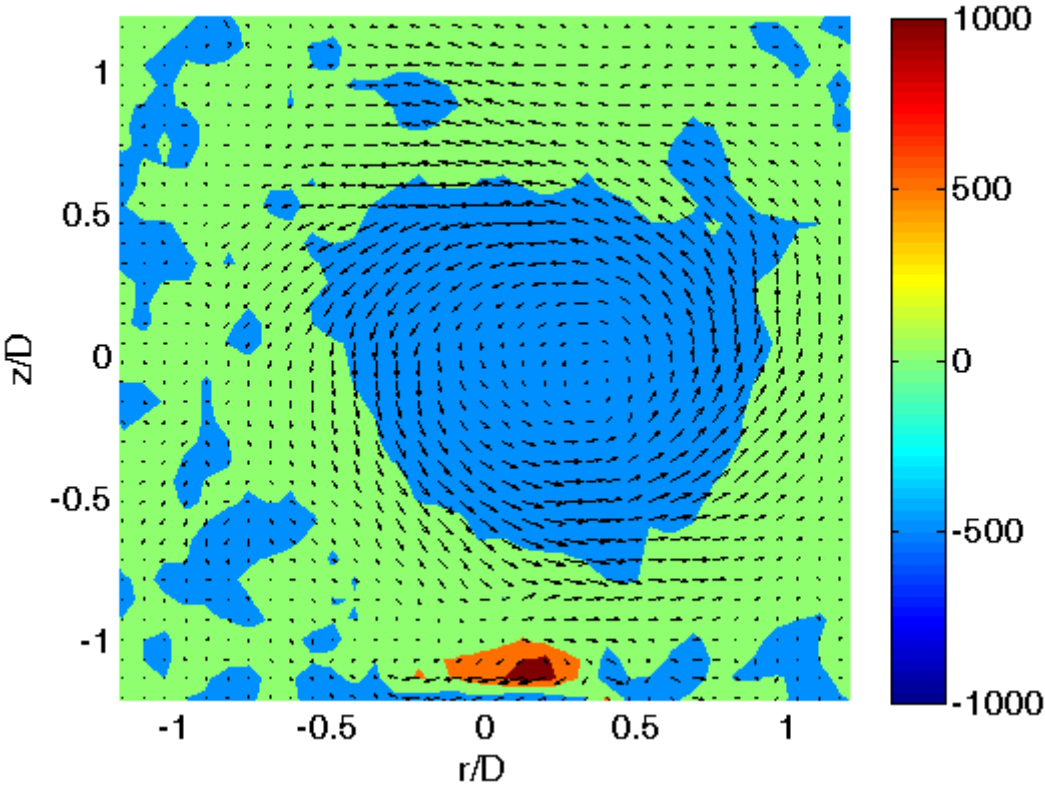
	Diagnostic	Diagnostic details	Reacting?	Swirl number	u_{bulk} [m/s]	Phi	Frequency [Hz]	Amplitude [mV]	Symmetry
1	PIV	r-theta cut 0D	Non-reacting	0.85	10		400	1000	in-phase

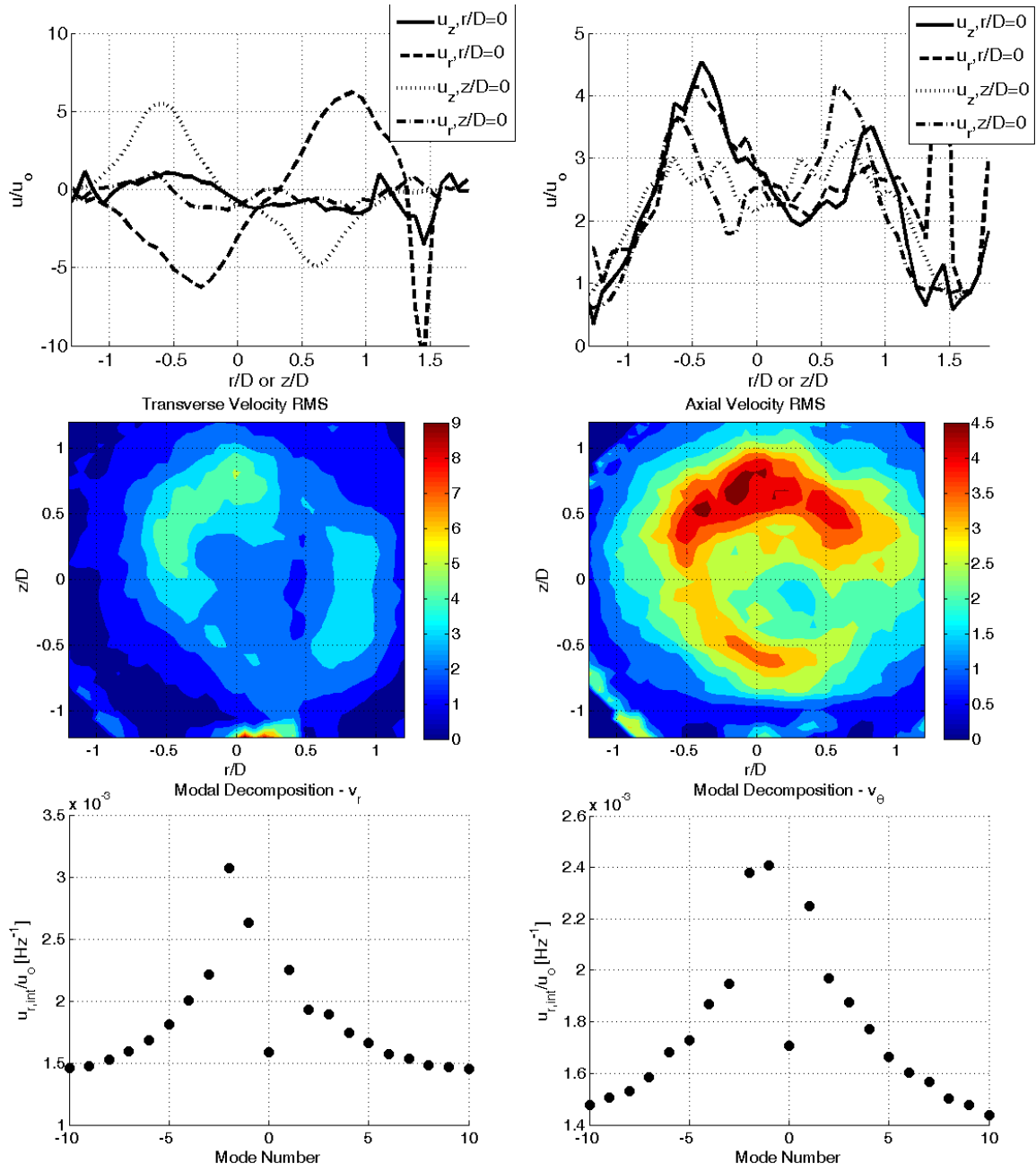


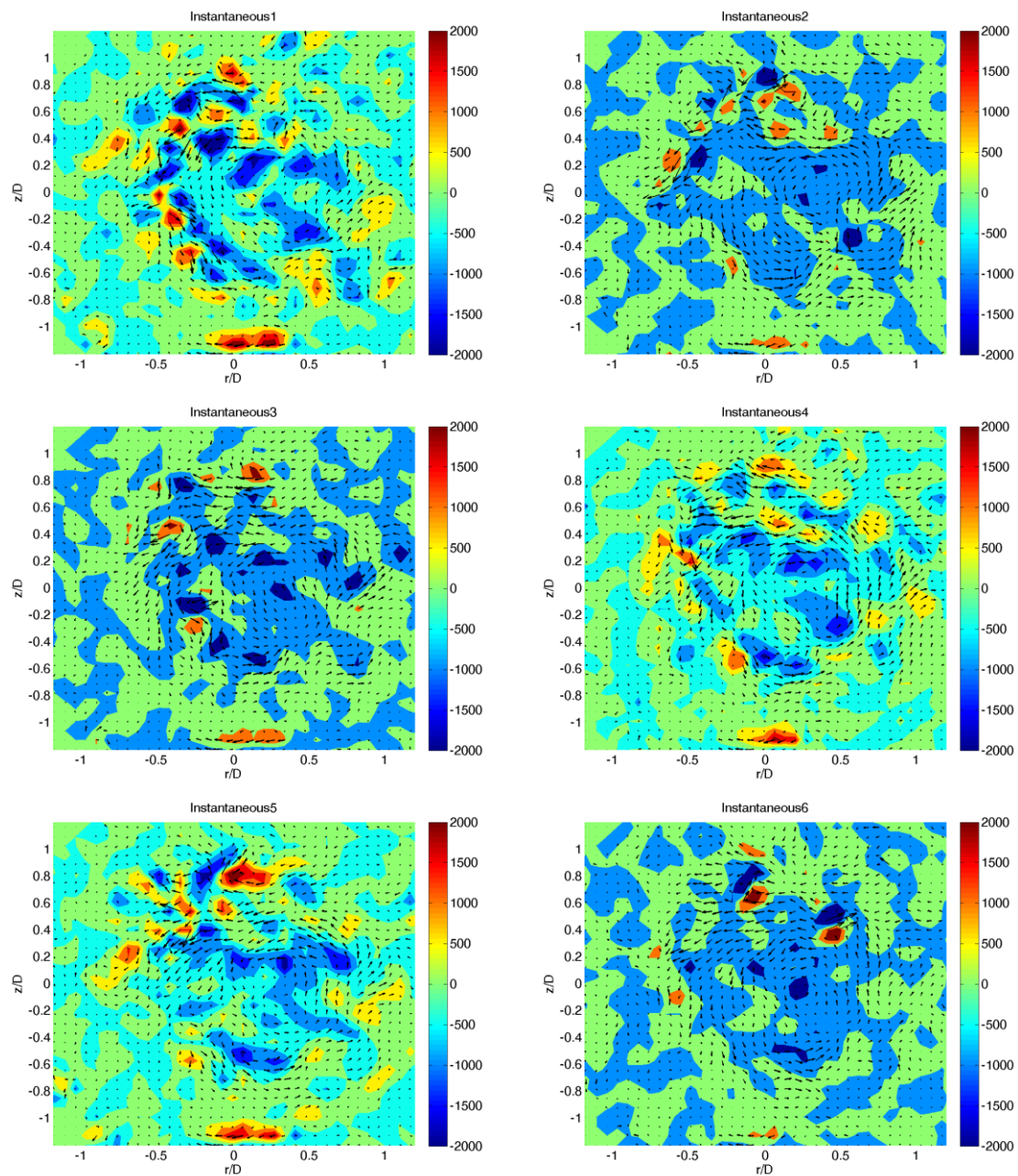




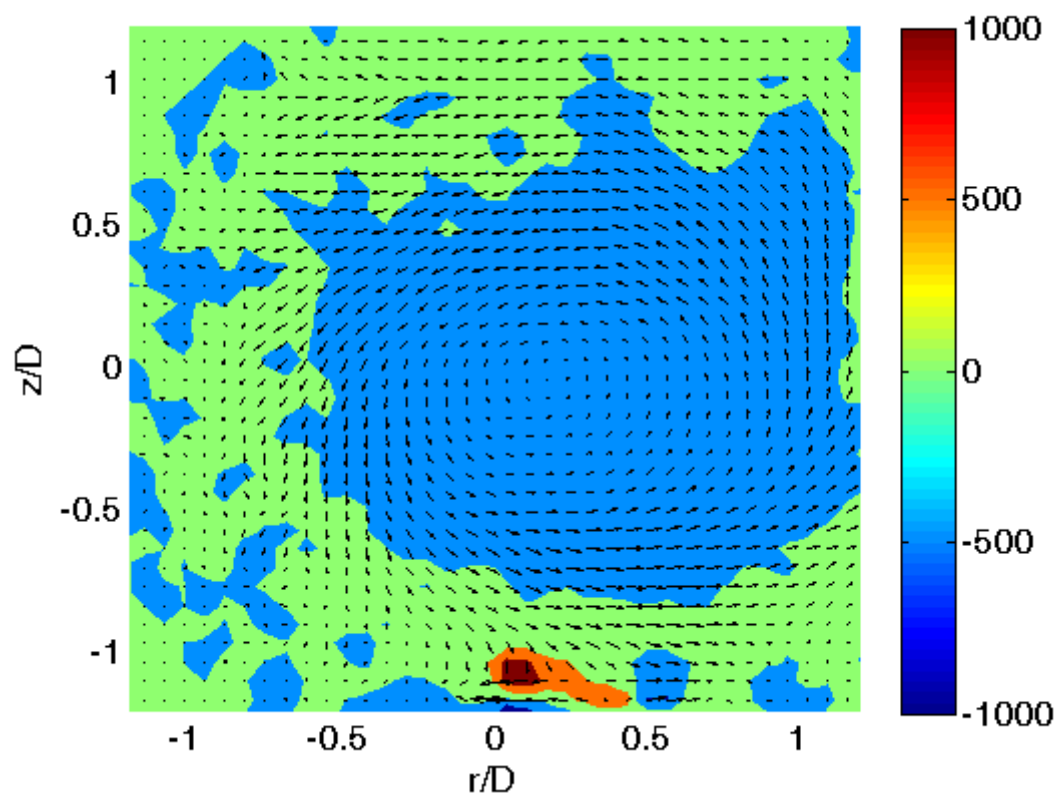
	Diagnostic	Diagnostic details	Reacting?	Swirl number	u_bulk [m/s]	Phi	Frequency [Hz]	Amplitude [mV]	Symmetry
1	PIV	r-theta cut 1D	Non-reacting	0.85	10		1200	1000	out-of-phase

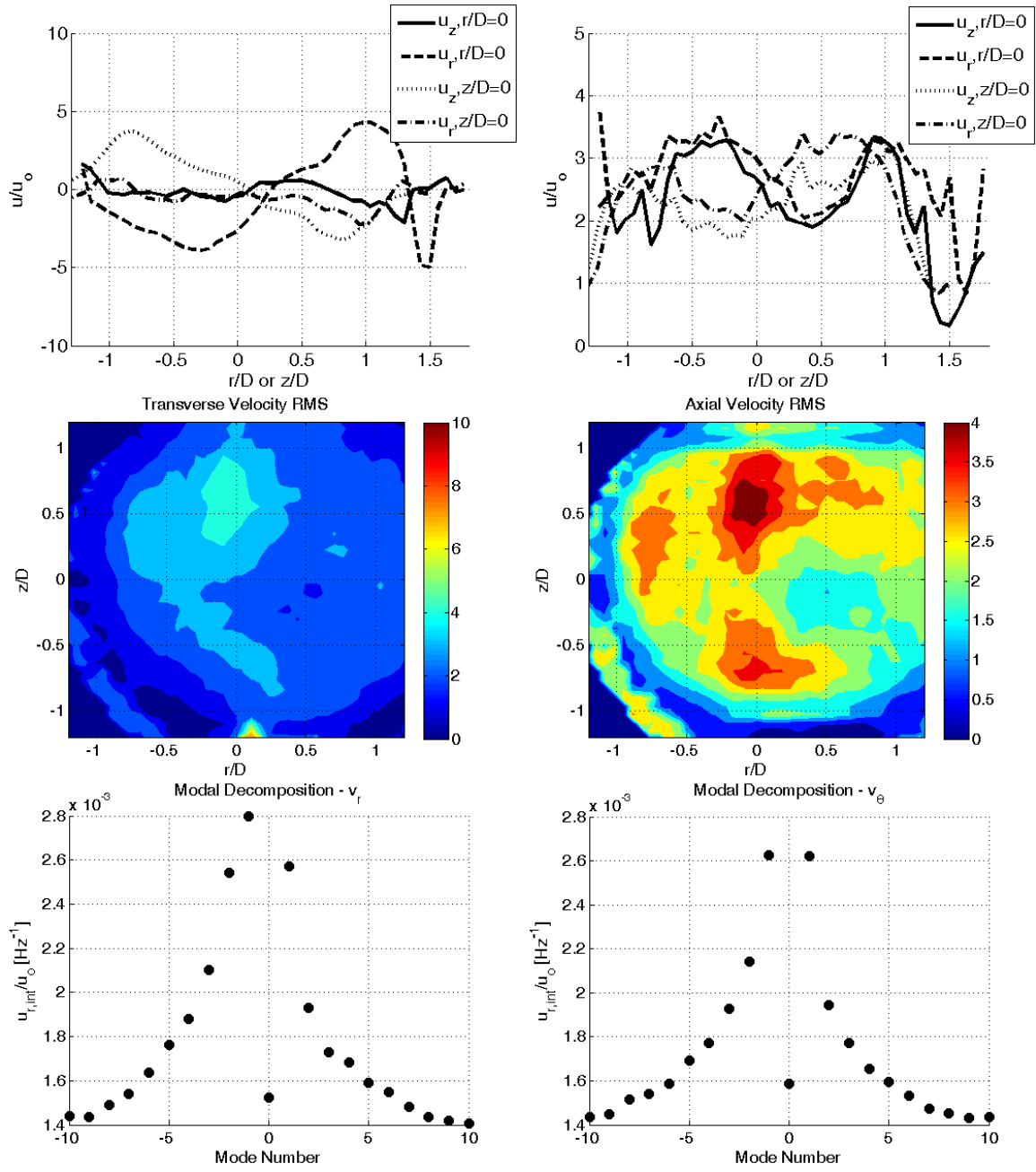






	Diagnostic	Diagnostic details	Reacting?	Swirl number	u_bulk [m/s]	Phi	Frequency [Hz]	Amplitude [mV]	Symmetry
1	PIV	r-theta cut 2D	Non-reacting	0.85	10		800	1000	out-of-phase





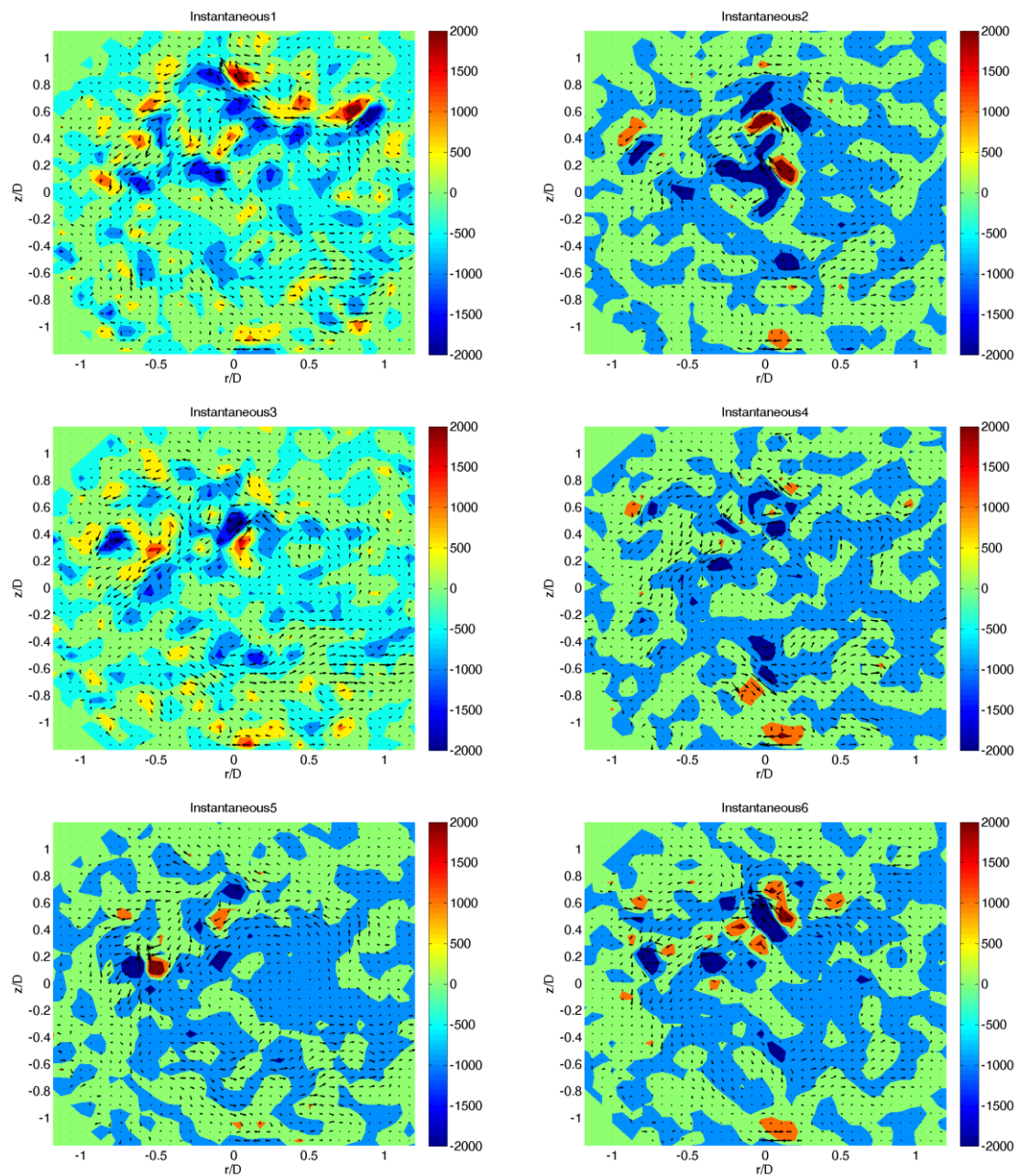


Table 6. Overview of luminescence flame data.

	Swirl number	u_bulk [m/s]	Phi	Frequency [Hz]	Amplitude [mV]	Symmetry
1	0.5	10	0.9	400	250	out-of-phase
2	0.5	10	0.9	500	250	out-of-phase
3	0.5	10	0.9	600	400	out-of-phase
4	0.5	10	0.9	700	600	out-of-phase
5	0.5	10	0.9	800	200	out-of-phase
6	0.5	10	0.9	900	600	out-of-phase
7	0.5	10	0.9	1000	1100	out-of-phase
8	0.5	10	0.9	1100	500	out-of-phase
9	0.5	10	0.9	1200	1800	out-of-phase
10	0.5	10	0.9	1300	600	out-of-phase
11	0.5	10	0.9	1400	500	out-of-phase
12	0.5	10	0.9	1500	1300	out-of-phase
13	0.5	10	0.9	1600	750	out-of-phase
14	0.5	10	0.9	1700	1100	out-of-phase
15	0.5	10	0.9	1800	1100	out-of-phase
16	0.5	10	0.9	400	250	in-phase
17	0.5	10	0.9	500	250	in-phase
18	0.5	10	0.9	600	400	in-phase
19	0.5	10	0.9	700	600	in-phase
20	0.5	10	0.9	800	200	in-phase
21	0.5	10	0.9	900	600	in-phase
22	0.5	10	0.9	1000	1100	in-phase
23	0.5	10	0.9	1100	500	in-phase
24	0.5	10	0.9	1200	1800	in-phase
25	0.5	10	0.9	1300	600	in-phase
26	0.5	10	0.9	1400	500	in-phase
27	0.5	10	0.9	1500	1300	in-phase
28	0.5	10	0.9	1600	750	in-phase
29	0.5	10	0.9	1700	1100	in-phase
30	0.5	10	0.9	1800	1100	in-phase
31	0.5	10	0.9	400	200	out-of-phase
32	0.5	10	0.9	400	400	out-of-phase
33	0.5	10	0.9	400	600	out-of-phase
34	0.5	10	0.9	400	800	out-of-phase
35	0.5	10	0.9	400	1000	out-of-phase
36	0.5	10	0.9	400	200	in-phase
37	0.5	10	0.9	400	400	in-phase

38	0.5	10	0.9	400	600	in-phase
39	0.5	10	0.9	400	800	in-phase
40	0.5	10	0.9	400	1000	in-phase
41	0.5	10	0.9	800	200	out-of-phase
42	0.5	10	0.9	800	400	out-of-phase
43	0.5	10	0.9	800	600	out-of-phase
44	0.5	10	0.9	800	800	out-of-phase
45	0.5	10	0.9	800	1000	out-of-phase
46	0.5	10	0.9	800	200	in-phase
47	0.5	10	0.9	800	400	in-phase
48	0.5	10	0.9	800	600	in-phase
49	0.5	10	0.9	800	800	in-phase
50	0.5	10	0.9	800	1000	in-phase
51	0.5	10	0.9	1200	200	out-of-phase
52	0.5	10	0.9	1200	400	out-of-phase
53	0.5	10	0.9	1200	600	out-of-phase
54	0.5	10	0.9	1200	800	out-of-phase
55	0.5	10	0.9	1200	1000	out-of-phase
56	0.5	10	0.9	1200	200	in-phase
57	0.5	10	0.9	1200	400	in-phase
58	0.5	10	0.9	1200	600	in-phase
59	0.5	10	0.9	1200	800	in-phase
60	0.5	10	0.9	1200	1000	in-phase
61	0.5	10	0.9	1800	200	in-phase
62	0.5	10	0.9	1800	400	in-phase
63	0.5	10	0.9	1800	600	in-phase
64	0.5	10	0.9	1800	800	in-phase
65	0.5	10	0.9	1800	1000	in-phase

Table 7. Overview of PLIF data.

	Swirl number	u_bulk [m/s]	Phi	Frequency [Hz]	Amplitude [mV]	Symmetry
1	0.5	10	0.9			
2	0.5	10	0.9	400	500	in-phase
3	0.5	10	0.9	400	600	in-phase
4	0.5	10	0.9	400	700	in-phase
5	0.5	10	0.9	400	800	in-phase
6	0.5	10	0.9	400	900	in-phase
7	0.5	10	0.9	400	1000	in-phase
8	0.5	10	0.9	400	1100	in-phase
9	0.5	10	0.9	400	1200	in-phase
10	0.5	10	0.9	400	1220	in-phase
11	0.5	10	0.9	400	1240	in-phase
12	0.5	10	0.9	400	1260	in-phase
13	0.5	10	0.9	400	1280	in-phase
14	0.5	10	0.9	400	1300	in-phase
15	0.5	10	0.9	400	1320	in-phase
16	0.5	10	0.9	400	1340	in-phase
17	0.5	10	0.9	400	1360	in-phase
18	0.5	10	0.9	400	1380	in-phase
19	0.5	10	0.9	400	1400	in-phase
20	0.5	10	0.9	400	500	out-of-phase
21	0.5	10	0.9	400	1500	out-of-phase
22	0.5	10	0.9	400	500	in-phase
23	0.5	10	0.9	400	1500	in-phase
24	0.5	10	0.9	800	500	out-of-phase
25	0.5	10	0.9	800	1500	out-of-phase
26	0.5	10	0.9	800	500	in-phase
27	0.5	10	0.9	800	1500	in-phase
28	0.5	10	0.9	1200	500	out-of-phase
29	0.5	10	0.9	1200	1500	out-of-phase
30	0.5	10	0.9	1200	500	in-phase
31	0.5	10	0.9	1200	1500	in-phase
32	0.5	10	0.9	1500	500	out-of-phase
33	0.5	10	0.9	1500	1500	out-of-phase
34	0.5	10	0.9	1500	500	in-phase
35	0.5	10	0.9	1500	1500	in-phase
36	0.5	10	0.9	1800	500	out-of-phase
37	0.5	10	0.9	1800	1500	out-of-phase
38	0.5	10	0.9	1800	500	in-phase
39	0.5	10	0.9	1800	1500	in-phase

Table 8. Overview of global chemiluminescence and two-microphone method pressure data.

	Swirl number	u_bulk [m/s]	Phi	Frequency [Hz]	Amplitude [mV]	Symmetry
1	0.5	10	0.9			
2	0.5	10	0.9	200	4000	longitudinal
3	0.5	10	0.9	220	4000	longitudinal
4	0.5	10	0.9	240	4000	longitudinal
5	0.5	10	0.9	260	4000	longitudinal
6	0.5	10	0.9	280	4000	longitudinal
7	0.5	10	0.9	300	4000	longitudinal
8	0.5	10	0.9	320	4000	longitudinal
9	0.5	10	0.9	340	4000	longitudinal
10	0.5	10	0.9	360	4000	longitudinal
11	0.5	10	0.9	380	4000	longitudinal
12	0.5	10	0.9	400	2000	longitudinal
13	0.5	10	0.9	420	2000	longitudinal
14	0.5	10	0.9	440	2000	longitudinal
15	0.5	10	0.9	460	2000	longitudinal
16	0.5	10	0.9	480	2000	longitudinal
17	0.5	10	0.9	500	2000	longitudinal
18	0.5	10	0.9	520	2000	longitudinal
19	0.5	10	0.9	540	2000	longitudinal
20	0.5	10	0.9	560	2000	longitudinal
21	0.5	10	0.9	580	2000	longitudinal
22	0.5	10	0.9	600	2000	longitudinal
23	0.5	10	0.9	620	2000	longitudinal
24	0.5	10	0.9	640	2000	longitudinal
25	0.5	10	0.9	660	2000	longitudinal
26	0.5	10	0.9	680	2000	longitudinal
27	0.5	10	0.9	700	2000	longitudinal
28	0.5	10	0.9	720	2000	longitudinal
29	0.5	10	0.9	740	2000	longitudinal
30	0.5	10	0.9	760	2000	longitudinal
31	0.5	10	0.9	780	2000	longitudinal
32	0.5	10	0.9	800	2000	longitudinal
33	0.5	10	0.9	820	2000	longitudinal
34	0.5	10	0.9	840	2000	longitudinal
35	0.5	10	0.9	860	2000	longitudinal

36	0.5	10	0.9	880	2000	longitudinal
37	0.5	10	0.9	900	2000	longitudinal
38	0.5	10	0.9	920	2000	longitudinal
39	0.5	10	0.9	940	2000	longitudinal
40	0.5	10	0.9	960	2000	longitudinal
41	0.5	10	0.9	980	2000	longitudinal
42	0.5	10	0.9	1000	2000	longitudinal
43	0.5	10	0.9	1020	2000	longitudinal
44	0.5	10	0.9	1040	2000	longitudinal
45	0.5	10	0.9	1060	2000	longitudinal
46	0.5	10	0.9	1080	2000	longitudinal
47	0.5	10	0.9	1100	2000	longitudinal
48	0.5	10	0.9	1120	2000	longitudinal
49	0.5	10	0.9	1140	2000	longitudinal
50	0.5	10	0.9	1160	2000	longitudinal
51	0.5	10	0.9	1180	2000	longitudinal
52	0.5	10	0.9	1200	2000	longitudinal
53	0.5	10	0.9	1220	2000	longitudinal
54	0.5	10	0.9	1240	2000	longitudinal
55	0.5	10	0.9	1260	2000	longitudinal
56	0.5	10	0.9	1280	2000	longitudinal
57	0.5	10	0.9	1300	2000	longitudinal
58	0.5	10	0.9	1320	2000	longitudinal
59	0.5	10	0.9	1340	2000	longitudinal
60	0.5	10	0.9	1360	2000	longitudinal
61	0.5	10	0.9	1380	2000	longitudinal
62	0.5	10	0.9	1400	2000	longitudinal
63	0.5	10	0.9	1420	2000	longitudinal
64	0.5	10	0.9	1440	2000	longitudinal
65	0.5	10	0.9	1460	2000	longitudinal
66	0.5	10	0.9	1480	2000	longitudinal
67	0.5	10	0.9	1500	2000	longitudinal
68	0.5	10	0.9	1520	2000	longitudinal
69	0.5	10	0.9	1540	2000	longitudinal
70	0.5	10	0.9	1560	2000	longitudinal
71	0.5	10	0.9	1580	2000	longitudinal
72	0.5	10	0.9	1600	2000	longitudinal
73	0.5	10	0.9	1620	2000	longitudinal
74	0.5	10	0.9	1640	2000	longitudinal
75	0.5	10	0.9	1660	2000	longitudinal

76	0.5	10	0.9	1680	2000	longitudinal
77	0.5	10	0.9	1700	2000	longitudinal
78	0.5	10	0.9	1720	2000	longitudinal
79	0.5	10	0.9	1740	2000	longitudinal
80	0.5	10	0.9	1760	2000	longitudinal
81	0.5	10	0.9	1780	2000	longitudinal
82	0.5	10	0.9	1800	2000	longitudinal
83	0.5	10	0.9	400	250	out-of-phase
84	0.5	10	0.9	420	250	out-of-phase
85	0.5	10	0.9	440	250	out-of-phase
86	0.5	10	0.9	460	250	out-of-phase
87	0.5	10	0.9	480	250	out-of-phase
88	0.5	10	0.9	500	250	out-of-phase
89	0.5	10	0.9	520	250	out-of-phase
90	0.5	10	0.9	540	250	out-of-phase
91	0.5	10	0.9	560	250	out-of-phase
92	0.5	10	0.9	580	250	out-of-phase
93	0.5	10	0.9	600	400	out-of-phase
94	0.5	10	0.9	620	400	out-of-phase
95	0.5	10	0.9	640	400	out-of-phase
96	0.5	10	0.9	660	400	out-of-phase
97	0.5	10	0.9	680	400	out-of-phase
98	0.5	10	0.9	700	600	out-of-phase
99	0.5	10	0.9	720	600	out-of-phase
100	0.5	10	0.9	740	600	out-of-phase
101	0.5	10	0.9	760	600	out-of-phase
102	0.5	10	0.9	780	600	out-of-phase
103	0.5	10	0.9	800	200	out-of-phase
104	0.5	10	0.9	820	200	out-of-phase
105	0.5	10	0.9	840	200	out-of-phase
106	0.5	10	0.9	860	200	out-of-phase
107	0.5	10	0.9	880	200	out-of-phase
108	0.5	10	0.9	900	600	out-of-phase
109	0.5	10	0.9	920	600	out-of-phase
110	0.5	10	0.9	940	600	out-of-phase
111	0.5	10	0.9	960	600	out-of-phase
112	0.5	10	0.9	980	600	out-of-phase
113	0.5	10	0.9	1000	1100	out-of-phase
114	0.5	10	0.9	1020	1100	out-of-phase
115	0.5	10	0.9	1040	1100	out-of-phase

116	0.5	10	0.9	1060	1100	out-of-phase
117	0.5	10	0.9	1080	1100	out-of-phase
118	0.5	10	0.9	1100	500	out-of-phase
119	0.5	10	0.9	1120	500	out-of-phase
120	0.5	10	0.9	1140	500	out-of-phase
121	0.5	10	0.9	1160	500	out-of-phase
122	0.5	10	0.9	1180	500	out-of-phase
123	0.5	10	0.9	1200	1800	out-of-phase
124	0.5	10	0.9	1220	1800	out-of-phase
125	0.5	10	0.9	1240	1800	out-of-phase
126	0.5	10	0.9	1260	1800	out-of-phase
127	0.5	10	0.9	1280	1800	out-of-phase
128	0.5	10	0.9	1300	600	out-of-phase
129	0.5	10	0.9	1320	600	out-of-phase
130	0.5	10	0.9	1340	600	out-of-phase
131	0.5	10	0.9	1360	600	out-of-phase
132	0.5	10	0.9	1380	600	out-of-phase
133	0.5	10	0.9	1400	500	out-of-phase
134	0.5	10	0.9	1420	500	out-of-phase
135	0.5	10	0.9	1440	500	out-of-phase
136	0.5	10	0.9	1460	500	out-of-phase
137	0.5	10	0.9	1480	500	out-of-phase
138	0.5	10	0.9	1500	1300	out-of-phase
139	0.5	10	0.9	1520	1300	out-of-phase
140	0.5	10	0.9	1540	1300	out-of-phase
141	0.5	10	0.9	1560	1300	out-of-phase
142	0.5	10	0.9	1580	1300	out-of-phase
143	0.5	10	0.9	1600	750	out-of-phase
144	0.5	10	0.9	1620	750	out-of-phase
145	0.5	10	0.9	1640	750	out-of-phase
146	0.5	10	0.9	1660	750	out-of-phase
147	0.5	10	0.9	1680	750	out-of-phase
148	0.5	10	0.9	1700	1100	out-of-phase
149	0.5	10	0.9	1720	1100	out-of-phase
150	0.5	10	0.9	1740	1100	out-of-phase
151	0.5	10	0.9	1760	1100	out-of-phase
152	0.5	10	0.9	1780	1100	out-of-phase
153	0.5	10	0.9	1800	1100	out-of-phase
83	0.5	10	0.9	400	250	in-phase
84	0.5	10	0.9	420	250	in-phase

85	0.5	10	0.9	440	250	in-phase
86	0.5	10	0.9	460	250	in-phase
87	0.5	10	0.9	480	250	in-phase
88	0.5	10	0.9	500	250	in-phase
89	0.5	10	0.9	520	250	in-phase
90	0.5	10	0.9	540	250	in-phase
91	0.5	10	0.9	560	250	in-phase
92	0.5	10	0.9	580	250	in-phase
93	0.5	10	0.9	600	400	in-phase
94	0.5	10	0.9	620	400	in-phase
95	0.5	10	0.9	640	400	in-phase
96	0.5	10	0.9	660	400	in-phase
97	0.5	10	0.9	680	400	in-phase
98	0.5	10	0.9	700	600	in-phase
99	0.5	10	0.9	720	600	in-phase
100	0.5	10	0.9	740	600	in-phase
101	0.5	10	0.9	760	600	in-phase
102	0.5	10	0.9	780	600	in-phase
103	0.5	10	0.9	800	200	in-phase
104	0.5	10	0.9	820	200	in-phase
105	0.5	10	0.9	840	200	in-phase
106	0.5	10	0.9	860	200	in-phase
107	0.5	10	0.9	880	200	in-phase
108	0.5	10	0.9	900	600	in-phase
109	0.5	10	0.9	920	600	in-phase
110	0.5	10	0.9	940	600	in-phase
111	0.5	10	0.9	960	600	in-phase
112	0.5	10	0.9	980	600	in-phase
113	0.5	10	0.9	1000	1100	in-phase
114	0.5	10	0.9	1020	1100	in-phase
115	0.5	10	0.9	1040	1100	in-phase
116	0.5	10	0.9	1060	1100	in-phase
117	0.5	10	0.9	1080	1100	in-phase
118	0.5	10	0.9	1100	500	in-phase
119	0.5	10	0.9	1120	500	in-phase
120	0.5	10	0.9	1140	500	in-phase
121	0.5	10	0.9	1160	500	in-phase
122	0.5	10	0.9	1180	500	in-phase
123	0.5	10	0.9	1200	1800	in-phase
124	0.5	10	0.9	1220	1800	in-phase

125	0.5	10	0.9	1240	1800	in-phase
126	0.5	10	0.9	1260	1800	in-phase
127	0.5	10	0.9	1280	1800	in-phase
128	0.5	10	0.9	1300	600	in-phase
129	0.5	10	0.9	1320	600	in-phase
130	0.5	10	0.9	1340	600	in-phase
131	0.5	10	0.9	1360	600	in-phase
132	0.5	10	0.9	1380	600	in-phase
133	0.5	10	0.9	1400	500	in-phase
134	0.5	10	0.9	1420	500	in-phase
135	0.5	10	0.9	1440	500	in-phase
136	0.5	10	0.9	1460	500	in-phase
137	0.5	10	0.9	1480	500	in-phase
138	0.5	10	0.9	1500	1300	in-phase
139	0.5	10	0.9	1520	1300	in-phase
140	0.5	10	0.9	1540	1300	in-phase
141	0.5	10	0.9	1560	1300	in-phase
142	0.5	10	0.9	1580	1300	in-phase
143	0.5	10	0.9	1600	750	in-phase
144	0.5	10	0.9	1620	750	in-phase
145	0.5	10	0.9	1640	750	in-phase
146	0.5	10	0.9	1660	750	in-phase
147	0.5	10	0.9	1680	750	in-phase
148	0.5	10	0.9	1700	1100	in-phase
149	0.5	10	0.9	1720	1100	in-phase
150	0.5	10	0.9	1740	1100	in-phase
151	0.5	10	0.9	1760	1100	in-phase
152	0.5	10	0.9	1780	1100	in-phase
153	0.5	10	0.9	1800	1100	in-phase

REFERENCES

1. Rayleigh, B.J.W.S., *The Theory of Sound*. 1896.
2. Shreekrishna, *Response mechanisms of attached premixed flames to harmonic forcing*, in *Aerospace Engineering*. 2011, Georgia Institute of Technology: Atlanta.
3. Ducruix, S., T. Schuller, D. Durox, and S. Candel, *Combustion dynamics and instabilities: Elementary coupling and driving mechanisms*. Journal of Propulsion and Power, 2003. **19**(5): p. 722-734.
4. Sensiau, C., F. Nicoud, and T. Poinso, *A tool to study azimuthal standing and spinning modes in annular combustors*. International Journal of Aeroacoustics, 2009. **8**(1&2): p. 57-68.
5. Hield, P.A., M.J. Brear, and S.H. Jin, *Thermoacoustic limit cycles in a premixed laboratory combustor with open and choked exits*. Combustion and flame, 2009. **156**(9): p. 1683-1697.
6. Lawn, C.J., S. Evesque, and W. Polifke, *A model for the thermoacoustic response of a premixed swirl burner, Part I: acoustic aspects*. Combustion Science and Technology, 2004. **176**(8): p. 1331-1358.
7. Reddy, A.P., R.I. Sujith, and S.R. Chakravarthy, *Swirler flow field characteristics in a sudden expansion combustor geometry*. Journal of Propulsion and Power, 2006. **22**(4): p. 800-808.
8. Alemela, P.R., D. Fanaca, C. Hirsch, T. Sattelmayer, and B. Schuermans, *Determination and scaling of thermo acoustic characteristics of premixed flames*. International Journal of Spray and Combustion Dynamics, 2010. **2**(2): p. 169-198.
9. Venkataraman, K.K., L.H. Preston, D.W. Simons, B.J. Lee, J.G. Lee, and D. Santavicca, *Mechanism of combustion instability in a lean premixed dump combustor*. Journal of Propulsion and Power, 1999. **15**(6): p. 909-918.
10. Lacarelle, A., Faustmann, T., Greenblatt, D., Paschereit, C. O., Lehmann, O., Luchtenburg, D. M., and Noack, B. R., *Spatiotemporal Characterization of a Conical Swirler Flow Field Under Strong Forcing*. Journal of Engineering for Gas Turbines and Power, 2009. **131**: p. 031504.
11. Stow, S.R. and A.P. Dowling, *Thermoacoustic oscillations in an annular combustor*, in *ASME Turbo Expo*. 2001, ASME: New Orleans, LA. p. 0037.
12. Lieuwen, T. and V. Yang, *Combustion Instabilities in Gas Turbine Engines*. Progress in Astronautics and Aeronautics, ed. F.K. Lu. Vol. 210. 2005, Washington D.C.: AIAA.
13. Elias, I., *Acoustical Resonances Produced by Combustion of a Fuel-Air Mixture in a Rectangular Duct*. The Journal of the Acoustical Society of America, 1959. **31**: p. 296.
14. Kaskan, W.E. and A.E. Noreen, *High-frequency oscillations of a flame held by a bluff body*. ASME Transactions, 1955. **77**(6): p. 855-891.
15. Rogers, D.E. and F.E. Marble, *A mechanism for high frequency oscillations in ramjet combustors and afterburners*. Jet Propulsion, 1956. **26**(1): p. 456-462.

16. Macquisten, M.A. and A.P. Dowling, *Combustion Oscillations in a Twin-Stream Afterburner*. Journal of Sound and Vibration, 1995. **188**(4): p. 545-560.
17. Karnesky, A.L. and S.E. Colucci, *Recent Occurrences of Combustion Instability in Solid Rocket Motors-An Overview*. Journal of Spacecraft and Rockets, 1975. **12**(1): p. 33-38.
18. Price, E.W., *Solid Rocket Combustion Instability—An American Historical Account*. Nonsteady Burning and Combustion Stability of Solid Propellants, 1992: p. 1-16.
19. Harje, D.T. and F.H. Reardon, *Liquid propellant rocket combustion instability*. 1972: Scientific and Technical Information Office, National Aeronautics and Space Administration;[for sale by the Supt. of Docs., US Govt. Print. Off.].
20. Berman, K. and S.E. Logan, *Combustion Studies with a Rocket Motor Having a Full-Length Observation Window*. Jour. Am. Rocket Soc, 1952. **22**(2): p. 78-85.
21. Marshall, W., Pal, S., Woodward, R., Santoro, R. J., Smith, R., Xia, G., Sankaran, V., and Merkle, C. L., *Experimental and Computational Investigation of Combustor Acoustics and Instabilities, Part II: Transverse Modes*, in *44th Aerospace Sciences Meeting and Exhibit*. 2006: Reno, NV.
22. Ellis, M., Xia, G., Sankaran, V., Anderson, W., and Merkle, C., *Acoustic Mode Simulations in Experimental Rocket Combustors*, in *41st Joint Propulsion Conference and Exhibit*. 2005: Tuscon, AZ.
23. Richecoeur, F., P. Scoufflaire, S. Ducruix, and S. Candel, *High-Frequency Transverse Acoustic Coupling in a Multiple-Injector Cryogenic Combustor*. Journal of Propulsion and Power, 2006. **22**(4): p. 790-799.
24. Davis, D.W. and B. Chehroudi, *Shear-Coaxial Jets From a Rocket-Like Injector in a Transverse Acoustic Field at High Pressures*, in *44th Aerospace Sciences Meeting and Exhibit*. 2006: Reno, NV.
25. Staffelbach, G., L.Y.M. Gicquel, G. Boudier, and T. Poinso, *Large Eddy Simulation of self excited azimuthal modes in annular combustors*. Proceedings of the Combustion Institute, 2009. **32**(2): p. 2909-2916.
26. Wolf, P., G. Staffelbach, A. Roux, L. Gicquel, T. Poinso, and V. Moureau, *Massively parallel LES of azimuthal thermo-acoustic instabilities in annular gas turbines*. Comptes Rendus Mecanique, 2009. **337**: p. 385-394.
27. Schuermans, B., C. Paschereit, and P. Monkiewicz, *Non-linear combustion instabilities in annular gas-turbine combustors*, in *44th AIAA Aerospace Sciences Meeting and Exhibit*. 2006: Reno, NV.
28. Hauser, M., M. Lorenz, and T. Sattelmayer. *Influence of Transversal Acoustic Excitation of the Burner Approach Flow on the Flame Structure*. in *ASME Turbo Expo*. 2010. Glasgow, Scotland.
29. Morgans, A.S. and S.R. Stow, *Model-based control of combustion instabilities in annular combustors*. Combustion and flame, 2007. **150**(4): p. 380-399.
30. Krebs, W., S. Bethke, J. Lepers, P. Flohr, and B. Prade, *Thermoacoustic Design Tools and Passive Control: Siemens Power Generation Approaches*, in *Combustion Instabilities in Gas Turbine Engines*, T. Lieuwen and V. Yang, Editors. 2005, AIAA. p. 89-112.

31. Sewell, J. and P. Sobieski, *Monitoring of Combustion Instabilities: Calpine's Experience*, in *Combustion Instabilities in Gas Turbine Engines*, T. Lieuwen and V. Yang, Editors. 2005, AIAA. p. 147-162.
32. Smith, K. and J. Blust, *Combustion Instabilities in Industrial Gas Turbines: Solar Turbines' Experience*, in *Combustion Instabilities in Gas Turbine Engines*, T. Lieuwen and V. Yang, Editors. 2005, AIAA: Washington D.C. p. 29-42.
33. Cohen, J. and W. Proscia, *Characterization and Control of Aeroengine Combustion Instability: Pratt & Whitney and NASA Experience*, in *Combustion Instabilities in Gas Turbine Engines*, T. Lieuwen and V. Yang, Editors. 2005, AIAA: Washington D.C. p. 113-146.
34. Mongia, H.C., T.J. Held, G.C. Hsiao, and R.P. Pandalai, *Incorporation of Combustion Instability Issues into Design Process: GE Aeroderivative and Aero Engines Experience*, in *Combustion Instabilities in Gas Turbine Engines*, T. Lieuwen and V. Yang, Editors. 2005, American Institute of Aeronautics and Astronautics: Washington, D. C.
35. Schwieger, R.G., *Combined Cycle Journal*, PSI Media: Las Vegas, NV.
36. Poinso, T.J., A.C. Trounev, D.P. Veynante, S.M. Candel, and E.J. Esposito, *Vortex-driven acoustically coupled combustion instabilities*. *Journal of Fluid Mechanics*, 2006. **177**: p. 265-292.
37. Preetham, S.H. and T.C. Lieuwen, *Dynamics of Laminar Premixed Flames Forced by Harmonic Velocity Disturbances*. *Journal of Propulsion and Power*, 2008. **24**(6): p. 1390-1402.
38. Birbaud, A.L., D. Durox, S. Ducruix, and S. Candel, *Dynamics of confined premixed flames submitted to upstream acoustic modulations*. *Proceedings of the Combustion Institute*, 2007. **31**(1): p. 1257-1265.
39. Schadow, K.C. and E. Gutmark, *Combustion instability related to vortex shedding in dump combustors and their passive control*. *Progress in Energy and Combustion Science*, 1992. **18**(2): p. 117-132.
40. Hemchandra, S. and T. Lieuwen, *Local Consumption Speed of Turbulent Premixed Flames—an analysis of “Memory effects”*. *Combustion and Flame*, 2010. **157**(5).
41. Birbaud, A.L., S. Ducruix, D. Durox, and S. Candel, *The nonlinear response of inverted “V” flames to equivalence ratio nonuniformities*. *Combustion and Flame*, 2008. **154**(3): p. 356-367.
42. Shreekrishna and T. Lieuwen, *High Frequency Premixed Flame Response to Acoustic Perturbations*, in *15th AIAA/CEAS Aeroacoustics Conference*. 2009: Miami, FL.
43. Syred, N., *A review of oscillation mechanisms and the role of the precessing vortex core (PVC) in swirl combustion systems*. *Progress in Energy and Combustion Science*, 2006. **32**(2): p. 93-161.
44. Cala, C.E., Fernandes, E. C., Heitor, M. V., and Shtork, S. I., *Coherent structures in unsteady swirling jet flow*. *Experiments in Fluids*, 2006. **40**(2): p. 267-276.
45. Huang, Y., H.G. Sung, S.Y. Hsieh, and V. Yang, *Large-eddy simulation of combustion dynamics of lean-premixed swirl-stabilized combustor*. *Journal of Propulsion and Power*, 2003. **19**(5): p. 782-794.

46. Ghoniem, A. and A. Krishnan. *Origin and manifestation of flow-combustion interactions in a premixed shear layer*. in *Twenty-second Symposium (International) on Combustion*. 1989: The Combustion Institute.
47. Thummuluru, S.K., M.K. Bobba, and T. Lieuwen, *Mechanism of the Nonlinear Response of a Swirl Flame to Harmonic Excitation*, in *ASME Turbo Expo 2007: Power for Land, Sea and Air*. 2007: Montreal, Canada.
48. Ho, C.M. and L.S. Huang, *Subharmonics and vortex merging in mixing layers*. *Journal of Fluid Mechanics Digital Archive*, 2006. **119**: p. 443-473.
49. Wang, S. and V. Yang, *Unsteady flow evolution in swirl injectors with radial entry. II. External excitations*. *Physics of Fluids*, 2005. **17**: p. 045107.
50. Thummuluru, S.K. and T. Lieuwen, *Characterization of acoustically forced swirl flame dynamics*. *Proceedings of the Combustion Institute*, 2009. **32**(2): p. 2893-2900.
51. Huang, Y. and V. Yang, *Dynamics and stability of lean-premixed swirl-stabilized combustion*. *Progress in Energy and Combustion Science*, 2009. **35**: p. 293-364.
52. Shtork, S.I., N.F. Vieira, and E.C. Fernandes, *On the identification of helical instabilities in a reacting swirling flow*. *Fuel*, 2008. **87**(10-11): p. 2314-2321.
53. Lieuwen, T., *Nonlinear kinematic response of premixed flames to harmonic velocity disturbances*. *Proceedings of the Combustion Institute*, 2005. **30**(2): p. 1725-1732.
54. Durox, D., T. Schuller, N. Noiray, and S. Candel, *Experimental analysis of nonlinear flame transfer functions for different flame geometries*. *Proceedings of the Combustion Institute*, 2009. **32**: p. 1391-1398.
55. Paschereit, C.O., B. Schuermans, W. Polifke, and O. Mattson, *Measurement of transfer matrices and source terms of premixed flames*. *Journal of Engineering for Gas Turbines and Power*, 2002. **124**: p. 239.
56. Kim, D., J.G. Lee, B.D. Quay, D.A. Santavicca, K. Kim, and S. Srinivasan, *Effect of flame structure on the flame transfer function in a premixed gas turbine combustor*. *Journal of Engineering for Gas Turbines and Power*, 2010. **132**: p. 021502.
57. Bellows, B.D., M.K. Bobba, A. Forte, J.M. Seitzman, and T. Lieuwen, *Flame transfer function saturation mechanisms in a swirl-stabilized combustor*. *Proceedings of the Combustion Institute*, 2007. **31**(2): p. 3181-3188.
58. Gentemann, A., C. Hirsch, K. Kunze, F. Kiesewetter, T. Sattelmayer, and W. Polifke. *Validation of flame transfer function reconstruction for perfectly premixed swirl flames*. in *ASME Turbo Expo*. 2004. Vienna, Austria.
59. Armitage, C.A., A.J. Riley, R.S. Cant, A.P. Dowling, and S.R. Stow. *Flame transfer function for swirled LPP combustion from experiments and CFD*. 2004: ASME.
60. Rayleigh, L., *The Theory of Sound*. 2 ed. Vol. 2. 1896, London: Macmillan.
61. Preetham, S. Hemchandra, and T. Lieuwen, *Dynamics of Laminar Flames Forced by Harmonic Velocity Disturbances*. *Journal of Propulsion Power*, 2008. **24**(6): p. 1390-1402.

62. Ducruix, S., D. Durox, and S. Candel, *Theoretical and experimental determinations of the transfer function of a laminar premixed flame*. Proceedings of the Combustion Institute, 2000. **28**(1): p. 765-773.
63. Poinso, T.J., A.C. Trounev, D.P. Veynante, S.M. Candel, and E.J. Esposito, *Vortex-driven acoustically coupled combustion instabilities*. Journal of Fluid Mechanics, 1987. **177**: p. 265-292.
64. Ghoniem, A.F., S. Park, A. Wachsman, A. Annaswamy, D. Wee, and H.M. Altay, *Mechanism of combustion dynamics in a backward-facing step stabilized premixed flame*. Proceedings of the Combustion Institute, 2005. **30**(2): p. 1783-1790.
65. Hirsch, C., D. Fanaca, P. Reddy, W. Polifke, and T. Sattelmayer. *Influence of the swirler design on the flame transfer function of premixed flames*. 2005: ASME.
66. Palies, P., D. Durox, T. Schuller, and S. Candel, *The combined dynamics of swirler and turbulent premixed swirling flames*. Combustion and Flame, 2010. **157**: p. 1698-1717.
67. Hirsch, C., D. Fanaca, P. Reddy, W. Polifke, and T. Sattelmayer. *Influence of the swirler design on the flame transfer function of premixed flames*. in ASME Turbo Expo. 2005. Reno, NV.
68. Ghosh, A., Q. Diao, G. Young, and K. Yu, *Effect of Density Ratio on Shear-Coaxial Injector Flame-Acoustic Interaction*, in 42nd AIAA/ASME/SAE/ASEE Joint Propulsion Conference & Exhibit. 2006: Sacramento, CA.
69. O'Connor, J. and T. Lieuwen, *Disturbance Field Characteristics of a Transversely Excited Burner*. Combustion Science and Technology, 2011. **183**(5): p. 427-443.
70. Schuller, T., D. Durox, and S. Candel, *Self-induced combustion oscillations of laminar premixed flames stabilized on annular burners*. Combustion and Flame, 2003. **135**(4): p. 525-537.
71. Noiray, N., D. Durox, T. Schuller, and S. Candel, *Self-induced instabilities of premixed flames in a multiple injection configuration*. Combustion and Flame, 2006. **145**(3): p. 435-446.
72. Brown, G.L. and J.M. Lopez, *Axisymmetric vortex breakdown Part 2. Physical mechanisms*. Journal of Fluid Mechanics, 1974. **64**(4): p. 775-816.
73. Darmofal, D.L. *The role of vorticity dynamics in vortex breakdown*. in 24th fluid dynamic conference. 1993: AIAA.
74. Faler, J.H. and S. Leibovich, *Disrupted states of vortex flow and vortex breakdown*. Physics of Fluids, 1977. **20**: p. 1385-1400.
75. Liang, H. and T. Maxworthy, *An experimental investigation of swirling jets*. Journal of Fluid Mechanics, 2005. **525**: p. 115-159.
76. Billant, P., J.M. Chomaz, and P. Huerre, *Experimental study of vortex breakdown in swirling jets*. Journal of Fluid Mechanics, 1998. **376**: p. 183-219.
77. Sarpkaya, T., *Turbulent vortex breakdown*. Physics of Fluids, 1995. **7**: p. 2301.
78. Sarpkaya, T., *On stationary and travelling vortex breakdowns*. Journal of Fluid Mechanics, 1971. **45**(03): p. 545-559.
79. Hall, M.G., *Vortex breakdown*. Annual Review of Fluid Mechanics, 1972. **4**: p. 195-218.

80. Faler, J.H. and S. Leibovich, *An experimental map of the internal structure of a vortex breakdown*. Journal of Fluid Mechanics, 1978. **86**(2): p. 313-335.
81. Ludwig, H., Z. Flugwiss, 1962. **10**: p. 242-249.
82. Gallaire, F. and J.M. Chomaz, *Mode selection in swirling jet experiments: a linear stability analysis*. Journal of Fluid Mechanics, 2003. **494**: p. 223-253.
83. Olendraru, C., A. Sellier, M. Rossi, and P. Huerre, *Inviscid instability of the Batchelor vortex: Absolute-convective transition and spatial branches*. Physics of Fluids, 1999. **11**: p. 1805.
84. Lopez, J.M., *On the bifurcation structure of axisymmetric vortex breakdown in a constricted pipe*. Physics of Fluids, 1994. **6**(11): p. 3683-3693.
85. Benjamin, T.B., *Theory of the vortex breakdown phenomenon*. Journal of Fluid Mechanics, 1962. **14**(04): p. 593-629.
86. Randall, J.D. and S. Leibovich, *The critical state: a trapped wave model of vortex breakdown*. Journal of Fluid Mechanics, 1973. **58**(03): p. 495-515.
87. Darmofal, D.L. and E. Murman, *On the trapped wave nature of axisymmetric vortex breakdown*, in *25th Fluid Dynamics Conference*. 1994, AIAA: Colorado Springs, CO.
88. Kirkpatrick, D., *Experimental investigation of the breakdown of a vortex in a tube*. 1964, Aeronautics Research Council.
89. Wang, S. and Z. Rusak, *The effect of slight viscosity on a near-critical swirling flow in a pipe*. Physics of Fluids, 1997. **9**: p. 1914.
90. Healey, J.J., *Inviscid axisymmetric absolute instability of swirling jets*. Journal of Fluid Mechanics, 2008. **613**(-1): p. 1-33.
91. Rusak, Z., A.K. Kapila, and J.J. Choi, *Effect of combustion on near-critical swirling flow*. Combustion Theory and Modelling, 2002. **6**(4): p. 625-645.
92. Umeh, C., Z. Rusak, and E. Gutmark. *Experimental study of reaction and vortex breakdown in a swirl-stabilized combustor*. in *ASME Turbo Expo*. 2009. Orlando, FL.
93. Stein, O. and A. Kempf, *LES of the Sydney swirl flame series: A study of vortex breakdown in isothermal and reacting flows*. Proceedings of the Combustion Institute, 2007. **31**(2): p. 1755-1763.
94. Ho, C.M. and P. Huerre, *Perturbed free shear layers*. Annual Review of Fluid Mechanics, 1984. **16**(1): p. 365-422.
95. Brown, G.L. and A. Roshko, *On density effects and large structure in turbulent mixing layers*. Journal of Fluid Mechanics, 1974. **64**(04): p. 775-816.
96. Sheen, H.J., W.J. Chen, and S.Y. Jeng, *Recirculation zones of unconfined and confined annular swirling jets*. AIAA Journal, 1996. **34**(3): p. 572-579.
97. Zhang, Q., S.J. Shanbhogue, T. Lieuwen, and J. O Connor, *Strain Characteristics Near the Flame Attachment Point in a Swirling Flow*. Combustion Science and Technology, 2011. **183**(7): p. 665-685.
98. Durbin, M.D., M.D. Vangsness, D.R. Ballal, and V.R. Katta, *Study of Flame Stability in a Step Swirl Combustor*. Journal of Engineering for Gas Turbines and Power, 1996. **118**(2): p. 308-315.

99. Kim, D., J.G. Lee, B.D. Quay, and D. Santavicca, *Effect of Flame Structure on the Flame Transfer Function in a Premixed Gas Turbine Combustor*, in *ASME Turbo Expo*. 2008: Berlin, Germany.
100. Huerre, P. and P.A. Monkewitz, *Local and global instabilities in spatially developing flows*. Annual Review of Fluid Mechanics, 1990. **22**(1): p. 473-537.
101. Gaster, M., E. Kit, and I. Wygnanski, *Large-scale structures in a forced turbulent mixing layer*. Journal of Fluid Mechanics, 1985. **150**: p. 23-40.
102. Oster, D. and I. Wygnanski, *The forced mixing layer between parallel streams*. Journal of Fluid Mechanics, 1982. **123**(1): p. 91-130.
103. Fiedler, H.E. and P. Mensing, *The plane turbulent shear layer with periodic excitation*. Journal of Fluid Mechanics, 1985. **150**(1): p. 281-309.
104. Ho, C.M. and L.S. Huang, *Subharmonics and vortex merging in mixing layers*. Journal of Fluid Mechanics, 2006. **119**: p. 443-473.
105. Ho, C.M. and N.S. Nosseir, *Dynamics of an impinging jet. Part 1. The feedback phenomenon*. Journal of Fluid Mechanics, 1981. **105**: p. 119-142.
106. Crow, S.C. and F.H. Champagne, *Orderly structure in jet turbulence*. Journal of Fluid Mechanics, 2006. **48**(03): p. 547-591.
107. Cohen, J. and I. Wygnanski, *The evolution of instabilities in the axisymmetric jet. Part 1. The linear growth of disturbances near the nozzle*. Journal of Fluid Mechanics, 1987. **176**: p. 191-219.
108. Chan, W.T. and N.W.M. Ko, *Coherent structures in the outer mixing region of annular jets*. Journal of Fluid Mechanics, 1978. **89**(03): p. 515-533.
109. Panda, J. and D.K. McLaughlin, *Experiments on the instabilities of a swirling jet*. Physics of Fluids, 1994. **6**: p. 263.
110. Lacarelle, A., T. Faustmann, D. Greenblatt, C.O. Paschereit, O. Lehmann, D.M. Luchtenburg, and B.R. Noack, *Spatiotemporal Characterization of a Conical Swirler Flow Field Under Strong Forcing*. Journal of Engineering for Gas Turbines and Power, 2009. **131**: p. 031504.
111. O'Connor, J. and T. Lieuwen, *Further Characterization of the Disturbance Field in a Transversely Excited Swirl-Stabilized Flame*. Journal of Engineering for Gas Turbines and Power, 2012. **134**(1).
112. Gallaire, F., S. Rott, and J.M. Chomaz, *Experimental study of a free and forced swirling jet*. Physics of Fluids, 2004. **16**: p. 2907.
113. Khalil, S., K. Hourigan, and M.C. Thompson, *Response of unconfined vortex breakdown to axial pulsing*. Physics of Fluids, 2006. **18**: p. 038102.
114. Schimek, S., J.P. Moeck, and C.O. Paschereit, *An experimental investigation of the nonlinear response of an atmospheric swirl-stabilized premixed flame*. Journal of Engineering for Gas Turbines and Power, 2011. **133**.
115. Bellows, B.D., M.K. Bobba, J.M. Seitzman, and T. Lieuwen, *Nonlinear Flame Transfer Function Characteristics in a Swirl-Stabilized Combustor*. Journal of Engineering for Gas Turbines and Power, 2007. **129**(954).
116. Lieuwen, T. and Y. Neumeier, *Nonlinear pressure-heat release transfer function measurements in a premixed combustor*. Proceedings of the Combustion Institute, 2002. **29**(1): p. 99-105.

117. Kim, K.T. and S. Hochgreb, *The nonlinear heat release response of stratified lean-premixed flames to acoustic velocity oscillations*. Combustion and Flame, 2011. (in press).
118. Syred, N., C. Wong, V. Rodriguez-Martinez, J. Dawson, and R. Kelso. *Characterisation of the occurrence of the precessing vortex core in partially premixed and non-premixed swirling flow*. in *12th International Symposium on Applications of Laser Techniques to Fluid Mechanics*. 2004. Lisbon, Portugal.
119. Dawson, J.R., V.M. Rodriguez-Martinez, N. Syred, and T. O'Doherty, *The effect of combustion instability on the structure of recirculation zones in confined swirling flames*. Combustion Science and Technology, 2005. **177**(12): p. 2349-2371.
120. Pier, B., *Open-loop control of absolutely unstable domains*. Proceedings of the Royal Society of London. Series A: Mathematical, Physical and Engineering Sciences, 2003. **459**(2033): p. 1105.
121. Masselin, M. and C. Ho, *Lock-On and Instability in a Flat Plate Wake*, in *AIAA Shear Flow Control Conference*. 1985: Boulder, CO.
122. Iudiciani, P. and C. Duwig, *Large Eddy Simulation of the Sensitivity of Vortex Breakdown and Flame Stabilisation to Axial Forcing*. Flow, Turbulence and Combustion, 2011. **86**: p. 639-666.
123. Meier, W., P. Weigand, X.R. Duan, and R. Giezendanner-Thoben, *Detailed characterization of the dynamics of thermoacoustic pulsations in a lean premixed swirl flame*. Combustion and Flame, 2007. **150**(1-2): p. 2-26.
124. Gursul, I., *Effect of nonaxisymmetric forcing on a swirling jet with vortex breakdown*. Journal of Fluids Engineering, 1996. **118**: p. 316.
125. Matta, L.M., H. Wuersig, A. Choung, J.I. Jagoda, and B.T. Zinn, *Excitation of a round jet by transverse standing acoustic oscillations*, in *34th Aerospace Sciences Meeting and Exhibit*. 1996: Reno, NV.
126. Cary, A.W., D.L. Darmofal, and K.G. Powell, *Evolution of asymmetries in vortex breakdown*, in *29th Fluid Dynamics Conference*, AIAA, Editor. 1998: Albuquerque, NM.
127. Reynolds, W.C., D.E. Parekh, P.J.D. Juvet, and M.J.D. Lee, *Bifurcating and Blooming Jets*. Annual Review of Fluid Mechanics, 2003. **35**(1): p. 295-315.
128. Preetham and T. Lieuwen, *Nonlinear Flame-Flow Transfer Function Calculations: Flow Disturbance Celerity Effects*, in *40th AIAA/ASME/SAE/ASEE Joint Propulsion Conference and Exhibit*. 2004: Fort Lauderdale, FL.
129. Wang, S., S.Y. Hsieh, and V. Yang, *Unsteady flow evolution in swirl injector with radial entry. I. Stationary conditions*. Physics of Fluids, 2005. **17**: p. 045106.
130. Huang, Y., S. Wang, and V. Yang, *Systematic Analysis of Lean-Premixed Swirl-Stabilized Combustion*. AIAA Journal, 2006. **44**(4): p. 724-740.
131. Lasheras, J.C., J.S. Cho, and T. Maxworthy, *On the origin and evolution of streamwise vortical structures in a plane, free shear layer*. Journal of Fluid Mechanics, 1986. **172**(1): p. 231-258.
132. Michalke, A., *On the inviscid instability of the hyperbolic tangent velocity profile*. Journal of Fluid Mechanics, 1964. **19**(04): p. 543-556.

133. Hermanson, J.C. and P.E. Dimotakis, *Effects of heat release in a turbulent, reacting shear layer*. Journal of Fluid Mechanics, 1989. **199**: p. 333-375.
134. Ghosh, A., Q. Diao, and K. Yu, *Effects of Fuel Density, Velocity, and Composition on Flame-Acoustic Interaction*, in *45th Aerospace Sciences Meeting and Exhibit*. 2007: Reno, NV.
135. Batchelor, G.K. and A.E. Gill, *Analysis of the stability of axisymmetric jets*. J. Fluid Mech, 1962. **14**(4): p. 529-551.
136. Cohen, J. and I. Wygnanski, *The evolution of instabilities in the axisymmetric jet. Part 1. The linear growth of disturbances near the nozzle*. J. Fluid Mech, 1987. **176**: p. 191–219.
137. Martin, J.E. and E. Meiburg, *Numerical investigation of three-dimensionally evolving jets subject to axisymmetric and azimuthal perturbations*. Journal of Fluid Mechanics, 1991. **230**(1): p. 271-318.
138. Ko, N.W.M. and W.T. Chan, *The inner regions of annular jets*. Journal of Fluid Mechanics, 1979. **93**(03): p. 549-584.
139. García-Villalba, M., J. Fröhlich, and W. Rodi, *Identification and analysis of coherent structures in the near field of a turbulent unconfined annular swirling jet using large eddy simulation*. Physics of Fluids, 2006. **18**: p. 055103.
140. Huang, Y. and V. Yang, *Effect of swirl on combustion dynamics in a lean-premixed swirl-stabilized combustor*. Proceedings of the Combustion Institute, 2005. **30**(2): p. 1775-1782.
141. Schwing, J., T. Sattelmayer, and N. Noiray, *Interaction of Vortex Shedding and Transverse High-Frequency Pressure Oscillations in a Tubular Combustion Chamber*, in *ASME Turbo Expo*. 2011: Vancouver, Canada.
142. Bechert, D. and E. Pfizenmaier, *On wavelike perturbations in a free jet travelling faster than the mean flow in the jet*. Journal of Fluid Mechanics, 2006. **72**(02): p. 341-352.
143. Gupta, A.K., D.G. Lilley, and N. Syred, *Swirl Flows*. 1984: Abacus Press.
144. Petrie, H.L., A.A. Fontaine, M.H. Krane, M.J. Weldon, and B.R. Elbing. *Practical Estimation of PIV Uncertainty using Pseudo Image Pairs for CFD Validation and Verification*. in *PIV Uncertainty Workshop*. 2011. Las Vegas, NV.
145. Coleman, H.W. and W.G. Steele, *Experimentation and uncertainty analysis for engineers*. 1999: Wiley-Interscience.
146. Bodén, H. and M. Åbom, *Influence of errors on the two microphone method for measuring acoustic properties in ducts*. The Journal of the Acoustical Society of America, 1986. **79**: p. 541.
147. Bendat, J. and A. Piersol, *Random Data*. 2010, Hoboken, NJ: John Wiley & Sons, Inc.
148. Shreekrishna and T. Lieuwen, *Comparitive Study of Harmonically Forced, High Frequency Premixed Flame Response Mechanisms*, in *47th AIAA/ASME/SAE/ASEE Joint Propulsion Conference*. 2011: San Diego, CA.
149. Acharya, V., Shreekrishna, D.H. Shin, and T. Lieuwen, *Swirl effects on harmonically excited, premixed flame kinematics*. Combustion and Flame, 2011(in press).

150. Lieuwen, T. and V. Yang, *Combustion Instabilities in Gas Turbine Engines: Operational Experience, Fundamental Mechanisms, and Modeling*. Progress in Astronautics and Aeronautics Series, ed. F.K. Lu. 2006: AIAA.
151. Fuchs, H.V., E. Mercker, and U. Michel, *Large-scale coherent structures in the wake of axisymmetric bodies*. Journal of Fluid Mechanics, 1979. **93**(01): p. 185-207.
152. Paschereit, C.O., E. Gutmark, and W. Weisenstein, *Excitation of thermoacoustic instabilities by interaction of acoustics and unstable swirling flow*. AIAA journal, 2000. **38**(6): p. 1025-1034.
153. Loiseleux, T., J.M. Chomaz, and P. Huerre, *The effect of swirl on jets and wakes: Linear instability of the Rankine vortex with axial flow*. Physics of Fluids, 1998. **10**: p. 1120.
154. Healey, J.J., *Inviscid axisymmetric absolute instability of swirling jets*. Journal of Fluid Mechanics, 2008. **613**(1): p. 1-33.
155. Shanbhogue, S., *Dynamics of perturbed exothermic bluff-body flow-fields*, in *Aerospace Engineering*. 2008, Georgia Institute of Technology: Atlanta, GA.
156. Ho, C.M. and L.S. Huang, *Subharmonics and vortex merging in mixing layers*. Journal of Fluid Mechanics, 1982. **119**: p. 443-473.
157. Ho, C.-M. and N.S. Nosseir, *Dynamics of an impinging jet. Part 1. The feedback phenomenon*. Journal of Fluid Mechanics, 1981. **105**: p. 119-142.
158. García-Villalba, M. and J. Fröhlich, *LES of a free annular swirling jet-Dependence of coherent structures on a pilot jet and the level of swirl*. International Journal of Heat and Fluid Flow, 2006. **27**(5): p. 911-923.
159. Bechert, D. and E. Pfizenmaier, *On wavelike perturbations in a free jet travelling faster than the mean flow in the jet*. Journal of Fluid Mechanics, 1975. **72**(2): p. 341-352.
160. Shanbhogue, S., D.H. Shin, S. Hemchandra, D. Plaks, and T. Lieuwen, *Flame sheet dynamics of bluff-body stabilized flames during longitudinal acoustic forcing*. Proceedings of the Combustion Institute, 2009. **32**(2): p. 1787-1794.
161. Aroussi, A., S. Kucukgokoglan, M. Menacer, and S.J. Pickering. *PIV Measurements Of Swirling Flows From Two Adjacent Burners*. in *The 9th International Symposium on Flow Visualization*. 2000. Edinburgh, Scotland.

VITA

Jacqueline Antonia O'Connor was born on July 15, 1984 in Manchester, CT to John and Sheryl O'Connor. Raised in South Windsor, CT with her brother Tom, she attended the Loomis Chaffee School from 1998-2002. She earned a Bachelors of Science in Aeronautics from the Massachusetts Institute of Technology in 2006, a Masters of Science in Aerospace Engineering from the Georgia Institute of Technology in 2009, and will receive her Ph.D. in 2012. She was a National Science Foundation Graduate Fellow from 2006-2009 and has won numerous awards from the AIAA, ASME, and Georgia Tech. She enjoys playing the violin in small chamber ensembles and traveling with her partner, Alexander Pace.